Towards degradable photonic biosensors for the microbiological screening of water samples

Geert-Jan Graulus

Promotors: prof. dr. P. Dubruel, prof. dr. ir. H. Ottevaere
          prof. dr. S. Van Vlierberghe, prof. dr. ir. H. Thienpont

Dissertation submitted in fulfillment of the requirements
for the academic degree of

Doctor (Ph.D.) of Science: Chemistry

Department of Organic and Macromolecular Chemistry
Faculty of Sciences
Ghent University

Academic year 2017-2018

GHENT
UNIVERSITY

Members of the examination committee

Promotors

Prof. Dr. Peter Dubruel (Ghent University)
Prof. Dr. Ir. Heidi Ottevaere (Vrije Universiteit Brussel)
Prof. Dr. Sandra Van Vlierberghe (Ghent University)
Prof. Dr. Ir. Hugo Thienpont (Vrije Universiteit Brussel)

Internal members

Prof. Dr. Filip Du Prez (chairman, Ghent University)
Prof. Dr. Richard Hoogenboom (secretary, Ghent University)
Prof. Dr. Ir. Christian Stevens (Ghent University)
Prof. Dr. Christophe Detavernier (Ghent University)

External experts

Prof. Dr. Ir. Hubert Rahier (Vrije Universiteit Brussel)
Prof. Dr. Christine Jérôme (Université de Liège)
Prof. Dr. Jean-Marie Raquez (Université de Mons)

Preface

> *"If I have seen a little further it is by standing on the shoulders of giants."*
>
> — Sir Isaac Newton

With the submission of this manuscript an important chapter in my life comes to an end. It has been a great journey and luckily I did not have to walk the path by myself. Therefore, I would like to thank my fellow travellers who have helped me along the way.

First of all, I wish to thank my promotors prof. dr. Peter Dubruel, prof. dr. Sandra Van Vlierberghe, prof. dr. ir. Heidi Ottevaere and prof. dr. ir. Hugo Thienpont who started my wandering by giving me the opportunity to do a PhD in their research groups. Being the first PhD student sharing his time between the Polymer Chemistry & Biomaterials group and the Brussels Photonics team wasn't easy, but you pushed me to keep going even when the results were not as great as I liked them to be. Also a big thank you for the many conferences, symposia, team buildings, group drinks and pizza seminars I was allowed to attend during the past 4-5 years. I hope we will meet again on many such events in the future. On a personal note, Sandra as a founding member of the PBM running club, you have inspired me to hit the gym as soon as this thesis is defended. Since this promise is now written black-on-white, there is no turning back.

I would also like to thank the jury members for their valuable input after reading the manuscript and during the discussion at the closed session. Thanks to your feedback, I was able to further improve this PhD thesis. I know I have been very demanding of you (e.g. a second closed session and a very tight time schedule regarding the continuation of my work at Hasselt University). I appreciate

your flexibility and look forward to the discussion during the public defense.

Project related, I would like to express my gratitude to Jens De Pelsmaeker. It was great to share this project with you and combine your background in photonics with mine in chemistry. I think we have come to new insights that non-interdisciplinary teams would not have been able to notice. Next, it was a pleasure to be able to share the polyester work, and the occasional whiff of phosgene, with Maxime Vagenende and Jasper Van Hoorick, the polyestars. I hope you can finish what we started. I also owe my gratitude to Myriam Gómez Tardajos, Lara Misseeuw, Lien Smeesters, Liesbeth Tytgat and Julie Verdood for their help with X-ray photoelectron spectroscopy, atomic force microscopy, optical transmission measurements and optical profilometry. Regarding polymer processing, I would like to thank the team at VKC-Centexbel and ing. Kurt Rochlitz at B-Phot for the fabrication of uniform plastic substrates and all hot embossing experiments, respectively.

Next, I would like to thank all the current and past group members I had the pleasure to get to know. Unfortunately, there are simply too many to sum up here, so please know that "*all*" is the most important word in the previous sentence. Not only did we have many fruitful discussions about our research, but the team members at PBM and B-Phot have become good friends. On good days it was great to share the success with my lab mates, while on bad days, I knew someone would cheer me up. However, I think everyone will agree that our lab manager Veerle Boterberg deserves to be mentioned by name in these acknowledgements: when some equipment broke down or when "someone" cut their finger on a piece of glass , you were always there to save us. In addition, I want to thank Arne Goes and Valérie Kodeck for being the most epic lab responsibles a master and junior PhD student could wish for. Regarding laboratory morale and general well being, I would like to thank my truly great adversaries during the lunch time games of Carcassone and Settlers of Catan. This is especially true for Dr. Ir. Arn Mignon (known from rules IV and VI of the PBM house rules), although it has been over 3 semesters since he was able to win a championship. Best of luck in the future.

be able to start my work in the Biomolecule Design Group. I am also particularly grateful to Ms. Isabel Thys, who was particularly understanding the past weeks and exhausted all her possibilities to avoid jeopardizing my job application at Hasselt University.

Last but definitely not least, I would like to thank Linde, who after 6 years became my wife, disregarding the previously mentioned bad jokes and my somewhat autistic tendencies when it comes to shopping and home decoration. Dear Linde, with this chapter coming to a close, I am looking forward to starting the next one closer to home together with you and baby Jasper.

Geert-Jan Graulus

List of Abbreviations

E. coli	*Escherichia coli*
µTAS	Micro total analysis systems
AB	Antibody
AFM	Atomic force microscopy
ATR	Attenuated total reflection
CCD	Charge-coupled device
COC	Cyclic olefin copolymer
DIPEA	N,N-diisopropylethylamine
DIW	Deionised water
DNA	Deoxyribonucleic acid
EAHEC	Enteroaggregative haemorrhagic *E. coli*
EHEC	Enterohaemorrhagic *E. coli*
ELISA	Enzyme-linked immunosorbent assay
EPA	United States Environmental Protection Agency
EU	European Union
Fab	Antigen binding fragment of an antibody
Fc	Crystallisable fragment of an antibody

FDA	American food and drug administration
FISH	Fluorescent *in situ* hybridisation
FT-IR	Fourier transform infrared
Fv	Variable fragment of an antibody
HPLC	High Performance Liquid Chromatography
HUS	Haemolytic uraemic syndrome
IUPAC	International union of pure and applied chemistry
lacOCA	O-carboxy anhydride derived from lactic acid
LoC	Lab-on-a-chip
LSPR	Localised Surface Plasmon Resonance
M_n	Number average molecular weight
$M_n^{Targ.}$	Molecular weight expected at 100% conversion
MA	Mandelic acid
MALDI	Matrix assisted laser desorption/ionisation
ManOCA	O-carboxy anhydride derived from mandelic acid
MF	Membrane filtration
MO	Microorganism
MPN	Most probable number
MRSA	methicillin-resistant *Staphylococcus aureus*
MS	Mass Spectrometry
MTF	Multiple-tube fermentation
MUG	4-methylumbelliferyl-B-D-glucuronide
NCA	N-carboxy anhydride

OCA	O-carboxy anhydride
P/A	Presence/absence
P3HB3HV	poly(3-hydroxybutyrate-co3-hydroxyvalerate)
PCR	Polymerase chain reaction
PD	Power density
PDA	poly(dopamine)
PEI	poly(ethylene imine)
PHA	poly(β-hydroxyalkanoates)
PHB	poly(3-hydroxybutyrate)
PTFE	Poly(tetrafluoroethylene)
PVD	Physical vapour deposition
RIID	Radiation isotope identifier
RNA	Ribonucleic acid
SAM	Self-assembled monolayer
SCA	Static contact angle
SCA	Static contact angle
SERS	Surface enhanced raman scattering
SPP	Surface plasmon polariton
SPR	Surface Plasmon Resonance
SPRi	Surface plasmon resonance imaging
SVR	Surface to volume ratio
T_g	Glass transition temperature
THF	Tetrahydrofuran

TIR	Total internal reflection
TM	Transverse-magnetic
TOF	Time of flight
TTir	Through Transmission IR
WHO	World Health Organisation
XPS	X-ray photoelectron spectroscopy

List of Figures

List of Tables

Contents

CONTENTS

Chapter 1

Introduction

> *"Water should not be judged by its history, but by its quality"*
>
> — Lucas Van Vuuren

1.1 Problem Statement

It is hard to imagine life as we know it without water simply because water is one of the bare necessities needed to stay alive. However, despite its high abundance, not all water reservoirs contain water suitable for consumption, making potable water a lot more uncommon than one would expect.

To declare water potable, analytical tests are performed to discover any form of pollution. Water pollution can be defined very broadly as any change in the biological, physical or chemical characteristics of a particular water source. However, a more relevant description of water pollution would be the presence of certain chemicals and pathogens. Unfortunately, even today the consumption of contaminated water constitutes a major health issue. This health effect, in turn, causes economic and social problems, since those affected can often no longer fulfill their daily activities.

The consumption of unsafe drinking water may result in severe dehydration as a result of diarrhoea.[1] This gastrointestinal infection can be life-threatening when combined with bad hygiene and lack of

medication. According to the World Health Organization (WHO),
diarrhoeal disease is responsible for the deaths of 1.5 million people
annually from which 88% are due to unsafe drinking water, inappro-
priate sanitation and lack of hygiene.[2,3]

A large share of these casualties occur in poor and developing
countries where insufficient clean (drinking) water is present, fig-
ure 1.1), e.g. Sub-Saharan Africa where less than 75% of the popula-
tion has access to improved drinking water sources. Moreover water-
borne pathogens remain the most predominant cause of death among
young children in developing countries as unsafe water is linked to
the deaths of about 1000 children aged 0-5 per day.[1,3,4]

This situation is further aggravated by natural disasters and con-
flict, forcing people to turn to refugee camps, which are not always
equipped to handle large groups of people.[5–8] This puts additional
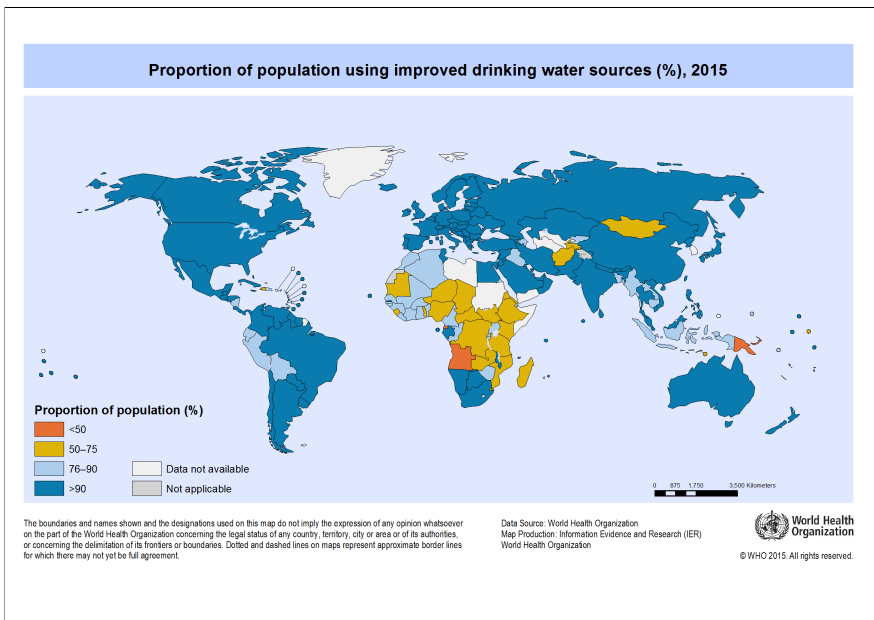
Figure 1.1: Map classifying countries based on the proportion of their
population that has access to improved water sources (2015). As can be
seen, some developing countries are not yet able to provide safe drinking
water to most of their citizens. Map reproduced with permission of the
World Health Organisation (WHO)

strain on the available water sources and increases the risk for disease outbreaks like diarrhoea, cholera and typhus.[9] The seasonal influence on pathogen concentrations in turn poses an additional difficulty to ensure the safety of local water sources.[10]

It has to be stressed that also industrialised countries are at risk, as confirmed by water contaminations in Canada,[11,12] the United States,[13–15] and Germany.[16,17] Especially the 2011 outbreak in Germany is an interesting case-study as it illustrates the difficulty associated with identifying the specific source of infection. This not only led to the death of 53 people, but the anxiety among the population as a result of the wide media coverage also resulted in vast economic losses (€ 812 million).[18] Both in Germany and the rest of the European Union (EU), certain food products were destroyed without a definite ruling with respect to their supposed risk to the public health. In the end, vegetable sprouts contaminated with enteroaggregative hemorrhagic *Eschericia coli* (EAHEC) were identified as the responsible disease vector.[19]

In order to prevent future outbreaks and unnecessary deaths, it is thus of great importance to remain vigilant and continuously monitor the quality of (drinking) water sources. In the following section, water contamination will be further specified and an overview of the most common analysis methods will be provided.

1.2 Assessment of Water Safety

Considering the broad definitions provided in the previous section, water pollution can be further subdivided into three categories: radiological, chemical and biological contamination. Radiological hazards are associated with ionising radiation emitted by certain radioisotopes present in water sources. Given their low prevalence in nature, such compounds rarely have a significant effect on public health. The radiation dose, and thus the health effect, resulting from ingestion of radionuclides also depends on a number of chemical and biological factors, e.g. the fraction that is adsorbed by tissue, the type of tissue or organ that is affected and the nature of the radiation (i.e. α, β or γ-radiation). Needless to say, this class of water contamination gains importance when confronted with severe nuclear incidents like

the meltdown in Chernobyl (1986) or the flooding of the Fukushima power plant (2011). Ionising radiation can be easily detected using a Geiger-Muller tube, or Geiger counter, but to obtain more details about the specific radionuclides present, more specialised techniques like a radiation isotope identifier (RIID) should be applied.[20] These types of devices measure the energy of the emitted radiation, which allows the identification of the radionuclides present in a sample.

When considering chemical pollution, the focus usually lies on the presence of toxic and/or harmful compounds. However, substances that result in an unpleasant smell, taste or look of the water are also to be classified under this form of contamination.[21] Limiting the scope to the detection of harmful chemicals, the emphasis lies mainly on the detection of heavy metals (e.g. As, Cd, Hg, Pb, Sn), pesticides and water-soluble toxins.[22–24] Recently, the extraction of oil and natural gas from shale rock, has revived the interest in the detection of other compounds (e.g. aliphatic and aromatic hydrocarbons, volatile organic compounds and endocrine disruptive chemicals) as well.[25–27] The presence of chemical contaminants can easily be verified through analysis of a water sample with e.g. high performance liquid chromatography (HPLC), mass spectrometry (MS) and spectroscopic techniques.[28] The detection limit of this equipment is very low (down to $ng\,L^{-1}$), which means that any chemical pollution can be determined qualitatively and quantitatively in a relatively short time span (approx. 30 minutes for conventional HPLC-MS experiments) as the samples generally do not require any preconcentration.[29]

In contrast to the previous classes, the detection of biological pollution is not as straightforward as compared to the determination of chemical pollution. Not only are the analytes themselves much more complex, the concentrations at which they can induce negative health effects tend to be very low. In principle, even a single bacterium could develop into a colony when exposed to the appropriate environmental conditions. This is why the WHO imposes very stringent requirements when it comes to drinking water. At present, the biological water quality is generally monitored via culture-based methods.[17] These techniques exhibit a high sensitivity (1 cell per 100 mL) as the organisms originally present are allowed to multiply to detectable numbers. On the other hand, this methodology requires

long culture times (24-48 h) and high cost facilities, which are not always available to the people most in need of drinking water screening methods.

In this work, detection of water pollution will be narrowed down to the detection of Escherichia coli, or *E. coli* . This strain of bacteria is considered to be an important bacterial indicator for polluted water streams,[30,31] which will be further elaborated in the following section along with common detection methods for *E. coli*.

1.2.1 *Escherichia coli*

Faecal contamination of water is a common cause of water pollution through the release of bacteria which may induce infections in the consumer. The presence of coliforms may therefore serve as an indicator or this type of water contamination.[30] *E. coli* is the only member of coliforms that is found invariably within the faeces of a broad range of warm-blooded animals.[19] This together with the fact that it outnumbers other coliforms, makes it the preferred microbial indicator.[30] Other microbial indicators, like *Clostridium perfringes*, *Enterococci*, *Bacteroidales* and *Lachnospiraceae* have been suggested as well.[32,33] One should however keep in mind that the absence of bacterial indicators in a water sample does not imply the absence of viruses and protozoa.[30,34,35]

Since prevention is preferred over curing, the detection of *E. coli* is of great importance to society. Both the U.S. Environmental Protection Agency (EPA) as well as the Council of the European Union defined the absence of coliforms as the criterion to consider water potable in order to prevent waterborne disease outbreaks.[36,37] *E. coli* is a rod-shaped bacterium (figure 1.2) from the coliform group. Coliforms are defined as all facultative anaerobic, gram-negative, non spore-forming, oxidase-negative, rod-shaped bacteria that ferment lactose to acid and gas within 48h at 35°C.[21,30]

These coliforms are commonly found in the gastrointestinal tract of humans and other warm-blooded animals and thus in their faecal matter. Both genetically and phenotypically, *E. coli* is a quite diverse species as only 20% of its genome is shared among all strains.[39] This high degree of diversity has led to the identification of many *E. coli* subgroups, which differ on the molecular level (e.g. the ability to use
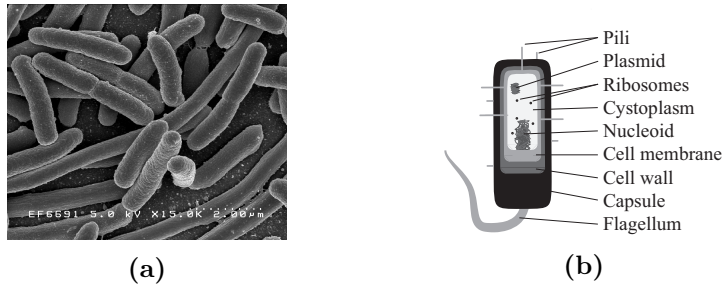
Figure 1.2: Visual representation of the *E. coli* bacillus, with (a) showing a scanning electron micrograph of *Escherichia coli*, grown in culture and adhered to a cover slip and (b) showing an illustration highlighting its key cellular components.[38]

a specific carbon source, toxin producing capabilities or antibiotic resistance). In addition, it has been argued from an evolutionary point of view that some members of the *Shigella* genus (i.e. *S. dysenteriae*, *S. flexneri*, *S. boydii*, and *S. sonnei*) could be reclassified as *E. coli*.[40] In practice, however, *E. coli* strains are not distinguished on an evolutionary or genetic basis, but rather based on the presence of specific surface antigens.[19] In this method, a distinction is made among the O-polysaccharide antigens, the flagellar H-antigens and the capsular K-antigens. Since at the time of their discovery only a limited number of laboratories were able to distinguish different K-antigens, O/H serotyping became common practice. At present, 186 O-groups and 53 H-types have been identified.[19]

Most strains of *E. coli* are harmless and in fact important for the human intestinal flora and vitamin K production.[41–43] However, the enterohaemorrhagic *E. coli* (EHEC, serotype O157:H7), among others, is known to cause diarrhoeal disease owing to the production of Shiga-like toxins.[17] When infected, symptoms can include diarrhoea, abdominal cramps and even vomiting. A large share of the infected patients can recover within approximately 10 days. However, 5% of all patients, mainly children and elderly, may develop the life-threatening post-diarrhoeal haemolytic uraemic syndrome (HUS).[44] This is a severe disease known to cause acute kidney failure and microangiopathic haemolytic anaemia.

1.2.2 Common detection methods for bacteria

Already in 1905, initiatives, like the publication of the *Standard Methods for the Examination of Water and Wastewater*, were set up to provide a clear overview of the possible procedures for the enumeration of bacteria and to establish some common practices when analysing water samples.[45] Nowadays, many different techniques are in use for the detection of coliforms and other pathogenic bacteria in water samples based on the guidelines of the WHO.

Important requirements for the detection of pathogens include good sensitivity and specificity. Sensitivity means that very low numbers of target organisms can be detected (i.e. low detection limit), whereas specificity means that only the target organism is detected. Inadequate sensitivity may lead to false negative results, allowing coliform contamination to remain undetected. In the case of cell culture-based techniques, false negatives may for example occur when bacteria are stressed or injured and therefore lack culturability or when bacteria are masked by biofilm formation.[46] Inadequate specificity, on the other hand, may lead to false positive results, when harmless bacteria are mistaken for pathogens. This could result in the application of the wrong treatment in a clinical setting or large economic losses when uncontaminated products are wrongfully destroyed.

The ideal characteristics of a diagnostic test for resource-limited settings are described by so-called 'ASSURED'-tests, coined by the WHO:[47]

Affordable	by those at risk of infection
Sensitive	yielding few false negative results
Specific	yielding few false positive results
User-friendly	simple to perform, requiring minimal training
Rapid and robust	enable treatment at first visit; no need for refrigerated storage
Equipment-free	ready to use
Deliverable	to those who need it

In what follows, several methods for the detection of *E. coli* will be described briefly to identify the shortcomings of currently applied detection strategies.

Multiple-tube fermentation

The multiple-tube fermentation (MTF) technique is a very time-consuming test to detect total coliforms in water samples. Graduated quantities of the water sample of interest are added to a series of fermentation tubes filled with lauryl tryptose broth. The test tubes are incubated for 48h at 35 °C. Any production of gas, acid formation or abundant growth in the tubes constitutes a positive presumptive test. The amount of microorganisms present are expressed in terms of the Most Probable Number (MPN), which is a statistical estimate of the mean number of coliforms in the water sample, with 1 positive test in a series of 15 experiments (three dilutions in fivefold) corresponding to an MPN of 1.8 colony forming units (CFU).[48] MTF is thus a semi-quantitative technique. The attainable precision is also rather low, since sample preparation has a large influence given the subsequent dilutions.[48] Moreover, a confirmation step is needed to exclude false positives. Nevertheless, it may be useful when the conditions, e.g. turbid or coloured waters, do not allow the use of membrane filtration techniques.[49]

Membrane filtration

Membrane filtration (MF) consists of filtering bacteria from the water sample on a sterile filter with a 0.45 mm pore size. The filter is incubated on a selective medium during 24-48 hours, where after the typical colonies, formed on the filter, are counted.[49] However, high numbers of background heterotrophic bacteria are shown to decrease the coliform recovery by MF.[50] Another disadvantage is the inability to recover stressed or injured coliforms. There are lots of selective media in use indicating that no universal medium exists to allow enumeration of different coliforms. Similar to MTF, MF is a time-consuming technique. Advantages compared to MTF are the greater sensitivity (limit of detection as low as 1 cell per 100 mL), reliability and the possibility for quantitative enumeration.[51]

Presence/Absence Test

As the total coliform rule comprises zero tolerance of any coliform in water, knowing whether or not coliform contamination occurs, is more important than its exact quantification. The Presence/Absence (P/A) test provides a simple and straightforward control.[52] This test uses the fluorogenic compound 4-methylumbelliferyl-B-D-glucuronide (MUG), which is hydrolysed by glucuronidase to yield a fluorescent product.[53] *E. coli* and some other pathogenic bacteria produce glucuronidase, which leads to straightforward identification of these pathogens. Although the detection limit is not as low as the previous methods (e.g. 10 CFU in a 4 mL sample), this method can be performed in 30 min and is able to detect stressed bacteria.[54,55] The disadvantage of this reliable test is again the need for a time-consuming incubation step (multiple hours) when very low numbers are to be detected.

Mass spectrometry

Mass spectrometry (MS) techniques are able to identify pathogens in samples of unknown composition. Each pathogen creates a specific fingerprint in the mass spectrum, providing trustworthy identification. Advantages include high resolution, speed (as low as 5 minutes), high degree of automation and no need for specialised manpower.[56] However, the complexity and the bulky laboratory equipment render in-field applications questionable.[57] Like for the P/A test, the bacteria have to be isolated and multiplied (10^5-10^6 cells per sample) before mass spectroscopical techniques can be applied, which again increases the time necessary for identification.

Nucleic acid detection

Nucleic acid-based detection methods rely on the specific recognition between a nucleic acid probe and a nucleic acid target. The recognition event includes the sequence-specific interaction between complementary nucleic acid strands, either deoxyribonucleic acid (DNA) or ribonucleic acid (RNA). The two main types of this detection method are polymerase chain reaction (PCR) and hybridization.[32]

During PCR, the target nucleic acid sequence (DNA or RNA) will be amplified to enable its detection. To achieve this, the target nucleic acid sequence is heated to induce denaturation, where after a primer is allowed to bind specifically to the beginning of the target sequence. The PCR primers are very specific and thus only the target will be read and copied when the enzyme polymerase binds to the primer and subsequently produces a complementary DNA strand. This replication process is repeated several times (10 - 35 cycles) and target identification is provided by gel electrophoresis.[58,59] Despite the fact that this method is able to detect low numbers of the target nucleic acid, the need for multiple repetitions again leads to longer analysis times (multiple hours). When applied for the detection of *E. coli* LODs of 6-10 CFU mL^{-1} have been achieved within 5 h.[60]

Hybridization involves the specific binding of a labeled nucleotide probe to a target nucleic acid sequence. If the label is a fluorochrome, the method is called fluorescent *in situ* hybridization (FISH). The fluorescence intensity is used for quantification.[32] Like PCR, this method thus requires the lysing of the bacterium which complicates the analysis and prevents in-field applications. However, FISH has been applied as an alternative for cell cultures following the isolation of bacteria via MF.[61] In this report the authors mention a detection limit as low as 1 cell mL^{-1} after performing a 2 h hybridisation with ribosomal RNA.

Immunosensing

Immunological methods rely on the specific recognition between antibodies and antigens. The high affinity of this recognition reaction provides high sensitivity. As the taxonomic level of targeted antigens can be chosen, very specific detection of antigens at the family, genus, species or serotype level is possible.[49] Labelling the antibodies with an enzyme or fluorochrome enables their detection. Immunosensing is a rapid, straightforward and specific method. However, interference with non-target organisms can occur if the targeted antigen is expressed by multiple types of bacteria. For this reason the bacteria of interest are often first immobilised using one antibody, followed by washing away any unbound bacteria. Identification is achieved via a second enzyme-linked antibody that will only be retained if the

targeted bacterium is present. This process is known as the enzyme-linked immunosorbent assay (ELISA) and the associated limit of detection is estimated to be 100 pg mL^{-1} for a 100 kDa protein[62] or 10^3-10^5 cells mL^{-1} for *E. coli* O157:H7.[63,64] However, the protocol also becomes more complex thereby impeding in-field applications.

Trends in the detection of micro-organisms

As was discussed for detection methods techniques relying on the binding potential of antibodies or nucleic acids, biological recognition elements (a.o. antibodies, enzymes or nucleic acids) are currently being explored to increase the specificity of various sensing methodologies. The thus obtained devices are commonly called biosensors, although the International Union of Pure and Applied Chemistry (IUPAC) adopted a more comprehensive definition: a biosensor is a self-contained integrated device which is capable of providing specific quantitative or semi-quantitative analytical information using a biological recognition element which is in direct spatial contact with a sensor element and a signal processing system.[65] The recognition element thus ensures the selectivity, while the transducer translates the binding event to a measurable signal that can be processed by the signal processing system.[66,67] This modular approach allows the application of a certain set-up for the detection of multiple analytes by simply interchanging the immobilised recognition molecules.

As indicated in the previous sections, to date the enumeration of bacteria is performed in laboratory environments as portability remains an important issue in conventional detection methods. To solve this blind spot and allow analyses to be run in the field, the interest in miniaturised set-ups has been growing over the past years.

Keeping in mind the problem statement (section 1.1), there is a need for portable, sensitive detection methods to enable the assessment of water safety, especially in developing countries and remote area's that lack the laboratory infrastructure required for today's microbiological methods. Miniaturised biosensors will therefore form the basis for the discussion presented in the upcoming section.

1.3   The concept of Lab-on-a-Chip

Lab-on-a-chip (LoC) devices, also known as micro total analysis systems (μTAS), are being designed as an alternative for the traditional (cell culture-based) techniques mentioned earlier (section 1.2.2).[68–70] As the name suggests, an entire laboratory is integrated on a microchip. The purpose of a LoC is to analyse a liquid (or gaseous) sample in-field by performing all stages of the analytical process on a small scale. Hence, the LoC must be able to perform standard laboratory functions like sample treatment, mixing, reacting, separation and detection. The general architecture of LoC devices is described in several papers.[71–74] In brief, LoC devices contain miniaturised components, such as pumps, mixers, reactors and detectors. The miniaturisation of these devices is only possible thanks to advances in microfabrication technology realised in recent years.

Miniaturisation offers several advantages in line with the principle of positive downscaling.[68] Sample consumption as well as reagent and solvent consumption are significantly reduced (from mL to pL). Owing to the smaller sample size, the analysis time also shortens. The small dimension of the channels in the microfluidic device offer a high surface to volume ratio (SVR), meaning that the contact between the liquid sample and the channel surface is increased. This provides a method to further decrease the detection limits to within the fM range, with the ultimate goal being single-molecule detection within the nanoliter samples.[75] Specificity is introduced through functionalisation of the sensing zone, which leads to selective capture of the target molecule under continuous flow.[76] Integrating many LoC devices into one larger device makes massive parallel data generation possible, thereby further decreasing the overall analysis time as compared to running the individual analyses in succession.[68]

1.3.1   Biological recognition elements for LoC

As mentioned in section 1.2.2, a biosensor is a device that combines biological recognition elements with sensitive transducers to obtain (semi-)quantitative information. Given the low sample volumes that are analysed in LoCs, it comes as no surprise that most LoC sensors are in fact biosensors that utilise the inherent specificity of biological

receptors. Enzymes were the first recognition elements to be applied in biosensing,[77,78] but whole cells,[79,80] nucleic acids,[81,82] and phages are also commonly applied.[83,84]

Besides the above-mentioned naturally occurring recognition elements, the interest in fully synthetic alternatives has increased over the past years. Aptamers form a first class of antibody-mimetics and consist of highly specific single strands of nucleic acids (RNA or single-stranded DNA) obtained via the SELEX-method (Systematic evolution of ligands by exponential enrichment).[85] Given their synthetic origin, it is possible to introduce various modifications to further increase the stability, affinity and specificity of the applied aptamers.[86–89] Building upon the success of aptamers, it has become possible to fabricate peptides and proteins with a great affinity towards specific target molecules.[90] These antibody-mimetic polypeptides (AMPs) are also known as affimers or affibodies.[88,90–93] Molecularly imprinted polymers (MIPs) offer a third class of synthetic receptors. MIPS are obtained by forming a polymer network around a template molecule, yielding binding sites with stereo-chemical complementarity towards the template.[94–96]

Antibodies, or immunoglobulins, are protein complexes produced by plasma B-cells that are part of the immune system and carry specific antigen recognition sites. Antibodies bind their target antigens via non-covalent interactions, often with relatively high affinity, rendering them very suitable candidates for biosensing applications.

An antibody consists of two parts: the antigen-binding fragments (Fabs) and a crystallisable, or constant, region (Fc). The antigen-binding portions of the molecule are composed of the VH (heavy chain variable region) and the VL (light chain variable region) regions, which both fold to provide a "lock and key" fit for the specific antigen (figure 1.3).[96,97] The antibody's specificity for its antigen originates from the amino acid sequence in the variable part (Fv) of the antigen binding domain.

Antibodies can be subdivided in classes, or isotypes, based on differences in the heavy chain. In placental mammals, five antibody isotypes can be distinguished: IgA, IgD, IgE, IgG and IgM (figure 1.3). The structure of these isotypes differs mainly in the structure of the heavy chains and in the way both halves of the antibody are joined

IgG

Fv

Fab

Fc

IgD

IgA

IgE

IgM

◯ Heavy chain domain   ◕ J Chain

◯ Light chain domain   ● Secretory component
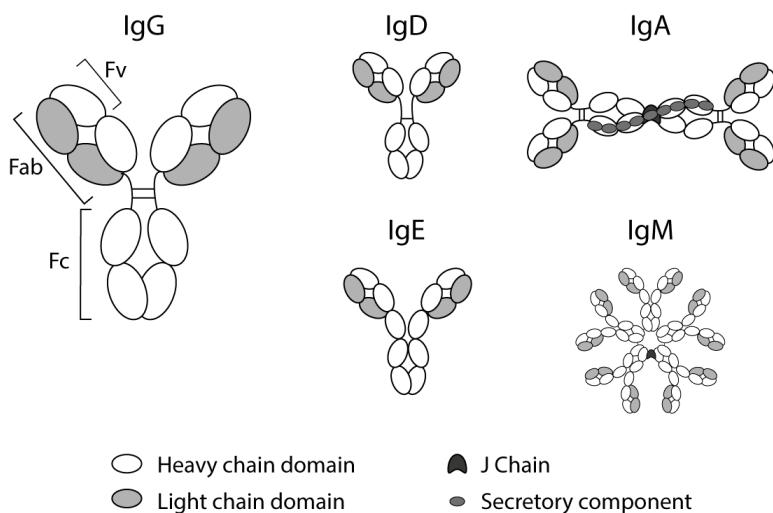
Figure 1.3: Scheme showing the different classes of antibodies. The structure of these isotypes differs mainly in the structure of the heavy chains and in the way both halves of the antibody are joined.[98]

(IgG, IgD and IgE). In some cases, antibodies are present as dimers (IgA) or pentamers (IgM).

From an application viewpoint, a distinction can also be made between polyclonal and monoclonal antibodies. Polyclonal antibodies are secreted by different B cell lineages within the body, whereas monoclonal come from a single lineage. Monoclonal antibodies are therefore structurally identical, whereas polyclonal antibodies are a mixture of different antibodies for a specific analyte.

1.3.2 Detection techniques compatible with LoCs

Although the development of LoC devices has witnessed a tremendous progress in recent years and although they have been touted well, their application has been limited to laboratory prototypes without widespread routine use in clinical or high-throughput applications.[99–101] This can be ascribed to the non-straightforward chemical analysis of low-level analytes to be detected in the nanoliter volumes. Despite

these difficulties, various classes of biosensors can be distinguished based on the applied transduction method. A rough distinction can be made between acoustic, electrochemical, thermal and optical detection techniques.[65,75,102] A non-exhaustive overview of common detection principles is provided in table 1.1.

With respect to the detection of pathogens, optical techniques are particularly interesting given their excellent track-record in chemical analysis in the laboratory.[103–111] Most present-day lab-on-a-chip implementations, however, still rely on bulk optical instrumentation external to the LoC (such as confocal microscopes) for read-out, monitoring or analysis. This has led to the phrase 'a chip-in-a-lab instead of a lab-on-a-chip'. To fully exploit the advantages of optical LoC devices, miniaturized and integrated optical detection systems have been proposed.[112–115]

Optical methods can be subdivided based on their need to label the target molecule to induce a detectable signal. Labelling the target or the receptor can be a time-consuming step. In addition, the analyte can be altered during the labelling procedure, thereby preventing its recognition by the immobilised biorecognition molecules.[116]

Label-free techniques including ellipsometry, interferometry, grating-coupled guided mode sensors, resonant mirrors, surface enhanced raman scattering (SERS), surface plasmon resonance (SPR), do not rely on an additional sample preparation step. These methods depend on the binding-induced changes in e.g. the refractive index of the sample. Label-free methods are thus more interesting for in-field applications and are being considered to be applied in medical diagnostics,[117–120] food analysis,[121,122] environmental monitoring,[123,124] drug discovery,[107,125] and (bio)defense.[126–128]

1.4 Surface Plasmon Resonance

In this PhD thesis, refractive index measurements will be elaborated as the detection method of choice based on their wide applicability in biosensing. More specifically, the present work will rely on the evanescent field technique surface plasmon resonance (SPR), which outperforms other methods in terms of specificity, sensitivity, cost and required analysis time.[80,120,129–137] As can be seen in table 1.2,

Table 1.1: Overview of common biosensor detection techniques

Transduction mode	Detection method	Measured signal	Ref.
Acoustic	Resonant sensing	Damping of the resonance frequency	[138,139]
	Piezoelectric sensing	Damping of the resonance frequency	[140–147]
Electrical	Voltammetry	Current as a function of potential or time	[148,149]
		or as a function of time	[67,150]
	Potentiometry	Potential as a function of concentration	[150]
	Conductimetry	Conductivity as a function of time	[151–153]
	Resistometry	Resistance as a function of time	[154]
	Impedance	Out-of-phase current response	[133]
Optical	Luminescence	Intensity of luminescent signal	[106,155]
	Fluorescence	Intensity of fluorescent signal	[156,157]
	Absorbance	Absorbed intensity	[158,159]
	Scatterometry	Intensity of scatterd light	[160,161]
	Ellipsometry	Change in polarisation	[162]
	Interferometry	Change in phase	[106,163–165]
	Guided mode sensors	Change in waveguide mode	[166]
	Resonant mirror	Change in excitation angle	[167–169]
	Ring resonator	Change in resonance condition	[170–174]
	SERS	Fingerprint Raman spectrum	[175,176]
	SPR	Change in absorption maximum	[103,104,106,117]
Thermal	Thermometry	Absorption or evolution of reaction heat	[177,178]

Table 1.2: Relative scoring of biosensors transduction modes compared to SPR-based sensors. The methods were qualified based on a literature review with a + indicating the technique is competitive to SPR, while – indicates the method is inferior to SPR for that property, finally ± corresponds to contradicting reports. The reviewed papers were narrowed down to those focusing on the detection of bacteria and take into account portability given the interest in in-field measurements.

Detection mode	Specificity	Sensitivity	Pretreatment	Portability	Time	Cost
Cell cultures	-	+	-	-	-	-
Polymerase chain reaction	+	+	-	-	-	-
Electrochemical detection	-	±	+	+	+	+
Acoustic biosensors	+	+	+	-	+	+
Colorimetry	+	±	+	+	+	+
Luminescence	±	±	-	+	-	+
Fluorescence	±	+	-	+	-	+
Scatterometry	±	±	-	±	-	±
Raman spectroscopy	±	+	+	±	+	+
Ring resonator	+	+	+	±	+	+
SPR	+	+	+	+	+	+

some methods require prior labelling (luminescence and fluorescence) or multiplication of the pathogens (scatterometry) which increases the analysis time. The other techniques differ in their associated sensitivities or specificities. Sensors based on surface enhanced raman scattering, ring resonating structures and surface plasmon resonance have gained a lot of interest for the development of LoC sensors owing to their high sensitivity and specificity. However, portable SERS and ring resonator devices for the detection of pathogens are still in their infancy, whereas the first SPR-based prototypes are emerging (section 1.4.2).

Surface plasmons, or surface plasmon polaritons (SPP), are surface electromagnetic waves that propagate in a direction parallel to a metal-dielectric interface. Since the wave is on the boundary of the metal and the external medium, these oscillations are very sensitive to any change at this boundary, i.e. changes in the refractive index near the metal-dielectric interface.[103,104]

Besides allowing high sensitivities, SPR-based sensors do not require the prior labelling of the analyte which reduces both the complexity of the sensing methodology as well as the required measurement time. Instead, selectivity can be introduced by functionalising the interface with biological recognition elements that show high affinity towards a specific target molecule. The detected RI-changes can then be correlated to the presence of this target analyte in a straightforward way. This also implies that a working prototype can be easily adjusted to detect other analytes, by simply interchanging the applied biorecognition moiety.

1.4.1   Theoretical background

An SPP is a longitudinal charge density wave propagating along the interface between two media with dielectric constants of opposite signs, like a metal and a dielectric. This electromagnetic wave propagates along the metal-dielectric interface with a magnetic vector parallel to the plane of the interface, i.e. a transverse-magnetic (TM) wave (figure 1.4).

The SPR condition requires the wave vectors of the SPP and the incident light to match, so that an SPP can absorb the energy delivered by the incident photon. It is important to note that the SPP
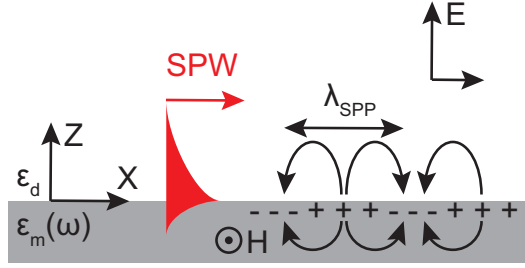
Figure 1.4: A schematic representation of the surface plasmon wave

can only be excited by p-polarized light as they are TM waves.[179] The longitudinal wave vector k_{sp} of the SPP moving at the metal-dielectric interface, is given by equation 1.1:

$$k_{sp} = \frac{\omega}{c}\sqrt{\frac{\epsilon(\omega)\epsilon_d}{\epsilon(\omega) + \epsilon_d}} = \frac{\omega}{c}\sqrt{\frac{\epsilon(\omega)n_d^2}{\epsilon(\omega) + n_d^2}} \qquad (1.1)$$

in which, ω is the angular frequency, c the speed of light in vacuum, $\epsilon(\omega)$ the metal's complex dielectric function dependent upon ω, ϵ_d the dielectric constant of the dielectric and n_d the refractive index of the dielectric medium ($\epsilon_d = n^2$).[104,117,180] Equation 1.1 describes an SPP if the real part of ϵ_m is negative ($\epsilon_{m,r} < 0$ and $|\epsilon_m| < \epsilon_d$).[117] Another way of describing this condition is: $\epsilon_m < -n_d^2$.[104]

At wavelengths of 390-700 nm, the condition $\epsilon_{m,r} < 0$ is fulfilled by several metals. However, the optical excitation of an SPP requires that the electrons in the metal exhibit free electron like behaviour.[181] This requirement restricts the number of possible metals to those which can be described by the free-electron model.[182] Metals like gold, silver, copper and aluminium are candidates for optical excitation of surface plasmons. To date, most experimental work has been performed on gold and silver.[104]

The wave vector k_x for the incident light with an angular frequency ω propagating through a medium with dielectric constant ϵ_d can in turn be given by equation 1.2:

$$k_x = \frac{\omega}{c}\sqrt{\epsilon_d} \qquad (1.2)$$

(a) $k_x = \frac{\omega}{c}\sqrt{\epsilon_d}$ **(b)** $k_x = \frac{\omega}{c}\sqrt{\epsilon_p}\sin\theta$
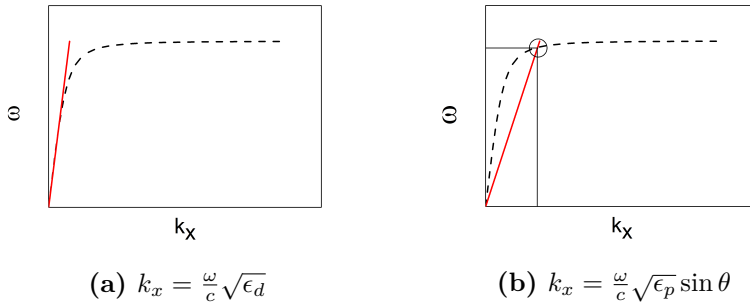
Figure 1.5: Schematic representation of the SPR condition. The red curves show the angular frequency ω as a function of the wave vector k_x of the incident light. The black, dashed curves show the surface plasmon polariton dispersion function. In figure (a) the wave vector k_{sp} for SPP is higher than the wave vector k_x of the incident light for every wavelength. Figure (b) shows that by applying attenuated total reflection in e.g. the so-called Kretschmann configuration, the SPR condition is satisfied for a specific ω and ϑ.

If the imaginary part of ε(ω) is neglected, ε(ω) in equation 1.1 can be approximated by:

$$\epsilon(\omega) \approx 1 - \frac{\omega_p^2}{\omega^2} \tag{1.3}$$

in which ω_p is the bulk plasmon frequency and $\omega < \omega_p$ for SPR to occur. Therefore, k_{sp} from equation 1.1 is always larger than the wave vector for the incident light given by equation 1.2 (figure 1.5a). In other words, the parallel wave vector k_x of the incident light and the longitudinal wave vector k_{sp} of the SPP never match for any value of ω and it is thus not possible to excite an SPP through direct reflection of light onto a metal surface.[181,183]

To circumvent this issue, attenuated total reflection (ATR) can be applied as suggested by Kretschmann.[184] The conditions for total internal reflection (TIR) to occur, can be derived from Snell's law, which relates the angle of refraction (ϑ_r) across an interface with the refractive indices of both media (n_1 and n_2) and the incident angle (ϑ_i) (equation 1.4).

$$n_1 \sin(\theta_i) = n_2 \sin(\theta_r) \Leftrightarrow \sin(\theta_i) = \frac{n_2}{n_1} \sin(\theta_r) \qquad (1.4)$$

At a certain, critical angle of incidence ϑ_c, no refracted beam will be observed, i.e. $\theta_r = 90°$. Therefore, equation 1.4 can be written as:

$$\theta_c = \theta_i = \arcsin(\frac{n_2}{n_1}) \qquad (1.5)$$

It should be noted that for TIR to occur n_1 should be larger than n_2 since $\arcsin(\theta)$ is not defined for values of ϑ larger than 1. TIR thus only occurs at the interface between two media, when the light wave propagates from the denser to the less dense medium, above a critical angle.

The negative ε_m alone does not result in surface plasmon resonance when ambient light is reflected on a metal surface. However, when considering a very thin metal film coated onto a prism as proposed by Kretschmann, SPR can become possible (figure 1.5b).[184] This is due to the fact that the incident light on the prism-metal interface will also affect the metal-dielectric interface, as it evanescently migrates through the thin metal film. The wave vector k_x of light propagating through the prism at an incident angle ϑ, is given by equation 1.6 (figure 1.6):

$$k_x = \frac{\omega}{c}\sqrt{\epsilon_p}\sin\theta \qquad (1.6)$$

in which ε_p is the dielectric constant of the prism material and ϑ is the angle of incidence.[185] It is important to note that no light penetrates the interface. The electrical field of the photons extends about a quarter of a wavelength beyond the reflecting surface (typically 100-500 nm).[117] The evanescent wave is thus able to interact with the metal's surface electrons if the metal film thickness is only a fraction of a wavelength (typically around 50 nm).[117,180]

Considering equation 1.1 and equation 1.6, there exists an angle of incidence ϑ_{SPR} at which the parallel wave vector k_x of the incident light matches the wave vector k_{sp} of the SPP, thereby fulfilling the resonance condition (equation 1.7).[180,185] It must be noted that k_x and k_{sp} will not match exactly due to evanescent losses in the thin metal film.[186]
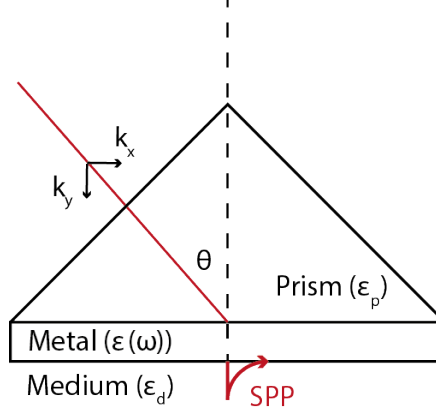
Figure 1.6: Schematic representation of the interfaces involved in the prism-coupled Kretschmann configuration. Light propagating through the prism with a wave vector $k = \frac{\omega}{c}\sqrt{\epsilon_p}$ propagates through the prism. Since only p polarised light can excite surface plasmons, only the wave vector k_x ($k_x = k\sin\theta$) should be considered.

$$\sqrt{\epsilon_p}\sin\theta_{SPR} \approx \sqrt{\frac{\epsilon'(\omega)\epsilon_d}{\epsilon'(\omega) + \epsilon_d}} \qquad (1.7)$$

The coupling between k_x and k_{sp} can also be achieved in other configurations using total internal reflection a.o. by wave diffraction in grating structures or in dielectric waveguides.[180] Considering the detection of *E. coli* in water, the prism coupler, particularly the Kretschmann geometry (figure 1.7), is the most important configuration, as it is commonly applied in SPR-based biosensing.[117]

When, for a given angular frequency, light waves with varying incident angles ϑ are focused on the sensing region, the coupling between k_x and k_{sp} will induce a dip in the reflected intensity at the resonance angle ϑ_{SPR}. This sharp reduction in reflectivity can be measured and results in a typical curve (figure 1.8a).

During the recognition event between the biological recognition element (e.g. an antibody) and the target (*E. coli*), the effective refractive index (ϑ_d) changes. Subsequently, the associated SPR angle (equation 1.7) ϑ_{SPR} at which the reflectivity is reduced will shift. Since the evanescent field of the induced SPPs extends for a few 100
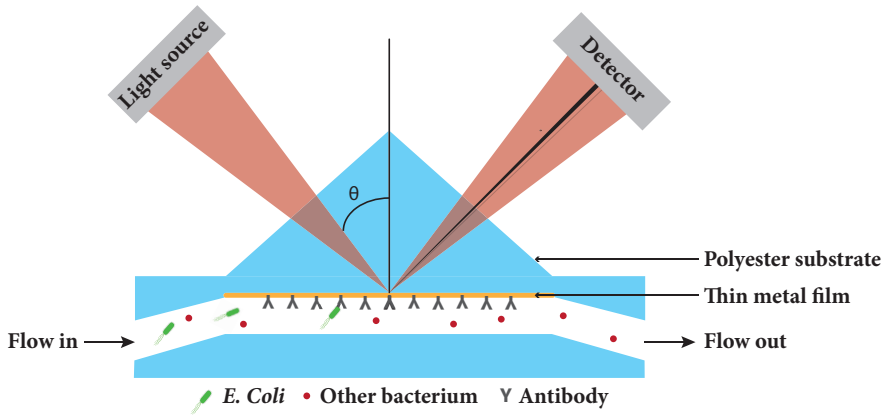
Figure 1.7: Illustration showing an SPR sensor in the Kretschmann configuration. Polarised light is reflected on a metal-coated prism. For a specific wavelength, angle of incidence and refractive index of the water sample, the light is coupled into the metal layer resulting in a reduced reflection. Since the refractive index of the medium depends on its composition, the shift in resonance angle allows sensing applications.

nm into the dielectric medium, SPR-based biosensors are extremely sensitive towards changes near the interface.[109,180] Besides detecting binding events, SPR can also be used to investigate the kinetics of the recognition event by determining the association and dissociation rate constants. This is done by analysing how the response signal changes over time, resulting in a typical SPR sensorgram (figure 1.8b).[187] Despite the fact that the angle interrogation method is the most commonly used for lab-based SPR devices, it should be noted that other methods also exist. Instead of monitoring the angle of incidence, it is possible to measure changes in the wavelength at which resonance takes place,[188] the amplitude of the reflected beam,[189] or the phase of the reflected light.[190,191]

   In the current PhD the angle-resolved interrogation method will be applied, given its simplicity and robustness with respect to the development of a proof-of-concept demonstrator. Amplitude-interrogated sensors are less suitable in this respect since the detector response first has to be optimised based on the background refractive index of the medium to be analysed. Wavelength-interrogated sensors require
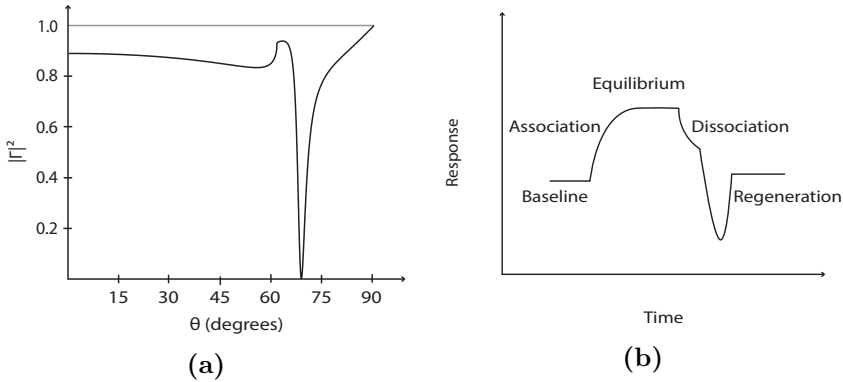
Figure 1.8: Typical SPR curve with the reflectance $|\Gamma|^2$ depicted as a function of the incident angle ϑ. A characteristic sharp dip is observed when the SPR condition is fulfilled (**a**). By plotting the shift of the peak minimum as a function of time, an SPR sensorgram can be obtained (**b**). Such sensorgrams can be used in sensing applications or to determine rate constants in binding experiments.

more costly optical components to control the wavelength of the incident light (e.g. a tunable laser or a diffraction grating), which would also increase the cost per analysis. Finally, the inherent complexity of phase-interrogated systems excludes point-of-care applications, which is one of the objectives of this PhD. A more elaborate overview of the strengths and weaknesses of each kind of modulation can be found in a recent review by Puiu and Bala.[192]

1.4.2   State-of-the-art

The SPR phenomenon was first described by Wood in 1902.[193] About sixty years later, Kretschmann and Otto demonstrated the optical excitation of SPP by attenuated total reflection.[184,194] In 1982, the use of SPR for gas detection and biosensing was demonstrated by Nylander and Liedberg.[179] The first commercially available SPR-based biosensor was released by Biacore AB in 1990.[195] Over the past years, SPR has become an emerging detection method in the microfluidic world. In the following sections, an overview will be presented on the state-of-the-art of SPR sensing in terms of sensor configuration and its application in the detection of pathogens.

SPR configurations

The theoretical background listed in section 1.4.1 was based on the so-called Kretschmann configuration.[184] By applying a prism, the momentum of the incident light is increased to induce SPR in a thin metal film. This configuration is by far the most commonly applied in the domain of SPR-based biosensors. As already mentioned, this method makes use of the principle of attenuated total internal reflection to induce surface plasmon resonance. However, the same effect can be applied in different configurations. The most commonly applied alternatives include the Otto configuration,[194] waveguide-coupled SPR sensors,[101,196–199] and configuration relying on metal gratings rather than prisms to excite SPPs.[200–204]

As already mentioned, the current PhD will focus on the Kretshman configuration previously discussed in section 1.4.1, as this configuration is commonly applied in proof-of-concept demonstrators given its simplicity and the possibility to perform kinetic studies. Grating coupled set-ups on the other hand are less robust as they may experience interference when coloured solutions are analysed.[192] Waveguide coupled sensors were excluded since these apply either phase- or wavelength-interrogation, which were previously excluded based on their higher complexity and cost (section 1.4.1).

With the advent of miniaturised SPR set-ups, the equipment needed for the read-out of the sensor signal became the bottleneck towards portable sensors. However, the past years have witnessed great advances towards biosensor development. One interesting approach worth mentioning is the application of smartphones in portable sensors.[115] Smartphones not only offer processing capabilities and battery power, most models are equipped with a CCD camera. For example, an angle resolved SPR sensor was developed by Prechaburana *et al.* and resulted in the detection of β_2 microglobuline, an important biomarker associated with certain cancers, some inflammatory diseases and kidney problems.[205] An LOD of $2.5\,\mu g\,mL^{-1}$ was obtained which was adequate for clinical applications. More recently a smartphone-based sensor was developed that could detect refractive index changes with a sensitivity similar to traditional lab-based SPR devices (10^{-5} RIU).[114] Both previously mentioned devices detected the reflected light using the smartphone's camera and relied on the

refraction of the incident light in a prism. However, diffractive structures have also been explored.[112] In these devices the incident light is diffracted by a photonic crystal (*i.e.* a periodic optical nanostructure) and captured by the cell phone's camera, resulting in a specific transmission spectrum. When a binding event takes place, the transmission spectrum changes as a function of concentration allowing *e.g.* the detection of protein absorption on the photonic crystal.

The interest in SPR sensing peaked in the period 2008-2010 and has since reached a plateau.[192] The amount of effort gone into the development of SPR-based sensors has resulted in sensitivities that are sufficient to detect large biomolecules (> 500 Da) like DNA, proteins and antibodies in diagnostic applications.[130,206,207] However, the detection of smaller molecules (toxins, drugs, vitamins) or low-copy analytes (bacteria or virusses) requires further improvement of the available LODs.[208] Localised SPR (LSPR) has been an emerging technique to further improve the sensitivity. Unlike traditional SPR, this method relies on the absorption of light by nanoscopic metallic structures. When a binding event occurs, the absorption by the nanoparticles changes. This method has the benefit that temperature control is no longer necessary since the RI changes are measured indirectly via changes in absorption.[192] Applications of LSPR sensors in complex matrices, however, are limited since non-specific binding often interferes with the measurements.[209]

A last innovation that has emerged in the past decade, consists of surface plasmon resonance imaging (SPRi).[192] Using this approach, the metal layer used to generate the SPPs is divided in discrete patches, with each location containing a biorecognition element for a specific analyte. The incident light hits all these sensing zones simultaneously and is reflected to a charge-coupled device (CCD) camera which can be considered to be a 2D-intensity detector.[210] The reflected light of each patch will now be collected on its particular location on the CCD-camera. When the target(s) bind to the surface, dark spots will appear for the patches that contain the appropriate ligands. SPRi devices thus allow the detection of several hundreds of analytes in a single experiment, thereby further reducing the analysis time per analyte.[120,211]

Application of SPR in pathogen detection

With SPR set-ups being commercially available, breakthroughs have been realized on the detection of bacteria using these devices. [59,212,213] The SPREETA biosensor has been applied to detect *E. coli* O157:H7 in complex matrices like apple juice, milk and ground beef, with a detection limit of around 10^2-10^3 CFU mL^{-1}. [214] The same device was also used to detect other pathogens like *Salmonella enteritidis* and *Salmonella typhimurium* with LODs of 10^5 CFU mL^{-1} and 10^6 CFU mL^{-1}, respectively. [215,216]

Bokken *et al.* focused on the detection of *Salmonella* serovars and report a lower limit of detection of 1.7 x 10^3 CFU mL^{-1}. [217] The authors applied antibodies as the recognition element in combination with the Biacore set-up and demonstrated the high selectivity of their method by also including 30 *non-Salmonella* serovars in their study.

Leonard *et al.* applied the Biacore 3000 for the rapid (30 min) detection of *Listeria monocytogenes*. [218] The gold surface was functionalised with anti-Fab antibodies, which were used to capture priorly labelled *Listeria* cells, which resulted in an LOD of 10^5 CFU mL^{-1}.

Very low detection limits were obtained for *E. coli* and *Salmonella* with LODs of 25 CFU mL^{-1} and 23 CFU mL^{-1}, respectively. [219] This increased sensitivity compared to the report by Bokken *et al.* may be explained by the difference in sampling (5 min at 5 µL min^{-1} compared to a single injection of 10 µL).

Wang *et al.* applied the Biacore system in a subtractive assay in which unbound *E.coli* O157:H7 antibodies were first isolated via centrifugation and subsequently quantified. This resulted in a LOD of 3 x 10^4 CFU mL^{-1}. [220]

Despite these initial successes, SPR-based detection of pathogens still is concomitant with a low sensitivity (10^2-10^4 CFU mL^{-1}) compared to cell culture techniques. This is mainly attributed to the limited penetration depth of the evanescent wave in the sample solution and the similarity in RI between the bacterial cytoplasm and the surrounding aqueous medium. [221,222] This issue can be overcome via cell-lysis followed by the detection of characteristic fragments. although, such methods increase the time necessary per analysis (+ 0.5 - 1.5 h). Taylor *et al.* applied this principle to compare two *E. coli* pretreatments (heat-killed and detergent-lysed *E. coli*) with the dir-

ect detection of the bacterium. The detection of detergent-lysed and heat-killed bacteria resulted in an LOD of 10^5 and 10^6 CFU mL^{-1}, respectively, which is an improvement by 1-2 orders of magnitude compared to the direct detection (10^7 CFU mL^{-1}).[223]

In case of whole cell detection, the lower sensitivity can be overcome by an enrichment step prior to the actual analysis.[136] Besides applying cell culture to multiply the bacteria in the sample, immunological techniques are also interesting. For example, antibody-coated magnetic nanoparticles can be applied to concentrate the analyte solution, which has resulted in a LOD of 3 CFU mL^{-1}.[224] Other authors allowed the bacteria to multiply in the sensing zone by combining cell cultures with SPR sensing.[225] This resulted in very low LOD values (approx. 3 CFU mL^{-1}), but increased the measurement time up to 5 h, when very low numbers of bacteria (< 100 CFU mL^{-1}) are concerned.

Attempts to increase the penetration depth of the evanescent wave have also been applied successfully with LODs as low as 50 CFU mL^{-1} for this kind of long-range grating-coupled SPR sensors.[226] An improvement by 4 orders of magnitude was achieved compared to conventional grating-coupled SPR set-ups.

As already mentioned, LSPR has also gained importance as a sensitive SPR-based technique.[227] Yoo *et al.* applied aptamer-coated gold nanoparticles (NPs) to detect three different bacteria in a single experiment with an LOD of 30 CFU mL^{-1}.[136] It can be anticipated that the sensitivity of LSPR sensors will further increase by increasing their reflectivity index sensitivity and optimising the decay length of the evanescent field in order for the binding event to occur within the appropriate range.[228,229]

Although most SPR devices rely on antibodies for the detection of pathogens, it comes as no surprise that also bacteriophages have been applied given their selectivity towards bacteria. Most SPR-sensors containing phages are based on the direct detection of the target and are limited to applications for which the analyte results in a sufficiently large RI shift at the concentration of interest.[230] The immobilisation of phages is not straightforward, but the use of self-assembled monolayers (SAMs) in combination with carbodiimide chemistry has resulted in a 10^3-fold increase in activity for the lysis

of *methicillin-resistant Staphylococcus aureus* (MRSA) compared to physisorbed phages.[231] The same authors had previously reported the application T4 bacteriophages and the specific BP14 phage for the detection of respectively *E. coli* and *S. aureus.*[232] Detection limits of 10^3 CFU mL^{-1} could be reached within 20 minutes and results were obtained without prior labelling or enrichment.

Finally, it should be noted that SPR lends itself perfectly towards multiplexed systems that are able to detect different pathogens in a single measurement. This was achieved by Taylor *et al.* who relied on a multi-channel SPR sensor and reported LODs in the range of 10^3-10^5 CFU mL^{-1} for *E.coli*, *S. choleraesuis typhi*, *C. jenuni* and *L. monocytogenes.*[233]

Given the broad range of reported LOD values for the above-mentioned reports, it should be noted that these values are influenced by multiple parameters including among others the targeted analyte, the applied recognition moiety, the applied preconcentration step, the flow rate and sensor design. All these parameters should thus be taken into account when striving towards lower limits of detection.

Despite these recent advances, the straightforward detection of pathogens via SPR in portable sensors has not yet been achieved to date. The next and final section of this chapter will therefore provide an overview of the aspects that the current research envisions to improve.

1.5 PhD rationale and outline

As indicated in the problem statement, even today the microbiological contamination of water poses a serious health risk. Current detection techniques heavily rely on cell cultures in order to quantify the number of microorganisms present in a sample. These techniques are however time-consuming and require specialised facilities and personnel. Therefore, miniaturised lab-on-a-chip biosensors are gaining interest to allow the rapid in-field screening of water samples. The present work will contribute to these research efforts and will focus on surface plasmon resonance-based sensing. SPR was selected based on its high sensitivity without the need for prior labeling of the target analyte. Moreover, SPR-experiments are performed in real-time

which enables for short measurements (approx. 30 minutes) which is a significant advantage over the current screening methods.

Since the consumption of contaminated water particularly affects those living in developing countries, the cost per analysis is another important parameter to be taken into account. Therefore, the envisioned LoC sensor will consist of sensor cartridges that are placed in an external read-out system. By reusing the optical instrumentation for multiple measurements, the cost per analysis decreases offering an additional advantage. In turn, the disposable sensor chips need to be mass-manufacturable and low-cost, which has its implications on the materials that can be used.[129] In this context, polymers offer an interesting possibility over alternatives such as glass or silicon. Not only are polymers more cost-effective, these materials are readily processed via common processing techniques including injection moulding and hot embossing.

Considering the optical detection method that will be elaborated in the present work, the materials should be chemically inert under the experimental conditions, mechanically stable and optically transparent (661 nm, considering the wavelength that will be applied in a laboratory demonstrator). In addition, other optical characteristics of the material will influence sensor performance. For example, the colour of the polymer is an obvious factor to be taken into account as coloured materials will interact differently with incident light of various wavelengths. This is particularly important for e.g. wavelength-interrogated set-ups.[192] Within the framework of this PhD thesis, colour will be considered as an undesired property and e.g. the yellowing of the polymer during processing should be minimised. Next, the refractive index of the applied material will influence the sensor's sensitivity as was established by simulations performed within the B-Phot group.[234] The influence of temperature and the applied wavelength (i.e. the thermo-optic effect and the dispersion relationship) will therefore also need to be evaluated as these parameters may influence the reliability of the obtained results.

Due to their micrometer scale channels LoC biosensors are generally troublesome to rinse, which is why most LoCs are designed for single-use applications.[129,235] In order to anticipate the associated waste stream, the current PhD will therefore explore the applicability

of degradable polyesters as base material for the development of microfluidic sensors. This is especially important for the application of the envisioned sensors in developing countries as these countries generally lack the appropriate recycling infrastructure.[236] Moreover, the regions where access to potable water is limited tend to be scarcely populated and therefore the necessary economics of scale are difficult to achieve, thereby discouraging the recycling of resources.[237] Under such conditions degradable materials would thus allow the disintegration of the applied sensors over time, thereby preventing the generation of an additional waste stream. In the mainpart of the western world on the other hand, laboratory analyses are more prevailing than in developing countries (e.g. clinical analyses in hospitals). This makes it easier to achieve sufficient economics of scale to justify the collection and recyling of the (micro)biologically contaminated plastic sensor chips. The application of hydrolytically unstable polymers would enable the straightforward separation of the polymer from the applied metal layers. The latter wouldd sink to the bottom of a reactor, thereby facilitating their recovery and recycling. Since polyesters are among the front-runners in the domain of degradable polymers, this class of polymers will constitute the main focus of this thesis.

Chapter 2 will focus on the synthesis of degradable polyesters that can be applied in SPR-based sensors. However, commonly applied degradable polyesters such as poly(glycolide), poly(lactide) and poly(ε-caprolactone) are either semi-crystalline limiting their optical performance, or exhibit a relatively low glass-transition temperature (up to 50 °C) which may result in deformation of the sensors when applied in tropical conditions. The materials developed in this thesis should thus exhibit an increased glass transition temperature (> 60 °C) and should be optically transparent and thus completely amorphous. Poly(mandelide) has been reported to yield polymers with a glass transition temperature of 100 °C, but this material is quite stable and degradation will only result in mass loss after incubating the material for 3 months at 55 °C. Therefore, the copolymerisation of lactide with its mandelic acid analogue (mandelide) will be applied to obtain polyesters with a higher glass transition temperature. The obtained (co)polymers will be characterised allowing this hypothesis

to be tested as well as to assess their other relevant parameters such as transparency, molecular weight and refractive index.

In addition, a second class of monomers will be evaluated to synthesise degradable polyesters for application in microfluidics. O-carboxy anhydrides (OCAs) have been identified as a class of reactive five-membered ring that can be applied in ring-opening polymerisations and are characterised by favourable polymerisation kinetics. Both the lactic acid as well as the mandelic acid OCA derivative have been synthesised via direct carbonylation of the α-hydroxy acids. Given the toxicity of the diphosgene required for the monomer synthesis, the scale at which the OCA-monomers could be synthesised in a safe way was limited. Therefore, the potential of flow chemistry for the continuous synthesis of OCA-monomers was evaluated based on a number of preliminary experiments in simple flow reactors as well as in a packed bed reactor. The obtained monomers are subsequently applied in solution (co)polymeriations that yield structurally identical polymers to the ones obtained by polymerising cyclic diesters. The results will be compared to the previously mentioned lactide based monomers in terms of monomer yield and polymerisation characteristics. As for the materials developed in chapter 2, the obtained polymers are characterised physicochemically and optically to assess their applicability within degradable SPR sensorchips, keeping in mind the same specifications as mentioned for chapter 2.

Chapter 4 focuses on the surface modification methodology of the metal layer that is required for the excitation of surface plasmon polaritons. In order to correlate changes in the observed SPR resonance condition to the sample's composition, the sensor should be made selective towards the analyte of interest. Given, the fact that silver has superior optical properties as compared to gold (e.g. a higher reflectivity).[238] The surface plasmon wave observed for silver layers also extents further into the medium.[104] Based on these properties, silver-based SPR sensors are reported to have a higher sensitivity (+50%) which is promising given the low detection limits desired for microbiological screening methods.[234] Given the weak nature of the silver-sulphur bond, the formation of a self-assembled monolayer of thiol-containing groups is not straightforward. Therefore, the surface functionalisation of silver was explored by applying

a bioinspired modification methodology relying on poly(dopamine). Since the structure of poly(dopamine) is still subject of debate, the amount of surface anchors (i.e. biotin moieties) was controlled by co-depositing biotinylated poly(ethylene imine). The performance of this surface modification is evaluated by means of x-ray photo-electron spectroscopy, atomic force microscopy and static contact angle measurements.

Next, chapter 5 introduces the processing methodologies required to convert polymer materials into leak-proof microfluidic chips. Considering their application in an SPR-based sensor, the formed parts have to meet the requirements associated with optical quality. This implies that the obtained surfaces need to be smooth as indicated by a rooth-mean-square surface roughness ($R_q < 60$ nm) to minimise scatter losses. Since SPR is only observed for TM-polarised light, internal material stress resulting in birefringence should also be avoided. Both prerequisites can be obtained by applying hot embossing to introduce channels in the polymer materials as this techniques is associated with limited material flow. However, since the surface roughness is determined by the applied polymer preform, polymers were first processed into thin polymer sheets via injection moulding. Since hot embossing results in open channels, the thus obtained chips have to be sealed in such a way that the optical quality of the parts is conserved, which is difficult with conventional techniques as solvent or thermal bonding. To this end, through transmission laser welding will be evaluated as a tool to seal the microfluidics in a straightforward way. By laser welding a series of commercial polymers and evaluating the obtained shear strengths of the welds, the results will be correlated to certain material properties in order to predict the performance of the materials synthesised in chapters 2 and 3. Three polymers that performed well in the laser welding experiments, were subsequently hot embossed and sealed via laser welding to obtain microfluidic chips. The leak-proof nature of these chips was finally evaluated by means of static leak tests.

Finally, chapter 6 summarises the performed work and provides an outlook on planned experiments and future developments within the field of SPR sensing.

References

[1] World Health Organization, *Preventing diarrhoea through better water, sanitation and hygiene*, World Health Organization, Geneva, **2014**, pp. 1–48.

[2] A. Prüss-Üstün, R. Bos, F. Gore, J. Bartram, *World Health Organization* **2008**, 53.

[3] L. Liu, H. L. Johnson, S. Cousens, J. Perin, S. Scott, J. E. Lawn, I. Rudan, H. Campbell, R. Cibulskis, M. Li, C. Mathers, R. E. Black, *The Lancet* **2012**, *379*, 2151–2161.

[4] R. E. Black, S. S. Morris, J. Bryce, *Lancet* **2003**, *361*, 2226–2234.

[5] W. Kimbrough, V. Saliba, M. Dahab, C. Haskew, F. Checchi, *The Lancet Infectious Diseases* **2012**, *12*, 950–965.

[6] S. I. S. Ali, S. I. S. Ali, J.-F. Fesselet, A. S.I., A. S.S., F. J.-F., *Bulletin of the World Health Organization* **2015**, *93*, 550–558.

[7] E. De Buck, V. Borra, E. De Weerdt, A. Vande Veegaete, *PLoS ONE* **2015**, *10*, 1–14.

[8] A. Ramesh, K. Blanchet, J. H. J. Ensink, B. Roberts, *PLoS ONE* **2015**, *10*, 1–20.

[9] T. Fredrick, M. Ponnaiah, M. V. Murhekar, Y. Jayaraman, J. K. David, S. Vadivoo, V. Joshua, *Journal of health population and nutrition* **2015**, *33*, 31–38.

[10] S. Rebaudet, B. Sudre, B. Faucher, R. Piarroux, *Journal of Infectious Diseases* **2013**, *208*, 46–54.

[11] M. T. Osterholm, *Clinical Infectious Diseases* **2000**, *31*, i—–iii.

[12] S. E. Hrudey, P. Payment, P. M. Huck, R. W. Gillham, E. J. Hrudey, *Water Science and Technology* **2003**, *47*, 7–14.

[13] J. Zawisza, S. Bro, *FDA Statement on Foodborne E. coli O157:H7 Outbreak in Spinach*, **2006**, http://www.fda.

gov/NewsEvents/Newsroom/PressAnnouncements/2006/
ucm109578.htm(accessed2016-05-06).

[14] K. D. Beer, J. W. Gargano, V. A. Roberts, V. R. Hill, L. E.
Garrison, P. K. Kutty, E. D. Hilborn, T. J. Wade, K. E. Fuller-
ton, J. S. Yoder, *Morbidity and Mortality Weekly Report* **2015**,
64, 842–848.

[15] M. Hanna-Attisha, J. LaChance, R. C. Sadler, A. Champney
Schnepp, *American journal of public health* **2015**, *106*, e1—-e8.

[16] Robert Koch Institute, *Final presentation and evaluation of the
epidemiological findings in the EHEC O104:H4 outbreak, Ger-
many 2011*, Robert koch institute technical report, **2011**.

[17] C. Frank, D. Werber, J. P. Cramer, M. Askar, M. Faber,
M. an der Heiden, H. Bernard, A. Fruth, K. G. Prager R, Spode
A, Wadl M, Zoufaly A, Jordan S, Kemper MJ, Follin P, Müller
L, King LA, Rosner B, Buchholz U, Stark K, *New England
Journal of Medicine* **2011**, *365*, 1771–1780.

[18] European Commission, *Commision Staff Working Document:
Lessons learned from the 2011 outbreak of Shiga toxin-producing
Escherichia coli (STEC) O104:H4 in sprouted seeds*, European
commission technical report, **2011**.

[19] P. M. Fratamico, C. DebRoy, Y. Liu, D. S. Needleman, G. M.
Baranzoni, P. Feng, *Frontiers in Microbiology* **2016**, *7*, 1–8.

[20] M. Alamaniotis, A. Heifetz, A. C. Raptis, L. Member, L. H.
Tsoukalas, *IEEE Transactions on nuclear science* **2013**, *60*,
3014–3024.

[21] H. G. Gorchev, G. Ozolins, *WHO chronicle* **2011**, *38*, 104–108.

[22] W. S. Darwish, Y. Ikenaka, S. M. M. Nakayama, M. Ishizuka,
Journal of Veterinary Medical Science **2014**, *76*, 789–797.

[23] A. C. A. Sousa, M. R. Pastorinho, S. Takahashi, S. Tanabe,
Environmental Chemistry Letters **2014**, *12*, 117–137.

[24] P. Hadi, M. H. To, C. W. Hui, C. S. K. Lin, G. McKay, *Water Research* **2015**, *73*, 37–55.

[25] S. Sauvé, M. Desrosiers, *Chemistry Central journal* **2014**, *8*, 15.

[26] M. Annevelink, J. A. J. Meesters, A. J. Hendriks, *Science of The Total Environment* **2016**, *550*, 431–438.

[27] C. D. Kassotis, L. R. Iwanowicz, D. M. Akob, I. M. Cozzarelli, A. C. Mumford, W. H. Orem, S. C. Nagel, *Endocrine disrupting activities of surface water associated with a West Virginia oil and gas industry wastewater disposal site*, **2016**.

[28] R. Loos, B. M. Gawlik, G. Locoro, E. Rimaviciute, S. Contini, G. Bidoglio, *Environmental Pollution* **2009**, *157*, 561–568.

[29] Y. Picó, C. Blasco, G. Font, *Mass Spectrometry Reviews* **2004**, *23*, 45–85.

[30] H. Leclerc, D. a. Mossel, S. C. Edberg, C. B. Struijk, *Annual review of microbiology* **2001**, *55*, 201–234.

[31] J. S. Gruber, A. Ercumen, J. M. Colford, *PLoS ONE* **2014**, *9*, 1–14.

[32] P. Tallon, B. Magajna, C. Lofranco, K. T. Leung, *Water Air and Soil Pollution* **2005**, *166*, 139–166.

[33] S. L. McLellan, A. M. Eren, *Trends in Microbiology* **2014**, *22*, 697–706.

[34] F. Baggi, A. Demarta, R. Peduzzi, *Research in Microbiology* **2001**, *152*, 743–751.

[35] Z. Altintas, M. Gittens, J. Pocock, I. E. Tothill, *Biochimie* **2015**, *115*, 144–154.

[36] US Environmental Protection Agency, *National Primary Drinking Water Regulations*, **2007**.

[37] The Council of the European Union, *Official Journal of the European Communities* **1998**, *L330*, 32–54.

[38] N. Rocky Mountain Laboratories, NIAID, *Escherichia coli: Scanning electron micrograph of Escherichia coli, grown in culture and adhered to a cover slip.*, `http://www.niaid.nih.gov/topics/biodefenserelated/biodefense/publicmedia/Pages/image_library.aspx(accessed2017-03-03)`.

[39] O. Lukjancenko, T. M. Wassenaar, D. W. Ussery, *Microbial Ecology* **2010**, *60*, 708–720.

[40] R. Lan, P. R. Reeves, *Microbes and Infection* **2002**, *4*, 1125–1132.

[41] R. Bentley, R. Meganathan, *Microbiological reviews* **1982**, *46*, 241–280.

[42] S. Hudault, J. Guignot, A. L. Servin, *Gut* **2001**, *49*, 47–55.

[43] G. Reid, J. Howard, B. S. Gan, *Trends in Microbiology* **2001**, *9*, 424–428.

[44] M. Norris, G. Remuzzi, *Outbreak Inc* **2015**, 1035–1050.

[45] F. W. Gilcreas, *American Journal of Public Health and the Nations Health* **1966**, *56*, 387–388.

[46] M. M. Doolittle, J. J. Cooney, D. E. Caldwell, *Journal of Industrial Microbiology* **1996**, *16*, 331–341.

[47] D. Mabey, R. W. Peeling, A. Ustianowski, M. D. Perkins, *Nat Rev Micro* **2004**, *2*, 231–240.

[48] E. B. Braun-Howland, P. S. Berger, R. J. Blodgett, C. H. Johnson, S. Lin, M. C. Meckes, E. W. Rice, *9921 Multiple-tube Fermentation Technique For Members Of The Coliform Group*, Standard Methods Committee Technical Report 9000, **2006**.

[49] A. Rompré, P. Servais, J. Baudart, M.-R. De-Roubin, P. Laurent, *Journal of Microbiological Methods* **2002**, *49*, 31–54.

[50] J. A. Clark, *Canadian Journal of Microbiology* **1980**, *26*, 827–832.

[51] ALS Environmental Limited, *Limit of Detection: Microbiology*, Als environmental limited technical report, **2017**.

[52] J. A. Clark, A. H. El-shaarawi, *Applied and environmental microbiology* **1993**, *59*, 380–388.

[53] P. C. S. Feng, P. A. Hartman, *Applied and Environmental Microbiology* **1982**, *43*, 1320–1329.

[54] I. George, M. Petit, P. Servais, *Journal of Applied Microbiology* **2000**, *88*, 404–413.

[55] N. Hesari, A. Alum, M. Elzein, M. Abbaszadegan, *Enzyme and Microbial Technology* **2016**, *83*, 22–28.

[56] L. Krás, R. Hynek, I. Hochel, *International Journal of Mass Spectrometry* **2013**, *353*, 67–79.

[57] F. S. Rodrigues Ribeiro Teles, *Analytica Chimica Acta* **2011**, *687*, 28–42.

[58] J. M. Henson, R. French, *Annual Review of Phytopathology* **1993**, *31*, 81–109.

[59] J. W.-F. Law, N.-S. Ab Mutalib, K.-G. Chan, L.-H. Lee, *Frontiers in Microbiology* **2015**, *5*, 770.

[60] U. Dharmasiri, M. A. Witek, A. A. Adams, J. K. Osiri, M. L. Hupert, T. S. Bianchi, D. L. Roelke, S. A. Soper, *Analytical Chemistry* **2010**, *82*, 2844–2849.

[61] M. Tortorello, K. Reineke, *Food Microbiology* **2000**, *17*, 305–313.

[62] S. Zhang, A. Garcia-D'Angeli, J. P. Brennan, Q. Huo, H. Ma, Q. Huang, C. Fan, J. Q. Xiang, Q. H. Jin, J. L. Zhao, *The Analyst* **2014**, *139*, 439–445.

[63] B. W. Blais, J. Leggate, J. Bosley, A. Martinez-Perez, *Letters in Applied Microbiology* **2004**, *39*, 516–522.

[64] A. Gehring, J. Brewster, Y. He, P. Irwin, G. Paoli, T. Simons, S.-I. Tu, J. Uknalis, *Sensors* **2015**, *15*, 30429–30442.

[65] J. Kirsch, C. Siltanen, Q. Zhou, A. Revzin, A. Simonian, *Chemical Society Reviews* **2013**, *42*, 8733–8768.

[66] C. Nylander, *Journal of Physics E-Scientific Instruments* **1985**, *18*, 736–750.

[67] S. P. Mohanty, E. Kougianos, *IEEE Potentials* **2006**, *25*, 35–40.

[68] S. J. Trietsch, T. Hankemeier, H. J. van der Linden, *Chemometrics and Intelligent Laboratory Systems* **2011**, *108*, 64–75.

[69] M. H. Ghanim, M. Z. Abdullah, *Talanta* **2011**, *85*, 28–34.

[70] D. Bhatta, a. a. Michel, M. Marti Villalba, G. D. Emmerson, I. J. G. Sparrow, E. a. Perkins, M. B. McDonnell, R. W. Ely, G. a. Cartwright, *Biosensors and bioelectronics* **2011**, *30*, 78–86.

[71] P. A. Auroux, D. Iossifidis, D. R. Reyes, A. Manz, *Analytical Chemistry* **2002**, *74*, 2637–2652.

[72] S. J. Lee, S. Y. Lee, *Applied Microbiology and Biotechnology* **2004**, *64*, 289–299.

[73] S. Haeberle, R. Zengerle, *Lab on a Chip* **2007**, *7*, 1094–1110.

[74] Y. C. Lim, a. Z. Kouzani, W. Duan, *Microsystem Technologies* **2010**, *16*, 1995–2015.

[75] S. Prakash, M. Pinti, B. Bhushan, *Philosophical Transactions of the Royal Society A: Mathematical Physical and Engineering Sciences* **2012**, *370*, 2269–2303.

[76] J. Heo, S. Z. Hua, *Sensors* **2009**, *9*, 4483–4502.

[77] X. Wang, X. Lu, J. Chen, *Trends in Environmental Analytical Chemistry* **2014**, *2*, 25–32.

[78] C. I. L. Justino, A. C. Freitas, R. Pereira, A. C. Duarte, T. A. P. Rocha Santos, *Recent developments in recognition elements for chemical sensors and biosensors*, **2015**.

[79] T. Vo-Dinh, B. Cullum, *Fresenius' Journal of Analytical Chemistry* **2000**, *366*, 540–551.

[80] V. Velusamy, K. Arshak, O. Korostynska, K. Oliwa, C. Adley, *Biotechnology Advances* **2010**, *28*, 232–254.

[81] S. Tyagi, F. R. Kramer, *Nat Biotech* **1996**, *14*, 303–308.

[82] S. W. Dutse, N. A. Yusof, *Sensors* **2011**, *11*, 5754–5768.

[83] Y. Chai, S. Horikawa, A. Simonian, D. Dyer, B. A. Chin, *Wireless magnetoelastic biosensors for the detection of Salmonella on fresh produce*, **2013**.

[84] N. Tawil, E. Sacher, R. Mandeville, M. Meunier, *Analyst* **2014**, *139*, 1224–1236.

[85] C. Tuerk, L. Gold, *Science* **1990**, *249*, 505 LP – 510.

[86] C. Yao, T. Zhu, Y. Qi, Y. Zhao, H. Xia, W. Fu, *Sensors (Basel Switzerland)* **2010**, *10*, 5859–5871.

[87] L. Barthelmebs, A. Hayat, A. W. Limiadi, J. L. Marty, T. Noguer, *Sensors and Actuators B: Chemical* **2011**, *156*, 932–937.

[88] K.-M. Song, S. Lee, C. Ban, *Sensors* **2012**, *12*, 612–631.

[89] V. Niederberger, J. Eckl-Dorna, G. Pauli, *Methods* **2014**, *66*, 96–105.

[90] C. I. L. Justino, A. C. Duarte, T. A. P. Rocha-Santos, *TrAC Trends in Analytical Chemistry* **2015**, *65*, 73–82.

[91] P.-A. Nygren, *The FEBS journal* **2008**, *275*, 2668–76.

[92] H. S. Song, T. H. Park, *Biotechnology journal* **2011**, *6*, 1310–6.

[93] J. Daprà, L. H. Lauridsen, A. T. Nielsen, N. Rozlosnik, *Biosensors and Bioelectronics* **2013**, *43*, 315–320.

[94] K. Haupt, K. Mosbach, *Chemical Reviews* **2000**, *100*, 2495–2504.

[95] S. Li, S. Cao, M. J. Whitcombe, S. A. Piletsky, *Progress in Polymer Science* **2014**, *39*, 145–163.

[96] S. Mross, S. Pierrat, T. Zimmermann, M. Kraft, *Biosensors and Bioelectronics* **2015**, *70*, 376–391.

[97] A. C. A. Roque, C. R. Lowe, M. Â. Taipa, *Biotechnology Progress* **2004**, *20*, 639–654.

[98] Absolute Antibody Inc., *Antibody isotypes and subtypes*, http://absoluteantibody.com/antibody-resources/ antibody-overview/antibody-isotypes-subtypes/.

[99] M. N. Velasco-Garcia, T. Mottram, *Biosystems Engineering* **2003**, *84*, 1–12.

[100] G. Boas, *Photonics Spectra* **2011**, *45*, 52–56.

[101] G. Liang, Z. Luo, K. Liu, Y. Wang, J. Dai, Y. Duan, *Critical Reviews in Analytical Chemistry* **2016**, *46*, 213–223.

[102] E.-H. Yoo, S.-Y. Lee, *Sensors* **2010**, *10*, 4558–4576.

[103] S. Lofas, M. Malmqvist, I. Ronnberg, E. Stenberg, B. Liedberg, I. Lundstrom, *Sensors and Actuators B-Chemical* **1991**, *5*, 79–84.

[104] J. Homola, S. S. Yee, G. Gauglitz, *Sensors and Actuators B-Chemical* **1999**, *54*, 3–15.

[105] G. Gauglitz, *Analytical and Bioanalytical Chemistry* **2005**, *381*, 141–155.

[106] R. Ince, R. Narayanaswamy, *Analytica Chimica Acta* **2006**, *569*, 1–20.

[107] X. Fan, I. M. White, S. I. Shopova, H. Zhu, J. D. Suter, Y. Sun, *Analytica Chimica Acta* **2008**, *620*, 8–26.

[108] H. C. Hunt, J. S. Wilkinson, *Microfluidics and Nanofluidics* **2008**, *4*, 53–79.

[109] C. Situ, M. H. Mooney, C. T. Elliott, J. Buijs, *TrAC - Trends in Analytical Chemistry* **2010**, *29*, 1305–1315.

[110] J. Wu, M. Gu, *Journal of Biomedical Optics* **2011**, *16*, 080901–080901.

[111] A. L. Washburn, R. C. Bailey, *The Analyst* **2011**, *136*, 227–236.

[112] D. Gallegos, K. D. Long, H. Yu, P. P. Clark, Y. Lin, S. George, P. Nath, B. T. Cunningham, *Lab Chip* **2013**, *13*, 2124–2132.

[113] V. Oncescu, D. O'Dell, D. Erickson, *Lab on a Chip* **2013**, *13*, 3232–3238.

[114] C. A. d. S. Filho, A. M. N. Lima, H. Neff, *Smartphone based, portable optical biosensor utilizing surface plasmon resonance*, **2014**.

[115] D. Zhang, Q. Liu, *Biosensors and bioelectronics on smartphone for portable biochemical detection*, **2016**.

[116] S. Sang, Y. Wang, Q. Feng, Y. Wei, J. Ji, W. Zhang, *Critical Reviews in Biotechnology* **2015**, *00*, 1–17.

[117] J. J. Homola, *Analytical and Bioanalytical Chemistry* **2003**, *377*, 528–539.

[118] S. Pal, A. R. Yadav, M. A. Lifson, J. E. Baker, P. M. Fauchet, B. L. Miller, *Biosensors and Bioelectronics* **2013**, *44*, 229–234.

[119] B. Bottazzi, L. Fornasari, A. Frangolho, S. Giudicatti, A. Mantovani, F. Marabelli, G. Marchesini, P. Pellacani, R. Therisod, A. Valsesia, *Journal of Biomedical Optics* **2014**, *19*, 17006.

[120] S. Mariani, M. Minunni, *Analytical and Bioanalytical Chemistry* **2014**, *406*, 2303–2323.

[121] T. F. McGrath, K. Andersson, K. Campbell, T. L. Fodey, C. T. Elliott, *Biosensors and Bioelectronics* **2013**, *41*, 96–102.

[122] X. Xu, X. Liu, Y. Li, Y. Ying, *Biosensors and Bioelectronics* **2013**, *47*, 361–367.

[123] Z. Zhong, M. Fritzsche, S. B. Pieper, T. K. Wood, K. L. Lear, D. S. Dandy, K. F. Reardon, *Biosensors and Bioelectronics* **2011**, *26*, 2407–2412.

[124] S. Liu, Z. Zheng, X. Li, *Analytical and Bioanalytical Chemistry* **2013**, *405*, 63–90.

[125] C. A. Wartchow, F. Podlaski, S. Li, K. Rowan, X. Zhang, D. Mark, K.-S. Huang, *Journal of Computer-Aided Molecular Design* **2011**, *25*, 669–676.

[126] D. V. Lim, J. M. Simpson, E. A. Kearns, M. F. Kramer, *Clinical Microbiology Reviews* **2005**, *18*, 583–607.

[127] J. J. Gooding, *Analytica Chimica Acta* **2006**, *559*, 137–151.

[128] K. E. Brown, M. T. Greenfield, S. D. McGrane, D. S. Moore, *Analytical and Bioanalytical Chemistry* **2016**, *408*, 35–47.

[129] F. S. Rodrigues Ribeiro Teles, L. A. Pires de Távora Tavira, L. J. Pina da Fonseca, *Critical Reviews in Clinical Laboratory Sciences* **2010**, *47*, 139–169.

[130] C. I. L. Justino, T. A. Rocha-Santos, A. C. Duarte, T. A. Rocha-Santos, *TrAC Trends in Analytical Chemistry* **2010**, *29*, 1172–1183.

[131] S. Xu, *Microchimica Acta* **2012**, *178*, 245–260.

[132] H. Sharma, R. Mutharasan, *Biosensors and bioelectronics* **2013**, *45*, 158–62.

[133] R. Radhakrishnan, I. I. Suni, C. S. Bever, B. D. Hammock, *ACS Sustainable Chemistry and Engineering* **2014**, *2*, 1649–1655.

[134] M. L. Y. Sin, K. E. Mach, P. K. Wong, J. C. Liao, *Expert review of molecular diagnostics* **2014**, *14*, 225–244.

[135] G. Bülbül, A. Hayat, S. Andreescu, *Sensors* **2015**, *15*, 30736–30758.

[136] S. M. Yoo, S. Y. Lee, *Trends in Biotechnology* **2015**, *34*, 7–25.

[137] F. Cecchini, L. Fajs, S. Cosnier, R. S. Marks, *Trends in Analytical Chemistry* **2016**, *79*, 199–209.

[138] B. Cunningham, M. Weinberg, J. Pepper, C. Clapp, R. Bousquet, B. Hugh, R. Kant, C. Daly, E. Hauser, *Sensors and Actuators B: Chemical* **2001**, *73*, 112–123.

[139] J. Wang, W. Liu, Y. Xu, D. Chen, D. Li, L. Zhang, *Applied Physics A* **2014**, *116*, 1567–1572.

[140] K. K. Kanazawa, J. G. G. II, *Analytical Chemistry* **1985**, *57*, 1770–1771.

[141] S. Bruckenstein, M. Shay, *Electrochimica Acta* **1985**, *30*, 1295–1300.

[142] B. A. Čavić-Vlasak, L. J. V. Rajaković, *Fresenius' Journal of Analytical Chemistry* **1992**, *343*, 339–347.

[143] K. Keiji Kanazawa, *Faraday Discuss.* **1997**, *107*, 77–90.

[144] K. A. Marx, *Biomacromolecules* **2003**, *4*, 1099–1120.

[145] R. D. Vaughan, E. Geary, M. Pravda, G. G. Guilbault, *International Journal of Environmental Analytical Chemistry* **2003**, *83*, 555–571.

[146] K. Länge, B. E. Rapp, M. Rapp, *Analytical and Bioanalytical Chemistry* **2008**, *391*, 1509–1519.

[147] A. L. Kang, W. B. Wang, Y. Q. Liu, T. Han, *A wireless pressure sensor based on surface transverse wave*, **2011**.

[148] K. Kerman, D. Ozkan, P. Kara, B. Meric, J. J. Gooding, M. Ozsoz, *Analytica Chimica Acta* **2002**, *462*, 39–47.

[149] J. Wang in *Analytical Electrochemistry*, John Wiley and Sons, Inc., **2006**, pp. 1–28.

[150] D. Grieshaber, R. MacKenzie, J. Vörös, E. Reimhult, *Sensors* **2008**, *8*, 1400–1458.

[151] L. D. Watson, P. Maynard, D. C. Cullen, R. S. Sethi, J. Brettle, C. R. Lowe, *Biosensors* **1987**, *3*, 101–115.

[152] S. V. Dzyadevych, V. N. Arkhypova, A. P. Soldatkin, A. V. El'skaya, C. Martelet, N. Jaffrezic-Renault in *Handbook of Biosensors and Biochips*, John Wiley and Sons, Ltd, **2008**, Chapter 23.

[153] C. M. A. Brett, A. M. Oliveira-Brett, *Journal of Solid State Electrochemistry* **2011**, *15*, 1487–1494.

[154] E. Palmqvist, C. Berggren Kriz, K. Svanberg, M. Khayyami, D. Kriz, *Biosensors and Bioelectronics* **1995**, *10*, 283–287.

[155] A. Rabner, S. Belkin, R. Rozen, Y. Shacham, *Microfluidics, BioMEMS, and Medical Microsystems IV*, **2006**, pp. 611205–611210.

[156] P. A. E. Piunno, U. J. Krull, R. H. E. Hudson, M. J. Damha, H. Cohen, *Analytica Chimica Acta* **1994**, *288*, 205–214.

[157] E. A. Moschou, B. V. Sharma, S. K. Deo, S. Daunert, *Journal of Fluorescence* **2004**, *14*, 535–547.

[158] T. Dong, N. M. M. Pires, *Biosensors and Bioelectronics* **2017**, *94*, 321–327.

[159] M. El-Roz, H. Awala, F. Thibault-Starzyk, S. Mintova, *Sensors and Actuators B: Chemical* **2017**, *249*, 114–122.

[160] E. Bae, D. Ying, D. Kramer, V. Patsekin, B. Rajwa, C. Holdman, J. Sturgis, V. J. Davisson, J. P. Robinson, *Journal of biological engineering* **2012**, *6*, 12.

[161] J. P. Robinson, B. P. Rajwa, E. Bae, V. Patsekin, A. Roumani, A. Bhunia, J. Dietz, V. J. Davisson, M. M. Dundar, J. Thomas, E. Hirleman, *OPN Optics and Photonics News* **2011**, 20–27.

[162] A. Yalçin, K. C. Popat, J. C. Aldridge, T. A. Desai, J. Hryniewicz, N. Chbouki, B. E. Little, O. King, V. Van,

S. Chu, D. Gill, M. Anthes-Washburn, M. S. Ünlü, B. B. Gold-berg, *IEEE Journal on Selected Topics in Quantum Electronics* **2006**, *12*, 148–154.

[163] R. Heideman, R. Kooyman, J. Greve, *Sensors and Actuators B: Chemical* **1993**, *10*, 209–217.

[164] V. S. Lin, K. Motesharei, K. P. Dancil, M. J. Sailor, M. R. Ghadiri, *Science* **1997**, *278*, 840–843.

[165] F. J. Blanco, M. Agirregabiria, J. Berganzo, K. Mayora, J. Eliz-alde, A. Calle, C. Dominguez, L. M. Lechuga, *Journal of Mi-cromechanics and Microengineering* **2006**, *16*, 1006–1016.

[166] X. Wei, S. M. Weiss, *Optics Express* **2011**, *19*, 11330–11339.

[167] R. Gush, J. M. Cronin, W. J. Stewart, R. Cush, J. M. Cronin, W. J. Stewart, C. H. Maule, J. Molloy, N. J. Goddard, R. Gush, J. M. Cronin, W. J. Stewart, *Biosensors and Bioelectronics* **1993**, *8*, 347–354.

[168] N. J. Goddard, D. Pollard-Knight, C. H. Maule, *Analyst* **1994**, *119*, 583–588.

[169] J. Hulme, C. Malins, K. Singh, P. R. Fielden, N. J. Goddard, *Analyst* **2002**, *127*, 1233–1236.

[170] O. Gaathon, J. Culic-Viskota, M. Mihnev, I. Teraoka, S. Arnold, *Applied Physics Letters* **2006**, *89*, 223901.

[171] K. De Vos, I. Bartolozzi, E. Schacht, P. Bienstman, R. Baets, *Optics Express* **2007**, *15*, 7610–7615.

[172] V. Goral, Q. Wu, H. Sun, Y. Fang, *FEBS letters* **2011**, *585*, 1054–60.

[173] S. M. Grist, S. A. Schmidt, J. Flueckiger, V. Donzella, W. Shi, S. T. Fard, J. T. Kirk, D. M. Ratner, K. C. Cheung, L. Chrostowski, *Optics Express* **2013**, *21*, 7994–8006.

[174] G. Yuan, L. Gao, Y. Chen, X. Liu, J. Wang, Z. Wang, *Optik - International Journal for Light and Electron Optics* **2014**, *125*, 850–854.

[175] A. E. Grow, L. L. Wood, J. L. Claycomb, P. A. Thompson, *Journal of Microbiological Methods* **2003**, *53*, 221–233.

[176] A. Khetani, J. Riordon, V. Tiwari, A. Momenpour, M. Godin, H. Anis, *Optics express* **2013**, *21*, 12340–12350.

[177] K. Ramanathan, B. Danielsson, *Biosensors and Bioelectronics* **2001**, *16*, 417–423.

[178] U. von Ah, D. Wirz, A. U. Daniels, *BMC Microbiology* **2009**, *9*, 1–14.

[179] C. Nylander, B. Liedberg, T. Lind, *Sensors and Actuators* **1982**, *3*, 79–88.

[180] A. Abbas, M. J. Linman, Q. Cheng, *New trends in instrumental design for surface plasmon resonance-based biosensors*, **2011**.

[181] I. Lundström, *Biosensors and Bioelectronics* **1994**, *9*, 725–736.

[182] A. D. Boardman, *Electromagnetic Surface Modes*, Wiley, **1982**.

[183] A. R. Sadrolhosseini, A. S. M. Noor, M. M. Moksin, *Plasmonics: Princ. Appl.* **2012**, 253–282.

[184] E. Kretschmann, H. Raether, *Z. Naturforsch.* **1968**, *23*, 2135–2136.

[185] B. Liedberg, C. Nylander, I. Lunstrom, *Sensors and Actuators* **1983**, *4*, 299–304.

[186] S. J. Orfanidis, *Media* **2004**, *2*, 313–321.

[187] M. Malmqvist, *Current Opinion in Immunology* **1993**, *5*, 282–286.

[188] H. Zhang, D. Song, S. Gao, H. Zhang, J. Zhang, Y. Sun, *Talanta* **2013**, *115*, 857–862.

[189] G. Spoto, M. Minunni, *The Journal of Physical Chemistry Letters* **2012**, *3*, 2682–2691.

[190] A. V. Kabashin, P. Evans, S. Pastkovsky, W. Hendren, G. A. Wurtz, R. Atkinson, R. Pollard, V. A. Podolskiy, A. V. Zayats, *Nat Mater* **2009**, *8*, 867–871.

[191] M. Kashif, A. A. A. Bakar, N. Arsad, S. Shaari, *Sensors (Basel Switzerland)* **2014**, *14*, 15914–15938.

[192] M. Puiu, C. Bala, *Sensors (Basel Switzerland)* **2016**, *16*, 870.

[193] R. W. Wood, *Proceedings of the Physical Society of London* **1902**, *18*, 269–275.

[194] A. Otto, *Zeitschrift für Physikr Physik* **1968**, *216*, 398–410.

[195] R. L. Rich, D. G. Myszka, *Current opinion in biotechnology* **2000**, *11*, 54–61.

[196] A. K. Sharma, R. Jha, B. D. Gupta, *IEEE Sensors Journal* **2007**, *7*, 1118–1129.

[197] H. S. Jang, K. N. Park, C. D. Kang, J. P. Kim, S. J. Sim, K. S. Lee, *Optics Communications* **2009**, *282*, 2827–2830.

[198] J. Pollet, F. Delport, K. P. Janssen, K. Jans, G. Maes, H. Pfeiffer, M. Wevers, J. Lammertyn, *Biosensors and Bioelectronics* **2009**, *25*, 864–869.

[199] K. Knez, K. P. F. Janssen, D. Spasic, P. Declerck, L. Vanysacker, C. Denis, D. T. Tran, J. Lammertyn, *Analytical Chemistry* **2013**, *85*, 1734–1742.

[200] A. P. Hibbins, J. R. Sambles, C. R. Lawrence, *Journal of Applied Physics* **1999**, *86*, 1791.

[201] K. M. Byun, S. J. Kim, D. Kim, *Applied Optics* **2007**, *46*, 5703.

[202] M. Piliarik, M. Vala, I. Tichý, J. Homola, *Biosensors and Bioelectronics* **2009**, *24*, 3430–3435.

[203] M. Vala, K. Chadt, M. Piliarik, J. Homola, *Sensors and Actuators B: Chemical* **2010**, *148*, 544–549.

[204] A. Sonato, M. Agostini, G. Ruffato, E. Gazzola, D. Liuni, G. Greco, M. Travagliati, M. Cecchini, F. Romanato, F. Romanato, F. Romanato, M. Morpurgo, *Lab Chip* **2016**, *16*, 1224–1233.

[205] P. Preechaburana, M. C. Gonzalez, A. Suska, D. Filippini, *Angewandte Chemie (International ed. in English)* **2012**, *51*, 11585–11588.

[206] E. Helmerhorst, D. J. Chandler, M. Nussio, C. D. Mamotte, *The Clinical Biochemist Reviews* **2012**, *33*, 161–173.

[207] E. González-Fernández, N. De-los Santos-Álvarez, A. J. Miranda-Ordieres, M. J. Lobo-Castañón, *Talanta* **2012**, *99*, 767–773.

[208] Y. Yanase, T. Hiragun, K. Ishii, T. Kawaguchi, T. Yanase, M. Kawai, K. Sakamoto, M. Hide, *Sensors (Basel Switzerland)* **2014**, *14*, 4948–4959.

[209] L. Guo, J. A. Jackman, H.-H. Yang, P. Chen, N.-J. Cho, D.-H. Kim, *Nano Today* **2015**, *10*, 213–239.

[210] W. Peng, Y. Liu, P. Fang, X. Liu, Z. Gong, H. Wang, F. Cheng, *Optics Express* **2014**, *22*, 6174–6185.

[211] S. Scarano, M. Mascini, A. P. F. Turner, M. Minunni, *Biosensors and Bioelectronics* **2010**, *25*, 957–966.

[212] H. Baccar, M. B. Mejri, I. Hafaiedh, T. Ktari, M. Aouni, A. Abdelghani, *Talanta* **2010**, *82*, 810–814.

[213] S. D. Mazumdar, B. Barlen, P. Kämpfer, M. Keusgen, *Biosensors and Bioelectronics* **2010**, *25*, 967–971.

[214] J. Waswa, J. Irudayaraj, C. DebRoy, *LWT - Food Science and Technology* **2007**, *40*, 187–192.

[215] J. R. Son, G. Kim, A. Kothapalli, M. T. Morgan, D. Ess, *Journal of Physics: Conference Series* **2007**, *61*, 1086–1090.

[216] Y.-b. Lan, S.-z. Wang, Y.-g. Yin, W. C. Hoffmann, X.-z. Zheng, *Journal of Bionic Engineering* **2008**, *5*, 239–246.

[217] G. C. A. M. Bokken, R. J. Corbee, F. Van Knapen, A. A. Bergwerff, *FEMS Microbiology Letters* **2003**, *222*, 75–82.

[218] P. Leonard, S. Hearty, J. Quinn, R. O'Kennedy, *Biosensors and Bioelectronics* **2004**, *19*, 1331–1335.

[219] J. W. W. Waswa, C. Debroy, J. Irudayaraj, *Journal of Food Process Engineering* **2006**, *29*, 373–385.

[220] Y. Wang, Z. Ye, C. Si, Y. Ying, *Sensors (Basel Switzerland)* **2011**, *11*, 2728–2739.

[221] N. M. M. Pires, T. Dong, U. Hanke, N. Hoivik, *Sensors (Basel Switzerland)* **2014**, *14*, 15458–15479.

[222] O. Tokel, F. Inci, U. Demirci, *Chemical reviews* **2014**, *114*, 5728–5752.

[223] A. D. Taylor, Q. Yu, S. Chen, J. Homola, S. Jiang, *Sensors and Actuators B: Chemical* **2005**, *107*, 202–208.

[224] Ö. Torun, s. Hakkı Boyacı, E. Temür, U. Tamer, *Biosensors and Bioelectronics* **2012**, *37*, 53–60.

[225] S. Bouguelia, Y. Roupioz, S. Slimani, L. Mondani, M. G. Casabona, C. Durmort, T. Vernet, R. Calemczuk, T. Livache, *Lab on a Chip* **2013**, *13*, 4024–4032.

[226] Y. Wang, W. Knoll, J. Dostalek, *Analytical Chemistry* **2012**, *84*, 8345–8350.

[227] K. M. Mayer, J. H. Hafner, A. À. Antigen, *Chemical reviews* **2011**, *111*, 3828–3857.

[228] N. Nath, A. Chilkoti, *Analytical Chemistry* **2004**, *76*, 5370–5378.

[229] G. J. Nusz, A. C. Curry, S. M. Marinakos, A. Wax, A. Chilkoti, *ACS nano* **2009**, *3*, 795–806.

[230] R. Peltomaa, I. López-Perolio, E. Benito-Peña, R. Barderas, M. C. Moreno-Bondi, *Analytical and Bioanalytical Chemistry* **2016**, *408*, 1805–1828.

[231] N. Tawil, E. Sacher, R. Mandeville, M. Meunier, *The Journal of Physical Chemistry C* **2013**, *117*, 6686–6691.

[232] N. Tawil, E. Sacher, R. Mandeville, M. Meunier, *Biosensors and Bioelectronics* **2012**, *37*, 24–29.

[233] A. D. Taylor, J. Ladd, Q. Yu, S. Chen, J. Homola, S. Jiang, *Biosensors and Bioelectronics* **2006**, *22*, 752–758.

[234] J. De Pelsmaeker, H. Thienpont, H. Ottevaere, *to be submitted in Optics Express*.

[235] T. Nguyen, S. Kwak, S. J. Karpowicz, *BioTechniques* **2014**, *57*, 267–271.

[236] D. C. Wilson, C. Velis, C. Cheeseman, *Habitat International* **2006**, *30*, 797–808.

[237] J. Hopewell, R. Dvorak, E. Kosior, *Philosophical Transactions of the Royal Society B: Biological Sciences* **2009**, *364*, 2115–2126.

[238] K. M. McPeak, S. V. Jayanti, S. J. P. Kress, S. Meyer, S. Iotti, A. Rossinelli, D. J. Norris, *ACS Photonics* **2015**, *2*, 326–333.

Chapter 2

Synthesis and polymerisation of cyclic diesters

"Nothing on this earth lasts forever. Except maybe plastic."

— Patricia Dunn

2.1 Introduction

As already indicated in chapter 1, lab-on-a-chip devices could cause a paradigm shift in the microbiological evaluation of (drinking) water. If these miniaturised analytical devices are to become common practice, they need to be mass-manufacturable. Moreover, the applied materials should be mechanically stable to allow the handling of the chips and chemically inert to prevent undesired side reactions during the surface modification and/or application of the sensor. Considering the optical detection method that will be targeted in the present work, the materials should also be optically transparent at the applied wavelength (i.e. 661 nm for envisioned proof-of-concept demon-

---

The X-ray diffraction experiments mentioned in this chapter were performed by prof. dr. Kristof Van Hecke. Experiments involving optical profilometry were performed by Ms. Julie Verdood.

strator). Due to their micrometer scale channels, LoC biosensors are generally troublesome to rinse, which is why most LoCs are designed for single-use applications.[1]

Historically, LoC devices have been fabricated from glass, silicon and polymers.[2] Glass has excellent optical properties and is very resistant to solvents. However, the fabrication of microfluidic structures starting from glass is limited by the inability to produce high aspect ratio features and the curved bottoms which result from the applied etching process, thereby diminishing the optical properties.[2] Silicon is very strong and can be lithographically etched. However, it is not optically transparent in the desired wavelength range (visible and near infrared) and the conductive properties render electrokinetic flow (i.e. the transport of fluids by means of an electrical potential) impossible contrary to insulating materials like glass or polymers. Recently, polymers have become attractive materials owing to their straightforward surface modification, easy processing, low cost (0.03 - 4.5 € kg^{-1}),[3] disposability, optical transparency *etc.*[4]

Unfortunately, plastics have gathered a negative reputation as conventional polymers are able to resist degradation and can accumulate in the environment.[5] Moreover, since most plastic materials are derived from fossil natural resources, plastics are generally labeled unsustainable. The low price associated with their production renders them easily disposable, resulting in high amounts of plastic waste being discarded annually (25.8 million tonnes in Europe, 2014).[6]

To overcome the negative aspects of plastics, two strategies can be distinguished. In a first strategy, the research focuses on sustainability, which can be realised by selecting naturally occurring polymers such as starch or cellulose,[7,8] by polymerizing monomers derived from natural resources (i.e. biomass),[9,10] or by applying environmentally benign synthesis routes (e.g. biotechnological production of e.g. polyhydroxyalkanoates).[11–13]

A second strategy focuses on minimizing the environmental impact of plastics. A first way to achieve this goal is by applying more efficient sorting and recycling methodologies.[14] However, the recovery rate of plastics remains limited with 30% of plastics going to landfills.[6,15] An alternative approach to reduce the environmental impact therefore focuses on the materials applied and aims at engineering

(bio)degradable polymers. For example, polymers such as polyethylene and polypropylene can be blended with appropriate catalysts that induce degradation.[16] However, there remains concern that the catalysts, which are often based on heavy metals, may induce an environmental problem of their own. To circumvent this issue, polymers with the ability to degrade can be engineered by applying the appropriate monomers. The latter strategy will be the focus of the present work. Literature often refers to bioplastics for both bio-based as well as (bio)degradable materials. Herein, the distinction will be made between bio-based and biodegradable polymers as bio-based polymers are not necessarily degradable and vice versa.[17,18]

Biodegradation has been defined by the International Union of Pure and Applied Chemistry (IUPAC) as the degradability of substances by biological activity by lowering of the molar masses of the macromolecules that form the substance.[19] This IUPAC definition clearly excludes degradation through enzymatic activity as living cells have to be present to be able to use the term 'biodegradation'. Herein, however, an extended definition will be handled since enzymatic degradation and certain abiotic reactions (*e.g.* photo-degradation, hydrolysis and oxidation) will be included. Biodegradable should therefore be understood as environmentally degradable.[20]

Biodegradable and bio-based polymers make up about 300,000 metric tons of the total plastics market, which only accounts for 1% of the global market of synthetic plastics.[20,21] However, the market for degradable and sustainable plastics grows about 20-30% each year, which is considerably higher than the total market growth. Polyesters, like poly(lactic acid) and poly(glycolic acid), make up a large fraction ($> 35\%$) of the biodegradable plastics market.[22] As their name suggests, poly(esters) are a class of polymers in which the monomer units are linked together via ester bonds. Since these bonds are prone to hydrolysis, polyesters play an important role within the biodegradable materials. Polyesters can be generally subdivided into two groups: the aliphatic and the aromatic polyesters.

Degradable polyesters are generally derived from aliphatic monomers including lactic acid, glycolic acid, ε-caprolactone, *etc.* In these materials, no aromatic structures are present in the main chain, enabling hydrolysis to occur more easily. Although produced synthet-

(a) Step-growth   **(b)** Chain-growth   **(c)** Living/controlled
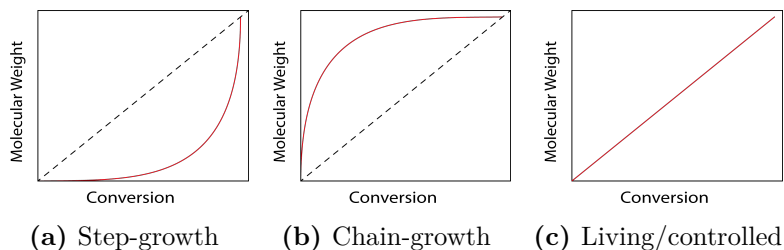
Figure 2.1: Overview of the molecular weight evolution for two synthesis routes compared to the situation observed for living polymerisations. Step-growth polymerisations (figure 2.1a) yield high molecular weights at high monomer conversion. Chain growth polymerisations (figure 2.1b) lead to high molecular weight at low monomer conversions. In living/controlled polymerisations (figure 2.1c), termination and chain transfer reactions are suppressed leading to a linear relationship between conversion and molecular weight.

ically, these polymers are often preferred over natural polymers, as their properties can be tailored and the resulting materials have more predictable lot-to-lot uniformity than their natural counterparts.[23] Poly(esters) can be synthesised via various synthesis routes, which will be discussed in the upcoming sections.

2.1.1   Polycondensation

A first synthesis route is the polycondensation of dicarboxylic acids with diols or the polycondensation of hydroxyacids. Since this procedure occurs according to a step-wise addition of monomer units, this method is associated with long reaction times as polymer is only obtained at high conversions (figure 2.1a). In some cases, the addition of a suitable catalyst (e.g. tetrabutyl titanate) can, however, decrease the required reaction time.[24]

Additionally, the control over this reaction is troublesome as the slightest imbalance in stoichiometry between the diol and the dicarboxylic acid will result in the termination of the growing chains. Hydroxyacids are therefore favoured, since these monomers do not pose the problem related to an unbalanced stoichiometry. Furthermore, any monofunctional acid or alcohol present in the reaction mixture will result in a dead chain-end. As a result, molecular weight

distributions are generally quite broad (Đ> 1.5). During the condensation reaction, water is generally formed as a side-product, although transesterifications can also be applied.[25,26]

When performing direct polycondensation polymerisations in the melt state, the obtained molecular weights are generally limited, since the increasing viscosity of the reaction mixture will hinder the efficient removal of water.[27,28] In addition, the same effect impedes the efficient diffusion of the growing chain ends, thereby reducing the polymerisation rate.[29] These disadvantages limit the use of the direct polycondensation method.[30]

To drive the condensation reaction towards completion and thus to increase the molecular weight of the obtained polymers, the water by-product can be removed more effectively via an azeotropic distillation. The reagents are dissolved in a suitable solvent (e.g. toluene or mixed xylenes) after which the water fraction is collected in a Dean-Stark trap, while the dried solvent is recycled back to the flask. This method can lead to high molecular weight polymers (> 10 kg mol^{-1}) in a one-step reaction, but the reaction can still be time-consuming (> 40 h).[31]

Alternatively, chain-coupling reagents can be applied. These di-carboxylic acids or diols are able to react with the alcohol or carboxylic acid end-groups respectively, effectively coupling two shorter polymer strands thereby increasing the overall molecular weight.

In case of semi-crystalline polymers, reports can be found on a two-step process in which short chains are crystallised after which the polymerisation is continued in the solid state to obtain high molecular weight PLLA.[32] In this process an inert gas stream is applied to remove by-products from the surface. The coupling mainly takes place in the amorphous regions of the materials, where the reactive end groups reside.

2.1.2 Ring-opening polymerisation of lactones

An alternative for the above-mentioned polycondensation mechanism can be found in the ring-opening polymerisation of cyclic (di)esters, which follows a chain growth mechanism (figure 2.1). The latter implies rapid polymer propagation resulting in high molecular weights (> 10 kg mol^{-1}) in shorter reaction times (minutes to hours) com-

pared to what is generally observed for polycondensations. In addition, narrow molecular weight distributions (< 1.5) can be achieved by using appropriate catalysts (among others, aluminium and tin catalysts) increasing the reproducibility of the obtained polymers.[33]

When transfer and termination reactions are completely absent, the polymerisation reaction can be considered as living.[34] The growing chains should therefore remain active, thus keeping the number of active species constant once the initiation phase has passed. This results in a linear correlation between conversion and molecular weight (figure 2.1c). As long as monomer is added, the chains will thus be able to grow. Polymerisations are considered "controlled" when transfer and termination reaction are suppressed to such an extent that the concentration of reactive chain ends remains stable.

Ring opening polymerisations are, however, limited by the number of available monomers. In contrast to the vast number of dicarboxylic acids and diols, the number of available cyclic (di)esters is far lower.[35,36] However, new lactones and di(esters) are being synthesised nowadays to further advance the field.[37–40]

Four classes of ROP can be distinguished including anionic, cationic, metal-insertion and organo-catalytic ROP, which will be introduced in the upcoming sections. It is beyond the scope of the current chapter to summarise all catalyst systems applied in the ROP of lactones, as the interested reader can find more information in an excellent review by Dechy-Cabaret *et al.*[41]

Anionic ring-opening polymerisation

In anionic ROP, nucleophilic metal alkoxides initiate the polymerisation reaction. Some bulky alkoxides, however, will rather act as base thereby introducing a new anionic centre on a monomer unit, which can subsequently act as the anionic initiator.[42,43] Two different propagation mechanisms can be distinguished as depicted in figure 2.2.

When no protic compounds are present, termination by quenching of the anionic centre will generally be negligible. The loss of control is thus mainly determined by the occurrence of transfer reactions. As the monomer gets depleted, the anionic centre can react with ester groups in the polymer chain as the reactivity of the ester groups in

Anionic ROP

acyl-oxygen scission

alkyl-oxygen scission
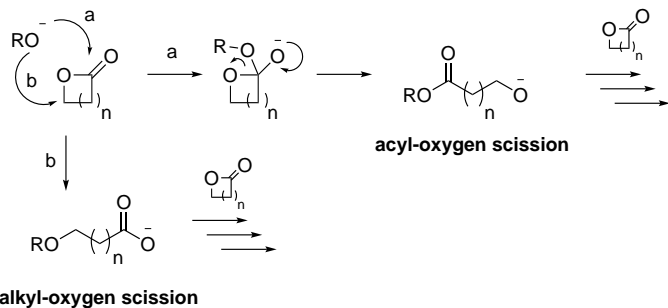
Metal-insertion ROP

Cationic ROP

R$_1$=alkylating reagent

R$_1$=H

R−OH

Organo-catalytic ROP

+ Nu
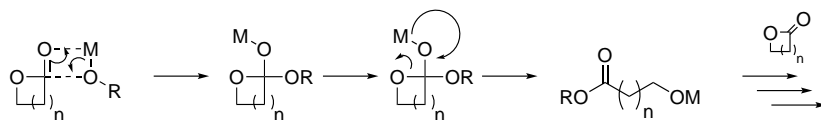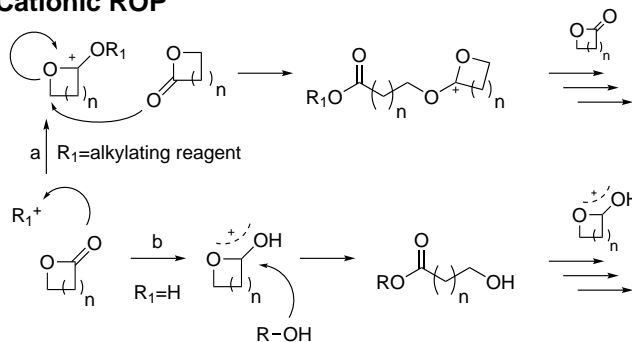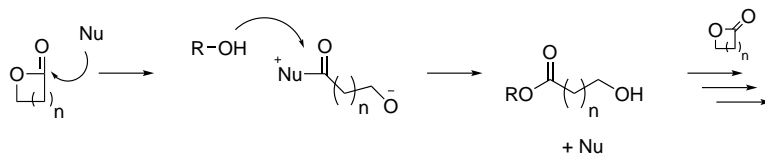
Figure 2.2: Scheme showing the most common types of ring-opening polymerisations for the synthesis of polyesters

the polymer differs only slightly from the lactone ester group. The so-called back-biting reactions will thus start to occur resulting in the formation of cyclic products.[29] In addition, intermolecular transesterification reactions will alter the obtained molecular weight.

Control over the polymerisation reaction can be increased using less reactive initiators, thereby disfavouring transesterification.[44] One strategy applies sterically hindered initiators to oppose reaction occurring with growing polymer chains.[30,45,46] Another strategy involves the use of certain less electropositive metals (e.g. Sn, Al, Zn). The latter will be further referred to as metal-insertion ROP.

Metal-insertion ring-opening polymerisation

It is possible to increase control over the ring-opening polymerisation by applying organometallic derivatives showing d-orbitals of favourable energy. Aluminium alkoxides have been shown to increase control over the reaction and are easily synthesised by reacting alcohols with triethylaluminium or aluminium isopropoxide. The applied alcohols can be substituted with reactive groups including bromides, olefins and tertiary amines to obtain end-group functionalised polymers.[47,48]

The metal-insertion ROP owes its name to the propagation mechanism (figure 2.2). After coordination of the metal-alkoxide with the carbonyl group of the lactone, the addition of the nucleophilic alkoxides takes place onto the electrophilic carbon atom of the ester bond. Subsequently, an elimination reaction occurs via acyl-oxygen scission. The novel alkoxide will act as the newly generated propagating species.

After the initial work on aluminium alkoxides, the metal-insertion ROP was extended to other metal ions including titanium,[49–51] tin (II),[52–54] tin (IV),[55–57] zirconium,[58,59] and more recently rare-earth metals (Y, Er, Sm, Dy, Nd and La).[60–62] Currently, tin(II) octoate, also known as tin(II) bis(2-ethylhexanoate), is the most frequently used catalyst for metal-insertion ROP. It owes its privileged position to the fact that it has been approved by the American Food and Drug Administration (FDA) for the formulation of polymer coatings which come in contact with food. In addition, tin octoate is less sensitive towards water and other protic impurities, rendering it even more interesting for laboratory and industrial purposes. Tin octoate con-

tains two carboxylates which have already been shown to be poor initiators for ROP. However, Kowalski *et al.* discovered that the actual initiating species is formed *in situ* by the reaction of tin octoate with water, alcohols or alkoxides.[52] When considering *in vivo* applications however, tin residues may still pose a problem. To circumvent this problem, less toxic catalysts including magnesium and calcium alkoxides are being developed.[30,45]

Cationic ring-opening polymerisation

In contrast to anionic ROP, cationic ring-opening polymerisations are far less utilised due to the poor control over the reaction outcome. Cationic ROP was first reported by Penczek et al. for the polymerisation of ε-caprolactone and β-propionolactone.[63] Afterwards, various initiating systems have already been reported which can be subdivided in four classes including alkylating agents (e.g. halonium salts), acylating agents (e.g. $CH_3CO^+SbF_6^-$), Lewis acids (e.g. $SnCl_4$, $FeCl_3$, $AlCl_3$, BCl_3) and protonic acids.[41,43,64–67] Depending on the type of initiating reagent, different mechanisms can be distinguished. When alkylating agents are applied, the main reaction pathway will involve the exocyclic oxygen (figure 2.2).

In case of Lewis acid initiation, a cationic ROP will only occur if the counterion is not too nucleophilic.[68] When nucleophilic counterions are present, the metal-insertion mechanism will be followed instead, as already reported for several catalytic systems including $ZnCl_2$,[67] $TiCl_4$ and $AlCl_3$.[69]

The final possibility includes the application of amines and alcohols as nucleophilic initiators under Brønsted acid catalysis. In this mechanism, activated monomers react with the initiator or the nucleophilic chain-end. After protonation of the exocyclic oxygen and the nucleophilic attack, ring-opening occurs via acyl-oxygen scission (figure 2.2). This mechanism is more favourable than polymerisations applying alkylating agents. However, the molecular weights obtained are generally limited, unless great care is spent on the selection of suitable catalysts.

Organo-catalytic ring-opening polymerisation

The last type of ring-opening polymerisation of lactones discussed in the present work involves the use of organic compounds as catalysts. Although alcohols and amines are generally not nucleophilic enough to initiate a polymerisation, in some cases, tertiary amines are able to efficiently initiate the polymerisation of highly reactive β-lactones.[43]

However, for less reactive monomers, catalysts are generally required. These compounds can activate the monomer, the initiator or both.[70–72] Hedrick and co-workers were pioneers in this field with the introduction of a metal-free route towards polyesters.[70–75] Organo-catalytic polymerisations generally involve nucleophiles activating the monomer ring followed by the release of the catalyst by the nucleophilic attack of the initiator (figure 2.2).

The most widely applied catalyst systems in organo-catalytic ROP include N-heterocyclic carbenes, guanidine and amidine bases and phosphorane-based compounds.[71,74–79] Strong organic acids are excluded from this section as their mechanism follows the one described for cationic ring-opening polymerisations.[80,81]

2.1.3   Enzymatic polyester synthesis

Finally, polyesters can also be synthesised via enzymatic processes using lipase or esterase enzymes. This type of polymerisations possesses some advantages over the earlier described chemical synthesis routes including mild reaction conditions, a higher selectivity, a high tolerance of functional groups and the synthesis of pure reaction products which are metal-free.[82–84] However, reaction times are longer (2-7 days) and yields lower (typically < 30 wt%) compared to chain growth polymerisations.[33,85]

Poly(β-hydroxyalkanoates) (PHAs) are a class of polyesters which are synthesised by many bacteria as energy reserve and carbon source when exposed to an excess of carbon under unbalanced growth conditions.[86] The produced PHAs can account for up to 80% of the bacterium's dry weight. This has led to the biotechnological production of PHAs. Depending on the substrates provided to the bacteria, different monomers can be produced which results in different PHA (co)polymers.[11]

Poly(3-hydroxybutyrate) (PHB) was the first PHA to be produced on an industrial scale under the trade name Biopol®, but its brittle nature (3-8% strain at break compared to 500-900% for PP) and its high production cost (10-20 € kg^{-1} compared to e.g. 3 € kg^{-1} for polypropylene) limited its application potential.[87] In the early 1990s, the industrial production of poly(3-hydroxybutyrate-co-3-hydroxyvalerate) (P3HB3HV) started. This material showed lower degrees of crystallinity and superior mechanical properties. Despite the large interest in PHAs, their application remains however limited due to their narrow processing window (T$_{max}$ 155 °C).[88,89]

2.1.4 Degradation of polyesters

The degradation of polymers generally encompasses the scission of the main and/or the side-chains of the polymer, resulting in any physical or chemical change. These scissions can be induced by thermal activation, oxidation, photolysis, radiolysis, biological activity, ozone or hydrolysis.[90–92]

The American Society for Testing and Materials (ASTM) defines biodegradation as the process which is capable of decomposition of materials into carbon dioxide, methane, water, inorganic compounds or biomass in which the predominant mechanism is the enzymatic action of microorganisms, that can be measured by standard tests, in a specified period of time, reflecting available disposal conditions. Biodegradation therefore can be described as the degradation of polymers due to biological environments (e.g. living cells, microorganisms) either by enzymatic or non-enzymatic hydrolysis. However, biotic and abiotic factors act synergistically and several studies have already reported that the abiotic degradation precedes microbial assimilation and therefore can not be neglected.[93] Abiotic factors include mechanical forces (e.g. shear or compressive forces), the action of light irradiation (e.g. photo-ionisation), thermal effects and chemical degradation (e.g. oxygen, hydrolysis).

Monitoring the (bio)degradation of polymers can be performed by the quantification of the molecular weight reduction. However, following this strategy, information regarding biodegradation into CO_2 and H_2O of the monomers and oligomers is excluded. Therefore, biodegradation is generally measured as the conversion of organic

carbon into inorganic carbon (i.e. conversion into CO_2). Standardised methodologies and procedures for testing polymer biodegradation have been introduced by the (ASTM), the Japanese Industrial Standards (JIS), the European Normative Reference (ECN) and the Organisation for Economic Co-operation and Development (OECD). For an elaborate description on validated and accepted test methods, the review from Eubeler *et al.* can be consulted.[94]

For most polymers, degradation in nature is a slow process. The mechanisms involved in biodegradation are complex due to the interaction of different oxidative processes which are caused by oxygen present in air, by the action of (micro)organisms or by a combination of both. The intrinsic chemical structure of the polymer will determine its biodegradability. Several mechanisms act during the biodegradation of polymers:[95]

Solubilisation: hydration based on the hydrophilicity of the polymer rendering it soluble and prone to chemical or enzyme-catalysed degradation;

Charge formation followed by dissolution: ionisation or protonation of a pendant group leading to increased solubility;

Hydrolysis: hydrolytically unstable bonds, resulting in chain scission and the formation of low molecular weight by-products;

Enzyme-catalysed degradation: enzymes catalyse specific reactions (*i.e.* oxidation, reduction, hydrolysis, ...);

Microbial degradation: microorganisms (MOs) such as bacteria, fungi, algae act in the polymer degradation.

Factors affecting the biodegradation process (figure 2.3) can be subdivided in polymer characteristics (*i.e.* mobility, tacticity, crystallinity, molecular weight, type of functional groups, substituents, plasticisers, additives) and environmental conditions (*i.e.* humidity, temperature, pH and availability of oxygen).[91,95–98] For example, increasing molecular weights generally result in a decline of the degradability induced by MOs.[99] Monomers, dimers and oligomers are thus more easily degraded and mineralised as these compounds are small

enough (< 2 nm) to be able to pass the bacterial cell wall.[18,92] Furthermore, generally, a small fraction of the polymeric material will be incorporated into microbial biomass, humus, and/or other natural products. As such, the biodegradation rate rarely reaches 100%. The aerobic biodegradation of polyesters can be described according to the following mechanism:[96,100]

$$\text{Polymer} \xrightarrow{\text{H}_2\text{O}} \text{Monomer} \xrightarrow{\text{O}_2} \text{Biomass} + \text{H}_2\text{O} + \text{CO}_2 \quad (2.1)$$
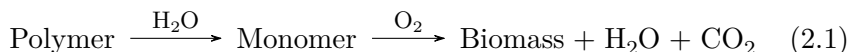
The first reaction is governed by the hydrolysis of the ester bonds, generally catalysed by extracellular enzymes, into oligomers and monomers (*i.e.* depolymerisation). However, polyesters may even undergo spontaneous hydrolysis at room temperature and neutral pH in the presence of moisture. This primary depolymerisation thus leads to water-soluble intermediates. If in the next step, these low molecular weight fragments migrate through the cell membrane and are mineralised by microorganisms, the degradation is called biomineralisation.[18,92] It can be deduced that a temporary build-up of monomers can arise in case the depolymerisation occurs at a higher rate than the biomineralisation.

In general, two modes of erosion for biodegradable polymers can be distinguished including bulk and surface erosion.[92] Both modes are schematically illustrated in figure 2.4.

In surface erosion, the polymer matrix is consumed from the surface inwards. This is governed by a slow reduction of the molecular weight. Typically, this results in volume reduction of the sample accompanied by a decrease in mass, yet the number average molecular weight M_n of the bulk remains unchanged. Surface erosion occurs when the degradation products diffuse into the surroundings faster than water can diffuse into the polymer matrix. The degradation rate constant (k) for the surface erosion model can be determined via equation 2.2:

$$x = -kt + C \quad (2.2)$$

where x is the mass fraction of remaining polymer, k is the degradation rate constant, t is time and C is a constant. Surface erosion leads to a linear decay of x as a function of t.[37]
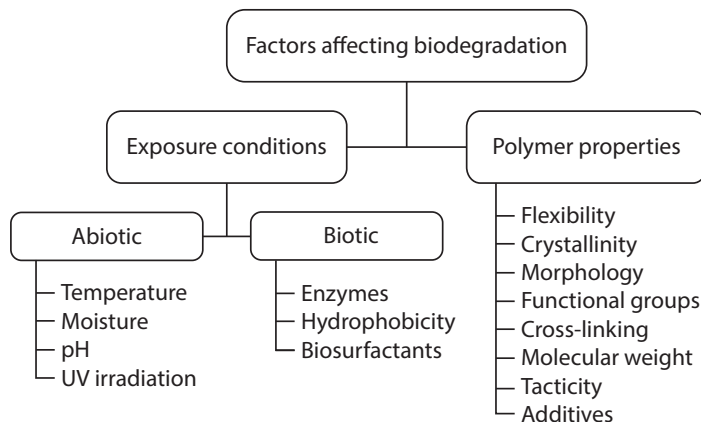
Figure 2.3: Illustration showing the factors affection (bio)degradation of polyesters. Given the clear distinction between material properties and environmental conditions, a degradable material will only degrade when the appropriate conditions are met.

Conversely, during bulk erosion, degradation occurs throughout the whole sample and the molecular weight may decrease without any mass loss, creating a more disperse molecular weight distribution. When bulk degradation takes place below the T_g of the polymer, the process can become autocatalytic as the degradation products are unable to leach out thereby creating pockets of increased acidity. When the degradation products become small enough, they are able to diffuse out of the polymer matrix and create an onset of mass loss. The
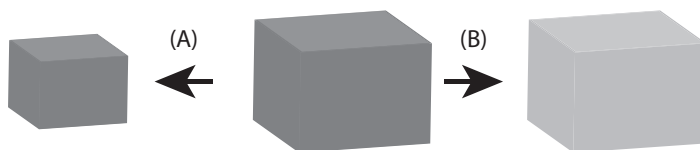
Figure 2.4: Erosion mechanisms of biodegradable polymers including (A) surface erosion which is limited to the material surface, leaving the bulk unaffected; and (B) bulk erosion, which decreases the average molecular weight throughout the sample (as visualised by the increased transparency of the cube) while maintaining the object's dimensions.

degradation rate constant for an autocatalysed bulk erosion model can be determined by the Prout-Tompkins equation (equation 2.3):[101]

$$ln(\frac{x}{1-x}) + C = kt \tag{2.3}$$

where x is the mass fraction of remaining polymer, k is the degradation rate constant, t is time and C is a constant. When plotting $ln(x/(1-x))$ as a function of t, a linear fit is observed after an induction period. The latter corresponds to the time required to reduce the molecular weight of the polymer to such a degree that the degradation products are able to diffuse from the sample. This process is included in the term C of the above-mentioned equation.

Although some classes of biodegradable polymers show a predisposition towards either surface or bulk erosion, both processes often proceed simultaneously.[30,37,99,102]

2.1.5 Selection of polymer building blocks

In order to apply degradable polyesters as sensor substrates, it is clear they should exhibit a high optical transmittance ($> 95\%$ at the applied wavelength i.e. 661 nm for the envisioned proof-of-concept demonstrator). As previously described, ring-opening polymerisations are also desired since these polymerisation methods are associated with a higher degree of control over polymer synthesis and material properties. Unfortunately, the most applied degradable polyesters (*i.e.* PGA, PLLA, PLA and PHAs) are all semi-crystalline. The crystalline domains will result in opaque materials due to scattering of the incident light.[103] The amount of scattering depends both on the wavelength of the incident light as well as the size of the crystalline domains.[104] Amorphous polyesters, *e.g.* PDLLA and copolymers of glycolic acid and lactic acid, provide a way to circumvent the issue of light scattering. However, these materials are characterised by a lower glass transition temperature ($T_g < 50$ °C). This implies that sensor chips would start deforming at considerably lower temperatures than when semi-crystalline polymers are applied.

Given the fact that the need for water analysis is most urgent in developing countries located around the equator, the application temperature would often be near the T_g of *e.g.* amorphous PLA (45-50

°C). Therefore, there is a need for sensor substrates with a sufficiently high T_g (> 60 °C) in order to build in some margin with respect to the maximum temperatures they can be exposed to (approx. 49-55 °C). This will ensure that the sensing chip will be mechanically robust at its application temperature, which is required for the straightforward alignment of the sensor within the external read-out unit.

A straightforward strategy to increase the T_g of aliphatic polymers is by replacing relatively small pendant groups by bulky substituents.[105] This approach was already proposed by Baker and coworkers by replacing PLA's methyl-group by a phenyl substituent.[37] The resulting polyester, poly(mandelide), indeed exhibited a high T_g (100 °C) and was thus considered to be a degradable alternative for polystyrene. Later, a cyclo-hexyl substituted PLA was also introduced by the same research group (T_g 96-98 °C).[38]

Poly(mandelide) is, however, characterised by a relatively slow hydrolytic degradation with significant mass losses ($> 10\%$) only being observed after incubating a sample at 55 °C for three months in phosphate buffer (pH 7.4). Since this PhD encompasses the development of sensor chips that degrade in a straightforward way, the degradation rate of pure poly(mandelic acid) is unsatisfactory. Therefore, this chapter will focus on the copolymerisation of lactide and mandelide as a means to obtain transparent, degradable materials with a T_g above 60 °C.

2.2   Synthesis of mandelide for application as monomer

Mandelide is not commercially available and therefore the cyclic dimer of mandelic acid had to be synthesised to make ROP feasible. ROP was selected over polycondensation reactions as high molecular weights can be obtained in a straightforward manner.[33,34] The synthesis procedure was derived from Liu *et al.*,[37] and can be found in more detail in appendix A (materials and methods). It should be noted that during synthesis, two diastereomers are formed, being (R,S)-mandelide, or meso-mandelide, and a racemic mixture of (R,R)- and (S,S)-mandelide (figure 2.5). This is important as both diastereomers exhibit very different properties. Meso-mandelide is char-

Meso-mandelide **(2.1)**   Racemic mandelide **(2.2)**
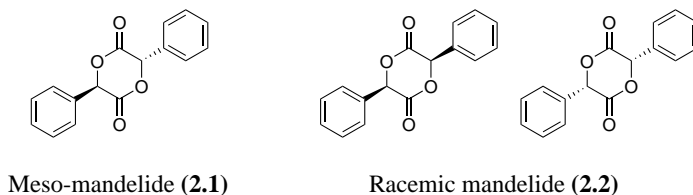
Figure 2.5: Scheme showing both fractions of mandelide obtained according to the synthesis procedure from Liu *et al.*[37]

acterised by a melting temperature (T_m) of 137 °C and a moderate solubility in common organic solvents, while rac-mandelide exhibits a lower solubility and decomposes at 193 °C rather than melting. This makes meso-mandelide the preferred monomer for both bulk as well as solution polymerisations.

The synthesis of mandelide was first performed in mixed xylenes as described in appendix A (section A.2.1). Racemic mandelide precipitated as a white powder, while meso-mandelide remained in solution. Evaporation of the solvent and subsequent recrystallisation from hot ethyl-acetate yielded white cubic crystals. The purity of both fractions was confirmed via ^{1}H-NMR spectroscopy and mass spectroscopy (appendix A).

The obtained yields for a number of reaction durations are shown in figure 2.6 and highlight the contributions of both the racemic, as well as the meso-fraction. It was observed that on average an excess of rac-mandelide was obtained, while a 50:50 distribution was expected since racemic mandelic acid was applied in the synthesis.[37] This discrepancy may be the result of the repeated recrystallisation steps that are needed to purify meso-mandelide, thereby removing impurities together with a small amount of the moderately soluble meso-diastereomer. It was observed that a reaction time of 3 days corresponded to the highest yield, which is in accordance with the observations of Liu *et al.* The decrease in yield after 3 days may be attributed to ring-opening of the formed mandelide by remaining mandelic acid molecules and/or formed oligomers. However, such compounds were not isolated since the washing step ($NaHCO_3$) applied to remove the p-toluenesulfonic acid also eliminates the remaining carboxylic acids from the reaction medium.
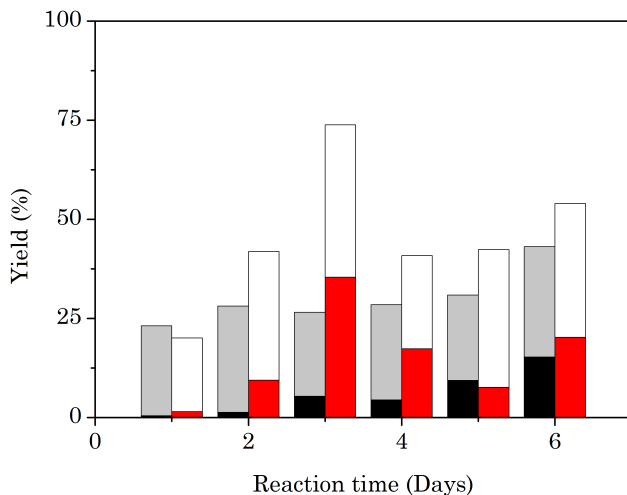
Figure 2.6: Graph showing the obtained yields (%) as a function of reaction time in (i) toluene (black: meso-mandelide; grey: racemic mandelide), and (ii) mixed xylenes (red: meso-mandelide; white: racemic mandelide).

It has been reported that mandelide can undergo epimerisation at elevated temperatures.[37] Therefore, the hypothesis was postulated that toluene, having a lower boiling temperature, might reduce the likeliness of epimerisation of meso-mandelide to the thermodynamically more stable rac-mandelide. This would increase the relative amount of meso-mandelide being obtained. However, the syntheses in toluene did not result in a yield of more than 50% and moreover, racemic mandelide remained the most abundant reaction product (figure 2.6).

From the unsatisfactory results obtained in toluene, it was proposed that the higher reaction temperature associated with mixed xylenes favoured the conversion to mandelide. Therefore, a reaction in 1,2,4-trimethylbenzene was attempted since this solvent would allow the reaction to be conducted at even higher temperatures (168°C). The goal of this experiment was thus to increase the overall yield of the reaction, disregarding the possibility of epimerisation. It was already observed during the experiments in xylenes and toluene that

rigorous degassing of the solvent was necessary to prevent oxidation of the starting compound. Unfortunately, the higher reaction temperatures in 1,2,4-trimethylbenzene resulted in a considerable darkening of the solution indicating oxidation reactions taking place, despite this degassing step. The latter side reactions also resulted in a very low meso-mandelide yield (4%), since extensive recrystallisations were required to remove the formed by-products.

Since neither higher nor lower boiling solvents allowed to increase the amount of meso-mandelide obtained, xylenes remained the solvent of choice for the synthesis of the required mandelide monomer. Despite the limited yield, the followed methodology yielded two pure fractions of racemic-mandelide and meso-mandelide, respectively.

2.2.1 Epimerisation of meso-mandelide

As already mentioned in the previous section, the synthesis of mandelide according to Liu *et al.* yielded two fractions, each composed of one of both mandelide diastereomers shown in figure 2.5. Initially, the purity of both fractions was assessed via ^{1}H-NMR spectroscopy using DMSO-d6 as solvent, as originally proposed in literature.[37]

However, the recorded ^{1}H-NMR spectra of both diastereomers (figure 2.7a) showed four distinct proton signals (6.61, 6.45, 6.43 and 6.2 ppm), even after multiple recrystallisations. Moreover, it was observed that solutions of meso-mandelide in DMSO quickly turned yellow (figure 2.7c). Interestingly, this colour change was absent when meso-mandelide was dissolved in $CDCl_3$.

Since this phenomenon has not been previously reported, the NMR spectra of both mandelide diastereomers were compared using deuterated chloroform and deuterated DMSO as solvent to better understand this unexpected observation. In deuterated chloroform, only two signals can be distinguished around 6.5 ppm corresponding to the protons of the six-membered diester ring (figure 2.7b). Each signal corresponds to either meso-mandelide (6.44 ppm) or rac-mandelide (6.61 ppm). The additional signals at 6.43 and 6.2 ppm observed in DMSO-d6 could not be attributed to unreacted mandelic acid (αH at 5.02 ppm), nor to one of both mandelide diastereomers. Although the position of the lower signal (6.2 ppm) coincides with the signal associated with mandelic acid oligomers (αH at 6-6.2 ppm), such com-

(a) DMSO-d6   **(b)** CDCl$_3$

(c)
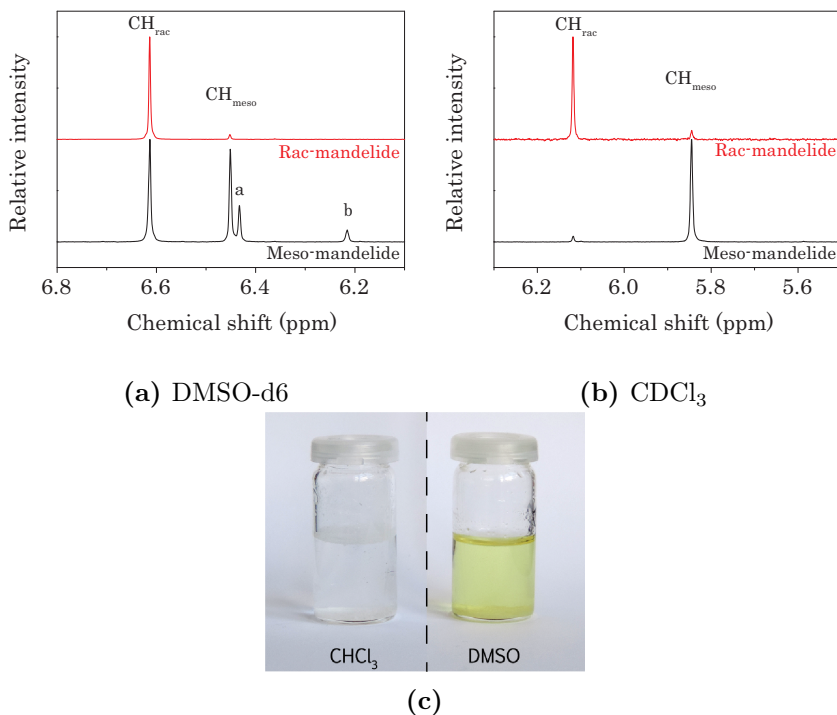
Figure 2.7: Comparison of the ^{1}H-NMR spectra recorded in DMSO-d6 (a) and CDCl$_3$ (b) for both meso-mandelide (black ——) as well as rac-mandelide (——). In DMSO-d6, two additional peaks (a-b) appear that are absent in CDCl$_3$. Figure c shows the colour difference observed when meso-mandelide is dissolved in chloroform (left) or DMSO (right).

pounds do not account for the observed yellow colour as they yield colourless solutions.

Table 2.1 shows the relative integrations of the signals corresponding to meso-mandelide as well as rac-mandelide dissolved in a selection of common organic solvents.* Since both signals correspond to the same number of α-protons, the relative integration of these signals, corresponds to the sample composition. The meso-mandelide fraction dissolved in CDCl$_3$ contained 96% meso-mandelide and 4% racemic mandelide, while this was the exact opposite case for the racemic mandelide (i.e. 96% racemic, 4% meso). In DMSO-d6, meso-mandelide

---

*The chemical shift of the observed signals may vary in different solvents

Table 2.1: Overview of the effect of the solvent choice on the ratio of both mandelide diastereomers.

Solvent	Polarity index[106]	[meso]/[rac] based on ^{1}H-NMR	
		Meso	Rac
Toluene	2.4	99/1	1/99
DCM	3.1	96/4	8/92
CHCl$_3$	4.1	96/4	4/96
THF	4.0	97/3	5/95
Acetone	5.1	95/5	6/94
ACN	5.8	93/7	6/94
DMF	6.4	60/40	15/85
DMSO	7.2	53/47	19/81

showed 67% meso-mandelide and 33% rac-mandelide, while rac-mandelide was composed of 19% meso-mandelide and 81% rac-mandelide.

The results for the other solvents mentioned in table 2.1 show that both meso- as well as rac-mandelide are relatively stable in most solvents studied. In the case of DMF and DMSO however, a considerable change in the diastereomeric ratio was observed for both mandelide diastereomers, although the effect was less pronounced in the case of rac-mandelide which may be explained by the fact that rac-mandelide is thermodynamically more stable than meso-mandelide.[37]

As mentioned earlier, rac-mandelide has a very low solubility in common organic solvents. In order to rule out this solubility effect as an explanation for the observed difference between DMF and DMSO on one hand and the other solvents on the other, meso-mandelide crystals were subjected to single crystal X-ray diffraction experiments. From these measurements, it was deduced that the crystal was indeed meso-mandelide constituting a chair conformation with the bulky phenyl groups in equatorial position (figure 2.8a). From the side, the crystal structure resembles stacking of chairs on top of each other (figure 2.8b). From the top, a herringbone motive can be observed owing to the alignment of phenyl side-chains (figure 2.8c). Multiple crystals were evaluated in this manner and results were reproducible,

(a)

(b)

(c)
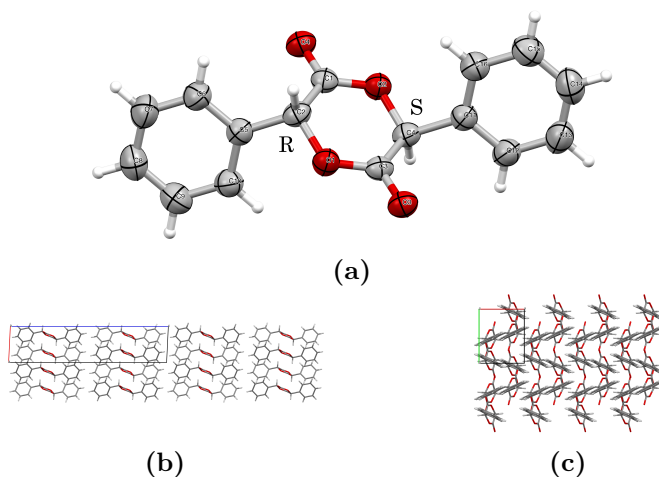
Figure 2.8: Structure of meso-mandelide obtained via X-ray diffraction experiments. The results confirm the proposed (R,S)-configuration.

thereby rendering the presence of rac-mandelide as an impurity within the meso-mandelide crystals highly unlikely.

The fact that DMSO changed the composition of both meso- as well as rac-mandelide, suggested the existence of an equilibrium between both diastereomers. A similar epimerisation has already been discussed in literature for meso-lactide at elevated temperatures (180-300 °C).[107] Shuklov *et al.* later extended the proposed racemisation to lactide dissolved in various solvents (toluene, ethyl acetate and tert-butylmethylether).[108] In contrast to our observations for meso-mandelide, prolonged dissolution (> 24 h) in the presence of homogeneous bases (NaOH, K_2CO_3 or K_3PO_4) was required to facilitate the epimerisation of meso-lactide. The presence of the aromatic rings in mandelide is believed to effectively stabilise the enolic form by extending the conjugated system.

Since the observed racemisation coincides with the yellowing of the solution, this aspect was also studied in the above-mentioned solvents. Therefore, UV-VIS spectroscopy was applied to evaluate the colour change, if present, at a 1 mg mL^{-1} dilution. Even at this low concentration, racemic mandelide would only dissolve in DMSO
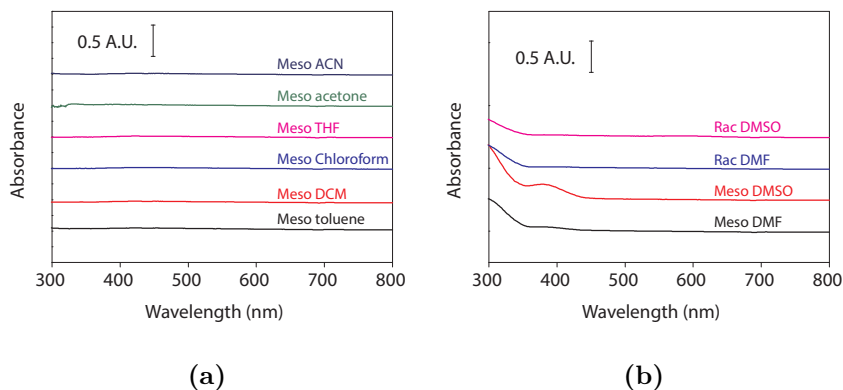
Figure 2.9: Overview of UV-VIS spectroscopy results. For clarity the individual measurements were spaced in the vertical axis by an increment of 0.5 A.U. (a) shows the results obtained for the solvents exhibiting a limited solubility for rac-mandelide at 25 °C. (b) shows the results for meso- and rac-mandelide in DMF and DMSO at 25 °C

and DMF. The results in figure 2.9 therefore focus primarily on meso-mandelide.

As anticipated based on the visual appearance of the vials containing meso-mandelide in DMSO and the above-mentioned NMR results, an additional absorbance around 379 nm could be observed when using DMSO and DMF as solvent. Given the broad absorbance peak, this band shows a considerable overlap with the human eye's absorption of blue light, thus resulting in the solution's yellow colour. The absorbance around 379 nm could not be observed in any of the other solvents evaluated. Moreover, increasing the temperature to 50 °C did not result in any measurable change of the absorption spectrum in the studied solvents (data not shown).

Given the yellowing of the solution and the position of the signal at 6.2 ppm, it was anticipated that a keto-enol equilibrium resulted in the racemisation with the enol-form being sufficiently stable in DMSO to become apparent in the NMR spectra. In this enol-adduct an extension of the conjugated system can be observed which could account for the yellow colour, as can be observed for e.g. caffeic acid (figure 2.10).

Enol-adduct   Caffeic acid
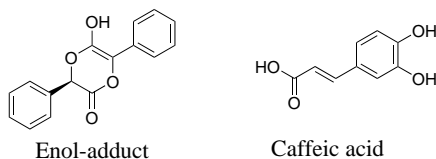
Figure 2.10: Figure showing the structural similarities between the proposed enol-adduct and caffeic acid. In both compounds electron withdrawing groups are present on a carbon-carbon double bond conjugated with an aromatic ring.

This hypothesis was evaluated by dissolving meso-mandelide (**2.1**, figure 2.11) in dry DMSO followed by enabling the equilibrium with racemic mandelide (**2.2**, figure 2.11) to occur. By adding trifluoro-acetyl isocyanate (TAIC) to the solution, any present alcohol functionalities in the enol-adduct (**2.3**, figure 2.11) would readily react with the isocyanate yielding a more stable urethane bond (**2.4**, figure 2.11). This procedure effectively locks the enol-adduct and prevents the subsequent racemisation to racemic mandelide. An excess of TAIC was added to make sure that the enol-adduct, if present, would be able to react quantitatively as described earlier when combining TAIC with OH-containing compounds.[109–111]

^{1}H-NMR spectra recorded before and after TAIC addition show an inversion of the isomer ratio (figure 2.12). When the same procedure was repeated for rac-mandelide, no change in the sample's composition was observed. These results indicate that meso-mandelide (**2.1**) is converted to the proposed TAIC adduct (**2.4**), while rac-mandelide is less likely to yield a reactive enol-species. This observation confirms that meso-mandelide is not the most thermodynamically stable diastereomer as suggested in literature.[37] Moreover, this observation corresponds to the above-mentioned results of the UV-VIS experiments for which only meso-mandelide in highly polar solvents gave rise to the formation of an additional absorbance band at room temperature. The equilibrium in figure 2.11 thus lies towards the side of racemic mandelide, whereby polar solvents facilitate the conversion of meso-mandelide. Addition of TAIC subsequently traps the formed enolic intermediate, driving the meso-mandelide conversion towards completion. When the same samples were reanalyzed after 24 hours,
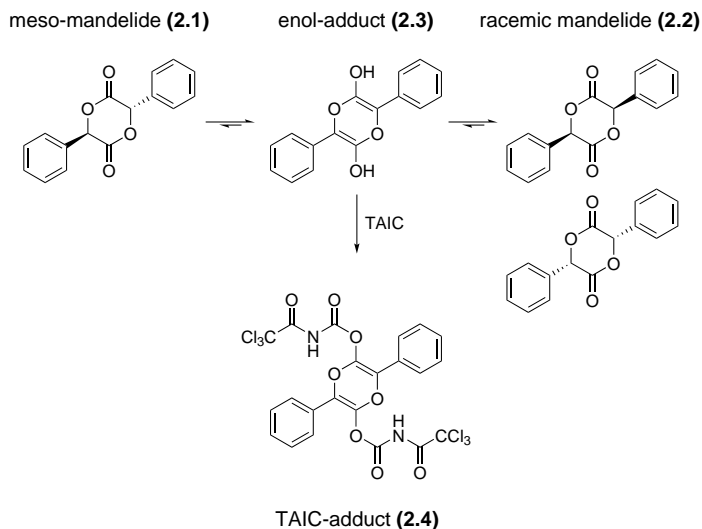
Figure 2.11: Scheme indicating the principle of the use of trichloro-acetyl isocyanate (TAIC). If the racemisation in DMSO indeed passes through an enol-adduct, the formed alcohol functions would react quantitatively with TAIC resulting in a urethane bond, thereby locking the enolic structure.

no change could be observed in the ratio meso-/rac-mandelide indicating that the added TAIC had been consumed at the time the samples were analysed the first time (approx. 20 minutes after TAIC addition).

In order to confirm the structure of the proposed TAIC-adduct, the reaction mixture was extracted with diethyl ether and washed with deionised water to remove the included DMSO. Via this method, the yellow colour was effectively transferred to the ether phase indicating a considerable change in solubility as compared to the unmodified mandelide. Unfortunately, the expected adduct could not be isolated after column chromatography or recrystallisations to allow its structure confirmation.

2.3 Polymerisations

Despite the relatively low yield and the observed spontaneous epimerisation in highly polar solvents, the obtained mandelide was sub-

(a)   **(b)**
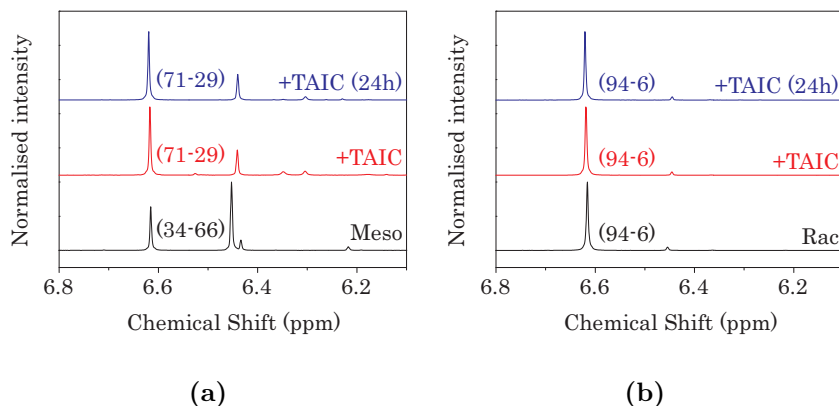
Figure 2.12: NMR spectra recorded in DMSO-d6 indicating the effect of TAIC on meso- (A) and rac-mandelide (B). The values between brackets indicate the composition (%) based on the signals at 6.61 and 6.44 ppm. For meso-mandelide the epimerisation can be observed, while for rac-mandelide, the amount of meso-mandelide remains limited (black curves). Upon addition of TAIC (red curve) the composition of the rac-mandelide sample did not change, the meso-diastereomer on the other hand showed a clear inversion of the ratio between meso- and rac-diastereomers indicating the reaction with TAIC depletes the meso-pool. The spectra did not change upon increasing the reaction times up to 24h (blue curves).

sequently applied in the synthesis of mandelide-based polymers. As previously mentioned, poly(mandelide) is an interesting degradable polyester with polystyrene like properties.[37] However, due to its bulky pendant groups and its hydrophobic nature, poly(mandelide)'s degradation is quite slow, with mass loss only being observed after incubating the material at elevated temperatures (55°C) for 3 months.[37] This makes its recycling more time and energy consuming than is the case for PLA which already shows mass loss after 2 weeks under similar conditions.[112] Therefore, the following section will focus on the copolymerisation of mandelide and lactide according to the metal-insertion mechanism discussed in section 2.1.2 (figure 2.2) with the aim to obtain materials that exhibit a T_g above 60 °C and thus to combine the best properties of both homopolymers. In the following sections, a distinction will be made between bulk and solution polymerisations.

2.3.1 Bulk polymerisations

Given the successful application of bulk polymerisations in the synthesis of PGA,[41] PLA,[41,46] and PCL,[113–115] the synthesis of copolymers was first performed via ROP in bulk. Mandelide has been reported to be applicable in bulk polymerisations.[37] With respect to the obtainable stereoisomers of mandelide, meso-mandelide is the preferred monomer because it has a lower melting temperature (T_m = 137 °C) while rac-mandelide decomposes prior to melting ($T_{decomposition}$ = 193 °C) thereby excluding bulk polymerisations of the latter diastereoisomer. Liu *et al.* however proposed a work-around for this issue by copolymerising both diastereomers in a 3-to-1 ratio (meso/rac).[37] This allows the rac-mandelide to dissolve in the melted meso-fraction.

As reference for the envisioned copolymers of lactide and mandelide, first a number of homopolymers were prepared using the tin octoate/neohexanol catalyst/initiator system according to the procedure described in appendix A (materials and methods). The choice for neohexanol as initiating species was made based on the fact that it is a liquid compound facilitating its drying and purification via distillation, and the fact that the compound's ^{1}H-NMR signals do not overlap with any of the signals observed for the applied monomers). To prevent the inclusion of water as an adventious initiator, all manipulations of the reagents were performed in an argon filled dry-box or via the appropriate Schlenk techniques. The results of the bulk polymerisation of lactide are shown in table 2.2. As can be derived from the reported molecular weights obtained via size exclusion chromatography (SEC), considerable deviations between the target $(M_n{}^{Targ.})^\dagger$ and experimental molecular weight $(M_n{}^{Exp.})$ were observed. It should be noted that SEC is a relative method in which the retention time on the column is related to the material molecular weight via an external calibration curve. Moreover, the material to be analysed often does not correspond to the applied standards. This results in deviations in the reported molecular weight as different polymers exhibit different solvodynamic volumes and thus different retention times. Since PS standards are applied throughout this PhD thesis, it should thus be noted that the reported molecular weights

---

†Throughout this PhD thesis, the term 'target molecular weight' refers to the expected molecular weight at 100% conversion.

Table 2.2: Overview of bulk polymerisations of lactide (La) and mandelide (Ma) performed using the neohexanol/tin octoate initiating system at 140 °C which resulted in a polymer precipitate ($M_n > 3$ kg mol^{-1}, determined via size exclusion chromatography relative to polystyrene standards).

Entry	Reaction mixture [La]/[Ma]/[C]/[I]	$M_n{}^{Targ.}$ [kg mol^{-1}]	$M_n{}^{Exp.}$ [kg mol^{-1}]	Đ [-]
a	100/0/1/2	7.6	44.6	1.49
b	100/0/1/2	7.6	23.7	1.73
c	200/0/1/2	14.8	43.6	1.41
d	200/0/1/2	14.8	6.2	2.66
e	400/0/1/2	29.2	52.4	1.48
f	400/0/1/2	29.2	37.6	2.23
g	64/16/1/2	7.2	10.9	1.75

are not the absolute values as to date no correction factors have been reported for poly(mandelide). Molecular weights will therefore only be used to compare the different materials relative to each other taking into account that differences in monomer feed composition will also affect the solvodynamic volume of the resulting polymer.

Moreover, the ring-opening polymerisation in the melt did not proceed in a reproducible way as demonstrated by the varying results for polymerisations applying the same reaction conditions. These high batch-to-batch differences observed for materials obtained under identical reaction conditions, are a point of concern. Moreover, with the exception of entry d (table 2.2), all polymerisations resulted in higher than expected molecular weights, which obstructs the synthesis of materials with a predefined molecular weight. The latter effect may be attributed to a lower effective initiator concentration since the temperatures required for monomer melting approached the initiator boiling point (143 °C).

The observed dispersities (Đ) were also relatively high (> 1.4) indicating limited control over the polymerisation as typically values below 1.3 are observed for the ROP of cyclic diesters when considering similar molecular weights.[37,40] This observation is quite common for bulk polymerisations, as the increasing viscosity associated with the rising molecular weights may affect the dispersity in two

ways. First, it was observed that the increasing viscosity resulted in blocked stirring bars, which may result in an inhomogeneous monomer distribution allowing some chains to grow more efficient than others. Secondly, if a reactive chain end is surrounded by other polymer strands, back-biting reactions may occur thereby enlarging the spread of the molecular weight distribution. The latter phenomenon can be expected in polyesters (especially for anionic polymerisation mechanisms) as both propagation as well as back-biting consist of a transesterification reaction.[29,30,45,116]

Next, the melt copolymerisation of rac- and meso-mandelide was performed based on the report by Liu *et al.*[37] However, no homogeneous melt could be obtained at 140 °C. Moreover, the monomer showed signs of discolouration indicating the occurrence of oxidative side reactions. Since rac-mandelide is unable to form a melt, the procedure was repeated for pure meso-mandelide. Unfortunately, even this reaction did not yield a homogeneous melt, which can be ascribed to the epimerisation of mandelide at elevated temperatures.[37] In addition, the obtained molecular weight (M_n approx. 2.3 $kg\,mol^{-1}$) remained well below the 10 $kg\,mol^{-1}$ reported by Liu *et al.* for an intended molecular weight of 13.4 $kg\,mol^{-1}$.[37]

Since lactide resulted in a homogeneous melt, a number of copolymers were synthesised (table A.3) by dissolving the mandelide monomer in the lactide melt. As anticipated, it was observed that for increasing mandelide content, a homogeneous melt was increasingly difficult to obtain. In addition, the reaction mixtures containing the most meso-mandelide again showed considerable yellowing. Despite these shortcomings, the reaction of lactide and meso-mandelide in a 80-20 ratio resulted in a copolymer with an average molecular weight of 10.9 $kg\,mol^{-1}$ (table 2.2, entry g). Previous attempts to synthesise copolymers of lactic and mandelic acid via direct polycondensation never yielded molecular weights in excess of 5 $kg\,mol^{-1}$.[117–121] However, it should be noted that the obtained molecular weight was still higher than expected based on the monomer-to-initiator ratio (8.4 $kg\,mol^{-1}$ instead of 7.2 $kg\,mol^{-1}$) and that the associated dispersity was too high (> 1.5) to be considered a controlled polymerisation. Nonetheless, this result confirmed the possibility to copolymerise both monomers. However, as has become apparent in the present section,

Table 2.3: Overview of the solution copolymerisations of lactide and mandelide performed at 70 °C in acetonitrile (1 mol L^{-1}) using the neohexanol/tin octoate initiating system

Entry	[La]/[Ma]/[C]/[I]	M_n Targ. [kg mol^{-1}]	M_n Exp. [kg mol^{-1}]	$Đ_M$ [-]
a	400/0/1/2	28.8	13.0	1.15
b	300/100/1/2	35.0	6.1	1.04
c	200/200/1/2	41.2	5.4	1.11
d	100/300/1/2	47.4	4.0	1.04
e	0/400/1/2	53.6	4.5	1.11

melt polymerisations yield unsatisfactory results in terms of molecular weight control with large batch-to-batch differences and poor dispersity values. Therefore, the focus will shift to solution polymerisations to increase the predictability of the obtained molecular weights while reducing the molecular weight distribution.

2.3.2   Solution polymerisations

Following the initial report by Liu *et al.*,[37] the first solution polymerisations were performed in acetonitrile at 70 °C, since this solvent exhibits a higher solubility (1.5 mol L^{-1}) towards mandelide than toluene, which is commonly applied for the solution polymerisation of lactide (analogues) under stannous octoate catalysis.[38,41,122]

Table 2.3, shows the obtained molecular weights for a series of copolymers of lactide and mandelide performed in ACN using the neohexanol/Sn(2-ethylhexanoate)$_2$ initiator/catalyst system. It was observed that these conditions performed rather badly for the controlled polymerisation of lactide as indicated by the much lower than expected molecular weight obtained. It was previously reported that solvent molecules with a free electron pair may complex to the catalyst, thereby reducing its activity.[14] This may explain why, this discrepancy is absent when the polymerisation of meso-lactide is performed in e.g. toluene as will be shown later on in this chapter (table 2.4).

Moreover, the solution polymerisation of mandelide in acetonitrile did not yield high molecular weights (Mn < 5 kg mol^{-1}). Lower than expected molecular weights were also observed for the copolymerisations of both monomers. This observation can be attributed to both the poor performance of lactide in acetonitrile as well as side reactions occurring for meso-mandelide e.g. among others the previously reported epimerisation of meso-mandelide. Similar observations were made by Liu *et al.*, but they did not further investigate the cause of the lower than expected molecular weights.[37] To exclude the solvent's effect on the diasteromeric ratio, meso-mandelide was dissolved in ACN-d3 and incubated at 70°C for 1 hour followed by repeating the ^{1}H-NMR analysis at the same temperature. No increase in epimerisation could be observed, which implies that the rapid epimerisation reported by Liu *et al.* was caused by the action of the catalyst/initiator system.[37] The latter phenomenon may thus explain the lower than expected molecular weights.

Determination of polymerisation kinetics in toluene

Following these poor results, toluene was selected as solvent for the solution (co)polymerisations of lactide and mandelide as this solvent showed the lowest degree of epimerisation of meso-mandelide as shown in table 2.1. Since no information is available on the polymerisation of mandelide when using the neohexanol/Sn(2-ethylhexanoate)$_2$ initiator/catalyst system in toluene, the polymerisation rate constants for both monomers were first determined. The higher temperature was necessary as poly(lactide) is characterised by a decreased solubility in toluene at temperatures far below the boiling point (110 °C).[123] Two 1 mol L^{-1} solutions in toluene were prepared in schlenk vials as discussed in appendix A (materials and methods) to ensure anhydrous reaction conditions. A premixed solution of initiator and catalyst was added to both vials via a syringe, followed by sampling the reaction medium at predetermined time points. The collected samples were subsequently analysed via ^{1}H-NMR spectroscopy and size exclusion chromatography. Given the difference in chemical shift between the monomers and the corresponding polymers, NMR spectroscopy allowed the straightforward determination of the monomer conversion.
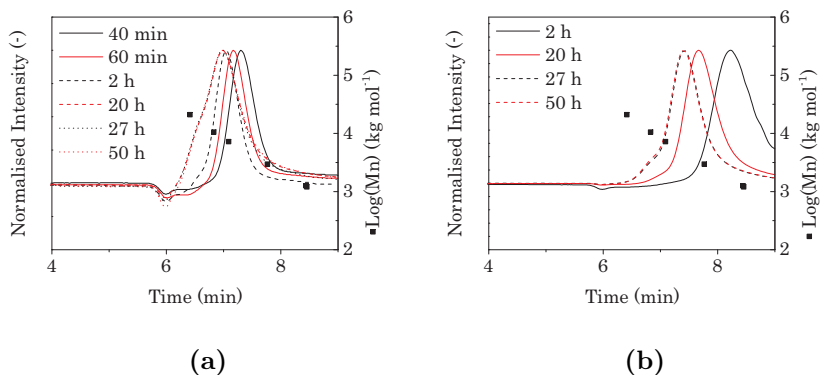
Figure 2.13: Graphs showing the normalised SEC traces obtained during the kinetic experiments for lactide (a) and mandelide (b). For clarity, only the SEC traces that are fully resolved from the solvent peak are included in the above-shown graphs. ■ indicates the molar masses of the applied PS standards (expressed as logarithmic values) as a function of elution time.

SEC analyses on the other hand allowed the determination of the evolution of the molecular weight (figure 2.13).

Figure 2.14a shows the monomer conversion as a function of time. The lactide monomer was shown to be almost completely depleted ($>$ 95%) after 4 hours reaction. Mandelide on the other hand only showed a conversion of 79% indicating a lower polymerisation rate, which can be easily rationalised by the increased sterical hindrance caused by the bulky phenyl-substituents on the 1,4-dioxane-2,5-dione ring. A similar trend was observed for isopropyl- and cyclohexyl-substituted lactides for which the polymerisation rate decreased with the size of the substituents (18.6 times slower for diisopropylglycolide and 71 times slower for dicyclohexylglycolide).[38] Moreover, the phenyl ring can be considered to be an electron withdrawing group due to the sp^2 hybridisation of these atoms (increase in electronegativity). This yields a partial positive charge on the α-carbon, which in turn reduced the partial positive charge on the carbonyl carbon and renders it less prone to nucleophilic attack.

As already mentioned in this chapter's introduction, the synthesis of polyesters from lactide-based monomers applying the neohexanol/ Sn(2-ethylhexanoate)$_2$ initiator/catalyst system can be considered to

(a)

(b)

(c)

(d)
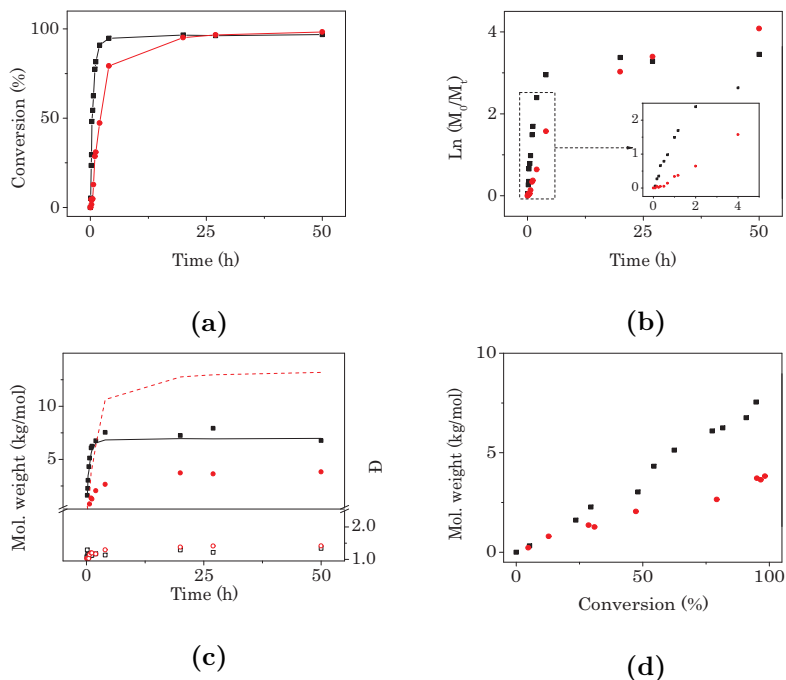
Figure 2.14: Graphs showing the results of the kinetic experiments performed in toluene at 100 °C for lactide (black ■) and mandelide (red ●). Graph (a) shows the degree of conversion as a function of reaction time; Graph (b) shows $\ln(M_0/M_t)$ as a function of reaction time with both monomers exhibiting first-order kinetics at low to moderate conversion (insert); graph (c) shows the correspondence between the molecular weight evolution (lactide: □, mandelide: ○) determined via SEC with the theoretical molecular weight based on monomer conversion (lactide: black line, mandelide: red dashed line). Both monomers show low dispersities (lactide: □, mandelide: red ○) at low to moderate conversion. The controlled nature of the performed polymerisations is visualised in (d) for both lactide (□) as mandelide (red ●) by plotting M_n as a function of conversion.

be a controlled polymerisation method, which implies that termination and chain transfer reactions are less likely to occur than monomer addition.[105] This corresponds to the low dispersities mentioned earlier for the (co)polymerisations of meso-lactide and meso-mandelide in ACN. Moreover, the initiator concentration can be considered to be constant, which enables the simplification of the relation between re-

action rate and monomer concentration (equation 2.4). Therefore, the polymerisations can be considered to proceed via first-order kinetics which corresponds to the rate of monomer depletion being proportional (k') to the monomer concentration (equation 2.4).[105]

$$Rate = -\frac{d[M]}{dt} = k[M][I] = k'[M] \qquad (2.4)$$

With k being the reaction rate constant dependent on the concentration of the monomer M and initiator I. For a constant initiator concentration, a new reaction rate constant k' can be defined to relate the reaction rate to the monomer concentration. Solving this differential equation gives:

$$ln(M_t) - ln(M_0) = -k't \qquad (2.5)$$

or

$$ln(\frac{M_0}{M_t}) = k't \qquad (2.6)$$

It is thus possible to obtain the reaction rate constant for both the polymerisation of lactide as well as the polymerisation of mandelide. Based on the conversion p, it is possible to calculate M_t according to equation 2.7.[105]

$$M_t = M_0 \times (1 - p) \qquad (2.7)$$

In figure 2.14b, $ln(M_0/M_t)$ is plotted versus t, whereby the constant k is given by the slope of the linear part of the curve. It can be observed that the expected linear trend does not hold at high monomer conversion ($> 70\%$). Under these conditions, the diffusion of the remaining monomers towards the growing chain ends becomes the rate determining factor.[124] By focusing on the results at low-to-moderate conversions ($< 70\%$), the effect of diffusion on the rate constant can be excluded. Values of $k = 4 \times 10^{-4} s^{-1}$ ($R^2 = 0.974$) and $k = 1 \times 10^{-4} s^{-1}$ ($R^2 = 0.987$) were obtained for respectively lactide and mandelide polymerised under identical conditions. When comparing these results to previously reported values the polymerisation of mandelide at 100 °C is 4 times faster than in ACN at 70 °C ($k = 0.25 \times 10^{-4} s^{-1}$).[37] For rac-lactide a value of $0.96 \times 10^{-4} s^{-1}$

was previously reported for the homopolymerisation in toluene (80 °C).[125]

From the monomer conversion, the theoretically obtained molecular weight at each time point can be derived by taking into account the relative amounts of monomer and initiator. In figure 2.14c these expected values are plotted together with the experimental values determined via SEC. In addition, figure 2.14c shows the evolution of the dispersity (Đ) as a function of time. In the case of meso-lactide, the experimental values are in close correspondence with the theory, while dispersities around 1.1 were maintained at moderate degrees of conversion. These results thus indicate good control over the polymerisation, which corresponds to literature and adds to PLA's prominent role in the field of degradable materials.[14,126,127]

For mandelide, however, the results show a large discrepancy with the theory and much lower than expected molecular weights are obtained ($M_n < 5$ kg mol^{-1} instead of 13.4 kg mol^{-1}). Dispersities on the other hand are satisfactory with values around 1.2 as long as first-order kinetics are considered. In order to verify that the molecular weight determined via SEC is not affected by the previously mentioned differences in solvodynamic volume with respect to the applied references, the molecular weight was determined via ^{1}H-NMR spectroscopy. By comparing the initiator signal at 1.2 ppm to the monomer signal at 5.9 ppm, the relative integrations revealed a DP of 19 (data not shown). This corresponds to a molecular weight of 5 kg mol^{-1}. This value is higher than the value obtained via SEC (i.e. 3.8 kg mol^{-1}) indicating some underestimation of the molecular weight via SEC. However, this effect is not sufficient to account for the observed deviation from the expected molecular weight. The observed discrepancy between the intended and the obtained molecular weight has been previously reported for poly(mandelide) and was attributed to side reactions occurring for the mandelide monomer.[37] Given the very low degree of racemisation occurring in toluene ($< 1\%$, even at 100 °C), this effect is expected to be a result of the interaction between the catalyst system and the mandelide monomer.
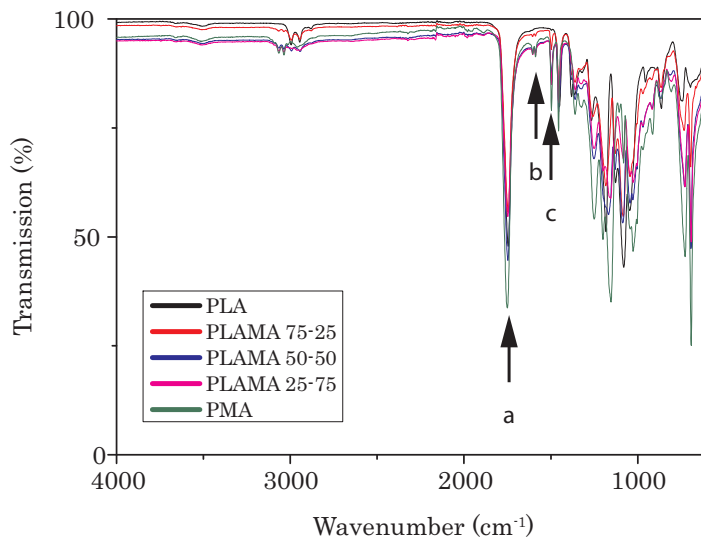
Figure 2.15: Overlay of the FT-IR spectra obtained for the studied lactide-mandelide (co)polymers. The spectra are dominated by the C=O stretch vibration around 1735 cm^{-1} which is characteristic for polyesters (a). Moreover, for the mandelide containing (co)polymers additional C=C stretch vibration appear which can be attributed to the phenyl pendant groups (b-c).

2.3.3 Characterisation of copolymers of meso-lactide and meso-mandelide

Following the kinetic study covering both meso-lactide as well as meso-mandelide in toluene for the neohexanol/Sn(2-ethylhexanoate)$_2$ initiator/catalyst system, these monomers were subsequently copolymerised under the same conditions. The synthesised compounds were first analysed via ^{1}H-NMR spectroscopy. The NMR analyses show both monomers being present in the polymer backbone of the copolymers and that the ratios determined based on the integration of the methine protons, follow the same trend as the initial monomer feed, although the polymers contain slightly more mandelide than expected based on the monomer composition (table 2.4). FT-IR spectra (figure 2.15) show the characteristic C=O stretch vibration (1735 cm^{-1}) and also confirm the presence of aromatic as well as methyl functionalities in the copolymers.

Table 2.4: Structural analysis of the obtained (co)polymers showing the observed monomer ratios (determined via ^{1}H-NMR spectroscopy) and obtained molecular weights (determined via SEC and compared to the target values).

Material	Monomer ratio Lac/Man	$\text{Mn}^{\text{Targ.}}$ [kg mol^{-1}]	$\text{Mn}^{\text{Exp.}}$ [kg mol^{-1}]	$Đ_{\text{M}}$ [-]
PLA	1.0 / 0.0	28.8	26.7	1.08
PLAMA 75-25	1.0 / 0.4	35.0	12.1	1.06
PLAMA 50-50	1.0 / 1.2	41.2	11.2	1.05
PLAMA 25-75	1.0 / 3.7	47.4	7.9	1.06
PMA	0.0 / 1.0	53.6	11.6	1.04

Next, the polymers were analysed via size exclusion chromatography (SEC) to assess the obtained molecular weights. As table 2.4 shows, the polymerisation of lactide in toluene, resulted in the expected molecular weight. However, when mandelide was added to the monomer feed, similar deviations from the target molecular weight were observed as discussed earlier for the polymerisation kinetics of mandelide. The obtained dispersities (Đ) remained well below 1.1. Despite the discrepancy between the target and experimental molecular weights (20-35% of the target M_n) the applied methodology surpassed earlier reports applying the direct polycondensation of lactic and mandelic acid.[117]

Despite the lower than anticipated molecular weights, the synthesised materials' thermal and optical properties were evaluated.

Thermal characterisation of lactide and mandelide copolymers

First, the materials were subjected to thermogravimetric analyses (TGA) to assess their thermal stability (figure 2.16). Since the materials will be processed into microfluidics, this offers an idea of the highest temperature that can be applied in their processing. The results are shown in table 2.5. PLA exhibited a degradation onset of 239 °C, while this value increased to values ranging from 269 °C to 291 °C for the mandelide containing polymers. In the case of PLA,
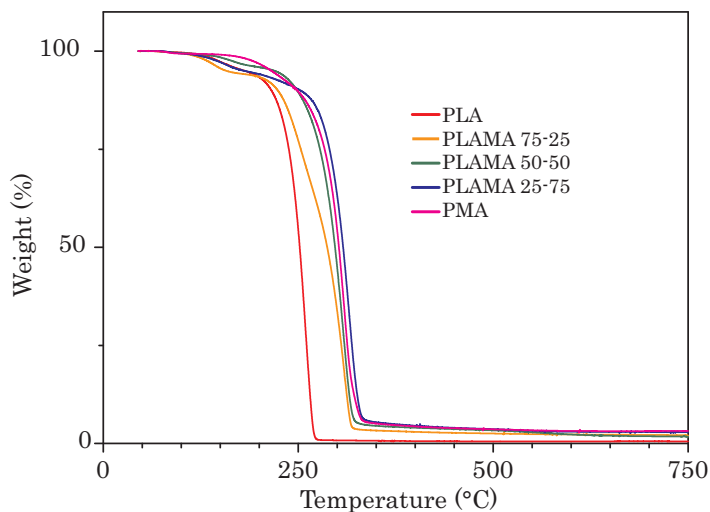
Figure 2.16: Overlay of the TGA curves obtained for the studied lactide-mandelide (co)polymers.

a small ($< 2\%$) mass loss was observed at low temperatures (< 150 °C), which may indicate the inclusion of solvent. The residue at 750 °C remained below 1% for PLA indicating complete degradation.[128] When mandelide was introduced to the monomer feed, the amount of residue increased as mandelic acid's aromatic moieties facilitate char formation.[129–131]

Following the assessment of the copolymers' thermal stability, the studied materials were subjected to differential scanning calorimetry (DSC) to determine their glass transition temperature (T_g). Since this is temperature at which polymers pass from the glass state to a rubbery state, the T_g determines at which temperatures the microfluidics can be applied without risking deformation of the sensor during manipulation. In order to be able to apply the sensor in developing countries around the equator a $T_g > 60$ °C is desired. The normalised heat flows shown in figure 2.17a indicate that the materials are amorphous since no crystallisation and/or melting transitions could be observed. This is beneficial considering the optical application since scattering of light on crystalline domains greatly reduces the transparency of the materials. Moreover, the goal to obtain de-

(a)

(b)
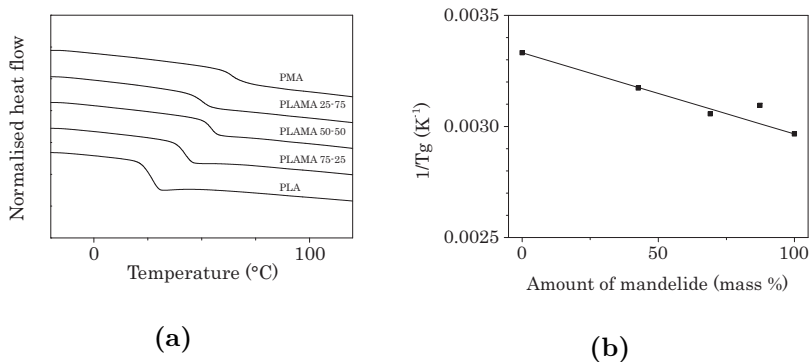
Figure 2.17: DSC thermograms obtained for the studied copolymers. The observed glass transition temperatures were shown to increase when mandelide was included in the monomer feed (subfigure a). Graph (b) compares the obtained T_g values (black ■) with the expected values based on the Fox equation (black ——).

gradable polyesters with a higher T_g than PLA was achieved by co-polymerising lactide with mandelide (table 2.5). As the mandelide content of the monomer feed rose, the T_g increased according to the Fox equation (equation 2.8) linking the observed T_g to the copolymer composition (w %) and the T_g of the corresponding homopolymers:

$$\frac{1}{T_g} = \frac{w_1}{T_g, 1} + \frac{w_2}{T_g, 2} \tag{2.8}$$

Table 2.5: Thermal analysis results for the studied copolymers showing the degradation onset, the residue at 750°C and the observed glass transition temperature.

Material	$T_{degradation}$ [°C]	Residue $_{750°C}$ [%]	T_g [°C]
PLA	239	0.5	27
PLAMA 75-25	269	2	42
PLAMA 50-50	280	1.7	54
PLAMA 25-75	291	2.8	50
PMA	287	3.2	64

In order to verify that the synthesised copolymers are indeed statistical copolymers and that the Fox equation may be applied, ^{13}C-NMR spectra were recorded. As can be seen in figure B.1 (appendix B), the signals corresponding with the carbonyl carbon atoms are quite broad and a bimodal distribution may be distinguished (especially for the 50-50 monomer ratio). The latter may indicate that different carbonyl functions experiencing different chemical environments are indeed present, which is consistent with statistical copolymers.[132] More elaborate experiments, with quantitative ^{13}C-NMR spectroscopy may be performed in the future to confirm this hypothesis.

Despite the lower than expected molecular weights, a 50/50 ratio of lactide and mandelide the T_g resulted in a T_g above 50 °C which can be achieved for commercial PDLLA materials. However, the predetermined goal of 60°C was only achieved for the poly(mandelide) homopolymer because of the lower than anticipated obtained molecular weights. Fitting the experimental data with equation 2.8 results in an R^2 of 0.921. The deviation from the linear trend proposed by the Fox equation is particularly clear for the PLAMA 25-75 sample, but this can be rationalised by the relatively large difference in molecular weight between this and the other mandelide containing copolymers (approx. 30% lower). The influence of molecular weight on the observed T_g is particularly important for low molecular weight polymers, as can be derived from the Flory-Fox equation (equation 2.9).[133]

$$T_g = T_{g,\infty} - \frac{K}{M_n} \tag{2.9}$$

Herein, a polymer's T_g is related to that of an infinitely long polymer chain, which is corrected by a material-specific constant K and the number average molecular weight M_n. The influence of M_n on the observed T_g is related to the free volume of the polymer, with T_gs decreasing as the free volume increases. This can be easily rationalised by the lower opposition towards segmental motion. The free volume is inversely proportional to the molecular weight. As chains become shorter, a given unit of volume will contain more chain ends, which are characterised by a higher mobility, and hence a larger free volume, than covalently linked monomer units along the main chain. Based on the TGA experiments, it could be expected that solvent inclusion

further reduced the observed T_g-values. This is particularly apparent for PLA for which a relatively high molecular weight (approx. 30 kg mol^{-1}) was obtained.

Optical characterisation of lactide and mandelide copolymers

Next, the materials' optical properties were assessed. Given their intended application in LoC sensors, transparent materials are required since the proposed sensor set-up relies on surface plasmon resonance, an optical detection method. Therefore, the materials were dissolved in acetone and subsequently solvent-cast on glass substrates after which the solvent was removed *in vacuo* at elevated temperatures (50 °C). Transmission measurements in the wavelength range 250-1800 nm were subsequently performed. The results were normalised to 1 mm thickness to compensate for differences in sample thickness and allow a valid comparison among the various samples by applying the law of Lambert-Beer (equation 2.10).

$$log(\frac{I}{I_0}) = -\epsilon Cd \qquad (2.10)$$

In the above-mentioned equation the molar extinction coefficient (ϵ), the absorber concentration (C) and the distance the light beam passes through the sample (d) are related to the ratio of the transmitted intensity (I) to the incident intensity (I_0).

The normalised transmission curves are shown in figure 2.18. As indicated, all materials are characterised by a strong absorption in the UV region of the spectrum (region a, figure 2.18), which is common for organic materials, especially when aromatic groups are present.[134] At higher wavelengths, all samples exhibit additional absorptions (regions b-d, figure 2.18) which can be attributed to C-H oscillations (table 2.6).[104]

However, the above-mentioned absorption bands do not negatively affect the proposed SPR-based sensor, since the laboratory prototype being constructed will operate at 661 nm. Looking at the more relevant wavelength range between 500 and 1000 nm, PLA exhibited excellent transparencies ($> 95\%$). However, as mandelide was included
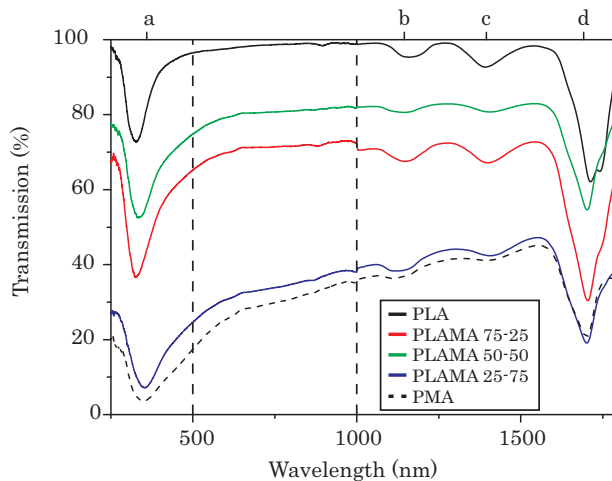
Figure 2.18: Transmission spectra recorded for lactide-mandelide copolymers solvent cast on glass slides. The results were normalised to 1 mm thickness. The materials show an absorption band in the UV-part of the spectrum (**a**). At higher wavelengths, C-H group oscillations can be distinguished (**b-d**).

in the monomer feed, the transparency decreased. This was particularly apparent in the case of the materials with the highest mandelide content (i.e. PLAMA 25-75 and PMA). A closer inspection of the mandelide-containing samples revealed considerable cracking of the polymer, which could result in increased scattering of the incident light and thus reduce the transparency of the samples.

The cracking was studied by performing optical profilometry to assess the surface quality of the obtained samples. The results are shown in figure 2.19 and indicate that the mandelide-containing samples are characterised by a larger surface roughness and/or corresponding standard deviation. This may be an indication of the stress-induced cracking of the materials. This is supported by the striking differences between the various samples as visualised in the topographical plots (a-e). Since brittleness of polymers is related to the polymer molecular weight and mandelide was shown to have a negative impact on the obtainable molecular weights, the mandelide-containing samples were found to be more sensitive to stress-induced cracking.[135–138] It

Table 2.6: Characteristic C-H group oscillations in the wavelength range between 1200 and 2500 nm.[104]

Oscillation type	Wavenumber [cm^{-1}]	Wavelength [nm]
Combination oscillation	4500-4200	2220-2350
1st high-order oscillation, stretching oscillation	5600-6200	1790-1610
Combination oscillation	6400-7700	1560-1300
2nd high-order oscillation, stretching oscillation	7800-8900	1280-1120

should be noted that these measurements only take into account the surface defects, as optical profilometry is unable to detect defects inside the material. However, the sample with the lowest molecular weight (PLAMA 25-75, M_n = 7.9 kg mol^{-1}) corresponded to the highest surface roughness value which greatly reduced the observed transparency ($< 60\%$). Further increasing the obtainable molecular weights (> 30 kg mol^{-1}) will thus be of great importance if these materials are to be applied in optical LoC sensors.

Finally, the materials' refractive indices (RI) were determined since the SPR resonance angle depends on the prism refractive index ($n_p = \epsilon_p^2$) as discussed in chapter 1 (equation 1.7). Table 2.7 provides an indication of the shift of the SPR angle as a function of the RI and shows the simulated absolute sensitivities that can be achieved for the reported prism materials.[139] Differences in prism RI (9% when comparing PS and PLA) values only have a minor influence ($< 5\%$) on sensor sensitivity.

In order to be able to assess the proper alignment when degradable polyesters are used, the materials' RI values were determined via optical refractometry. PLA was the optically rarest material in the present study with an RI value of 1.45559 ± 2.3E-6 (589 nm, 25 °C). The 589 nm wevelength was selected for the comparison with literature, since this is commonly applied wavelength in commercial refractometers.[140,141] As more mandelide was added to the monomer feed, the resulting material gradually became optically denser with

(a) PLA
$(41.6 \pm 2.6\text{nm})$

(b) PLAMA 75-25
$(95.7 \pm 27.9\text{nm})$

(c) PLAMA 50-50
$(45.6 \pm 32.8\text{nm})$

(d) PLAMA 25-75
$(268.5 \pm 211.9\text{nm})$

(e) PMA
$(39.1 \pm 8.3\text{nm})$
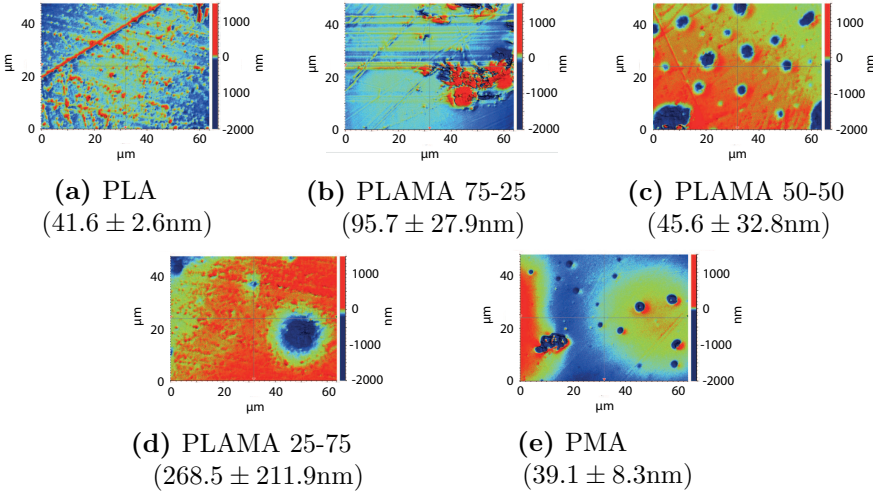
Figure 2.19: Evaluation of the surface quality of the solvent-cast samples applied in the transmission measurements. The RMS roughness values (R_q) and corresponding standard deviations are shown between brackets and reveal a large spread among the different samples. In addition, the studied samples have an irregular surface topography, which is consistent with large scatter losses.

the value for PMA (1.55189 ± 2.1E-6) approaching the value reported for polystyrene (1.5916 at 589 nm and 20 °C).[142] Figure 2.20a shows the results at 655.7 nm. This is the refractometer wavelength that is the closest to the 661 nm that will be applied in the SPR sensor. A materials' refractive index (n) may be related to the incident wavelength (λ, in µm) via the so-called Sellmeier equation (equation 2.11) which relies on a number of empirically determined constants (B and C):[143]

$$n^2(\lambda) = 1 + \frac{B_1\lambda^2}{\lambda^2 - C_1} + \frac{B_2\lambda^2}{\lambda^2 - C_2} + \frac{B_3\lambda^2}{\lambda^2 - C_3} \qquad (2.11)$$

Based on this equation, it can be derived that increasing the wavelength from 655.7 nm to 661 nm will change the refractive index by < 0.06%, which implies the value at 655.7 nm may serve as a close approximation.[144]

Table 2.7: Overview of the effect of the prism refractive index on the observed SPR resonance angle and simulated absolute sensitivities.[139]

Material	RI	SPR angle	Absolute sensitivity
	[-]	[°]	[RIU^{-1}]
PLA	1.456	75.361	62.65
PMMA	1.488	71.689	61.51
BK7 glass	1.515	68.823	60.86
PET	1.575	63.764	60.09
PC	1.578	63.544	60.07
PS	1.585	63.041	60.01

A clear trend can be observed between sample composition and measured RI values, which is related to the presence of increasing amounts of aromatic pendant groups that are characterised by a higher molar refractivity.[145,146] Considering the previously mentioned prism materials (table 2.7), the RI values obtained for the copolymers of meso-lactide and meso-mandelide are situated in the same range and thus exhibit the appropriate RI values for sensor development.

When increasing the temperature to 37 °C and 60 °C, all materials became optically less dense as a result of the thermal expansion.[147,148] The RI changes induced by thermal expansion of the prism are almost one order of magnitude smaller (approx. 1%) than the largest RI difference in table 2.7 (PLA-PS). However, it is not possible to rule out the effect of temperature fluctuations on the sensor's performance based on these observations. Indeed, changes in temperature may change the refractive index of a material. If the incident angle was alligned in such a way to allow the highest sensitivity, small changes may result in a small offset compared to this ideal angle thereby reducing the sensitivity.[139] Given the aim to perform short measurements (< 30 minutes), it can be expected that temperature fluctuations will be limited within the time frame of the measurement. If this is not the case, some sort of temperature control (e.g. a reference channel) can be added to the laboratory demonstrator to excluded the temperature dependency.

(a)

(b) PLA

(c) PLAMA 75-25

(d) PLAMA 50-50

(e) PLAMA 25-75

(f) PMA
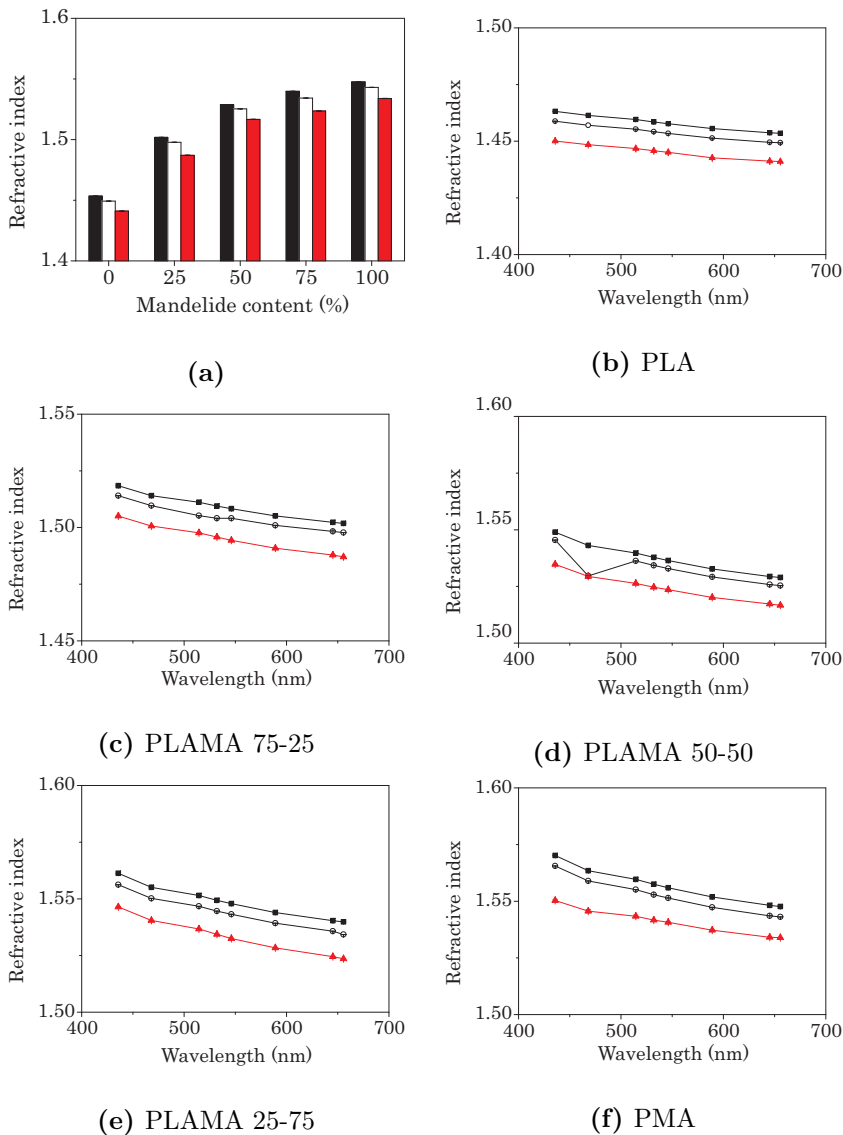
Figure 2.20: Figure (a) shows the refractive indices (RI) measured at 655.7 nm for the studied (co)polymers as a function of mandelide content, performed at three temperatures: 25 °C (black bars), 37 °C (white bars) and 60 °C (red bars). Figures b-f) show the obtained dispersion curves for the synthesised (co)polymers at the above-mentioned temperatures: 25°C (■), 37°C (○) and 60°C (▲)

Finally, the dispersion curves for these materials were derived by repeating the measurements at a total of 8 different wavelengths, which is the number of available wavelengths in the applied refractometer set-up. This enables the assessment of the influence of the incident light's wavelength on the observed refractive index. The results are shown in figures (2.20b)-(2.20f) for the various copolymers and reveal a limited influence ($< 1.5\%$) of the applied wavelength. This implies that sensor performance will not be negatively affected by small wavelength deviations.

2.4 Conclusions

Commonly used polyesters like PGA, PLA and PCL are either optically opaque due to their semi-crystalline nature and/or lack sufficient mechanical stability as a consequence of their low glass transition temperatures (< 50 °C). This should be taken into account when exposed to the environmental conditions associated with some developing countries.

Therefore, meso-lactide and meso-mandelide were copolymerised in bulk as well as in solution to obtain optically transparent polyesters with a high T_g (> 60 °C). In the case of solution polymerisations, the difference in polymerisation kinetics for both monomers was studied and mandelide was shown to polymerise 3 times slower, which was attributed to the larger sterical hindrance due to its phenyl substituents.

Molecular weights for the mandelide containing (co)polymers remained lower than expected based on the monomer to initiator ratio (approx. 20-35% of the target value), but surpassed earlier reports applying direct polycondensation. A possible cause for the lower than expected molecular weights may be attributed to a process similar to the spontaneous racemisation of meso-mandelide in highly polar solvents. It was shown that meso-mandelide does not readily racemise in the applied solvents (ACN at 70 °C or toluene at 100 °C). However, when the initiator and catalyst are added, racemisation was observed by Liu *et al.*[37] A relatively stable enol-adduct acted as the intermediate between meso-mandelide and its racemic counterpart as demonstrated by selectively reacting the formed alcohol functional

groups with TAIC, which led to an inversion of the diastereomeric excess. The existence of the latter enol-counterpart may thus serve as an adventious initiator, which is in accordance with the molecular weight control previously achieved by Liu *et al.*

When performing copolymerisations, the materials were found to be amorphous as derived from the absence of melting or crystallisation transitions in the DSC thermograms. Meso-mandelide was shown to have a positive influence on the glass transition temperature of co-polymers with meso-lactide. However, the targeted threshold of T_g > 60 °C could only be obtained for the mandelide homopolymer at the obtained molecular weights. However, based on the discussion of the DSC results, solvent inclusion may have reduced the observed T_g-values. Future experiments can therefore be performed using pierced lits, which would allow the solvent to escape during the first heating step. The observed high optical transparency (> 95%) observed for amorphous PLA, was diminished for the mandelide containing polymers as stress-induced cracking increased scattering by the analysed samples. Finally, the materials' RI values were influenced by the polymer composition, the temperature and the applied wavelength. However, none of these parameters have a significant (negative) effect on the sensor performance.

Given the correlation of the polymer molecular weight and both the glass transition temperature as well as the prevalence of stress-induced cracking, future work should primarily focus on further increasing the obtainable molecular weights (> 30 $kg\,mol^{-1}$) to allow these materials to be successfully implemented in shape-stable objects. MALDI-TOF (matrix assisted laser desorption/ionisation - time of flight) MS spectroscopy may be a useful technique in this respect, to characterise the polymer end groups. If mandelide end groups would be observed, this may prove the formulated hypothesis that mandelide is converted *in situ* to an initiating species. In addition, computational modelling of the racemisation of mandelide may further reveal the solvents' mode of action and to quantify the energy barriers encountered along the reaction coordinate.

Based on these analyses, the control over the polymerisations in terms of yield and attainable molecular weights may be further improved, which will allow subsequent (bio)degradation studies. The

latter have not been performed to date given the low amounts of polymer available and the low molecular weights obtained. Although the bulk polymerisation of mandelide and lactide has only been applied in a small number of experiments, the copolymerisation of both monomers in an 80-20 ratio (lactide-mandelide) was successful and may form the basis for further study. In this regard, alternative (organo)catalysts may also be explored to further improve the polymerisations in terms of reaction rate and molecular weight control. [149]

References

[1] T. Nguyen, S. Kwak, S. J. Karpowicz, *BioTechniques* **2014**, *57*, 267–271.

[2] A. Bange, H. B. Halsall, W. R. Heineman, *Biosensors and Bioelectronics* **2005**, *20*, 2488–2503.

[3] Plasticker.de, *Raw Materials and Prices*, `http://plasticker.de/preise/pms_en.php?show=ok&make=ok&aog=A&kat=Mahlgut`.

[4] G. Luka, A. Ahmadi, H. Najjaran, E. Alocilja, M. DeRosa, K. Wolthers, A. Malki, H. Aziz, A. Althani, M. Hoorfar, *Sensors (Basel Switzerland)* **2015**, *15*, 30011–31.

[5] H.-J. Jin, B.-Y. Lee, M.-N. Kim, J.-S. Yoon, *Journal of Polymer Science Part B: Polymer Physics* **2000**, *38*, 1504–1511.

[6] Plastics Europe, *An analysis of European plastics production, demand and waste data*, **2016**.

[7] M. Flieger, M. Kantorová, a. Prell, T. Rezanka, J. Votruba, *Folia microbiologica* **2003**, *48*, 27–44.

[8] M. R. Ishak, S. M. Sapuan, Z. Leman, M. Z. a. Rahman, U. M. K. Anwar, J. P. Siregar, *Carbohydrate polymers* **2013**, *91*, 699–710.

[9] L. Wu, R. Mincheva, Y. Xu, J.-M. Raquez, P. Dubois, *Biomacromolecules* **2012**, *13*, 2973–2981.

[10] M. M. Reddy, S. Vivekanandhan, M. Misra, S. K. Bhatia, A. K. Mohanty, *Progress in Polymer Science* **2013**, *38*, 1653–1689.

[11] E. Akaraonye, T. Keshavarz, I. Roy, *Journal of Chemical Technology and Biotechnology* **2010**, *85*, 732–743.

[12] J. Quillaguamán, H. Guzmán, D. Van-Thuoc, R. Hatti-Kaul, *Applied microbiology and biotechnology* **2010**, *85*, 1687–96.

[13] S. Doppalapudi, A. Jain, W. Khan, A. J. Domb, *Polymers for Advanced Technologies* **2014**, *25*, 427–435.

[14] S. Slomkowski, S. Penczek, A. Duda, *Polymers for Advanced Technologies* **2014**, *2014*, n/a–n/a.

[15] EPA, *Municipal Solid Waste in the United States: 2011 Facts and Figures*, Epa technical report, **2013**.

[16] H. J. Endres, A. Siebert-Raths, *Engineering Biopolymers: Markets, Manufacturing, Properties, and Applications*, Hanser Gardner Publications, **2010**.

[17] G. Scott, D. M. Wiles, *Biomacromolecules* **2001**, *2*, 615–22.

[18] K. Siegenthaler, A. Künkel, G. SKupin, M. Yamamoto in *Advanced Polymer Science*, *Vol. 245* (Eds.: B. Rieger, A. Künkel, G. W. Coates, R. Reichardt, E. Dinjus, T. A. Zevaco), Springer Berlin Heidelberg, Berlin, Heidelberg, **2012**, pp. 91–136.

[19] M. Vert, Y. Doi, K.-H. Hellwich, M. Hess, P. Hodge, P. Kubisa, M. Rinaudo, F. Schué, *Pure and Applied Chemistry* **2012**, *84*, 377–410.

[20] K. Madhavan Nampoothiri, N. R. Nair, R. P. John, *Bioresource technology* **2010**, *101*, 8493–501.

[21] Plastics Europe, *Plastics – the Facts 2013 An analysis of European latest plastics production , demand and waste data*, **2013**.

[22] D. Platt, *Biodegradable polymers: market report*, Smithers rapra limited technical report, **2006**.

[23] J. C. Middleton, A. J. Tipton, *Biomaterials* **2000**, *21*, 2335–2346.

[24] J.-b. Zeng, C.-l. Huang, L. Jiao, X. Lu, Y.-z. Wang, X.-l. Wang, *Industrial and Engineering Chemistry Research* **2012**, *51*, 12258–12265.

[25] N. Jacquel, F. Freyermouth, F. Fenouillot, A. Rousseau, J. P. Pascault, P. Fuertes, R. Saint-Loup, *Journal of Polymer Science Part A: Polymer Chemistry* **2011**, *49*, 5301–5312.

[26] D. S. Marques, M. H. Gil, C. M. S. G. Baptista, *Journal of Applied Polymer Science* **2012**, *125*, E283–E289.

[27] T. M. Pell, T. G. Davis, *Journal of Polymer Science Part A-2: Polymer Physics* **1973**, *11*, 1671–1682.

[28] S.-H. Luo, Z.-Y. Wang, C.-X. Mao, J.-P. Huo, *Journal of Polymer Research* **2011**, *18*, 2093–2102.

[29] A. Fradet, M. Tessier, *Polyesters*, John Wiley and Sons, Inc., Hoboken, NJ, USA, **2003**, pp. 17–134.

[30] A. P. Gupta, V. Kumar, *European Polymer Journal* **2007**, *43*, 4053–4074.

[31] M. Ajioka, K. Enomoto, K. Suzuki, A. Yamaguchi, *Journal of environmental polymer degradation* **1995**, *3*, 225–234.

[32] S.-I. Moon, C.-W. Lee, I. Taniguchi, M. Miyamoto, Y. Kimura, DOI 10.1016/S0032-3861(00)00889-2.

[33] C. Jérôme, P. Lecomte, *Advanced Drug Delivery Reviews* **2008**, *60*, 1056–1076.

[34] M. Szwarc, *Nature* **1956**, *178*, 1168–1169.

[35] C. Robert, F. de Montigny, C. M. Thomas, *Nature communications* **2011**, *2*, 586.

[36] H. Marubayashi, S. Asai, T. Hikima, M. Takata, T. Iwata, *Macromolecular Chemistry and Physics* **2013**, *214*, 2546–2561.

[37] T. Liu, T. L. Simmons, D. A. Bohnsack, M. E. Mackay, M. R. Smith, G. L. Baker, E. Lansing, *Macromolecules* **2007**, *40*, 6040–6047.

[38] F. Jing, M. R. Smith, G. L. Baker, *Macromolecules* **2007**, *40*, 9304–9312.

[39] X. Jiang, M. R. S. Iii, G. L. Baker, M. R. Smith, G. L. Baker, *Macromolecules* **2007**, *41*, 318–324.

[40] X. Jiang, E. B. Vogel, M. R. Smith, G. L. Baker, *Macromolecules* **2008**, *41*, 1937–1944.

[41] O. Dechy-Cabaret, B. Martin-Vaca, D. Bourissou, *Chemical Reviews* **2004**, *104*, 6147–6176.

[42] S. Penczek, M. Cypryk, a. Duda, P. Kubisa, S. Slomkowski, *Progress in Polymer Science* **2007**, *32*, 247–282.

[43] P. Lecomte, C. Jérôme, *Advances in Polymer Science* **2012**, *245*, 173–218.

[44] D. Garlotta, *Journal of Polymers and the Environment* **2002**, *9*, 63–84.

[45] M. Labet, W. Thielemans, *Chemical Society Reviews* **2009**, *38*, 3484–3504.

[46] M. J. Stanford, A. P. Dove, *Chemical Society Reviews* **2010**, *39*, 486–494.

[47] P. Dubois, R. Jerome, P. Teyssie, *Polymer Bulletin* **1989**, *22*, 475–482.

[48] N. Ropson, P. Dubois, R. Jerome, P. Teyssie, *Macromolecules* **1995**, *28*, 7589–7598.

[49] J. Okuda, I. L. Rushkin, *Macromolecules* **1993**, *26*, 5530–5532.

[50] A. D. Asandei, G. Saha, *Macromolecular Rapid Communications* **2005**, *26*, 626–631.

[51] J.-B. Zeng, M. Srinivansan, Y.-D. Li, R. Narayan, Y.-Z. Wang, *Journal of Polymer Science Part A: Polymer Chemistry* **2010**, *48*, 5885–5890.

[52] A. Kowalski, A. Duda, S. Penczek, *Macromolecular Rapid Communications* **1998**, *19*, 567–572.

[53] A. Kowalski, A. Duda, S. Penczek, *Macromolecules* **2000**, *33*, 689–695.

[54] M. Möller, R. Kånge, J. L. Hedrick, *Journal of Polymer Science Part A: Polymer Chemistry* **2000**, *38*, 2067–2074.

[55] H. R. Kricheldorf, S. Eggerstedt, *Macromolecular Chemistry and Physics* **1998**, *199*, 283–290.

[56] H. R. Kricheldorf, A. Stricker, D. Langanke, *Macromolecular Chemistry and Physics* **2001**, *202*, 2525–2534.

[57] H. R. Kricheldorf, *Journal of Polymer Science Part A: Polymer Chemistry* **2004**, *42*, 4723–4742.

[58] P. Dobrzynski, *Journal of Polymer Science Part A: Polymer Chemistry* **2002**, *40*, 1379–1394.

[59] A. J. Chmura, D. M. Cousins, M. G. Davidson, M. D. Jones, M. D. Lunn, M. F. Mahon, *Dalton Transactions* **2008**, 1437–1443.

[60] Y. Shen, Z. Shen, Y. Zhang, K. Yao, *Macromolecules* **1996**, *29*, 8289–8295.

[61] W. M. Stevels, M. J. K. Ankone, P. J. Dijkstra, J. Feijen, *Macromolecules* **1996**, *29*, 3332–3333.

[62] M. Yamashita, Y. Takemoto, E. Ihara, H. Yasuda, *Macromolecules* **1996**, *29*, 1798–1806.

[63] A. Hofman, R. Szymański, S. Słomkowski, S. Penczek, *Die Makromolekulare Chemie* **1984**, *185*, 655–667.

[64] A. Hofman, R. Szymański, S. Słomkowski, S. Penczek, *Die Makromolekulare Chemie* **1984**, *185*, 655–667.

[65] S. Słomkowski, R. Szymański, A. Hofman, *Die Makromolekulare Chemie* **1985**, *186*, 2283–2290.

[66] H. R. Kricheldorf, J. M. Jonté, R. Dunsing, *Die Makromolekulare Chemie* **1986**, *187*, 771–785.

[67] G. a. Abraham, A. Gallardo, A. E. Lozano, J. San Roman, *Journal of Polymer Science Part A: Polymer Chemistry* **2000**, *38*, 1355–1365.

[68] A.-C. Albertsson, R. Palmgren, *Journal of Macromolecular Science Part A* **1996**, *33*, 747–758.

[69] H. R. Kricheldorf, M.-V. Sumbél, *Die Makromolekulare Chemie* **1988**, *189*, 317–331.

[70] A. P. Dove, R. C. Pratt, B. G. G. Lohmeijer, R. M. Waymouth, J. L. Hedrick, *Journal of the American Chemical Society* **2005**, *127*, 13798–9.

[71] B. G. G. Lohmeijer, R. C. Pratt, F. Leibfarth, J. W. Logan, D. A. Long, A. P. Dove, F. Nederberg, J. Choi, C. Wade, R. M. Waymouth, J. L. Hedrick, *Macromolecules* **2006**, *39*, 8574–8583.

[72] N. E. Kamber, W. Jeong, R. M. Waymouth, R. C. Pratt, B. G. G. Lohmeijer, J. L. Hedrick, *Chemical reviews* **2007**, *107*, 5813–40.

[73] F. Nederberg, E. Connor, *Angewandte Chemie . . .* **2001**, *42*, 2712–2715.

[74] G. W. Nyce, T. Glauser, E. F. Connor, A. Möck, R. M. Waymouth, J. L. Hedrick, *Journal of the American Chemical Society* **2003**, *125*, 3046–56.

[75] A. P. Dove, R. C. Pratt, B. G. Lohmeijer, D. a. Culkin, E. C. Hagberg, G. W. Nyce, R. M. Waymouth, J. L. Hedrick, *Polymer* **2006**, *47*, 4018–4025.

[76] L. Zhang, F. Nederberg, R. C. Pratt, R. M. Waymouth, J. L. Hedrick, C. G. Wade, S. U. V, R. V. February, V. Re, M. Recei, V. April, *Macromolecules* **2007**, *40*, 4154–4158.

[77] E. a. Appel, V. Y. Lee, T. T. Nguyen, M. McNeil, F. Nederberg, J. L. Hedrick, W. C. Swope, J. E. Rice, R. D. Miller, J. Sly, *Chemical communications (Cambridge England)* **2012**, *48*, 6163–5.

[78] E. Brulé, V. Guérineau, P. Vermaut, F. F. F. Prima, J. Balogh, L. Maron, A. M. Z. Slawin, S. P. Nolan, C. M. Thomas, E. Brule,

V. Guerineau, P. Vermaut, F. F. F. Prima, J. Balogh, L. Maron, A. M. Z. Slawin, S. P. Nolan, C. M. Thomas, *Polymer Chemistry* **2013**, *4*, 2414.

[79] A. M. Goldys, D. J. Dixon, *Macromolecules* **2014**, *47*, 1277–1284.

[80] M. Kamigaito, J. Nakashima, K. Satoh, M. Sawamoto, *Society* **2003**, 3540–3544.

[81] K. Makiguchi, S. Kikuchi, T. Satoh, T. Kakuchi, *Journal of Polymer Science Part A: Polymer Chemistry* **2013**, *51*, 2455–2463.

[82] Z. Jiang, *Biomacromolecules* **2008**, *9*, 3246–3251.

[83] Y. Yang, Y. Yu, Y. Zhang, C. Liu, W. Shi, Q. Li, *Process Biochemistry* **2011**, *46*, 1900–1908.

[84] K. Matsumoto, S. Taguchi, *Applied microbiology and biotechnology* **2013**, *97*, 8011–21.

[85] S. Matsumura, K. Mabuchi, K. Toshima, *Macromolecular Rapid Communications* **1997**, *18*, 477–482.

[86] S. Philip, T. Keshavarz, I. Roy, *Journal of Chemical Technology and Biotechnology* **2007**, *247*, 233–247.

[87] R. Reichardt, B. Rieger in *Advances in Polymer Science* (Eds.: B. Rieger, A. Künkel, G. W. Coates, R. Reichardt, E. Dinjus, T. A. Zevaco), Springer Berlin Heidelberg, Berlin, Heidelberg, **2012**, Chapter Synthetic, pp. 49–90.

[88] W. J. Orts, G. A. R. Nobes, J. Kawada, S. Nguyen, G.-e. Yu, F. Raveneile, *Canadian Journal of Chemistry-Revue Canadienne De Chimie* **2008**, *86*, 628–640.

[89] Q. Wang, P. Yang, M. Xian, Y. Yang, C. Liu, Y. Xue, G. Zhao, *Bioresource technology* **2013**, *142*, 741–4.

[90] Y. Ikada, H. Tsuji, *Macromolecular Rapid Communications* **2000**, *21*, 117–132.

[91] A. A. Shah, F. Hasan, A. Hameed, S. Ahmed, *Biotechnology advances* **2008**, *26*, 246–65.

[92] S. Kasirajan, M. Ngouajio, *Agronomy for Sustainable Development* **2012**, *32*, 501–529.

[93] N. Lucas, C. Bienaime, C. Belloy, M. Queneudec, F. Silvestre, J.-E. Nava-Saucedo, *Chemosphere* **2008**, *73*, 429–42.

[94] J. P. Eubeler, M. Bernhard, T. P. Knepper, *TrAC Trends in Analytical Chemistry* **2010**, *29*, 84–100.

[95] B. Singh, N. Sharma, *Polymer Degradation and Stability* **2008**, *93*, 561–584.

[96] K. Leja, G. Lewandowicz, *Polish Journal of Environmental Studies* **2010**, *19*, 255–266.

[97] J. P. Eubeler, S. Zok, M. Bernhard, T. P. Knepper, *TrAC Trends in Analytical Chemistry* **2009**, *28*, 1057–1072.

[98] T. Kijchavengkul, R. Auras, *Polymer International* **2008**, *57*, 793–804.

[99] M. Malin, M. HiljanenVainio, T. Karjalainen, J. Seppala, *Journal of Applied Polymer Science* **1996**, *59*, 1289–1298.

[100] M. Siotto, E. Sezenna, S. Saponaro, F. D. Innocenti, M. Tosin, L. Bonomo, V. Mezzanotte, *Journal of Environmental Management* **2012**, *93*, 31–37.

[101] M. E. Brown, B. D. Glass, *International Journal of Pharmaceutics* **1999**, *190*, 129–137.

[102] M. A. Woodruff, D. W. Hutmacher, *Progress in Polymer Science* **2010**, *35*, 1217–1256.

[103] A. J. Peacock, A. R. Calhoun, *Polymer Chemistry: Properties and Applications*, Hanser Gardner Publications, **2006**, p. 397.

[104] R. Klein, *Laser welding of plastics*, Wiley-VCH Verlag, **2011**, pp. 59–60.

[105] C. E. Carraher, R. B. R. B. Seymour, *Seymour/Carraher's polymer chemistry.*, CRC Press, **2007**, p. 738.

[106] P. C. Sadek, *The HPLC Solvent Guide, 2nd Edition*, Wiley, 2nd ed., **2002**, p. 664.

[107] T. Tsukegi, T. Motoyama, Y. Shirai, H. Nishida, T. Endo, *Polymer Degradation and Stability* **2007**, *92*, 552–559.

[108] I. a. Shuklov, H. Jiao, J. Schulze, W. Tietz, K. Kühlein, A. Börner, *Tetrahedron Letters* **2011**, *52*, 1027–1030.

[109] A. Bose, P. Srinivasan, *Tetrahedron* **1975**, *31*, 3025–3029.

[110] W. Chaouch, F. Dieval, D. Le Nouen, A. Defoin, N. Chakfe, B. Durand, *Journal of biomedical materials research. Part A* **2009**, *91*, 939–52.

[111] W. Van Camp, T. Dispinar, B. Dervaux, F. E. Du Prez, J. C. Martins, B. Fritzinger, *Macromolecular Rapid Communications* **2009**, *30*, 1328–1333.

[112] S. Li, S. Mccarthy, *Biomaterials* **1999**, *20*, 35–44.

[113] F. Deng, R. A. Gross, *International Journal of Biological Macromolecules* **1999**, *25*, 153–159.

[114] R. F. Storey, J. W. Sherman, *Macromolecules* **2002**, *35*, 1504–1512.

[115] S. Y. Reyes-López, A. M. Richa, *Macromolecular Symposia* **2013**, *325-326*, 21–37.

[116] O. Coulembier, P. Degée, J. L. Hedrick, P. Dubois, *Progress in Polymer Science* **2006**, *31*, 723–747.

[117] H. Fukuzaki, Y. Aiba, M. Yoshida, M. Asano, M. Kumakura, *Die Makromolekulare Chemie* **1989**, *190*, 2407–2415.

[118] H. Fukuzaki, M. Yoshida, M. Asano, M. Kumakura, K. Imasaka, T. Nagai, T. Mashimo, H. Yuasa, K. Imai, H. Yamanaka, *European Polymer Journal* **1990**, *26*, 1273–1277.

[119] K. Imasaka, T. Nagai, M. Yoshida, H. Fukuzaki, M. Asano, M. Kumakura, *Die Makromolekulare Chemie* **1990**, *191*, 2077–2082.

[120] K. Imasaka, M. Yoshida, H. Fukuzaki, M. Asano, M. Kumakura, T. Mashimo, H. Yamanaka, T. Nagai, *International Journal of Pharmaceutics* **1992**, *81*, 31–38.

[121] J. K. Whitesell, J. A. Pojman, *Chemistry of Materials* **1990**, *2*, 248–254.

[122] D. W. Lim, S. H. Choi, T. G. Park, *Macromol. Rapid Commun.* **2000**, *21*, 464–471.

[123] A. J. R. Lasprilla, G. A. R. Martinez, B. H. Lunelli, A. L. Jardini, R. Maciel, *Biotechnology Advances* **2012**, *30*, 321–328.

[124] K. S. Anseth, C. M. Wang, C. N. Bowman, *Macromolecules* **1994**, *27*, 650–655.

[125] L. B. Manton, PhD thesis, University of Bath, **2014**.

[126] B. R. A. Auras, S. P. Singh, J. J. Singh, *Packaging technology and science* **2005**, *18*, 207–216.

[127] G. Kfoury, J.-M. Raquez, F. Hassouna, J. Odent, V. Toniazzo, D. Ruch, P. Dubois, *Frontiers in Chemistry* **2013**, *1*, 1–46.

[128] C. L. Beyler, M. M. Hirschler, *SPE Handbook of Fire Protection Engineering* **2001**, 110–131.

[129] V. N. Tsvetkov, I. N. Shtennikova, *Macromolecules* **1978**, *11*, 306–312.

[130] G. Montaudo, C. Puglisi, R. Rapisardi, F. Samperi, *Polymer Degradation and Stability* **1991**, *31*, 229–246.

[131] F. Kakali, J. K. Kallitsis, *Macromolecules* **1996**, *29*, 4759–4763.

[132] J. M. Raquez, P. Degee, P. Dubois, S. Balakrishnan, R. Narayan, *Polymer Engineering and Science* **2005**, *45*, 622–629.

[133] T. G. Fox, P. J. Flory, *Journal of Applied Physics* **1950**, *21*, 581–591.

[134] T. Li, C. Zhou, M. Jiang, *Polymer Bulletin* **1991**, *25*, 211–216.

[135] A. G. Mikos, N. A. Peppas, *The Journal of Chemical Physics* **1988**, *88*, 1337–1342.

[136] A. G. Mikos, N. A. Peppas, *Journal of Materials Science* **1989**, *24*, 1612–1616.

[137] A. G. Mikos, N. A. Peppas, *Journal of Polymer Science Part B: Polymer Physics* **1991**, *29*, 837–841.

[138] S. Nurkhamidah, E. M. Woo, *Journal of Applied Polymer Science* **2011**, *122*, 1976–1985.

[139] J. De Pelsmaeker, H. Thienpont, H. Ottevaere, *to be submitted in Optics Express.*

[140] Anton Paar, *Refractometer*, **2017**, `http://www.anton-paar.com/uk-en/products/group/refractometer/` `(accessed2017-06-28)`.

[141] Hanna Instruments, *Refractometers*, **2017**, `http://www.hannainstruments.be/be-nl/` `analyse-meet-instrumenten-apparatuur/refractometers.` `html(accessed2017-06-28)`.

[142] N. Sultanova, S. Kasarova, I. Nikolov, *Acta Physica Polonica A* **2009**, *116*, 585–587.

[143] J. W. Gooch in *Encyclopedic Dictionary of Polymers*, Springer New York, New York, NY, **2011**, pp. 653–654.

[144] I. Bodurov, I. Vlaeva, A. Viraneva, T. Yovcheva, S. Sainov, *Nanoscience and nanotechnology* **2016**, *16*, 31–33.

[145] W. Groh, A. Zimmermann, *Macromolecules* **1991**, *24*, 6660–6663.

[146] H. K. Shobha, H. Johnson, M. Sankarapandian, Y. S. Kim, P. Rangarajan, D. G. Baird, J. E. McGrath, *Journal of Polymer Science Part A: Polymer Chemistry* **2001**, *39*, 2904–2910.

[147] R. Moshrefzadeh, M. Radcliffe, T. Lee, S. Mohapatra, *Journal of Lightwave Technology* **1992**, *10*, 420–425.

[148] Z. Zhang, P. Zhao, P. Lin, F. Sun, *Polymer* **2006**, *47*, 4893–4896.

[149] L. Mezzasalma, A. P. Dove, O. Coulembier, *European Polymer Journal* **2017**, *95*, 628–634.

Chapter 3

Application of OCA-monomers in polyester synthesis

"Potential has a shelf life."

— Margaret Atwood

3.1 Introduction

As mentioned in chapter 2, the polymerisation of cyclic diesters using stannous octoate as a catalyst has been widely applied for the synthesis of PLA. Unfortunately, it was demonstrated that for the bulky mandelide monomer, the low yield (approx. 50%) associated with the monomer synthesis is a limiting factor towards mandelide's commercial viability. The latter is aggravated by the fact that the meso-diastereoisomer is the preferred monomer, while the thermodynamically more stable racemic mandelide is characterised by a low solubility (< 1 mg mL^{-1}) in most organic solvents and a degradation preceding the melt transition, thereby excluding its application in bulk polymerisations. Given the fact that only meso-mandelide is applicable in bulk and solution polymerisations, the practical monomer yield is reduced to approx. 25%.

Because of the above-mentioned drawbacks, O-carboxy anhydrides (OCAs) were previously evaluated as an alternative monomer family for the synthesis of degradable polyesters.[1] OCAs consist of a class of reactive five-membered rings obtained via direct carbonylation of α-hydroxy acids. The synthesis of OCAs dates back to the work by Davies in 1951,[2] but these compounds were only identified as potential monomers in 1973 by Smith and Tighe, who discussed the ring-opening of phenyl- and pentafluorophenyl-substituted OCAs.[3–7] In 1983, Kricheldorf and Jonté continued on the work of Smith and Tighe with the application of a lactic acid-derived OCA (lacOCA) for the synthesis of polyesters.[8] Unfortunately, only oligomers ($M_n < 3$ $kg\,mol^{-1}$) could be obtained in these initial studies.

More recently, the research field has been given a new impulse by opening up a route towards higher molecular weights up to 62 $kg\,mol^{-1}$ by applying an organocatalytic mechanism.[9] Since then, several groups have expanded the field by adding new monomers to the OCA family.[10–16]

Interestingly, the phenyl-substituted OCA derived from mandelic acid (hence manOCA) has recently been revisited by Buchard *et al.* and was successfully applied in the synthesis of well-defined (stereoregular) poly(mandelic acid).[17]

In the current chapter, both lacOCA and manOCA are copolymerised for the first time to obtain amorphous copolymers combining the increased glass transition temperature of mandelic acid-based polymers (up to 100 °C) with the straightforward degradability of poly(lactic acid). The obtained results will be compared to the ones obtained for cyclic diesters as discussed in chapter 2 and the corresponding homopolymers found in literature with respect to monomer yield and polymer characteristics including molecular weight, thermal and optical properties.

3.2   Synthesis of OCA monomers

As already mentioned, the synthesis of OCAs consists of the carbonylation of α-hydroxy acids, which can be achieved by reacting the hydroxy acid with phosgene according to the mechanism shown in figure 3.1. It is important to note that the synthesis of OCAs shows
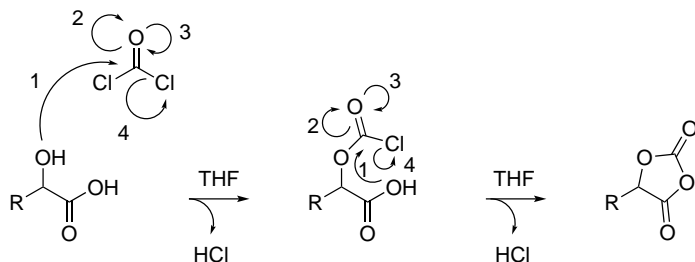
Figure 3.1: Scheme showing the mechanism for the synthesis of OCA-monomers. Within the context of the current PhD, R = -CH$_3$ or -C$_6$H$_5$.

many similarities with the synthesis of N-carboxy anhydrides (NCAs) which are used for the synthesis of polyamides.[18–24]

Unfortunately, phosgene is a toxic gaseous compound. Given the fact that phosgene gas can result in lung damage within 20 minutes at the odour recognition concentration (1.5 ppm), phosgene is difficult to handle in a safe and efficient way.[25] For this reason, carbonylation reactions often employ a different CO-source: *e.g.* trichloromethyl-chloroformate (*i.e.* diphosgene) or bis(trichloromethyl)carbonate (*i.e.* triphosgene) (figure 3.2). These compounds are respectively a liquid and a crystalline solid, making them more easy to handle in laboratory conditions. Unfortunately, these compounds show a lower reactivity than phosgene, as indicated by Pasquato *et al.* who demonstrated the reactivity of di- and triphosgene being respectively 19 and 170 times lower than phosgene, by reacting them with methanol as a model compound.[26]

Interestingly, both di- and triphosgene can be converted into phos-gene *in situ*, thereby combining the ease of handling di- and tri-
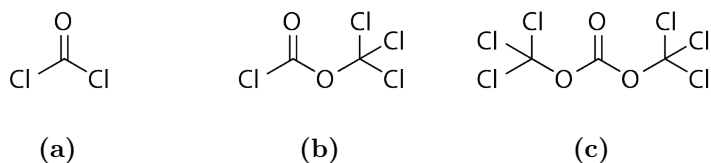
Figure 3.2: Overview of CO-sources that can be applied in the synthesis of OCAs: (a) phosgene; (b) diphosgene; and (c) triphosgene.
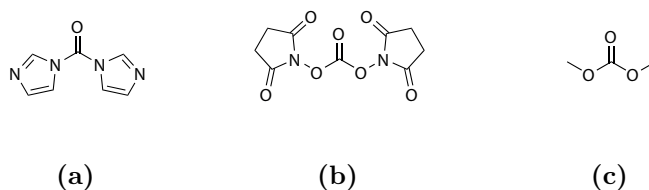
Figure 3.3: Overview of alternative carbonylation reagents: (a) carbonyldiimidazole; (b) disuccinimidylcarbonate; and (c) dimethylcarbonate.

phosgene with the reactivity of phosgene gas. This conversion can be performed thermally by heating the reaction mixture above 300 °C.[27] However, this method is not suitable for the synthesis of OCAs given their reported high reactivity. As an alternative to this thermal decomposition, several catalytic systems (e.g. Fe_2O_3, $FeCl_3$, or $AlCl_3$) can be applied to convert di- or triphosgene into phosgene gas under mild conditions.[27] Activated carbon is another well-known catalyst for this conversion and is commonly applied for the synthesis of OCAs, as this heterogeneous catalyst can be removed through filtration.[17] Besides the above-mentioned phosgene-based compounds a number of alternative reagents have been proposed as safer reagents in carbonylation reactions. These include a.o. carbonyldiimidazole, disuccinimidylcarbonate and dimethylcarbonate (figure 3.3).[28]

3.2.1 OCA synthesis in batch

Initially, both lactic acid as well as mandelic acid were reacted in a batch process following the method of Buchard *et al.*[17] Diphosgene was added dropwise to a stirred slurry of activated carbon and the racemic α-hydroxy acid in tetrahydrofuran (THF) given the aim to synthesise amorphous (co)polymers. In case of lactic acid, the solution was cooled with an ice bath since lactic acid reacts more violently than mandelic acid as indicated by the highly exothermic nature of the reaction. This observation is easily rationalised as lactic acid is characterised by lower sterical hindrance around the α-carbon atom. In addition, DL-lactic acid is available as a viscous liquid (10-15% H_2O), which complicates its drying via molecular sieves, while distilling lactic acid over a drying agent may yield lactide which is

difficult to separate from the formed lacOCA.[8] The residual water (approx. 10%) can be trapped by an excess of diphosgene, but contributes to the observed reaction heat. For this reason, lithium lactate has become an interesting alternative for the synthesis of lacOCA .[9] Triethylamine was also added to capture the hydrochloric acid formed during the reaction.

The mechanism for the conversion of α-hydroxy acid can be found in figure 3.1. The alcohol function readily initiates a nucleophilic acyl substitution on phosgene. Next, the carboxylic acid initiates a second nucleophilic acyl substitution resulting in ring-closure of the OCA-monomer and the formation of a second equivalent of hydrochloric acid.

The reaction procedure mentioned generally showed high yields for manOCA (> 85%), while lacOCA was obtained at yields of around 58%. Both results are in accordance with reports from literature.[9,17] One reason for this large difference in yield can be found in the relative stability of both monomers. Again considering the lower sterical hindrance around the α-carbon atom, lacOCA is much more prone to hydrolysis during the work-up of the reaction, despite all precautions including the use of thoroughly dried solvents and glassware. This evidently limits the amount of product obtained after recrystallisation, while most manOCA will remain unaffected.

Besides the demonstrated higher yield compared to lactide-based monomers, the above-mentioned synthesis yields a single reaction product as can be observed in ^{1}H-NMR spectroscopy (figure 3.4, a-b). FT-IR spectra in turn reveal a characteristic double carbonyl stretch vibration around $\nu = 1875$ cm^{-1} and $\nu = 1790$ cm^{-1}. Unlike the mandelide discussed in chapter 2, all of the formed monomer is suitable for solution polymerisations, which is preferential from an economical point of view.

Despite the overall good performance of the monomer synthesis presented here compared to the synthesis of mandelide in chapter 2, the application of phosgene sources limits the scale (approx. 20 g of monomer) at which the reaction can be run safely in a laboratory setting. Keeping in mind the potential application of these monomers in industry, scale-up of the reaction is desired without compromising process safety. Therefore, the next section will discuss the poten-

(a) lacOCA

(b) manOCA
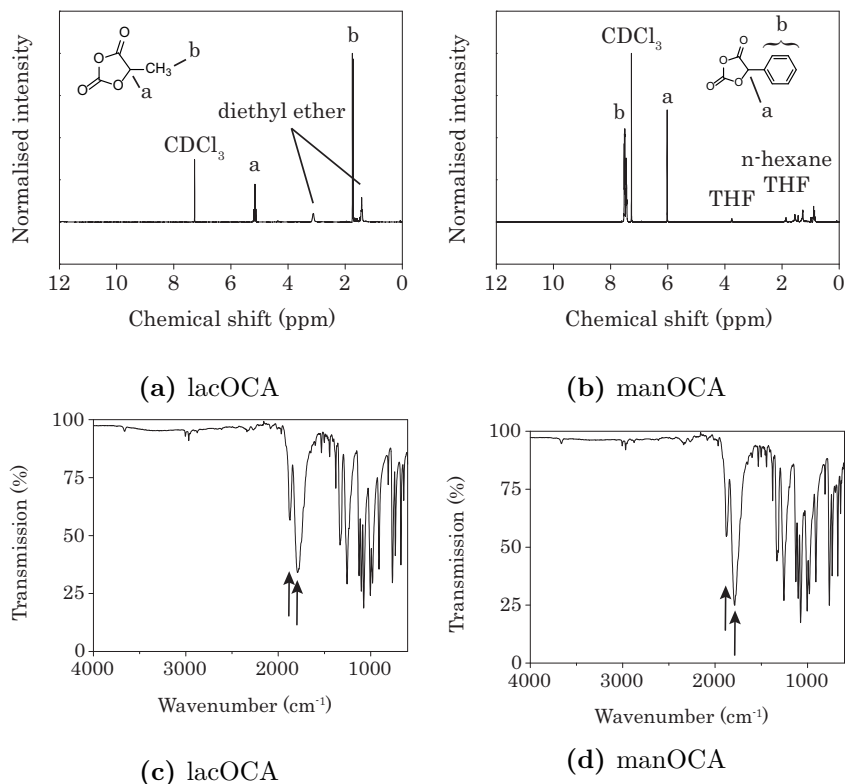
(c) lacOCA

(d) manOCA

Figure 3.4: Annotated ^{1}H-NMR spectra (a and b) obtained for lacOCA and manOCA along with the corresponding FT-IR spectra (c and d) indicating the characteristic carbonyl stretch vibrations associated with the OCA-ring (black arrows).

tial of flow chemistry for the (semi-)continuous synthesis of OCA-monomers since this would allow to limit the amount of (di)phosgene being present in the reactor.

3.2.2   OCA synthesis via flow chemistry

As already explained (section 3.2), the application of (di/tri)phosgene imposes a serious safety risk and thus limits the scale-up of this type of chemistry in a batch-wise procedure. Flow chemistry has been gaining interest over the past years to perform reactions in a con-
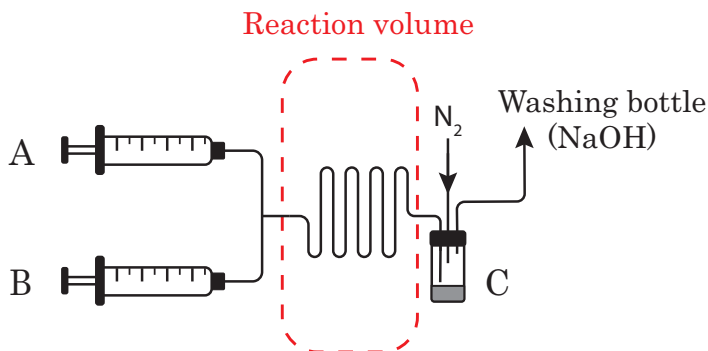
Figure 3.5: Schematic representation of the set-up applied in the flow chemistry experiments. A diphosgene solution in THF (A) and a mandelic acid solution in THF (B) were pumped through the reactor. The product was collected in a sealed vial under N_2 flow (C).

tinuous fashion.[29–32] Indeed, microflow reactors require only limited amounts of reagents and solvents which reduces the amount of *e.g.* phosgene present in the reactor.[33–36] Secondly, given the small channel dimensions, they allow efficient removal of the produced reaction heat thereby preventing runaway reactions as reaction rates increase with temperature.[37] Both aspects could thus greatly reduce the risk associated with the synthesis of OCA-based monomers. In addition, the conditions applied in microflow conditions can be translated to larger flow reactors thereby increasing the amounts of monomer that can be synthesised per unit of time.

To study the applicability of flow chemistry to the synthesis of OCA, manOCA was selected as a pilot compound given its superior performance in batch conditions compared to lacOCA. Three different microreactors have been applied: two conventional flow reactors and one packed bed reactor.[38,39] The synthesis was first attempted in an 11 µL flow reactor (table 3.1, entries b-g) without activated carbon as such systems can be scaled up to larger laboratory set-ups (e.g. a mL scale reactor coupled to HPLC pumps) in a more straightforward manner. A schematic representation of the set-up can be found in figure 3.5.

The first experiments were conducted at reduced concentration compared to the conditions applied in batch. This was done to pre-

vent blockage of the microchannels due to precipitation of the reaction products at the reactor outlet. Not only are blocked microreactors difficult/impossible to clean, pressure build-up in the system may result in safety issues given the application of diphosgene as a reactant. Solutions of mandelic acid and diphosgene in anhydrous THF were prepared and subsequently introduced into the reactor by means of 2 syringe pumps. Since no catalyst (activated carbon) was applied in this simplified set-up, the reactions were performed at slightly elevated temperatures (40 °C) compared to the batch conditions (room temperature). This is possible in a safe way given the limited reaction volume, which allows the straightforward dissipation of the produced reaction heat.[37] Since under these conditions diphosgene is expected to yield two phosgene molecules, 0.5 equivalents were applied to maintain the reaction stoichiometry and to prevent a buildup of (di)phosgene in the collecting vial. The reaction time was varied from 30 s to 5 min by applying the appropriate flow rate (table 3.1). Samples were collected at the reactor outlet and subsequently analysed via ^{1}H-NMR spectroscopy. Unfortunately, these experiments did not result in the formation of the desired manOCA monomer. This was initially attributed to the very short reaction times. Therefore, the reactions were repeated at a higher temperature (60 °C) as reaction kinetics increase with temperature, but still no manOCA could be observed in the ^{1}H-NMR spectra (table 3.1, entries e-g).

In order to be able to extend the reaction time, the set-up was changed to a 1.6 mL reactor consisting of poly(tetrafluoroethylene) (PTFE) tubing. By again selecting the appropriate flow rates, reaction times ranging from 2 to 8 min were applied. In addition, a slight excess of diphosgene was applied, taking into account the poor results obtained in the glass microreactor. The first reactions (table 3.1, entries h-j) were conducted at room temperature to take into account the increased reactor volume and the associated increase in reaction heat being generated.[37] Despite the increased reaction time and the application of an excess of diphosgene, the NMR analyses still did not show the desired manOCA monomer.

Since the experiments so far relied on the action of less reactive diphosgene, the following syntheses looked into methods to convert diphosgene *in situ* to the more reactive phosgene. Interestingly, N,N-
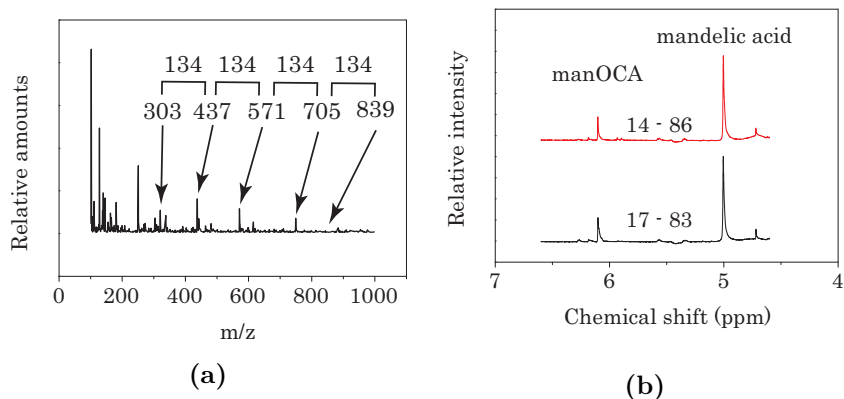
Figure 3.6: ^{1}H-NMR and mass spectroscopic evaluation of flow experiments. (a) shows the observed oligomers being formed in the conventional flow reactor. (b) shows the relative integrations of both manOCA and mandelic acid and thus visualises the degree of conversion obtained in a packed bed reactor at room temperature for a reaction time of respectively 4 (black ——) and 8 minutes (red ——).

diisopropylethylamine (DIPEA) was previously used by Fuse *et al.* to convert triphosgene *in situ* to the much more reactive phosgene to convert carboxylic acids into the corresponding acid chlorides.[34] Taking into account this information, a similar approach was applied for the synthesis of OCAs. Therefore, 7 equivalents of DIPEA were added to the mandelic acid solution (table 3.1, entries k-m). This large excess was necessary to prevent the blocking of the reactor's channels by salt precipitation due to the reaction of the excess of DIPEA with the formed hydrochloric acid.[34] For the same reason, the solvent was changed to dichloromethane (DCM) as trial experiments performed in batch revealed that the addition of DIPEA to the reaction mixture resulted in the formation of a white precipitate (DIPEA hydrochloride) when THF was used as a solvent. In contrast, DCM yielded a clear solution as expected based on the report by Fuse *et al.*[34]

The collected samples were again analysed by ^{1}H-NMR spectroscopy, but the position of the DCM signal (5.3 ppm in CDCl$_3$) prevented the determination of the conversion via ^{1}H-NMR spectroscopy (data not shown). Therefore, the samples were reanalysed via LC-MS. The mass spectra revealed that no OCA monomer was present

Table 3.1: Overview of the observed yield for the synthesis of manOCA under flow conditions for three reactor designs. †: relative to mandelic acid; *:7 equivalents of DIPEA were included.

	Reactor type	Solvent	$M_{mandelic\ acid}$ $[mol\,L^{-1}]$	Eq. diphosgene† $[-]$	Flow $[\mu L\,min^{-1}]$	t $[min]$	T $[°C]$	Yield $[\%]$
a	Glass microreactor	THF	0.56	1.2	Batch	960	RT	88
b	Glass microreactor	THF	0.2	0.5	22	0.5	40	-
c	Glass microreactor	THF	0.2	0.5	11	1	40	-
d	Glass microreactor	THF	0.2	0.5	2.2	5	40	-
e	Glass microreactor	THF	0.2	0.5	22	0.5	60	-
f	Glass microreactor	THF	0.2	0.5	11	1	60	-
g	Glass microreactor	THF	0.2	0.5	2.2	5	60	-
h	Teflon tubing	THF	0.09	0.55	800	2	RT	-
i	Teflon tubing	THF	0.09	0.55	400	4	RT	-
j	Teflon tubing	THF	0.09	0.55	200	8	RT	-
k	Teflon tubing	DCM	0.09*	0.55	800	2	RT	-
l	Teflon tubing	DCM	0.09*	0.55	400	4	RT	-
m	Teflon tubing	DCM	0.09*	0.55	200	8	RT	-
n	Packed bed reactor	THF	0.2	1	320	4	RT	17
o	Packed bed reactor	THF	0.2	1	640	8	RT	14
p	Packed bed reactor	THF	0.2	1	320	4	60	-
q	Packed bed reactor	THF	0.2	1	640	8	60	-

in the sample (figure 3.6a). Instead, the collected samples contained mandelic acid oligomers linking up to 6 mandelic acid units as indicated by the incremental increase by 134 m/z units. This result may be explained by ring-opening of manOCA by unconverted mandelic acid. However this hypothesis could not be verified given the diluted reaction conditions together with the overlap with the solvent signal in the ^{1}H-NMR spectra.

Given the large contrast between the results in batch and in the flow reactors discussed so far, a third reactor type was finally applied. A packed bed reactor was filled with activated carbon to mimic the conditions experienced in batch. By comparing the mass of the reactor prior to solvent injection with the mass of the filled reactor, the reaction volume was determined to be 5.12 mL. The flow was adjusted accordingly to result in reaction times of 4 and 8 minutes (table 3.1, entries n and o). Analysing the results via ^{1}H-NMR spectroscopy indicated that the applied conditions resulted in the formation of the desired manOCA monomer with 17% and 14% conversion for respectively 4 and 8 minutes of reaction. This is a considerable improvement to the reaction times in batch, although the obtained yields were still lower than the ones obtained in batch. Therefore, the reaction temperature was again increased to 60 °C in an attempt to increase the reactivity of the reagents (entries p and q). Unfortunately, increasing the temperature did not result in the formation of monomer. This observation may be ascribed to the inherent reactivity of OCAs.[9] The latter reactivity makes the formed monomers sensitive to ring-opening by nucleophiles e.g. unreacted mandelic acid. This hypothesis may be tested in future work by applying the packed bed reactor at reduced temperatures (e.g. 0 °C). In addition, shorter reaction times should be evaluated as the highest conversion was obtained after 4 minutes.

The results reported in entries n and o are the first report of the application of flow chemistry in the synthesis of OCAs. However, given the unsatisfactory yields obtained in these preliminary tests, the polymerisations discussed in the upcoming sections were performed using monomers that were synthesised in batch.
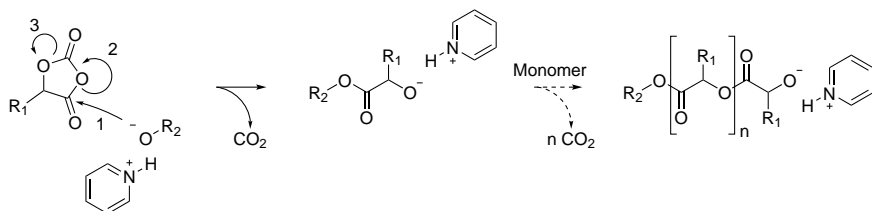
Figure 3.7: Illustration of the mechanism proposed for the nucleophilic initiation of the OCA ring-opening polymerisation catalysed by pyridine.[17]

3.3 Polymerisation of OCA monomers

Following the report by Buchard *et al.*, the manOCA monomer described in section 3.2 was subsequently applied in solution polymerisations.[17] The mechanism of these polymerisations is shown in figure 3.7. In this reaction, an alcohol initiator is activated by a base to allow the subsequent nucleophilic attack on the O-carboxy ring, which results in the expulsion of one CO_2 molecule.

The CO_2 release is one of the reasons for the inherent higher reactivity of OCA monomers compared to their lactide-based analogues (table 3.2).[9] The release of CO_2 not only prevents the reverse reaction according to Le Chatelier's principle,[40] it also reduces the entropy decrease associated with bond formation. In addition, the enthalpy change is higher for lacOCA in absolute values than for lactide, which roughly corresponds to the difference in ring strain previously reported for cycloalkanes (6.2 kcal mol^{-1} versus 0.1 kcal mol^{-1} for respectively 5- and 6-membered rings).[41] In accordance with the second law of thermodynamics, a system will behave in such a way as to reduce

Table 3.2: Comparison of the change in Gibbs free energy, reaction enthalpy and entropy between the polymerisation of lactide and lacOCA. Values reported by Thillaye Du Boullay *et al.*[9]

Monomer	ΔG_{298K} kcal mol^{-1}	ΔH_{298K} kcal mol^{-1}	ΔS_{298K} cal mol^{-1} K^{-1}
lactide	-6.1	-15.7	-32.2
lacOCA	-17.1	-19.5	-8.0

its free energy. The above mentioned enthalpic and entropic contributions thus explain the higher reactivity of OCAs (equation 3.1):

$$\Delta G = \Delta H - T\Delta S \tag{3.1}$$

In equation 3.1, ΔG represents the Gibbs free energy change of the system, ΔH the enthalpy change, ΔS the entropy change and T the temperature in Kelvin.

A similar trend is expected for manOCA, although the sterical constraints imposed by the bulky phenyl substituent will reduce the reaction rate constant compared to lacOCA.[42] The increased reactivity compared to the cyclic diesters presented in chapter 2 was therefore first confirmed by performing a kinetic study, described in the upcoming section.

3.3.1 Comparison of the polymerisation kinetics for cyclic diesters and OCAs

To study the polymerisation kinetics of manOCA, a polymerisation reaction was set up in toluene at 100 °C in order to have a valid comparison with the kinetics reported in chapter 2. The reaction medium was sampled at predetermined time points, and the collected samples subsequently analysed via both ^{1}H-NMR spectroscopy and size exclusion chromatography. Unfortunately, the signals corresponding to the α-proton in respectively monomer and polymer both lie around 6 ppm. Given the width of the polymer signal, the straightforward calculation of the monomer conversion was impeded (figure 3.8a).

Alternatively, size exclusion chromatography was a valid method to determine the evolution of the molecular weight as a function of time. As illustrated in figure 3.8b, a molecular weight of approximately 9.5 kg mol^{-1} was obtained within 10 minutes, which is a considerable improvement compared to the results presented in figure 2.14c (i.e. approx. 3.8 kg mol^{-1} after 24 hours). Moreover, dispersities around 1.1 were maintained throughout the polymerisation indicating excellent control over the molecular weight. It should be noted that the monomer to initiator ratio was set at 100, which should yield an average molecular weight of 13.4 kg mol^{-1}.

(a)

(b)
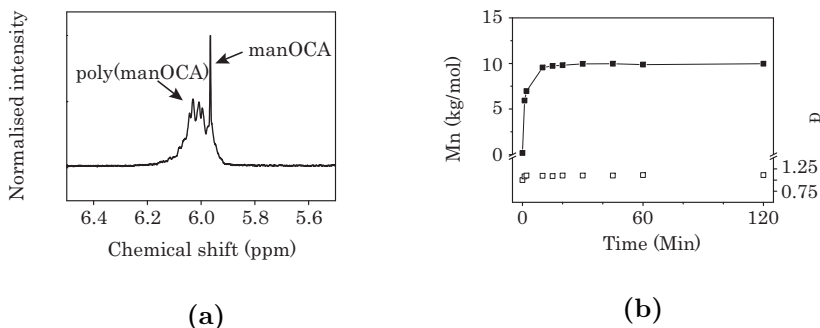
Figure 3.8: ^{1}H-NMR and mass spectroscopic evaluation of flow experiments. (a) shows the observed oligomers being formed in the conventional flow reactor. (a) shows the the overlapping monomer and polymer signals observed in the ^{1}H-NMR spectra (20 minutes reaction time); (a) shows the molecular weight (■) evolution observed for the polymerisation of manOCA as determined via SEC. Low dispersities (□) around 1.1 are maintained throughout the polymerisation.

The lower than expected molecular weight may thus indicate the presence of adventitious initiator, despite the drying procedures performed on all reagents/solvents (see materials & methods, appendix A). The observed discrepancy between the obtained and targeted molecular weight will be further covered in section 3.3.3.

3.3.2   (Co)polymerisation of lacOCA and manOCA

Based on the promising preliminary results obtained in the previous section (M_n = 9.5 kg mol^{-1} after 10 min), a number of copolymerisations of manOCA and lacOCA were initiated (table 3.3). Like the kinetic study, these polymerisations were performed at 100 °C in toluene in order to ensure a valid comparison with the mandelide-based materials discussed in chapter 2. Although the dispersities remained low, the results ($M_n^{Exp.}$) showed a much larger deviation from the expected molecular weight ($M_n^{Targ.}$) when lacOCA was added to the monomer feed (entries b-e). The latter issue is even more predominant in polymerisations aiming at higher molecular weights (entries f-h) and will be further investigated in section 3.3.3.

Table 3.3: Overview of the molecular weights obtained for (co)polymers of manOCA (man) and lacOCA (lac) obtained by solution polymerisation in toluene at 100 °C ($M_n^{Exp.}$) compared to the expected values ($M_n^{Targ.}$). Pyridine and neohexanol were applied as catalyst and initiator, respectively.

	Reaction mixture [man]/[lac]/[C]/[I]	Conc. [mol L^{-1}]	$M_n^{Targ.}$ [kg mol^{-1}]	$M_n^{Exp.}$ [kg mol^{-1}]	Đ [-]
a	100/0/1/1	2	13.4	10.3	1.09
b	75/25/1/1	2	11.9	5.3	1.16
c	50/50/1/1	2	10.3	3.2	1.05
d	25/75/1/1	2	8.8	-	-
e	0/100/1/1	2	7.2	4.0	1.05
f	375/125/1/1	2	43.0	1.6	1.03
g	250/250/1/1	2	51.5	1.9	1.11
h	125/375/1/1	2	59.3	2.5	1.15

Despite the lower molecular weights obtained for the copolymerisations with lacOCA, the synthesised copolymers were characterised physicochemically. First, the composition of the monomer feed was compared to the composition of the resulting polymers via ^{1}H-NMR spectroscopy. The obtained NMR-spectra are shown in figure 3.9 and reveal that the composition of the polymers closely corresponded with the monomer feed. Together with the single peaks observed in the SEC traces, this demonstrates the potential to copolymerise lacOCA and manOCA.

Next, the copolymers described in table 3.3 were subjected to thermogravimetric analyses. This was done in order to determine the materials' thermal stability which is of great importance in terms of subsequent polymer processing. The thermal degradation onset temperature can be seen as the upper limit for material processing. The obtained TGA curves are shown in figure 3.10. When comparing the obtained results for the copolymers with their monomer feed composition, no clear trend could be observed (table 3.4). This was expected given the fact that both monomers are linked via ester bonds. In addition, the results are very similar to the values reported in table 2.5, as the polymerisation of OCA monomers results in structurally similar copolymers as the ring-opening of cyclic diesters. As shown in
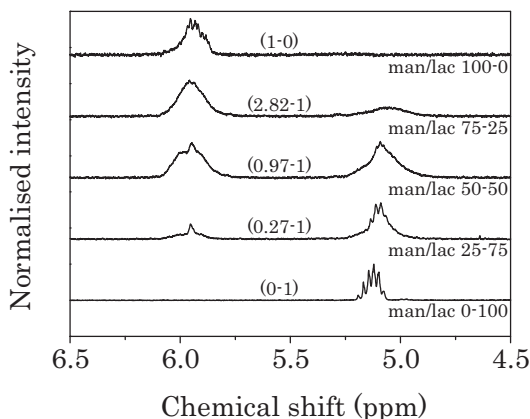
Figure 3.9: Zoom on the relevant part of the ^{1}H-NMR spectra for the copolymers of manOCA (M) and lacOCA (L). The relative integrations of both methine protons are shown between brackets.

figure 3.10, incorporating additional manOCA in the copolymer resulted in an increasing amount of residue at 400 °C, which can be attributed to char formation by the aromatic fraction.[43–45] Upon further increasing the temperature, the observed residue further degraded with residues at 750 °C being below 3% for all materials. The observed onset points for thermal degradation are lower than those published for high molecular weight PLA (approx. 330 °C) and poly(mandelic acid) (320 °C), although the latter used a higher heating rate (40 °C min^{-1}) which influences the result.[46,47] This is rationalised by the lower molecular weight which facilitates the diffusion of formed low molecular weight degradation products from the materials. This is consistent with the higher thermal stability compared to previous reports on low-molecular weight poly(mandelic acid) ($T_{\text{onset degr.}} \approx 205$ °C for $M_{\text{n}} < 4 \, \text{kg mol}^{-1}$).[7]

Differential scanning calorimetry was subsequently performed on the above-mentioned samples. DSC allows the determination of the glass transition temperature and, for semi-crystalline polymers, the melting temperature and corresponding degree of crystallinity. As was discussed previously, mandelic acid was selected as an interesting building block as the bulky phenyl substituent yields polymers with
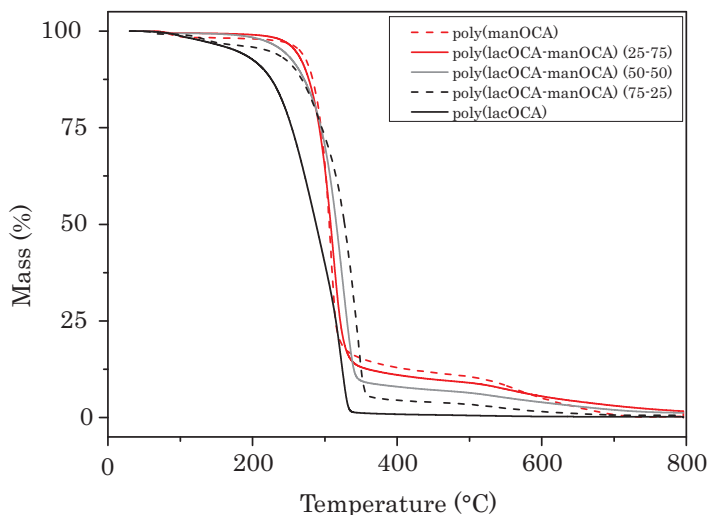
Figure 3.10: Results obtained via thermogravimetric analysis of selected OCA-based copolymers.

an increased rigidity as compared to e.g. poly(lactic acid) with its smaller methyl side group.

When evaluating the obtained results, the materials were shown to be amorphous with no crystallisation or melting transitions being observed in the DSC thermograms (figure 3.11a). This is important given the intended optical application (i.e. an SPR-based sensor), as crystalline domains scatter the incident light thereby reducing the amount of light able to reach the metal layer and subsequently be reflected towards the detector.[48]

As anticipated for the relatively low molecular weights (table 3.3), the in figure 3.11a observed glass transition temperatures were about 10-20 °C lower than values previously reported for higher molecular weights (> 16.5 kg mol^{-1}).[9,17,47,49] One of the objectives of the current PhD thesis was the development of copolymers that exhibit a higher T_g than PLA in order to prevent deformation of the sensor chip during manipulations (e.g. inserting the chip in the read out module) at elevated temperatures. Taking into account the obtained

Table 3.4: Results obtained through thermogravimetric analysis of selected OCA-based copolymers.

Material	T_{onset} [°C]	Residue$_{750\,°C}$ [%]
poly(lacOCA)	269	0.2
poly(lacOCA-manOCA) (75-25)	305	0.6
poly(lacOCA-manOCA) (50-50)	288	1.4
poly(lacOCA-manOCA) (25-75)	264	2.3
poly(manOCA)	291	0.2

molecular weights, adding 75% manOCA to the monomer feed results in a T_g in excess of 60 °C, thereby meeting the preset goal.

The Fox equation correlates the T_g of a copolymer to the mass fraction (w_1 and w_2) of both constituting monomers in the polymer and the glass transition of the corresponding homopolymers ($T_{g,1}$ and $T_{g,2}$) (equation 3.2).[50]

$$\frac{1}{T_g} = \frac{w_1}{T_g,1} + \frac{w_2}{T_g,2} \tag{3.2}$$

When fitting the results with the Fox equation, a close correspondence ($R^2=0.985$) with the values predicted by the Fox equation can be observed (figure 3.11b). The Fox equation only holds for copolymers starting from monomers that have a similar molecular weight and comparable changes in molar heat capacity when passing through the glass transition.[51] In this respect the Fox equation is a simplified expression of the relation derived by Couchman and Karasz.[52] Deviations from the Fox equation, can thus be attributed to favourable (positive deviation) or unfavourable (negative deviation) interactions between both monomers.[53] However, given the almost perfect fit only small interactions are expected. Since it was observed that the polymer composition closely matches the monomer feed (figure 3.9), the minimal amount of manOCA required to obtain a $T_g >$ 60 °C can be derived from equation 3.2. When the T_g values for high molecular weight poly(lacOCA)(i.e. 30-50 °C, > 22 kg mol^{-1}) and poly(manOCA) (i.e. 100 °C, 68 kg mol^{-1}) are entered, the monomer

Table 3.5: T_g values obtained through differential scanning calorimetry on selected OCA-based copolymers. The experimental results are compared to the theoretical values based on the T_g of both homopolymers following equation 3.2.

Material	$T_g{}^{Exp}$ [°C]	$T_g{}^{Fox}$ [°C]
poly(lacOCA)	19.9	19.9
poly(lacOCA-manOCA) (75-25)	37.5	35.2
poly(lacOCA-manOCA) (50-50)	48.3	53.0
poly(lacOCA-manOCA) (25-75)	62.2	66.8
poly(manOCA)	79.8	79.8

(a)

(b)
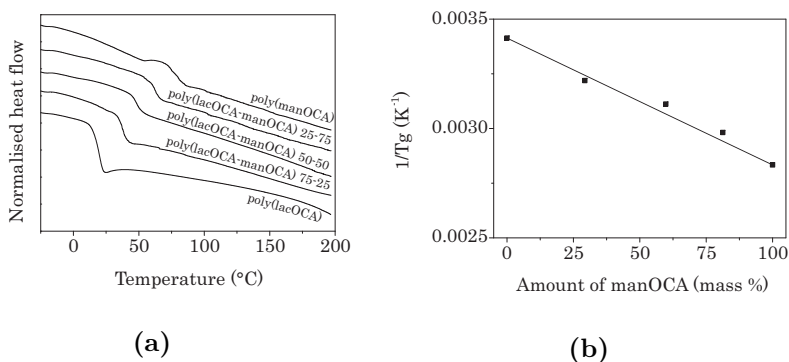
Figure 3.11: Overview of DSC results for selected OCA copolymers. (a) plot showing the normalised heat flow as a function of temperature for (co)polymers with increasing lacOCA content (top to bottom). The measured glass transitions (■) are fitted (black line, R^2=0.985) with the Fox equation (mass %) in b.

feed should contain at least 55% manOCA to result in a T_g exceeding 60 °C.

As already mentioned in chapter 1, SPR sensors rely on the total internal reflection of polarised laser light on the metal-coated prism base. As shown in chapter 2, it is important to know the materials' RI value in order to enable the proper alignment of the optical instrumentation with respect to the sensor chip following Snell's law (equation 1.4, chapter 1). Moreover, the prism RI will determine at

which angle the SPR-condition is fullfilled according to equation 1.7 (chapter 1) Therefore, the refractive indices were also determined for the OCA-based materials. The refractive indices were shown to increase as more manOCA was incorporated in the polymers (figure 3.12). The RI value varied from 1.456 for poly(lacOCA) to 1.571 for poly(manOCA). As expected, the results (figure 3.12) are very similar to the ones reported in the previous chapter (figure 2.20) illustrating increasing RI values as more aromatic side groups are introduced in the material.[54,55] Moreover, the observed linear correlation between RI and polymer composition offers an additional confirmation of both monomers being incorporated in the polymer, as already shown via ^{1}H-NMR spectroscopy (figure 3.9).

RI values again decreased for increasing temperatures as rationalised by the materials' thermal expansion.[56] It should be noted that when the glass transition temperature is surpassed, the effect of thermal expansion on the material's refractive index increases as the thermal expansion coefficient is higher for materials in the rubbery state.[56] However, the obtained results do not show a correlation with the above-mentioned glass transition temperatures, which can be attributed to the low molecular weight of the materials. Previous research on polystyrene has shown that the influence of temperature on the refractive index is less obvious for low molecular weight polymers ($M_n < 24 \, \mathrm{kg \, mol^{-1}}$).[56] Figures 3.12b-3.12f show the dispersion curves obtained for the (co)polymers by determining the RI value at the refractometer's eight available wavelengths (see materials and methods, appendix A). As was observed for the lactide-based copolymers a limited influence ($< 1.7\%$) is observed with higher wavelengths corresponding to lower RI values. The latter effect would not result in considerable reduction in sensor performance as was shown in chapter 2 (table 2.7).

(a)

(b) poly(lacOCA)

(c) poly(lacOCA-manOCA)
75-25

(d) poly(lacOCA-manOCA)
50-50

(e) poly(lacOCA-manOCA)
25-75

(f) poly(manOCA)
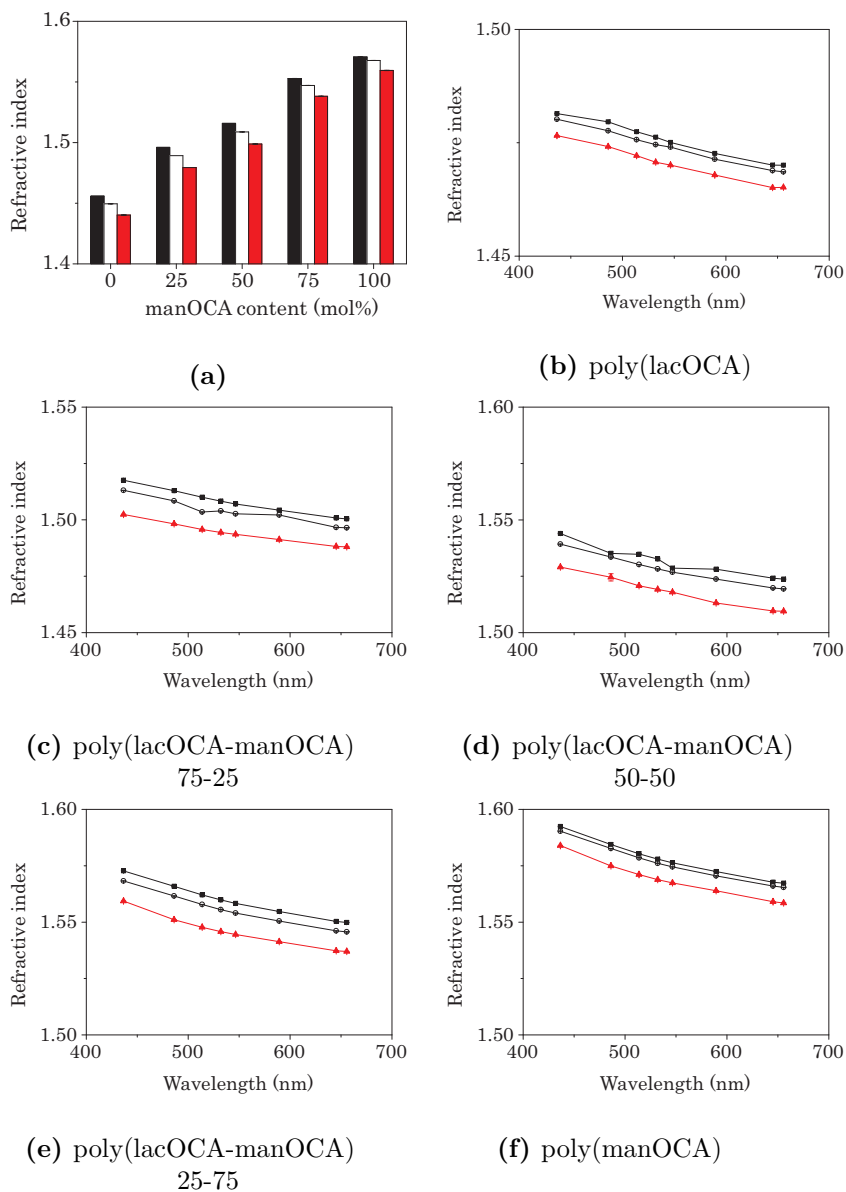
Figure 3.12: Figure (a) shows the refractive indices (RI) measured at 589 nm for the studied (co)polymers as a function of mandelide content, performed at three temperatures: 25 °C (black bars), 37 °C (white bars) and 60 °C (red bars). Figures (b-f) show the obtained dispersion curves for the various copolymers at the above-mentioned temperatures: 25 °C (black ■), 37 °C (○) and 60 °C (red ▲)

Table 3.6: Overview of the molecular weights obtained for homopolymers synthesised via solution polymerisation in toluene at 100 °C. Pyridine and neohexanol were applied as catalyst and initiator respectively.

	Monomer ratio [man/lac]	Conc. [$\mathrm{mol\,L^{-1}}$]	$M_n{}^{\mathrm{Targ.}}$ [$\mathrm{kg\,mol^{-1}}$]	$M_n{}^{\mathrm{Exp.}}$ [$\mathrm{kg\,mol^{-1}}$]	Đ [-]
a	0/100	2	7.2	1.4	1.01
b	0/100	2	36.0	-	-
c	100/0	2	13.4	4.3	1.20
d	100/0	2	67.0	10.1	1.20
e	0/100	1	7.2	-	-
f	100/0	1	13.4	4.9	1.25
g	0/100	1	36.0	-	-
h	100/0	1	56.0	3.8	1.04

3.3.3   Study with the aim to increase the polymer molecular weight

Following the low M_n values obtained for the copolymers of lacOCA and manOCA, additional homopolymerisations were performed following the conditions applied in section 3.3.2. Unfortunately, the results were far from reproducible with obtained molecular weights being limited to about 25-35% of the target value (table 3.6). Even more troubling was the fact that homopolymerisations of lacOCA did not always yield polymer ($M_n < 2$ $\mathrm{kg\,mol^{-1}}$). The reason for these unsatisfactory results will be discussed later in this section after comparing the obtained results to the previous reports on the application of OCA monomers.

The above-mentioned results are in contrast with the report from Thillaye du Boullay *et al.*[9] Although this paper shows that the degree of polymerisation determined via ^{1}H-NMR spectroscopy closely matched the target value, the obtained molecular weights were systematically higher than expected, although the authors did not address this issue. Other reports on the use of lacOCA, refer to lower than expected molecular weights being obtained.[14,16] Monomer-to-initiator ratios as high as 1200 were applied to achieve a degree of polymerisation of 500. The latter report thus seemingly corresponds

better to the observations made in the present work for the polymerisation of lacOCA.

Similar observations have already been made for other OCA-monomers. For example, a maleic acid OCA-derivative resulted in good correspondence with the target molecular weight at low monomer to initiator ratios (maximum 50/1).[11] For higher molecular weights, a considerable mismatch was again observed with polymers exhibiting a molecular weight that was 50% lower than expected based on the relative amounts of initiator and monomer. Finally, Cohen-Arazi *et al.* synthesised four different OCA-monomers from the amino acids phenylalanine, leucine, isoleucine and valine.[13] In their report, molecular weights in excess of 5 $kg\,mol^{-1}$ were only obtained for the OCA derived from phenylalanine. However, the authors of the above-mentioned papers did not look into the cause of these deviations.

Since the above-mentioned reports apply a different initiator/catalyst system, other initiator/catalyst combinations were also applied herein for the polymerisations of manOCA and lacOCA with the aim to further decrease the mismatch between the targeted and obtained molecular weights. The reaction conditions and corresponding molecular weights are listed in table 3.7. First, n-octanol was applied as a less sterically hindered initiator compared to neohexanol (entries a-e). However, similar to the previous copolymerisations (table 3.3), the molecular weights were limited to about 50% of the intended value. For the lacOCA homopolymerisation, no polymer could be precipitated. Next, the neopentanol-DMAP system was selected which is commonly applied for the polymerisation of lacOCA (entries f-i). These experiments resulted in even poorer results for the homopolymerisation of manOCA and lacOCA. Finally, the solid mandelic acid (MA)-pyridine adduct (figure 3.13) first described by Buchard *et al.*, was explored as initiator/catalyst (entry j).[17] The results were com-
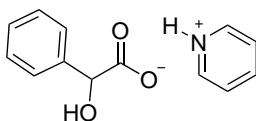
Figure 3.13: Mandelic acid-pyridine adduct proposed by Buchard *et al.* as a suitable initiator for the polymerisation of manOCA.[17]

Table 3.7: Comparison between the target and obtained molecular weight for OCA-based materials polymerised at 100 °C in toluene.

Entry	Reaction mixture [man]/[lac]/[C]/[I]	Init.	Cat.	Conc. [mol L^{-1}]	$M_n^{\text{Targ.}}$ [kg mol^{-1}]	$M_n^{\text{Exp.}}$ [kg mol^{-1}]	Đ [-]
a	100/0/1/1	n-octanol	pyridine	1	13.4	6.5	1.17
b	75/25/1/1	n-octanol	pyridine	1	11.9	4.0	1.07
c	50/50/1/1	n-octanol	pyridine	1	10.3	3.6	1.02
d	25/75/1/1	n-octanol	pyridine	1	8.6	4.1	1.02
e	0/100/1/1	n-octanol	pyridine	1	7.2	-	-
f	100/0/1/1	neopentanol	DMAP	1	13.4	1.9	1.21
g	100/0/1/1	neopentanol	DMAP	2	13.4	3.7	1.22
h	0/100/1/1	neopentanol	DMAP	2	7.2	1.5	1.02
i	500/0/1/1	neopentanol	DMAP	2	67.0	3.3	1.30
j	100/0/1/1	MA-pyridine adduct		2	13.4	6.2	1.08

Table 3.8: Comparison between the target molecular weight of 13.4 kg mol^{-1} ([M]/[C]/[I]=100/1/1) and the obtained molecular weights of poly(manOCA) synthesised at 25 °C in dichloromethane.

Entry	catalyst	Initiator	[M] [mol L^{-1}]	M$_n$$^{Exp.}$ [kg mol^{-1}]	Đ [-]
a	pyridine	neopentanol	1	5.1	1.04
b	pyridine	neopentanol	2	5.8	1.02
c	pyridine	neopentanol	4	5.2	1.04
d	MA-pyridine adduct		2	6.9	1.03
e	MA-pyridine adduct		2	7.0	1.09
f	pyridine	neohexanol	2	8.3	1.03

parable to the ones obtained at 100 °C in toluene and outperformed the results obtained under DMAP catalysis.

Given the reactivity of the OCA-monomers (section 3.3.1), the high temperature of the polymerisation was reduced to 25 °C. A series of manOCA polymerisations were conducted in dichloromethane since at 25 °C the monomers exhibit a higher solubility in DCM than in toluene (table 3.8).[17] Given the inferior results obtained for the DMAP catalyst, pyridine was applied as catalyst in combination with a neopentanol initiator at three different monomer concentrations (1-2-4 mol L^{-1}). Neopentanol was selected since it is a crystalline solid, that can be purified via sublimation in a straightforward way. These polymerisations resulted in similar molecular weights, with the polymerisation performed at a concentration of 2 mol L^{-1} resulting in almost 6 kg mol^{-1}. Next, the solid MA-pyridine adduct (figure 3.13) was applied at these reaction conditions, which resulted in a slight improvement compared to its application in toluene at 100 °C (table 3.7, entry j). Finally, the polymerisation was repeated using neohexanol as initiator, yielding a molecular weight of 8.3 kg mol^{-1} and a very low (1.01) associated dispersity. However, despite the lower reaction temperatures, the obtained molecular weights remained at least 40% lower than expected in contrast to the excellent control reported by Buchard *et al.*[17]

(a) N_2

(b) Ar

(c) Vacuum

(d) Drying pistol
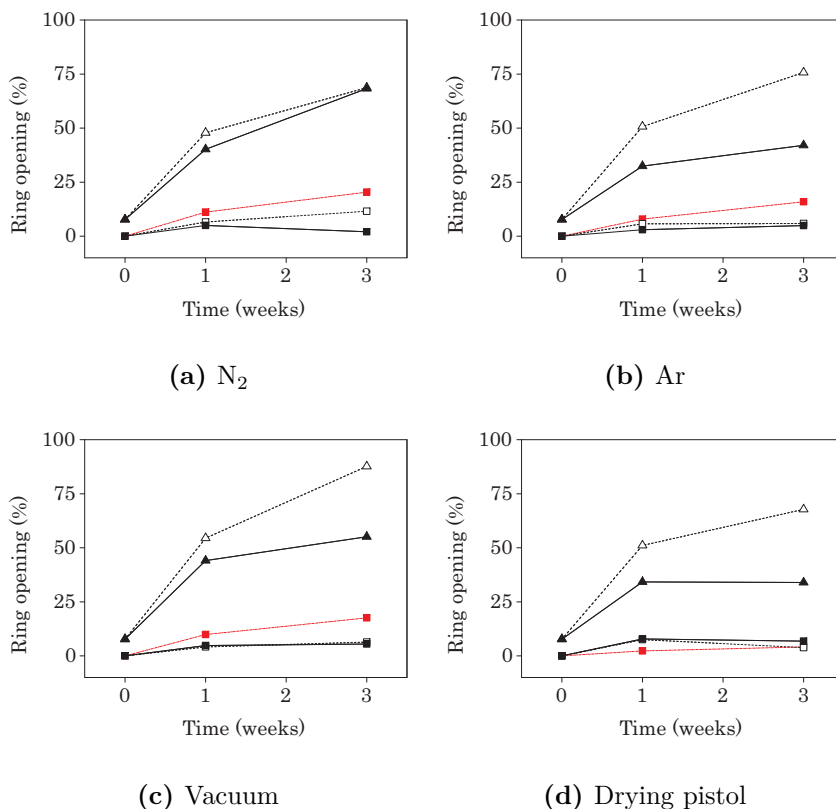
Figure 3.14: Observation of spontaneous ring opening for lacOCA (▲) and manOCA (■) at different temperatures: room temperature (red -·-), 4 °C (---) and -20 °C (black ——). Panels a, b, c and d show the results obtained when using respectively N_2, Ar, vacuum and a vacuum drying set-up containing P_2O_5.

Since the obtained molecular weights remained low irrespective of the applied reaction conditions, a stability study was performed to rule out potential monomer degradation taking place during storage. The results are shown in figure 3.14 and reveal that lacOCA is characterised by a very short shelf life in all storage conditions evaluated (N_2, Ar, vacuum and a vacuum drying set-up containing P_2O_5, at three different temperatures: -20°C, 4°C and room temperature). Moreover, the reference value obtained directly after monomer synthesis already

Table 3.9: Comparison between the target molecular weight of 13.4 $kg \, mol^{-1}$ and the obtained molecular weight of poly(manOCA) synthesised at $[M]=2 \, mol \, L^{-1}$ for the listed reaction conditions.

Entry	Initiator/catalyst	T [°C]	Solvent	$M_n^{Exp.}$ [kg mol^{-1}]	Đ [-]
a	neohexanol/pyridine	25	DCM	11.5	1.06
b	neopentanol/pyridine	25	DCM	11.5	1.08
c	neohexanol/pyridine	100	Tol.	11.2	1.07

indicated that some ring-opening had occurred (approximately 7%). The best result was found to be a vacuum drying set-up containing P_2O_5 at -20 °C for which only 18% monomer degradation was observed after 16 weeks of storage. All other samples showed that more than 50% of the monomer had reverted to lactic acid after 3 weeks. These results stand in contrast to the stability of manOCA for which most storage conditions revealed that more than 85% monomer was still unaffected after 16 weeks.

The observed spontaneous ring-opening thus provides an explanation for the inferior molecular weights of the polymers discussed in the previous paragraphs. Although the monomers were never stored for multiple weeks, special care should be taken as 1% degradation already results in a 50% decrease in molecular weight when a degree of polymerisation of 100 is targeted. Since lacOCA is more susceptible to this effect, this explains why the discrepancy between the obtained and targeted molecular weight is particularly apparent for (co)polymers of lac(OCA).

In order to obtain the best possible results, polymerisations should thus directly follow monomer synthesis. This is an important implication towards potential scale-up and industrialisation as monomer stockpiles are difficult to maintain for extended periods of time.

Putting the above-mentioned insights into practice, a fresh batch of manOCA was synthesised, dried *in vacuo* and immediately applied as starting material in polymerisations. Table 3.9 compares the obtained molecular weight with the target value and reveals a better correlation with the target molecular weight for both neopentanol as well as neohexanol initiation. Entry c (table 3.9) also shows that

immediately polymerising the formed monomer at 100 °C in toluene, allows to surpass the initial success observed in the kinetic study at these conditions. The adventitious initiator mentioned in section 3.3.1, was thus likely the result of spontaneous ring-opening of the monomer, which introduced additional alcohol functional groups in the polymerisation medium. The results obtained for freshly prepared monomers are comparable to the state-of-the-art in terms of deviation from the expected molecular weight.[17]

3.4   Conclusions

As indicated in the introduction, the current chapter focused on the application of O-carboxy anhydrides as an alternative for the cyclic diesters discussed in chapter 2.

OCA derivatives of both mandelic as well as lactic acid were successfully synthesised in batch. The yield of the mandelic acid-derived OCA (manOCA) was far superior to the yield obtained for meso-mandelide, while the yield of the lactic acid equivalent (lacOCA) was in accordance with the available literature. Given the high toxicity of the required diphosgene, continuous flow chemistry was for the first time explored as a safer method for the synthesis of OCAs. At present, the obtained yields in these initial flow experiments remain substantially lower than the ones achieved in batch. Since the yield again decreased by increasing the reaction time from 4 min to 8 min, it is likely that the longer residence time at the elevated reactor temperature results in ring-opening of the formed monomer. Future work may further increase the obtained yields by varying parameters including the reactor temperature, the reagent concentration, the number of equivalents of diphosgene applied. In addition, changes in the experimental setup (e.g. the application of static mixing units) may be explored.

Keeping in mind the aim to develop degradable, amorphous polyesters with a T_g above 60 °C, lacOCA and manOCA were for the first time copolymerised. As demonstrated, the higher reactivity of the above-mentioned OCA-monomers, allowed the polymerisations to be performed under mild reaction conditions using pyridine as catalyst in contrast to the higher reaction temperatures (100 °C) applied

in chapter 2. The same inherent reactivity, however, resulted in a large discrepancy between the achieved and the targeted molecular weights, since spontaneous ring-opening was observed irrespective of the applied storage conditions. This observation explained the lower than expected molecular weights for lacOCA-based polymers. For poly(mandelic acid) homopolymers on the other hand, satisfactory control over the molecular weight could be achieved when freshly prepared monomers were applied. In this regard, the manOCA monomer was shown to be far superior to the previously discussed meso-mandelide, as polymers of the latter building block were limited to approx. 25% of the target molecular weight (chapter 2).

The observed linear correlation between T_g and manOCA content was considered promising. However, given relatively low molecular weights obtained, the T_g values are approximately 10-20 °C lower than expected based on previous reports covering high molecular weight PLA and poly(mandelic acid). Besides T_g values, thermal stabilities and refractive indices were almost identical to the values obtained earlier for lactide-based polymers, as anticipated given the fact that both monomer families yield structurally similar polymers.

As was the case in chapter 2, future work should focus on further increasing the molecular weights to allow the implementation of the developed materials for the fabrication of disposable microfluidics. As was shown, the observed discrepancy between the targeted and obtained molecular weights could be greatly reduced by applying freshly prepared manOCA. By applying the same principle to lacOCA, it is expected that the obtained molecular weights can be increased for both lacOCA homopolymers as well as for copolymers with manOCA. Once this hurdle is overcome, the optical performance and the processability of the materials should be further studied. In addition, the upscaling of the polymer synthesis allows the fabrication of test samples that can be applied in thorough degradation studies to evaluate the degradability of these (co)polymers under various conditions.

References

[1] B. Martin Vaca, D. Bourissou, *ACS Macro Letters* **2015**, 792–798.

[2] W. H. Davies, *Journal of the Chemical Society (Resumed)* **1951**, 1357.

[3] J. S. Smith, B. J. Tighe, *Chemischer Informationsdienst* **1973**, *4*, 695–696.

[4] I. J. Smith, B. J. Tighe, *British Polymer Journal* **1975**, *7*, 349–360.

[5] I. J. Smith, B. J. Tighe, *Journal of Polymer Science: Polymer Chemistry Edition* **1976**, *14*, 949–960.

[6] I. J. Smith, B. J. Tighe, *Journal of Polymer Science: Polymer Chemistry Edition* **1976**, *14*, 2293–2305.

[7] I. J. Smith, B. J. Tighe, *Macromol. Chem.* **1981**, *182*, 313–324.

[8] H. R. Kricheldorf, J. M. Jonté, *Polymer Bulletin* **1983**, *9*, 276–283.

[9] O. Thillaye Du Boullay, E. Marchal, B. Martin-Vaca, F. P. Cossío, D. Bourissou, *Journal of the American Chemical Society* **2006**, *128*, 16442–16443.

[10] O. Thillaye du Boullay, C. Bonduelle, B. Martin-Vaca, D. Bourissou, *Chemical communications (Cambridge England)* **2008**, 1786–1788.

[11] R. J. Pounder, D. J. Fox, I. A. Barker, M. J. Bennison, A. P. Dove, R. Jerome, C. Jerome, P. Dubois, *Polymer Chemistry* **2011**, *2*, 2204–2212.

[12] Y. Lu, L. Yin, Y. Zhang, Z. Zhang, Y. Xu, R. Tong, J. Cheng, *ACS Macro Letters* **2012**, *1*, 441–444.

[13] N. Cohen-Arazi, A. J. Domb, J. Katzhendler, *Macromolecular Bioscience* **2013**, *13*, 2306–2315.

[14] Z. He, L. Jiang, Y. Chuan, H. Li, M. Yuan, *Molecules* **2013**, *18*, 12768–12776.

[15] Q. Yin, R. Tong, Y. Xu, K. Baek, L. W. Dobrucki, T. M. Fan, J. Cheng, *Biomacromolecules* **2013**, *14*, 920–929.

[16] M. Yuan, Z. He, H. Li, L. Jiang, M. Yuan, *Polymer Bulletin* **2014**, *71*, 1331–1347.

[17] A. Buchard, D. R. Carbery, M. G. Davidson, P. K. Ivanova, B. J. Jeffery, G. I. Kociok-Köhn, J. P. Lowe, *Angewandte Chemie* **2014**, *126*, 14078–14081.

[18] E. Peggion, M. Terbojevich, A. Cosani, C. Colombini, *Journal of the American Chemical Society* **1966**, *88*, 3630–3632.

[19] W. H. Daly, D. Poché, *Tetrahedron Letters* **1988**, *29*, 5859–5862.

[20] L. Dekie, V. Toncheva, P. Dubruel, E. H. Schacht, L. Barrett, L. W. Seymour, *Journal of Controlled Release* **2000**, *65*, 187–202.

[21] J. R. Hernández, H.-A. Klok, *Journal of Polymer Science Part A: Polymer Chemistry* **2003**, *41*, 1167–1187.

[22] K. Koga, A. Sudo, H. Nishida, T. Endo, *Journal of Polymer Science Part A: Polymer Chemistry* **2009**, *47*, 3839–3844.

[23] J. Cheng, T. J. Deming, *Top Curr Chem* **2011**, 1–26.

[24] H. Lu, J. Wang, Z. Song, L. Yin, Y. Zhang, H. Tang, C. Tu, Y. Lin, J. Cheng, N. Nishiyama, K. Kataoka, H. Nakahama, Y. Matsumura, A. I. Daud, *Chem. Commun.* **2014**, *50*, 139–155.

[25] B. Jugg, F. Aspects in *Chemical Warfare Toxicology: Volume 1: Fundamental Aspects*, *Vol. 1*, The Royal Society of Chemistry, **2016**, pp. 117–153.

[26] L. Pasquato, G. Modena, L. Cotarca, P. Delogu, S. Mantovani, *Journal of Organic Chemistry* **2000**, *65*, 8224–8228.

[27] L. Cotarca, H. Eckert in *Phosgenations - A Handbook*, Wiley-VCH Verlag GmbH and Co. KGaA, Weinheim, FRG, **2005**, pp. 3–31.

[28] P. Tundo, F. Aricò, A. E. Rosamilia, S. Grego, L. Rossi in *Green Chemical Reactions*, Springer Netherlands, Dordrecht, **2008**, pp. 213–232.

[29] L. N. Protasova, M. Bulut, D. Ormerod, A. Buekenhoudt, J. Berton, C. V. Stevens, *Organic Process Research and Development* **2013**, *17*, 760–791.

[30] F. E. A. Van Waes, S. Seghers, W. Dermaut, B. Cappuyns, C. V. Stevens, *Journal of Flow Chemistry* **2014**, *4*, 118–124.

[31] T. S. A. Heugebaert, C. V. Stevens, C. O. Kappe, *ChemSusChem* **2015**, *8*, 1648–1651.

[32] S. Seghers, F. E. Van Waes, A. Cukalovic, J.-C. M. Monbaliu, J. D. Visscher, J. W. Thybaut, T. S. Heugebaert, C. V. Stevens, *Journal of Flow Chemistry* **2015**, *5*, 220–227.

[33] T. S. Heugebaert, B. I. Roman, A. De Blieck, C. V. Stevens, DOI 10.1016/j.tetlet.2010.06.004.

[34] S. Fuse, N. Tanabe, T. Takahashi, *Chemical Communications* **2011**, *47*, 12661–12663.

[35] F. E. A. Van Waes, J. Drabowicz, A. Cukalovic, C. V. Stevens, *Green Chemistry* **2012**, *14*, 2776.

[36] M. Movsisyan, E. I. P. Delbeke, J. K. E. T. Berton, C. Battilocchio, S. V. Ley, C. V. Stevens, P. Camus, S. Hattou, C. Guermeur, S. J. Taylor, Y. Xiang, J. Young, *Chem. Soc. Rev.* **2016**, *45*, 4892–4928.

[37] B. K. Singh, C. V. Stevens, D. R. Acke, V. S. Parmar, E. V. Van der Eycken, DOI 10.1016/j.tetlet.2008.09.159.

[38] Chemtrix BV, *LABTRIX*, **2017**, `http://www.chemtrix.com/img/downloads/CHE_Leaflet-LABTRIX.pdf(accessed2017-07-19)`.

[39] Syrris Ltd, *Asia Solid Phase (Column) Reactors - Asia Flow Chemistry Modules - Syrris*, **2017**, `http://syrris.com/flow-products/asia-modules/asia-solid-phase-reactors`.

[40] H. L. Le Chatelier, *Comptes rendus hebdomadaires des séances de l'Académie des sciences* **1884**, *99*, 786–789.

[41] E. V. Anslyn, D. A. Dougherty, *Modern physical organic chemistry*, University Science, **2006**, p. 1099.

[42] D. F. DeTar, S. Binzet, P. Darba, *The Journal of Organic Chemistry* **1987**, *52*, 2074–2082.

[43] G. Montaudo, C. Puglisi, R. Rapisardi, F. Samperi, *Polymer Degradation and Stability* **1991**, *31*, 229–246.

[44] F. Kakali, J. K. Kallitsis, *Macromolecules* **1996**, *29*, 4759–4763.

[45] C. L. Beyler, M. M. Hirschler, *SPE Handbook of Fire Protection Engineering* **2001**, 110–131.

[46] C. C. Chen, J. Y. Chueh, H. Tseng, H. M. Huang, S. Y. Lee, *Biomaterials* **2003**, *24*, 1167–1173.

[47] T. Liu, T. L. Simmons, D. A. Bohnsack, M. E. Mackay, M. R. Smith, G. L. Baker, E. Lansing, *Macromolecules* **2007**, *40*, 6040–6047.

[48] C. F. Bohren, D. R. Huffman in *Absorption and Scattering of Light by Small Particles*, Wiley-VCH Verlag GmbH, **2007**, pp. 1–11.

[49] K. Jamshidi, S.-H. Hyon, Y. Ikada, *Polymer* **1988**, *29*, 2229–2234.

[50] T. G. Fox, *The Bulletin of the American Physical Society* **1956**, *1*, 123–132.

[51] W. Brostow, R. Chiu, I. M. Kalogeras, A. Vassilikou-Dova, *Materials Letters* **2008**, *62*, 3152–3155.

[52] P. R. Couchman, F. E. Karasz, *Macromolecules* **1978**, *11*, 117–119.

[53] A. Kulshreshtha, C. Vasile, *Handbook of Polymer Blends and Composites, Volume 3*, Rapra Technology, **2002**, pp. 390–393.

[54] W. Groh, A. Zimmermann, *Macromolecules* **1991**, *24*, 6660–6663.

[55] H. K. Shobha, H. Johnson, M. Sankarapandian, Y. S. Kim, P. Rangarajan, D. G. Baird, J. E. McGrath, *Journal of Polymer Science Part A: Polymer Chemistry* **2001**, *39*, 2904–2910.

[56] R. Moshrefzadeh, M. Radcliffe, T. Lee, S. Mohapatra, *Journal of Lightwave Technology* **1992**, *10*, 420–425.

Chapter 4

Surface modification strategies towards selective *E.coli* sensors

"We live beneath many layers. Some are for our protection, and some are for our control."

— Russel Eric Dobda

4.1 Introduction

So far the presented results focused on the development of materials that could be applied as sensor substrate, *i.e.* as main constituent of the microfluidic chip. However, in order to obtain SPR-based sensors, the interface with the sample of interest is equally important.

A first prerequisite to enable SPR sensing consists of the deposition of a thin metal layer (typically around 50 nm) on a glass or plastic prism to allow the excitation of surface plasmon polaritons (SPPs). With respect to SPR-based sensing, the most commonly applied metals are gold and, to a lesser extent, silver.[1,2] Gold owes

The silver deposition discussed in this chapter was performed by dr. Davy Deduytsche. XPS and some AFM experiments were performed by drs. Lara Misseeuw, dr. Myriam Gómez Tardajos, drs. Liesbeth Tytgat or Ms Julie Verdood, but were processed and analysed by the candidate.

Table 4.1: Comparison between gold and silver with respect to SPR-based sensing. Both reflectivity as well as the refractive index are reported for the wavelength that will be applied in the laboratory demonstrator.

	Au	Ag
Reflectivity (661 nm)[16]	97.161%	99.023%
Refractive index (661 nm)[16]	0.117160	0.053297
SPP penetration depth[1]	162 nm	219 nm
Chemical stability[7,10]	Stable	Tarnishes
Surface modification[3,4]	Well established	Troublesome
Cost[17]	€ 34189.12 kg^{-1}	€ 439.62 kg^{-1}

its privileged position to its high chemical stability and relatively straightforward surface modification (e.g. self-assembled monolayers of thiols).[3,4] Silver on the other hand, is more cost effective and is characterised by its superior reflectivity in the visible and near infrared range.[5] Previous reports in literature and simulations performed within the B-PHOT group have already demonstrated that the sensitivity of SPR-based sensors could be improved by a factor of 1.5 by shifting from gold to silver.[6–9] Unfortunately, silver readily tarnishes, a process involving the reaction of the silver surface with atmospheric sulphur-containing compounds. This process results in the gradual darkenening of the surface, thereby reducing its optical properties.[7,10] In addition, surface modifications on silver were found to be less stable as compared to gold.[11–15] An overview of both metals' strengths and weaknesses is presented in table 4.1.

For reasons of completeness, it should be noted that SPR has also been reported for other metals (*e.g.* aluminium or copper).[10,18] However, the surface modification of these metals is troublesome and in the case of aluminium, the SPR resonance condition is fulfilled for ultraviolet light which puts extra constraints on the necessary optical instrumentation as UV light gradually ablates the surface of the CCD-cameras applied in SPR sensing.[16,19] In what follows, the focus will therefore lie on the surface modification of gold and silver.

Considering the deposition of metals on optically transparent materials, it should be noted that metals have significantly different surface properties which affects their adhesion to other substrates.[20] This
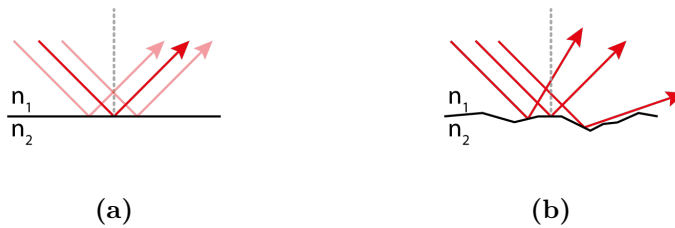
Figure 4.1: Schematic visualisation of the effect surface roughness has on reflection. For smooth surfaces (a) the photons from the incident beam are reflected in the same direction. For rough surfaces (b) diffuse reflection will be observed as each photon may reach the interface under a different angle with the normal and will therefore be reflected under a different angle.

observation is well documented for glass. To prevent the delamination of the metal layer, compatibilising layers can be applied. Indeed, the use of titanium oxide and chromium have been proposed in this context.[20] In case of polymer materials however, such compatibilising layers experience the same difficulties as the metal would.[21] Therefore, the adhesion of metal coatings on plastics is generally improved by etching the polymer surface.[22] The increased surface roughness, results in a larger contact area between metal and plastic, thereby stabilising the bonding of both layers.[23]

Bearing in mind the application of metal layers in SPR-based biosensors, the etching strategy would pose a major disadvantage. Recalling section 1.4, the sensing principle relies on the reflection of the incident light to the detector. The theoretical narrow resonance angle at which SPPs are generated, does not take into account surface roughness. Reflection occurs at the interface between two materials with different refractive indices.[24] For smooth surfaces, the angle between the incident beam and the normal will equal the angle between the normal and the reflected beam. This situation is called specular reflection (figure 4.1a). Increasing the surface roughness, however, distorts the reflection at the interface. In this situation, diffuse reflection is observed as photons interacting with the surface at different positions may have different entry angles relative to the normal (figure 4.1b). It should be clear that diffuse reflection is undesired for SPR-based sensors as the intensity of the reflected beam would

be significantly reduced, thereby lowering the sensor's sensitivity. For this reason, the surface roughness should be limited to one tenth of the wavelength of the incident light in order to deem the surface 'of optical quality'. For the envisioned laboratory demonstrator operating at 661 nm, this would imply that the surface roughness should not exceed 60 nm.

Although the application of a metal layer suffices for the excitation of SPPs, SPR-based sensing as such is not specific towards *E. coli* as only refractive index changes can be detected. In other words, recognition elements should be introduced on the metal surface to ensure the observed RI change is indeed the result of the presence of the analyte of interest. This can be achieved by depositing highly selective recognition elements on the metal surface.[2,25,26] This aspect will be discussed in section 4.3. In addition, false positive results can be reduced by passivating the surface.[27–30]

Based on the above-mentioned considerations, the current chapter will discuss the deposition of thin silver layers and their subsequent functionalisation with *E. coli*-specific antibodies. However, first the applied surface characterisation techniques are briefly introduced in the upcoming subsections.

4.1.1   Overview of surface characterisation techniques

The surface characterisation applied in the current chapter will rely on three complementary techniques to evaluate the success of the subsequent functionalisation steps. The surfaces will be analysed via atomic force microscopy (AFM), static contact angle (SCA) measurements and X-ray photoelectron spectroscopy (XPS).

Atomic force microscopy

AFM can be used to obtain high resolution (nm scale) topographical information from the surface. By bringing a probing tip mounted on a flexible cantilever into close contact with the sample surface, interaction forces (such as van der Waals interactions and electrostatic forces) will arise between the tip and the sample surface.[31] Because of these interactions, the cantilever will be attracted or repelled by the surface. Since the position of the cantilever is continuously monitored
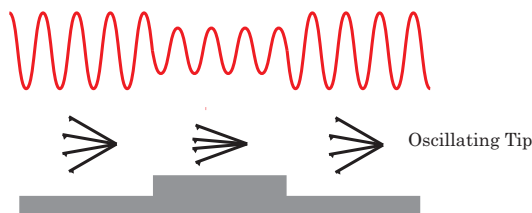
Figure 4.2: Illustration showing the principle of AFM running in tapping mode. Changes in amplitude of the tip correspond to changes in surface topology. Figure adapted from literature. [32]

via the reflection of a laser beam focused on the cantilever arm, its movements are continuously detected. By scanning the cantilever tip over the surface, the topography of the sample can be recorded (figure 4.2). The spatial resolution of the measurements is determined by the size and geometry of the applied tip. In the present work, a fine pyramidal silicon nitride tip was mounted onto a flexible cantilever.

AFM measurements can be conducted in different modes including the contact, the non-contact and the tapping mode. Given the destructive nature of the contact method and the lower lateral resolution of the non-contact method, herein the tapping mode was selected as this approach combines the high resolution of the contact mode and the non-destructive nature of the non-contact mode. [33]

Static contact angle measurements

Next, the modified surfaces were characterised via SCA measurements. When a droplet of liquid is sitting on a smooth, flat surface, an equilibrium will be reached when the net sum of the forces acting upon the droplet's surface is zero. For smooth, flat surfaces, this condition is shown in figure 4.3. At the edge of the droplet, the surface tensions between the three phases cancel out. The relationship is given by Young's equation: [34]

$$\gamma_{SG} - \gamma_{SL} - \gamma_{LG} \cos \theta_C = 0 \tag{4.1}$$

With γ_{xx}, the surface tension for each interface between the three phases (**S**olid, **L**iquid or **G**aseous) and ϑ_C being the contact angle for the observed droplet.
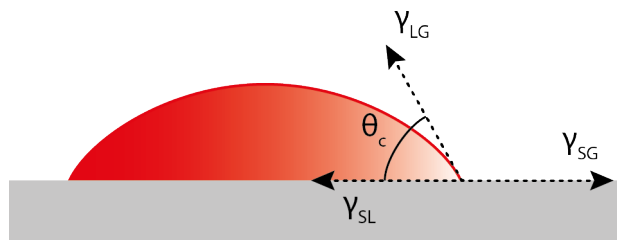
Figure 4.3: Illustration of a droplet sitting on a smooth, flat surface. At equilibrium, the surface tensions (γ) acting on the droplet's edge cancel out according to Young's equation (equation 4.1).

The wetting of the surface by the droplet is highly dependent on the interactions between the surface and the liquid. The droplet will retain its spherical shape when the interactions with other liquid molecules are favoured over interactions with the surrounding phase (e.g. oil droplets in water). On the other hand, when interactions with e.g. a solid are favoured, the system will minimise its energy by increasing the number of interactions with this solid and good wetting is observed resulting in the spreading of the droplet and therefore a lower θ_C. In case the applied liquid is water, SCA experiments thus allow the determination of the hydrophobic or hydrophilic nature of the surface.[35]

X-ray-photoelectron spectroscopy

Finally, XPS allows the determination of the atomic composition of a surface via interaction of incident X-rays with the solid sample under high vacuum conditions.[36] Typically, Mg (1253.6 eV) and Al-K$_\alpha$ (1486.6 eV) rays are used. Upon interaction with the surface, electrons from one of the inner shells or valence bands may be excited and ejected (figure 4.4). The emitted photoelectrons are detected and their number is expressed as a function of their binding energy. Based on the knowledge of the energy of the initial X-ray irradiating the surface (hν) and the detected kinetic energy of the emitted photoelectrons (E_{kin}), the binding energy ($E_{binding}$) of the latter can be calculated via:
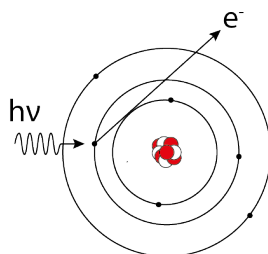
Figure 4.4: Schematic representation of the ejection of photoelectrons by incident X-rays. The energy level occupied by the electron will determine its kinetic energy thus carrying over information about the sample's atomic composition.

$$E_{binding} = E_{photon} - (E_{kinetic} + \phi) \qquad (4.2)$$

Herein, ϕ represents an instrument constant, which is determined via calibration upon installation of the device. The binding energy of an electron depends on the element from which the electron originated. The measured binding energies thus contain information about the elemental composition of the surface. Furthermore, information on the binding states of these elements, their oxidation numbers and chemical functionalities can also be deduced.[36]

4.2 Metal layers as a model for SPR sensors

As already mentioned in the introduction, a uniform metal deposition is required to obtain sensitive SPR-based biosensors.

A number of techniques exist that allow the uniform deposition of metals. Electroplating is a technique widely applied in industry to deposit metals on various substrates.[37] By running a current through an electrolyte solution containing the desired metal in solution, the metal ions will migrate towards the cathode where they are deposited as a solid metal layer. Although electroplating has been successfully applied to deposit thin films for a number of metals, the process requires that the object to be coated is conductive. Therefore, electroplating will not be applicable for the deposition of metals on glass or polymer prisms, unless a thin metal layer is applied via another
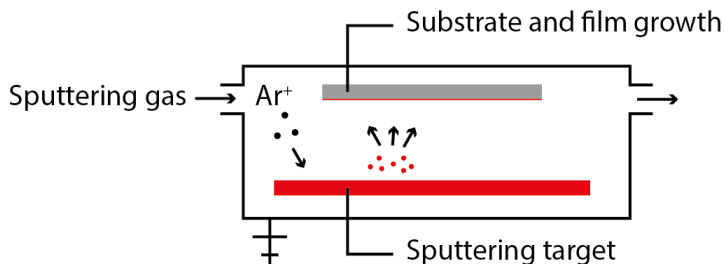
Figure 4.5: Schematic representation of the sputter deposition process. The sputter target and substrate are placed in a vacuum chamber. When the sputter gas is ionised, it is accelerated towards the sputter target which ejects particles, that are subsequently deposited onto the substrate.

technique. Moreover, since the first objective of this thesis consists of the synthesis and application of degradable (i.e. hydrolytically unstable) polyesters, this method may negatively affect the materials' properties (e.g. molecular weight).

Physical vapour deposition (PVD) may offer a viable alternative for electroplating. In this technique, the sample to be coated is placed in a high vacuum. Next, a source material is converted into a vapour by either boiling or sublimation. The vapour is subsequently transported in a straight line towards the object to be coated and condenses as a solid film on the surface. By choosing the appropriate exposure time, the thickness of the deposited metal can be controlled. Considering the thin metal films that are required for SPR-based sensing and the non-conducting nature of glass and polymer prisms, vapour deposition methods are preferred over the electroplating technique.[38] However, since gold and silver are characterised by relatively high melting points of respectively 1064 °C and 961.8 °C, simply evaporating these metals may be difficult or impossible.[38]

To circumvent this issue, sputter techniques can be applied in which a gold or silver target is bombarded with energetic ions (figure 4.5).[39] The sputtering gas is often an inert gas such as argon, which becomes ionised by applying a voltage over the substrate and the target. Next, the formed ions will be accelerated towards the target, where they may liberate target ions upon impact.[40] These target ions exhibit a relatively wide energy distribution (up to tens of eV).[41]

Two different deposition modes can be distinguished, which are dependent on the sputter gas pressure applied in the set-up. At low pressures, the sputtered ions are accelerated in straight lines towards the substrate which they will impact with higher energy.[42] This results in a high directionality of the deposition, although the energetic nature of the particles may negatively affect the substrate (e.g. by etching the substrate).[43,44] When using higher sputter gas pressures (approximately 10^{-3} mbar) on the other hand, the ionised particles will interact with the sputter gas thereby transferring (part of) their energy to the gas atoms.[45] This results in the sputtered particles exhibiting a 'random walk' towards the substrate, where they will condense. A higher pressure therefore results in milder conditions experienced by the substrate, although the deposition becomes less directional resulting in the deposition of some upright features e.g. the channel walls in microfluidics.[44] The latter implies that functionalisation of the metal would no longer be restricted to the actual sensing zone.

The above-described process can be further optimised by applying a strong magnetic field over the set-up. In this so-called magnetron sputtering, the generated ions will be concentrated near the target thereby increasing the sputter efficiency.[38]

Besides the possibility to deposit metals characterised by high melting points, sputtered layers tend to adhere better to the substrate than evaporated films.[38,46] However, some issues remain as a small mismatch in composition between target and deposited layer may exist when alloys are used as the target material. This difference can be attributed to the fact that lighter atoms will be deflected more easily than heavier ones.[47]

Based on silver's superior properties with respect to SPR-based sensing, silver was selected as starting material to further elaborate the surface chemistry. It should be noted that silver is known for its antibacterial properties, especially when considering gram negative bacteria like *E. coli*.[48] However, the effect of the silver surface on the bacteria to be detected is expected to be low given the short measurement times and the fact that surface modification was previously shown to reduce the toxicity of silver layers.[49]

Since the underlying substrate does not affect the surface modification performed on silver, homogeneous silver layers (approx. 100 nm thick) were deposited on glass slides (approx. 1 cm^2) via the above-mentioned magnetron sputter deposition technique. The layer thickness was controlled by selecting the appropriate exposure time based on calibration experiments (materials and methods, appendix A). The obtained samples were subjected to the surface modification strategy elaborated in section 4.3.3. The characterisation of the unmodified and functionalised samples is covered in section 4.4.

4.3   Surface modification of metal layers

The bare metal layers formed via magnetron sputter deposition do not possess any particular chemical handles and thus restrict the number of possible modification strategies that can be applied to immobilise biological recognition molecules. Therefore, a lot of research has been performed regarding the development of suitable surface modification strategies to functionalise metal surfaces with particular compounds that can serve as chemical handles for subsequent modifications.

4.3.1   Surface functionalisation of noble metals

With respect to the introduction of the above-mentioned chemical handles, two strategies are commonly applied. A first example consists of the formation of self-assembled monolayers via chemisorption, while another method was inspired by mussel adhesive proteins. In the upcoming sections, both strategies will be discussed in greater detail.

Self-assembled monolayers

As already mentioned earlier, gold surface chemistry with respect to SPR-based biosensing is well established. A common strategy consists of the formation of self-assembled monolayers (SAMs) of thiols on the gold surface.[2,15,50,51] As the name suggests, it suffices to simply incubate the gold surface in a thiol-containing solution.[52] The gold-sulphur bond is quite stable and has a semi-covalent character (45

kcal mol^{-1}).[11,12] This makes the sulphur-gold bond very suitable for the effective anchoring of various thiols and disulfides.[3,53–59]

Besides these sulphur-containing molecules, a number of researchers have made efforts to expand the list of available compounds. A first candidate was found in selenium-containing compounds, as selenium shares the same group with sulphur in the periodic table and thus shows similar chemical properties.[60,61]

Another possibility can be found in diazonium moieties that have been successfully applied to functionalise a number of metal surfaces including gold, platinum, palladium, ruthenium and titanium.[62–67] This strategy relies on the reductive cleaving of the diazonium-group which results in a reactive radical that subsequently enables the formation of a carbon-metal bond.

In case of silver surfaces, only a few reports can be found on the application of silver in SPR-based sensing.[6,8] However, silver nanoparticles are more frequently applied within the field of surface enhanced raman scattering, which offers additional information on suitable anchoring molecules and their stability on the Ag surface.[68–71] However, it should be noted that the behaviour of Ag nanoparticles with their many crystal facets and edges may differ from the planar silver layers to be applied in the proposed SPR-based sensors.[72,73]

Similar to gold, thiols are one of the most often used ligands for silver functionalisation.[11,74] However, due to silver's smaller atomic orbitals, the interaction with sulphur is less strong (16-20 kcal mol^{-1}), making the deposited compounds more prone to desorption.[11,14,15] In addition to thiols, nitrogen containing molecules have also been applied for silver functionalisation.[68,71]

Bioinspired polydopamine deposition

Mussels are marine organisms that are able to adhere to a wide range of surfaces. This ability is the result of the secretion of adhesion proteins that make up the bysal threads. It was found that these proteins consist largely of lysine and dihydroxy-phenylalanine amino acids. The latter molecule is also known as the anti-Parkinson drug DOPA, which is able to cross the blood brain barrier and is subsequently converted to the neurotransmitter dopamine.[75,76] With respect to coating applications, both DOPA as well as dopamine were
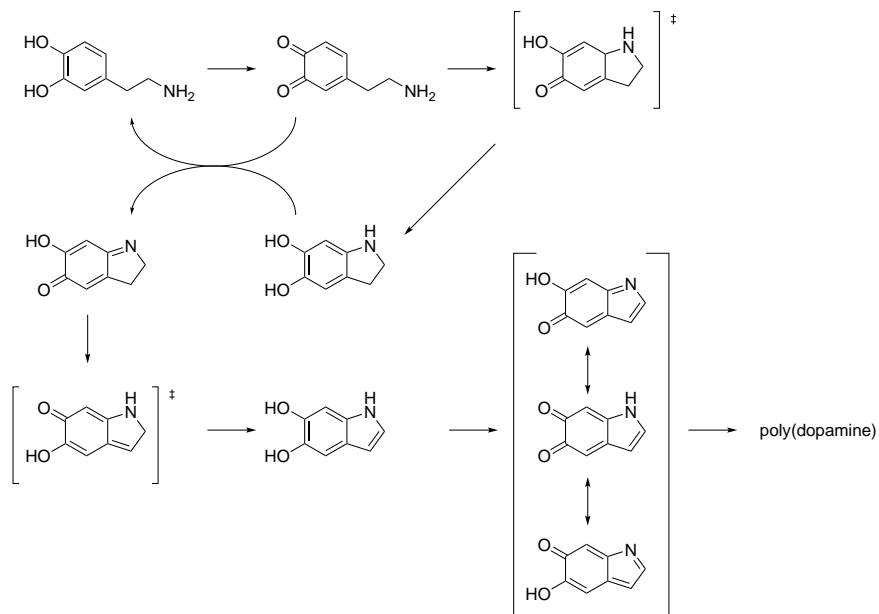
Figure 4.6: Scheme showing the conversion of dopamine to a quinone-derivative, which has been proposed to be a key intermediate in the deposition of poly(dopamine) coatings.[81]

found to be very interesting compounds to coat a wide variety of surfaces.[77–80]

The potential of these compounds arises from their spontaneous autopolymerisation under basic conditions in the presence of oxygen which results in the formation of a stable coating.[75,79,81–84] The mechanism of this reaction and the structure of the resulting poly(dopamine) (PDA), however, remain unclear.[80,85,86] Some authors claim that PDA is a supramolecular aggregate rather than an actual polymer linked via covalent bonds.[87] Other groups however proposed a polymerisation mechanism similar to the formation of melamin, the pigment responsible for the wide variety of human skin tones.[85,88] According to the latter hypothesis (figure 4.6), dopamine is first oxidised to a quinone-derivative which subsequently polymerises.

Surface modification strategies that utilise these bioinspired catechol groups have since then given a new dynamic to the field of sur-

face modification. Applications include the formation of novel adhesives,[89–91] non-fouling surfaces,[27,92–95] low-friction surfaces,[28] the immobilisation of biomolecules or the improvement of cell-adhesion.[96,97] It should not come as a surprise that this strategy has also been applied for the surface functionalisation of noble metals including gold and silver.[75,81]

4.3.2 Overview of antibody conjugation methods

As already discussed in the previous sections, the formation of SAMs and/or polydopamine layers has been established for gold and, to a lesser extent, for silver surfaces. Next, attention should be paid to the coupling of these anchoring molecules to the recognition moiety that will be applied to bind the analyte. In view of the commonly applied immunoglobulins or antibodies (ABs), figure 4.7 highlights the importance of selecting the appropriate conjugation chemistry. Ideally the immobilised antibodies should be linked via their Fc-region, thereby leaving both Fab-fragments accessible for antigen binding (figure 4.7, A).[98,99] However, some ABs may be linked to the surface in such a way that one or both Fab fragments are blocked (figure 4.7, B and C). In addition, physiological conditions are pre-
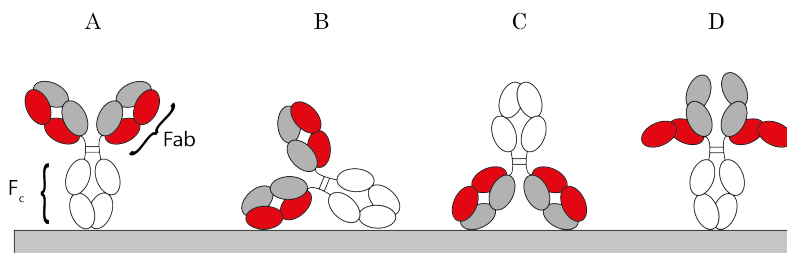
Figure 4.7: In order to guarantee optimal sensor performance, the proper orientation of the deposited antibodies (A) should be implemented. This can be realised by binding the antibody via the Fc region (white) which results in both Fab fragments (red/grey) pointing towards the target analyte. Non-specific deposition may result in the inaccessibility of one or both binding regions (B and C respectively). Moreover certain conjugation methods denature the antibody's structure (D).[98]

ferred, as harsher conditions may distort the antibody's conformation rendering it inactive (figure 4.7, D).

Antibody immobilisation strategies are commonly classified based on the nature of the bond (non-covalent vs. covalent linking) and the specificity towards a specific region and/or functional group present in the protein structure. It is beyond the scope of the current chapter to review these classes in detail. However, an excellent overview covering the latter aspects is provided in a review by Steen-Redeker *et al.*[100]

4.3.3   Preparation of biotinylated surfaces

As already discussed in the previous section, the ability to direct the antibody orientation is preferred as this leads to a higher binding capacity towards the target analyte.[101] Site-specific antibody immobilisation techniques are thus preferred to increase the sensor's sensitivity.

The biotin-streptavidin interaction is a well-known example that enables the non-covalent, yet site-specific conjugation of antibodies.[1,102–105] Although supramolecular in nature, this binding pair is characterised by a dissociation constant of 10^{-15} mol L^{-1}, rendering it the strongest non-covalent interaction.[106] By fusing an antibody to the so-called AviTag (i.e. a short peptide tag), the antibody can be made susceptible to the enzyme biotin ligase which introduces a biotin moiety at the position of the tag.[107] Since streptavidin is able to bind up to four biotin moieties, streptavidin can be applied to link the biotinylated antibody to biotin molecules anchored to the metal surface (figure 4.8).[3,108]

Given the high specificity of the interaction and the relatively straightforward manipulations, the biotin-streptavidin pair is often applied in proof-of-concept demonstrations.[103,109,110] Therefore, the present work will rely on the same methodology as a route towards antibody-functionalised silver surfaces.

However, given silver's inferior properties with respect to the chemisorption of thiols compared to gold (section 4.3.1), a dopamine-based methodology will be applied in the current PhD thesis to functionalise the silver surfaces. As already mentioned in section 4.3.1, catecholamines including DOPA and dopamine are able to form stable polydopamine (PDA) coatings on a wide variety of surfaces. Interest-
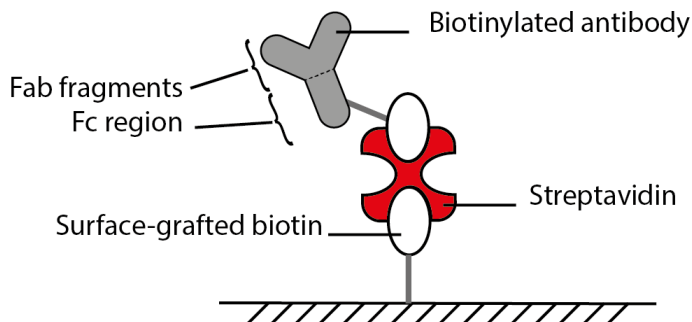
Figure 4.8: Illustration showing a tetravalent streptavidin molecule linking a biotinylated antibody to a surface-grafted biotin moiety

ingly, a few reports have also mentioned their applicability on silver surfaces.[111,112] Given the straightforward process of incubating the sample in a dopa(mine) solution, this offers an interesting alternative to the commonly applied thiol modification.

However, since the actual structure of polydopamine is still under debate, it is difficult to control the amount of biotin bound to the surface.[86] An interesting work-around for this issue has been presented by Tsai *et al.*[108] They have reported on the covalent coupling of biotin to the primary amines of branched poly(ethylene imine) (PEI) (figure 4.9). The latter are good nucleophiles and result in the formation of relatively stable bonds (*e.g.* the amide bond) upon reaction with the NHS-ester of biotin.[113–116] The modified PEI is subsequently mixed with a basic solution of dopamine. As the dopamine polymerises, the secondary amines in PEI are able to interact with the forming PDA layer and codeposition is realised. Although Tsai *et al.* only applied this methodology on polystyrene substrates, the previously reported deposition of polydopamine layers on silver suggests that the same methodology could also be applied for the biotinylation of silver surfaces.[81] In addition, the strategy has also been reported for other amine bearing polymers.[117–120]

A similar strategy was previously proposed by Messersmith *et al.*, who coupled both primary as well as secondary amines to a polydopamine coating in a two step process.[96] However the codeposition method according to Tsai *et al.* has the benefit of only requiring a
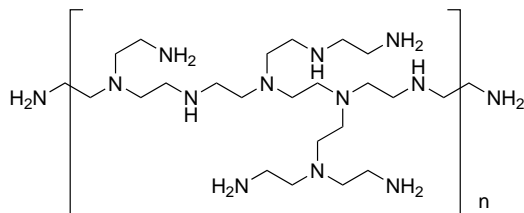
Figure 4.9: Chemical structure of branched PEI showing the presence of primary, secondary and tertiary amines along the polymer backbone.

single step. The formed polydopamine chains will thus enable the adhesion to silver, while the reaction between PEI and polydopamine covalently links both polymers in a stable three-dimensional network.

In order to enable the immobilisation of biotin moieties on the silver surfaces, biotin was first coupled to PEI according to the strategy depicted in figure 4.10. Carbodiimide chemistry is a straightforward method to couple carboxylic acids with primary amines yielding relatively stable amide bonds. Branched PEI was applied in accordance with the protocol of Tsai *et al.*, since a high degree of functionalisation is desired to provide more binding sites for *E. coli*. The latter results in a higher sensitivity of the resulting SPR-based sensor.
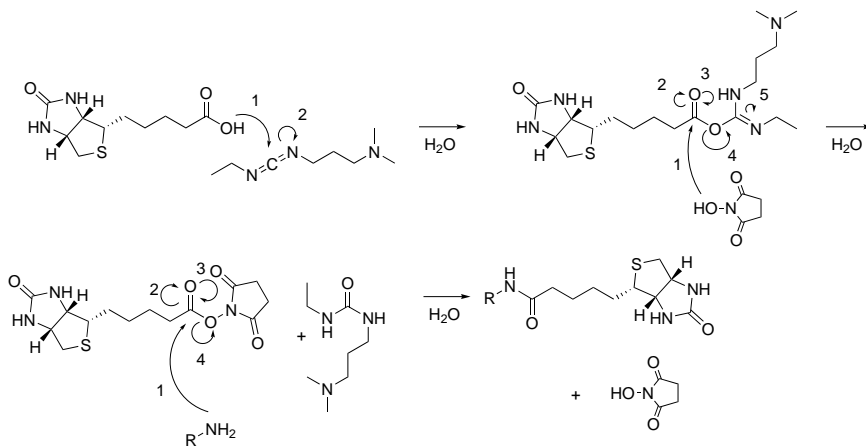
Figure 4.10: Scheme showing the reaction between the primary amines in PEI (R-NH$_2$) with the EDC/NHS-activated biotin yielding an amide bond.
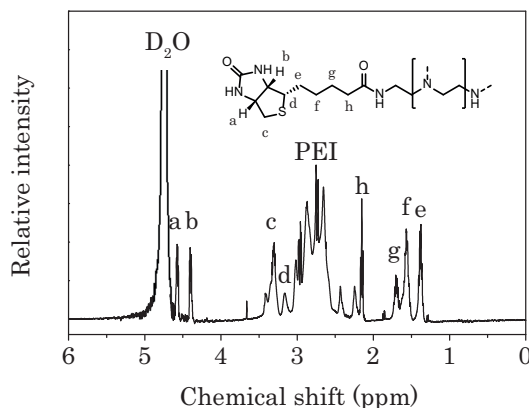
Figure 4.11: ^{1}H-NMR spectrum obtained for biotinylated PEI.

Figure 4.11 shows the ^{1}H-NMR spectrum recorded for the biotinylated PEI. By comparing the integrations of the signals corresponding to the biotin moieties to the broad multiplet associated with the PEI backbone, it could be determined that 20 PEI protons corresponded to one biotin. Since every PEI repeating unit corresponds to 4 protons and 25% of the amines in PEI is a primary amine, this ratio corresponded to a degree of modification of 80% of the primary amines present. The obtained biotinylated PEI was subsequently applied for the surface modification of the silver samples.

Three different modification conditions were applied and compared to unmodified silver (table 4.2). A series of samples were incubated in a dopamine solution (AgD) which serves as a control. Next, two series of samples were used for the codeposition of dopamine and biotinylated PEI (AgP1 and AgP2). The difference between both conditions lies in the relative amount (m/m) of biotinylated PEI to dopamine which was higher in the case of AgP2 (1 to 50) as compared to AgP1 (1 to 100). Deionised water (DIW) was added to ensure all modifications were performed at the same final dopamine concentration of $0.25\,\mathrm{mg\,mL^{-1}}$. The samples were incubated in these solutions for a period of 2 hours during which the solutions further darkened indicating the continuing formation of polydopamine.[81] During incubation, the solutions were continuously shaken to prevent the de-

Table 4.2: Composition of the applied incubation media in volumetric equivalents of solutions of dopamine, biotinylated PEI and deionised water: Ag (unmodified silver), AgD(polydopamine coated silver), AgP1(codeposition of biotinylated PEI and polydopamine (m/m 1/100) on silver), AgP2 (codeposition of biotinylated PEI and polydopamine (m/m 1/50) on silver)

Modification	Dopamine $[1 \text{ mg mL}^{-1}]$ Eq.	PEI-biotin $[0.04 \text{ mg mL}^{-1}]$ Eq.	DIW Eq.
Ag	N.A.	N.A.	N.A.
AgD	1	0	3
AgP1	1	0.25	2.75
AgP2	1	0.5	2.5

position of polydopamine clusters, which would reduce the surface homogeneity.[121] The modified samples were finally removed from their respective solutions and air dried overnight at room temperature.

For each modification condition, three samples were subsequently incubated in a solution containing streptavidin (SA) (0.1 mg mL^{-1} in PBS) to verify the presence of the grafted biotin on the surface. As a negative control, three untreated silver samples were also incubated in the same streptavidin solution. After 2 hours, the samples were removed from the solution, rinsed three times with PBS-buffer (pH 7.4) and air dried overnight.

4.4   Characterisation of functionalised silver surfaces

The surface modifications performed in the previous section were subsequently evaluated. In the upcoming sections, the effect of the proposed functionalisations will be evaluated by means of atomic force microscopy (AFM) to evaluate the effect on the surface topology, X-ray photoelectron spectroscopy (XPS) to determine the chemical composition of the deposited layer and finally static contact angle (SCA) measurements to assess the change in wettability of the surfaces.

4.4.1 X-ray photoelectron spectroscopy

As mentioned earlier, XPS is an interesting method to directly measure the atomic composition of the deposited layers. Depending on the preceding surface modification, the samples were characterised by the presence of silver, carbon, oxygen and nitrogen signals. Silver was only observed for the unmodified samples with a silver percentage of $41.5 \pm 5.6\%$ and $6.9 \pm 3.8\%$ for respectively the samples prior to and after incubation in a streptavidin solution. The large difference between both sample sets is a clear indication of the occurrence of non-specific physisorption of streptavidin on the silver surface. This is in line with the expectations based on earlier reports of the non-specific binding of proteins on metal surfaces.[122] The fact that the silver signal is not present in any of the other samples in turn is an indication that a thick (>10 nm) layer is deposited on silver under the applied modification conditions.

Among the various modification strategies, no significant difference ($p > 0.05$) was observed for the percentages of oxygen and carbon(table 4.3), although the relative amount of both elements was significantly increased compared to the unmodified silver substrate. It is well known that samples that have been exposed to the atmosphere, are characterised by an adventitious contamination of carbon and oxygen, which is the case for the unmodified silver surfaces.[123–125]

The nitrogen peak (± 400 eV) therefore provides the best indication of the successful surface functionalisation. The nitrogen percentages for the various samples are presented in figure 4.12. The results show that for the unmodified silver sample, no nitrogen was present. When dopamine with or without biotinylated PEI was deposited on the surface, a nitrogen content of 4.6-6% was observed. This corresponds to earlier work from our research group showing that 6% nitrogen corresponds to a uniform polydopamine layer.[126] The elemental composition observed for the samples obtained by the codeposition of biotinylated PEI with polydopamine (AgP1 and AgP2), were very similar to the values reported by Tsai *et al.* (i.e. 72.0%, 23.1% and 4.9% for respectively carbon, oxygen and nitrogen). The performed codeposition did not result in a significant difference ($p > 0.05$) with the polydopamine-modified samples (AgD), which may be a result of the low relative amount of PEI compared to dopamine

Table 4.3: Overview of the elemental composition (mean values for 3 samples per surface modification protocol, each analysed at 3 different positions) of the deposited layers for the applied surface modification strategies.

	Ag [%]	C [%]	O [%]	N [%]
	Prior to SA incubation			
Ag	41.5 ± 5.6	46.1 ± 2.8	12.2 ± 3.9	0.3 ± 0.9
AgD	-	73.5 ± 2.9	20.8 ± 3.6	5.8 ± 2.5
AgP1	-	71.3 ± 5.6	23.8 ± 6.9	4.7 ± 2.1
AgP2	-	75.6 ± 1.3	18.4 ± 1.2	6.0 ± 1.1
	After SA incubation			
	Ag [%]	C [%]	O [%]	N [%]
Ag	6.9 ± 3.8	49.9 ± 9.8	16.7 ± 4.1	26.5 ± 12
AgD	-	61.4 ± 4.0	28.0 ± 4.4	11.5 ± 1.1
AgP1	-	64.5 ± 2.3	23.8 ± 1.5	11.7 ± 1.6
AgP2	-	66.0 ± 3.2	23.2 ± 1.6	10.8 ± 2.3

(1/100 and 1/50 mg mg^{-1} for respectively AgP1 and AgP2 samples). Unfortunately, Tsai *et al.* do not report standard deviations for their XPS-results which impedes a more detailed comparison.

Finally, when comparing the situation prior to and after incubation in a streptavidin solution, the high amount of nitrogen retrieved on the silver samples incubated in a streptavidin solution is another indication of the occurrence of aspecific binding in biosensors. The results show that the above-mentioned reduction in silver content was caused by the deposition of streptavidin on the Ag surface. In addition, the large standard deviation on the obtained results highlights the difficulty to realise a uniform surface modification via purely physisorption of proteins. In the case of the modified samples, incubation in a streptavidin solution has a significant effect on the nitrogen content ($p < 0.05$) for each subset (AgD, AgP1 and AgP2). For all samples, the nitrogen content increases as a result of streptavidin deposition to values in the range of 10.8-11.7%. These values correspond to previously reported values for streptavidin immobilised on a poly-
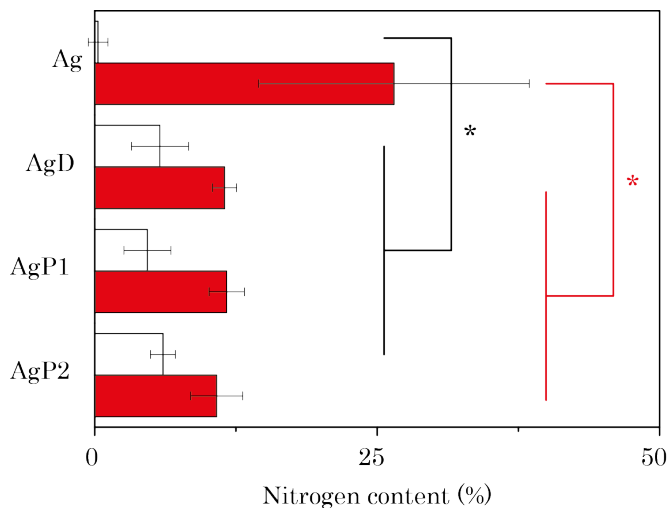
Figure 4.12: Graph comparing the nitrogen content for the various surface modifications. The situation prior to incubation in a streptavidin solution is given by the white bars, while the red bars represent the streptavidin treated surfaces. Streptavidin incubation was shown to significantly ($p < 0.05$) increase the samples' nitrogen content. Additional significant differences ($p < 0.05$) are indicated by *.

styrene surface.[127] Although dopamine deposition (AgD) seemingly reduces the amount of physisorption of streptavidin, the fact that no significant difference could be observed with the samples obtained by PEI codeposition (AgP1 and AgP2) shows that non-specific binding cannot be excluded completely.

4.4.2 Atomic force microscopy

In order to evaluate the effect of the various surface modifications on the silver surface, the surface roughness of the modified samples was determined as this property may be a first indication of a successful surface functionalisation. Considering SPR-based sensing, the penetration depth of the evanescent field was previously reported to be 214 nm for silver-coated prisms when applying a laser source with a wavelength of 630 nm.[1] Since the penetration depth is proportional to the applied wavelength, a similar value can be expected for the envi-

(a)   **(b)**
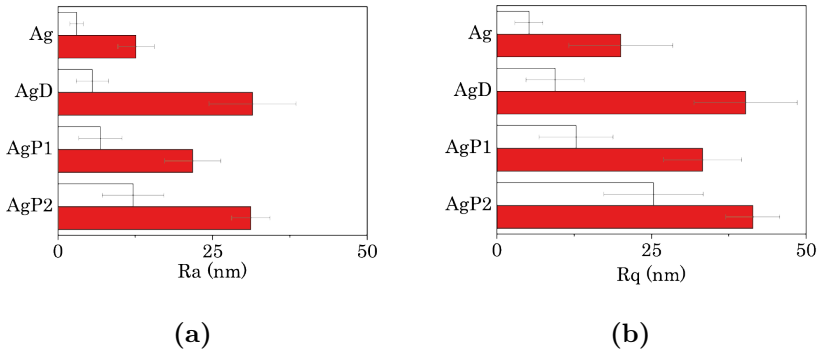
Figure 4.13: Surface roughness values obtained for the various modific-
ation routes prior to (white bars) and after incubation in a streptavidin
solution (red bars). Figure 4.13a shows the average roughness (R_a), while
figure 4.13b shows the RMS roughness (R_q). Values were determined for
25x25 µm^2 samples.

sioned laboratory demonstrator operating at 661 nm. Surface rough-
ness values should thus remain well below the above-mentioned value
to be able to detect the target analyte in straightforward way. Since
the evanescent field is the most intense near the interface between the
metal and the sample, both layer thickness as well as the associated
R_q values should be as low as possible.[128]

Therefore, three samples per modification condition were subjec-
ted to AFM analysis. For each sample, the local surface roughness was
determined on three different sample locations sized 25x25 µm^2. Both
the average surface roughness (R_a) as well as the root-mean-square
(RMS) roughness (R_q) are listed as mean values with corresponding
standard deviations in figure 4.13. The latter parameters are defined
by respectively equation 4.3 and equation 4.4:

$$R_a = \frac{1}{n} \sum_{i=1}^{n} |y_i| \tag{4.3}$$

$$R_q = \sqrt{\frac{1}{n} \sum_{i=1}^{n} y_i^2} \tag{4.4}$$

Both equations can be applied as a measure for the surface roughness, but R_q values are more heavily influenced by larger defects as compared to R_a, making R_q more relevant when considering optical applications.[129]

The results revealed the smoothness of the silver surfaces obtained via sputter deposition with values of 3.0 ± 1.2 nm and 5.2 ± 2.3 nm for respectively R_a and R_q. The measured mean roughnesses (R_a and R_q) increased for the various surface modifications (AgD < AgP1 < AgP2), but the obtained differences between these groups were not significant ($p > 0.05$). However, as already shown from the XPS results, incubating the samples in a streptavidin solution did alter the samples fundamentally. This observation can also be derived from the significantly ($p < 0.05$) higher surface roughnesses obtained after incubating the samples in a streptavidin solution (figure 4.13, red bars). Despite the relatively large differences among the sample sets, the surface roughnesses remained well below the reported penetration depth (i.e. 214 nm, $\lambda = 630$ nm) associated with silver-based SPR sensors.

To determine the origin of the increased roughness, figure 4.14 shows the obtained surface topography for a representative sample of each modification condition. The roughness of the silver samples is determined by a small number of particles present on the surface, but given the very low values of R_q this contamination is negligible. When polydopamine layers are deposited, larger aggregates are deposited, which is consistent with previous observations of this phenomenon.[126,130,131] The continuous shaking of the solution during incubation did not completely prevent the adherence of these particles to the incubated silver samples. For the samples subsequently incubated in the streptavidin solution, the surfaces are characterised by a more globular appearance (figure 4.15). This observation is also consistent with previous reports on the deposition of streptavidin on two organic semi-conductors.[132] The globular appearance thus confirms the presence of streptavidin as was expected based on the above-mentioned XPS results.

(a) Ag   **(b)** AgD   **(c)** AgP1   **(d)** AgP2

(e) AgSA   **(f)** AgDSA   **(g)** AgP1SA   **(h)** AgP2SA

xy-plane

25 µm

z-direction [nm]

0   250   500
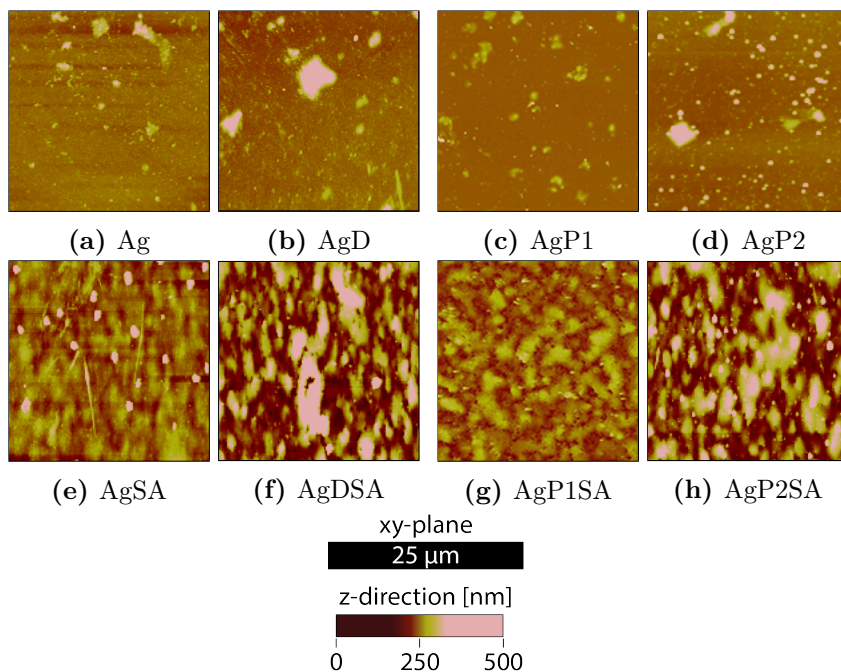
Figure 4.14: Visual representation of the effect of the various surface modifications on the sample's surface roughness as obtained via AFM. Figures a-d represent the modified samples prior to streptavidin application, while figures e-h represent the surfaces after incubation in a streptavidin solution during 2 hours. Each image shows a 25 µm by 25 µm square.

4.4.3   Static contact angle measurements

The static contact angles obtained for water droplets on the modified silver surfaces are visualised in figure 4.16 (black-and-white boxplots). The unmodified silver samples are characterised by a contact angle of $88.2 \pm 3.8°$, which corresponds closely with the reported value of $90°$.[133] This value decreased down to $74.9 \pm 7.1°$ upon polydopamine deposition, which is a significant decrease ($p < 0.05$). Previous reports on the deposition of polydopamine layers on various substrates mention a convergence towards a value of $50°$ which is considerably lower than the results obtained for the PDA-coated silver herein.[81] However, this difference with the state-of-the-art can be rationalised by the lower dopamine concentration and the shorter incubation time

(a) AgP1   **(b)** AgP1SA
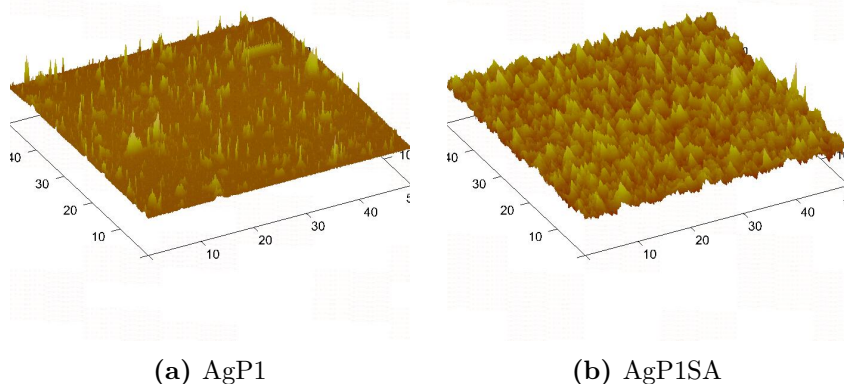
Figure 4.15: Three-dimensional representation of the effect of the strep-tavidin incubation on AgP1's surface roughness as obtained via AFM. Figure a represents the modified sample prior to streptavidin application, while fig-ure b represents the surface after incubation in a streptavidin solution for 2 hours. Each image shows a 50 µm by 50 µm square.

applied in the modification protocol applied in this PhD thesis. Both factors contribute to thinner dopamine layers being formed, which is desirable for SPR applications given the limited penetration depth of the evanescent field.[1,85]

When biotinylated PEI (AgP1 and AgP2) was codeposited, no significant change in the contact angle could be observed compared to the pure polydopamine layer with values of respectively $78.3 \pm 4.0°$ and $77.3 \pm 3.3°$. Although the mean values did not differ significantly, codeposition of biotinylated PEI did reduce the spread of the values in contrast to the values for the less reproducible polydopamine layers.

When the samples were subsequently incubated in a streptavidin solution, a considerable reduction in the observed contact angle was obtained (figure 4.16; red, dashed boxplots). As already indicated by the XPS data, a considerable amount of non-specific binding occurred when silver was incubated in the streptavidin solution. This resulted in an increased hydrophilicity as demonstrated by the contact angle decreasing down to $46.5 \pm 3.7°$. A similar drop in contact angles was observed for the modified silver samples with values of $26.2 \pm 12.8°$, $34.0 \pm 3.7°$ and $30.6 \pm 6.4°$ for respectively AgD, AgP1 and AgP2.
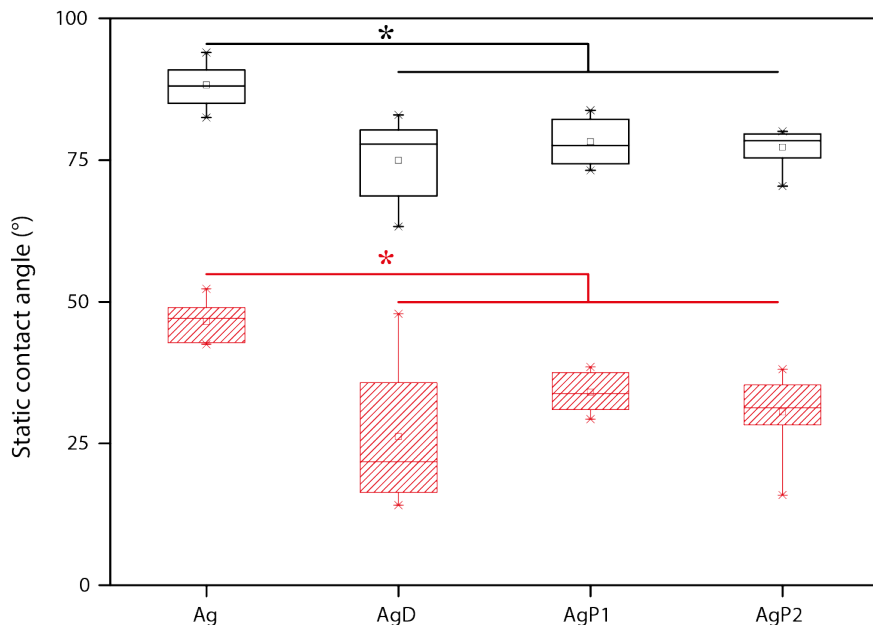
Figure 4.16: Graph showing the spread of the obtained static contact angles for the modified silver surfaces prior (white) and after (red dashed) incubation in a streptavidin solution. The mean values within each group are indicated by a square. Streptavidin incubation was shown to significantly alter the surface ($p < 0.05$). Additional significant differences ($p < 0.05$) are indicated with *.

These results show that streptavidin is able to bind to the surface regardless of the surface modification strategy applied. It is however expected that the biotinylated surfaces will show superior retention of the bound streptavidin when applied in biosensor set-ups based on the very strong interaction between the immobilised biotin moieties and streptavidin.[107,132,134–136] Future work should ideally include the assessment of the coating stability by repeating the experiments after prolonged incubation in e.g. aqueous buffer or under flow conditions that simulate the conditions experienced by the sensor during sample injection.

4.5 Application of PEGylation as a method to prevent aspecific binding

Since the results of the surface characterisation did not indicate a significant difference ($p > 0.05$) between the poly(dopamine) modified samples and the ones obtained after codeposition of biotinylated PEI, a second series of experiments was performed to rule out aspecific binding of streptavidin to the poly(dopamine) layer. Poly(ethylene glycol) has a long track record in terms of preventing surface fouling.[29,30,92,137] As a result, a PEGylated PEI-derivative was synthesised based on literature data.[138] In this procedure, PEG chains were grafted onto the branched PEI using cyanuric chloride (figure 4.17).
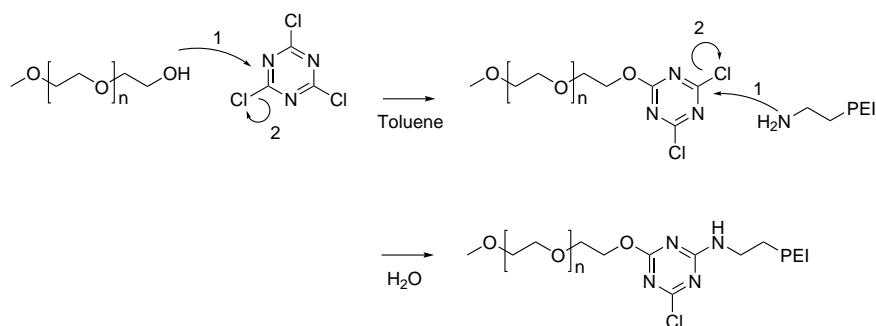
Figure 4.17: Scheme showing the reaction mechanism involved in the coupling of PEG chains to the PEI amine functionalities by using cyanuric chloride as a cross-linker.

Figure 4.18 shows the ^{1}H-NMR spectrum obtained after coupling the activated PEG to the primary amines of PEI. In contrast to the previously mentioned coupling of biotin, the PEI signals are dwarfed by the intense singlet associated with the PEG protons (3.7 ppm). The PEI protons (3.2-2.2 ppm) only became apparent upon zooming in on the spectrum (figure 4.18, inset). By comparing the relative integrations of the PEG and PEI signals (34/1), it could be deduced that for every PEI repeating unit, 0.5 PEG chains were present in the precipitated material. This corresponds to 3 PEG chains per primary amine present in PEI. Given the excess of PEG chains applied relative to the number of PEI primary amines, this may indicate the
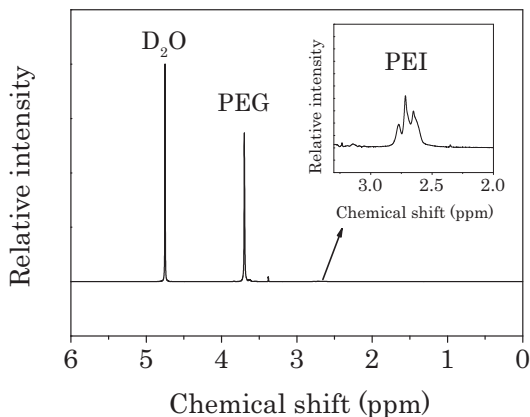
Figure 4.18: ^{1}H-NMR spectrum obtained for PEGylated PEI. As the spectrum is dominated by the PEG protons, an inset shows the PEI signals in the 3.2-2.2 ppm range.

entrapment of PEG chains in the PEG-PEI graft copolymer. Another possibility is that cyanuric chloride was able to react with two PEG alcohol functionalities, which effectively introduces two PEG chains per primary amine. The obtained PEG/PEI ratio was higher (+ 36%) than the value reported in literature and should be taken into account when comparing the results of the various surface modifications.[138]

The obtained PEGylated-PEI was subsequently applied in additional surface modification procedures, by incubating silver-coated glass slides in premixed solutions. The relative amounts associated with each surface modification procedure can be found in table 4.4.

4.5.1   X-ray photoelectron spectroscopy

The new series of samples was again first analysed via XPS. Similar to the previous samples, the XPS spectra revealed the presence of silver, carbon, oxygen and nitrogen (table 4.5), which was expected based on the composition of the deposited compounds. In order to assess the effect of the PEG chains on the binding potential of streptavidin, the new batch of samples were also incubated in a solution of biotinylated *E. coli*-specific antibodies, which are appropriate for the envisioned biosensor application.

Table 4.4: Composition of the applied incubation media in volumetric equivalents of solutions of dopamine, PEGylated PEI, biotinylated PEI and deionised water (DIW) based on:[108] AgD (polydopamine coated silver), AgD$_{PEG}$(codeposition of polydopamine and PEGylated PEI on silver), AgP1$_{PEG}$(codeposition of polydopamine, PEGylated PEI and biotinylated PEI (m/m 1/100 compared to dopamine) on silver), AgP2$_{PEG}$ (codeposition of polydopamine, PEGylated PEI and biotinylated PEI (m/m 1/50 compared to dopamine) on silver)

Modification	Dopamine [2 mg mL^{-1}] Eq.	PEI-PEG [2 mg mL^{-1}] Eq.	PEI-biotin [0.08 mg mL^{-1}] Eq.	DIW Eq.
AgD	0.5	N.A.	N.A.	3.5
AgD$_{PEG}$	0.5	2	N.A.	1.5
AgP1$_{PEG}$	0.5	2	0.5	1
AgP2$_{PEG}$	0.5	2	1	0.5

As was the case for the previous surface modifications, no significant differences ($p > 0.05$) among the various modifications (AgG, AgD$_{PEG}$, AgP1$_{PEG}$ and AgP2$_{PEG}$) could be derived based on the carbon and oxygen content. Surprisingly, silver was found to be present in low quantities (0.3-6%) in all samples. Together with the relatively high associated standard deviations, this may be an indication that the modification was inhomogeneous or that the obtained layer thickness is lower than 10 nm. Since Tsai *et al.* applied a polystyrene substrate in their report, they did not report any issues in terms of layer homogeneity as the carbon peak of the underlying polystyrene coincides with the previously mentioned adventious contamination with carbon and oxygen upon exposure of the samples to the atmosphere.[108,123–125] Moreover, no standard deviations were provided and thus no evidence was provided that they achieved homogeneous coatings.

The observed nitrogen content is visualised in figure 4.19 and shows a clear trend in terms of nitrogen content when the samples are incubated in a streptavidin solution and subsequently placed in a solution containing biotinylated *E. coli*-specific antibodies. This corresponds to our expectations based on the previous XPS experi-

Table 4.5: Overview of the elemental composition of the deposited layers for the applied surface modification strategies.

	Prior to SA incubation			
	Ag [%]	C [%]	O [%]	N [%]
AgD	1.9 ± 1.2	68.1 ± 3.2	25.4 ± 1.5	4.5 ± 2.9
AgD_{PEG}	2.5 ± 4.7	63.5 ± 5.3	32.3 ± 7.6	1.8 ± 2.6
$AgP1_{PEG}$	5.4 ± 3.1	61.2 ± 4.9	25.0 ± 4.5	8.4 ± 5.0
$AgP2_{PEG}$	0.5 ± 0.5	73.8 ± 10.0	21.8 ± 8.6	3.9 ± 3.0
	After SA incubation			
	Ag [%]	C [%]	O [%]	N [%]
AgD	0.9 ± 0.5	65.5 ± 5.4	27.4 ± 6.7	6.2 ± 4.0
AgD_{PEG}	0.5 ± 0.3	70.8 ± 3.5	23.8 ± 3.3	4.9 ± 1.4
$AgP1_{PEG}$	3.3 ± 3.0	64.8 ± 3.6	21.5 ± 2.8	10.3 ± 2.3
$AgP2_{PEG}$	0.3 ± 0.2	70.9 ± 7.9	21.3 ± 6.0	7.5 ± 2.7
	After AB incubation			
	Ag [%]	C [%]	O [%]	N [%]
AgD	1.5 ± 2.5	64.3 ± 3.4	26.0 ± 7.5	8.3 ± 5.1
AgD_{PEG}	2.2 ± 2.9	62.1 ± 5.0	27.9 ± 8.8	7.7 ± 4.9
$AgP1_{PEG}$	4.2 ± 3.7	62.8 ± 4.5	21.3 ± 4.1	11.7 ± 6.6
$AgP2_{PEG}$	0.4 ± 0.3	66.4 ± 4.3	24.5 ± 2.3	9.2 ± 4.0

ments as well as the high affinity of biotinylated antibodies towards streptavidin reported earlier in literature.[134] In figure 4.19, a significant increase in nitrogen content upon incubation in a SA solution, was observed for both AgD_{PEG} and $AgP2_{PEG}$. The nitrogen content prior to incubation in the SA solution was significantly higher ($p < 0.05$) for $AgP1_{PEG}$ as compared to the other PEG-containing modifications (AgD_{PEG} and $AgP2_{PEG}$). But given the large standard deviation on the mean value, this difference may be a result of local non-uniformities. Like for the previous XPS experiments, most other differences were not statistically significant ($p > 0.05$). However, the
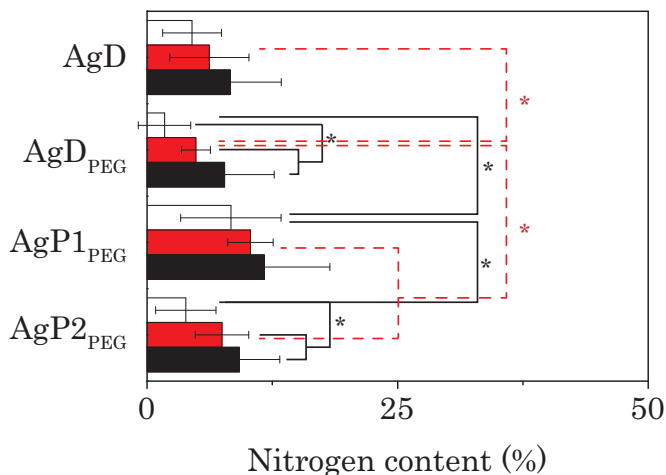
Figure 4.19: Graph comparing the nitrogen content for the various surface modifications. The situation prior to incubation in a streptavidin solution is given by the white bars, while the red bars represent the streptavidin treated surfaces. The black bars correspond to samples that were finally incubated in a solution of biotinylated antibodies. Significant differences (p < 0.05) are indicated by *.

nitrogen content prior to SA incubation was for all modifications comparable to the value reported by Tsai *et al.* (i.e. 4.9%) as well as prior work from our group (4-5% for poly(dopamine) on a PMMA substrate).[108,131] As previously mentioned, the report by Tsai *et al.* did not include any statistical analysis of the results making a more accurate comparison of the results impossible.

When the samples are compared to the ones that have been subsequently incubated in a $0.1 \ \mathrm{mg\,mL^{-1}}$ solution of streptavidin, the nitrogen content is not significantly different from the previous samples that did not contain PEGylated PEI. $\mathrm{AgD_{PEG}}$ is the exception to this rule and is significantly lower (p < 0.05) from the other samples (AgD, $\mathrm{AgP1_{PEG}}$ and $\mathrm{AgP2_{PEG}}$) after incubation in the streptavidin solution. Given the low nitrogen content prior to streptavidin application, it may be rationalised that the PEG chains also prevented the straightforward deposition of PEGylated PEI.

Finally, incubating the streptavidin-coated samples in a solution of *E. coli*-specific antibodies resulted in an increase in nitrogen content, although the increase was not statistically significant ($p > 0.05$). This can be rationalised by the fact that both streptavidin as well as the biotinylated antibodies are proteins and are thus difficult to distinguish based on nitrogen content.[139] XPS is thus unsuitable to provide a quantitative idea on the functionalisation of the surface with *E. coli*-specific antibodies. The amount of deposited antibodies should ideally be quantified via complementary techniques such as radiolabelling of antibodies using ^{125}I or ^{131}I.[140–142]

4.5.2   Atomic force microscopy

Next, the samples were subjected to atomic force microscopy to assess the influence of the various modification strategies on the surface roughness. As mentioned previously (section 4.4.2), higher R_q values indicate less homogeneous surfaces.[129] Moreover, based on the SPR penetration depth at a wavelength of 630 nm for silver coated prisms being 214 nm, the obtained values of R_q should remain well below this value.[1,128]

Figure 4.20 shows the obtained roughness values (R_q) for the various surface modification conditions applied. In contrast with the previous AFM results (figure 4.13), the samples show higher values of R_q prior to incubation in the streptavidin solution (i.e. 15-30 nm vs. 9-25 nm), while after incubation in the streptavidin solution, similar values are found. The increased roughness prior to streptavidin application is consistent with the observed silver signals in all samples and thus indicates a non-uniform deposition on the surfaces. The inhomogeneous surface topology also prevented the analysis via AFM of the AgP2$_{PEG}$ samples obtained after incubation in the antibody solution. This may indicate local height differences of > 5 nm. The increase in roughness may be attributed to the presence of PEG-grafts since Tsai *et al.* also noticed a significant increase in surface roughness (R_a) to values of 12.4 ± 2.5nm for the conditions that were also applied in this PhD.[138] This value is in agreement with the R_a values obtained for our samples (table 4.6). The increased roughness can be attributed to the effect of the PEG chains on the surface morphology. Yu *et al.* previously studied the surface roughness of PEGylated PLA
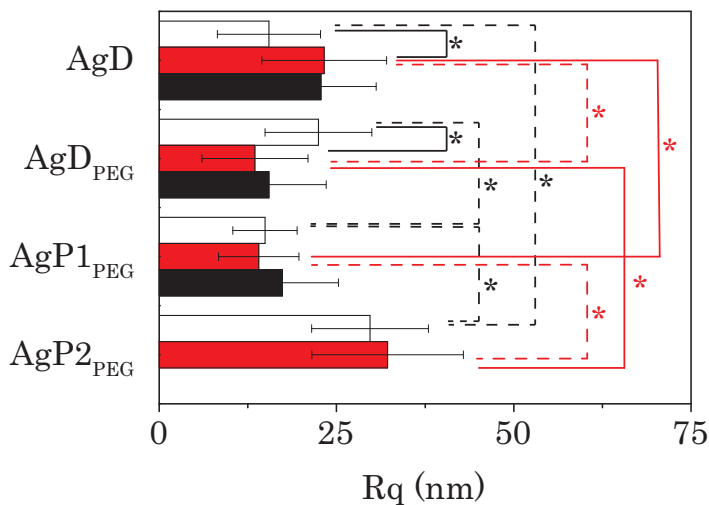
Figure 4.20: Surface roughness values (R_q) obtained for the various modification routes (white bars), the same samples after incubation in a streptavidin solution (red bars) and subsequent conjugation to *E.coli*-specific antibodies (black bars). It should be noted that none of the AgP2$_{PEG}$ samples obtained after incubation in the antibody solution, could be properly analysed via AFM.

membranes and found that the R_q values increased ($+ > 50\%$) when the PEG content exceeded 7%.[143]

Given the high roughness values prior to streptavidin immobilisation and the high obtained standard deviations, AFM was unable to reveal any clear trends with respect to the influence of the various modification protocols on the surface topography. Despite the relatively large differences among the sample sets (figure 4.20, significant differences are denoted with *), the surface roughness values did remain well below the reported penetration depth associated with silver-based SPR sensors.[1]

4.5.3 Static contact angle measurements

Finally, the static contact angles obtained for the modified silver surfaces are visualised in figure 4.21. The observed static contact angles

Table 4.6: R_a surface roughness values obtained for the samples containing PEGylated PEI. The surface roughness is provided prior to and after incubating the samples in a streptavidin solution and after the subsequent immobilisation of biotinylated *E. coli*-specific antibodies. * Given the inhomogeneous surface topography, no representative topographical image could be obtained.

	R_a [nm]		
		+ Streptavidin	+ Antibodies
AgD	8.9 ± 4.3	13.5 ± 5.0	12.4 ± 4.1
AgD$_{PEG}$	11.5 ± 2.3	7.7 ± 3.5	8.6 ± 8.9
AgP1$_{PEG}$	8.8 ± 3.4	8.1 ± 3.3	9.0 ± 4.2
AgP2$_{PEG}$	14.7 ± 4.1	19.9 ± 6.6	*
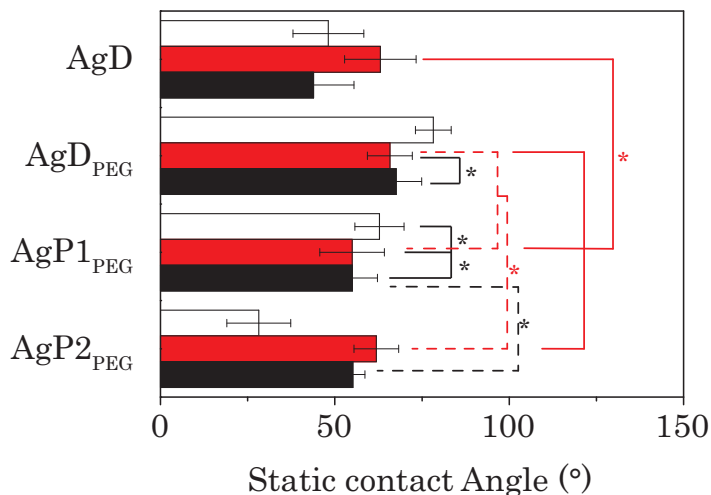
Figure 4.21: Graph showing the static contact angles for the modified silver surfaces (white bars), after incubation in a streptavidin solution (red bars) and after the subsequent incubation in a solution of *E. coli*-specific antibodies (black bars). The results obtained for the various modification strategies and between the incubation steps are significant ($p < 0.05$) unless they are marked by *.

were found to be lower than for the previous samples, with the exception of the AgD$_{PEG}$ sample. This decrease can be attributed to the hydrophilicity of the introduced PEG chains However, it should be noted that it is difficult to make a valid comparison between both series of samples, since it has been previously shown that the surface topography has a significant influence on the observed static contact angle in addition to the surface hydrophilicity.[144–146]

Tsai *et al.* did not perform contact angle measurements when evaluating the codeposition of dopamine, PEGylated PEI and biotinylated PEI. For an earlier paper focusing on the non-fouling properties of PEGylated PEI, the observed contact angle was found to be much lower (40-50°) than the value reported in this PhD (AgD$_{PEG}$, approx. 80°).[138] This may be rationalised by the inhomogeneous deposition which is indicated by the silver signal apparent in the XPS spectra and the R$_q$ values obtained via AFM analyses. This would imply that the underlying substrate (i.e. Ag) is exposed to some extent or that the coating thickness is below 10 nm. In the case of Tsai *et al.*, the substrate consisted of several layers of polyelectrolytes, which were applied to ensure the proper adhesion of the PEGylated PEI. Polyelectrolytes are characterised by low contact angles, while the contact angle for silver is exactly 90°. Therefore, inhomogeneous deposition of the dopamine layers on these substrates may account for the observed difference. The samples containing both PEGylated as well as biotinylated PEI (AgP1$_{PEG}$ and AgP1$_{PEG}$) show a similar contact angle as polydopamine coated PEG-based materials previously reported by Van De Walle *et al.*[131]

Looking at the effect of the subsequent incubation in solutions of streptavidin and biotinylated antibodies, the trend observed in the XPS results could not be confirmed and as a result, the expected reduction of aspecific binding by the PEG chains could not be determined.

4.6 Conclusions

The aim of the current chapter was to modify the metal coating required for SPR-sensing with chemical handles that could ultimately be applied to couple *E.coli*-specific antibodies to the metal surface.

Based on silver's superior optical properties over gold (higher reflectivity and lower refractive index), 100 nm thick silver layers were successfully sputter-coated on glass substrates as a model system for silver layers to be deposited on the polymers presented in chapters 2 and 3. The observed surface roughness was lower than 10 nm over a 25x25 µm^2 area, indicating that the necessary optical quality was achieved.

Due to silver's less explored functionalisation strategies and the inferior Ag-S binding strength (16-20 kcal mol^{-1}) compared to the Au-S bond (45 kcal mol^{-1}), the previously reported codeposition of polydopamine and biotinylated poly(ethylene imine) was applied on silver surfaces to allow the site-specific immobilisation of *E. coli*-specific antibodies. X-ray photoelectron spectroscopy indicated the presence of the deposited polymer(s). Moreover, the measured nitrogen content was shown to be in correlation with previous reports in literature. Atomic force microscopy experiments revealed that the modification strategies resulted in homogeneous modification of the silver samples. Wettability experiments via static contact angle measurements in turn confirmed this observation. The results thus confirm the successful codeposition of biotinylated PEI and poly(dopamine), although no significant differences were observed between the samples covered with polydopamine on the one hand and the samples used for the codeposition of PEI on the other hand.

Incubation of the functionalised samples in a streptavidin solution demonstrated their binding potential towards streptavidin. However, no significant difference was observed between the biotinylated surfaces (AgP1 and AgP2) and the polydopamine layer (AgD). This is an indication that binding of streptavidin can occur via both specific binding to the immobilised biotin as well as via weak, non-specific interactions to the polydopamine layer. Non-functionalised silver samples in turn showed considerable physisorption of streptavidin.

To solve the issue associated with aspecific binding, the surface modifications were repeated in the presence of PEGylated PEI. A clear trend was observed in terms of nitrogen content when first incubating the samples in a solution of streptavidin and subsequently placing them in a solution containing *E. coli*-specific antibodies. However, this trend could not be confirmed via AFM nor via SCA exper-

iments, as these experiments indicated the inhomogeneous coating of the silver substrates.

Given the large standard deviation observed for the various surface modification protocols, more work will be required to increase the reproducibility of the obtained protocols. Given silver's superior optical properties in terms of SPR sensitivity and the straightforward surface modification of gold, an interesting report on the coating of silver layers with thin gold layers would be an interesting workaround for the functionalisation of silver.[4] Given the large influence of aspecific binding, techniques that allow the direct bioconjugation of antibodies to the metal surface and thus do not rely on the application of streptavidin, may also be explored as an alternative to the herein pursued biotin-streptavidin based modification methodology. Given the evanescent decay of the surface plasmon wave from the metal surface, the layer thickness achieved via both methodologies should be compared via e.g. ellipsometry since thinner layers would increase sensor performance (i.e. sensitivity). In order to allow the quantification of the immobilised antibodies, future work should also explore the potential of radiolabelling to compare the effectiveness of the studied modification protocols in a quantitative way.

References

[1] J. Homola, S. S. Yee, G. Gauglitz, *Sensors and Actuators B-Chemical* **1999**, *54*, 3–15.

[2] S. Mariani, M. Minunni, *Analytical and Bioanalytical Chemistry* **2014**, *406*, 2303–2323.

[3] C. Pradier, M. Salmain, L. Zheng, G. Jaouen, *Surface science* **2002**, *503*, 193–202.

[4] A. Gutés, R. Maboudian, C. Carraro, *Langmuir* **2012**, *28*, 17846–17850.

[5] C. Wang, S. Wang, W. Cai, X. Shao, *Talanta* **2017**, *162*, 123–129.

[6] S. Szunerits, X. Castel, R. Boukherroub, *The Journal of Physical Chemistry C* **2008**, *112*, 15813–15817.

[7] Z. Wang, Z. Cheng, V. Singh, Z. Zheng, Y. Wang, S. Li, L. Song, J. Zhu, *Analytical chemistry* **2014**, *86*, 1430–6.

[8] S. Unser, I. Bruzas, J. He, L. Sagle, *Sensors* **2015**, *15*, 15684–15716.

[9] J. De Pelsmaeker, H. Thienpont, H. Ottevaere, *to be submitted in Optics Express*.

[10] V. G. Kravets, R. Jalil, Y.-J. Kim, D. Ansell, D. E. Aznakayeva, B. Thackray, L. Britnell, B. D. Belle, F. Withers, I. P. Radko, Z. Han, S. I. Bozhevolnyi, K. S. Novoselov, A. K. Geim, A. N. Grigorenko, *Scientific Reports* **2014**, *4*, 5517.

[11] H. Sellers, A. Ulman, Y. Shnidman, J. E. Eilers, *Journal of the American Chemical Society* **1993**, *115*, 9389–9401.

[12] J. C. Love, L. A. Estroff, J. K. Kriebel, R. G. Nuzzo, G. M. Whitesides, *Chemical reviews* **2005**, *105*, 1103–69.

[13] S. Subramanian, S. Sampath, *Journal of the* **2013**, *89*, 1–7.

[14] A. H. Pakiari, Z. Jamshidi, *The Journal of Physical Chemistry A* **2010**, *114*, 9212–9221.

[15] H. Hakkinen, *Nat Chem* **2012**, *4*, 443–455.

[16] K. M. McPeak, S. V. Jayanti, S. J. P. Kress, S. Meyer, S. Iotti, A. Rossinelli, D. J. Norris, *ACS Photonics* **2015**, *2*, 326–333.

[17] Gold Price Group Limited., *Silver Price*, **2017**, `http://silverprice.org/`.

[18] W. Li, K. Ren, J. Zhou, *Trends in Analytical Chemistry* **2016**, *80*, 486–494.

[19] C. Reagan, *Imaging UV Light with CCD Cameras*, **2017**.

[20] S. Agarwal, Y. K. Prajapati, V. Singh, *Optics Communications* **2017**, *383*, 113–118.

[21] B. Escaig, *Journal de Physique* **1993**, *03*, 753–761.

[22] L. A. C. Teixeira, M. C. Santini, *Journal of Materials Processing Technology* **2005**, *170*, 37–41.

[23] A. Lahmar, A. Assaf, M. J. Durand, S. Jouanneau, G. Thouand, B. Garnier, *Reviews of Adhesion and Adhesives* **2016**, *4*, 47–68.

[24] E. Hecht, *Optics*, Pearson Addison Wesley 2002 (1), 4th ed., **2002**, pp. 95–100.

[25] B. Van Dorst, J. Mehta, K. Bekaert, E. Rouah-Martin, W. De Coen, P. Dubruel, R. Blust, J. Robbens, *Biosensors and Bioelectronics* **2011**, *26*, 1178–1194.

[26] O. Torun, I. s. Hakkı Boyacı, E. Temür, U. Tamer, Ö. Torun, I. s. Hakkı Boyacı, E. Temür, U. Tamer, *Biosensors and Bioelectronics* **2012**, *37*, 53–60.

[27] J. L. Dalsin, L. Lin, S. Tosatti, J. Vörös, M. Textor, P. B. Messersmith, *Langmuir* **2005**, *21*, 640–6.

[28] K. Chawla, S. Lee, B. P. Lee, J. L. Dalsin, P. B. Messersmith, N. D. Spencer, *Journal of Biomedical Materials Research Part A* **2009**, *90A*, 742–749.

[29] R. Konradi, C. Acikgoz, M. Textor, *Macromolecular rapid communications* **2012**, *33*, 1663–76.

[30] B. Liu, P.-J. J. Huang, X. Zhang, F. Wang, R. Pautler, A. C. Ip, J. Liu, *Analytical Chemistry* **2013**, *85*, 10045–10050.

[31] D. J. Muller, Y. F. Dufrene, *Nat Nano* **2008**, *3*, 261–269.

[32] A. Alessandrini, P. Facci, *Meas. Sci. Technol* **2005**, *16*, 65–92.

[33] Q. Zhong, D. Inniss, K. Kjoller, V. Elings, *Surface Science Letters* **1993**, *290*, L688–L692.

[34] T. Young, *Philosophical Transactions of the Royal Society of London* **1805**, *95*, 65–87.

[35] D. Janssen, R. De Palma, S. Verlaak, P. Heremans, W. Dehaen, *Thin Solid Films* **2006**, *515*, 1433–1438.

[36] D. Pleul, F. Simon in *Polymer Surfaces and Interfaces: Characterization, Modification and Applications* (Ed.: M. Stamm), Springer Berlin Heidelberg, Berlin, Heidelberg, **2008**, pp. 71–89.

[37] W. Kern, K. K. Schuegraf in *Handbook of Thin Film Deposition Processes and Techniques (Second Edition)* (Ed.: K. B. Seshan), William Andrew Publishing, Norwich, NY, **2001**, Chapter 1, pp. 11–43.

[38] S.-I. Park, Y.-J. Quan, S.-H. Kim, H. Kim, S. Kim, D.-M. Chun, C. S. Lee, M. Taya, W.-S. Chu, S.-H. Ahn, *International Journal of Precision Engineering and Manufacturing-Green Technology* **2016**, *3*, 397–421.

[39] P. J. Kelly, R. D. Arnell, *Vacuum* **1999**, *56*, 159–172.

[40] S. M. Rossnagel, J. Hopwood, *Journal of Vacuum Science and Technology B: Microelectronics and Nanometer Structures Processing Measurement and Phenomena* **1994**, *12*, 449–453.

[41] T. Jung, A. Westphal, *Materials Science and Engineering: A* **1991**, *140*, 528–533.

[42] S. M. Rossnagel, D. Mikalsen, H. Kinoshita, J. J. Cuomo, *Journal of Vacuum Science and Technology A: Vacuum Surfaces and Films* **1991**, *9*, 261–265.

[43] S. M. Rossnagel, J. Hopwood, *Applied Physics Letters* **1993**, *63*, 3285–3287.

[44] M. R. Rashidian Vaziri, F. Hajiesmaeilbaigi, M. H. Maleki, *Journal of Applied Physics* **2011**, *110*, 43304.

[45] D. M. Mattox in *The Foundations of Vacuum Coating Technology*, Elsevier Inc., **2003**, pp. 11–33.

[46] E. Kay, *Journal of Applied Physics* **1963**, *34*, 760–768.

[47] S. M. Rossnagel, I. Yang, J. J. Cuomo, *Thin Solid Films* **1991**, *199*, 59–69.

[48] Q. L. Feng, J. Wu, G. Q. Chen, F. Z. Cui, T. N. Kim, J. O. Kim, *Journal of Biomedical Materials Research* **2000**, *52*, 662–668.

[49] J. L. Clement, P. S. Jarrett, *Metal-based drugs* **1994**, *1*, 467–82.

[50] C. Vericat, M. E. Vela, G. Benitez, P. Carro, R. C. Salvarezza, *Chem. Soc. Rev.* **2010**, *39*, 1805–1834.

[51] E. Pensa, E. Cortés, G. Corthey, P. Carro, C. Vericat, M. H. Fonticelli, G. Benítez, A. A. Rubert, R. C. Salvarezza, *Accounts of chemical research* **2012**, *45*, 1183–92.

[52] A. Jakubowicz, H. Jia, R. M. Wallace, B. E. Gnade, *Langmuir : the ACS journal of surfaces and colloids* **2005**, *21*, 950–5.

[53] M. Wirde, U. Gelius, L. Nyholm, *Langmuir* **1999**, *15*, 6370–6378.

[54] J. A. Fischer, V. C. Zoldan, G. Benitez, A. a. Rubert, E. A. Ramirez, P. Carro, R. C. Salvarezza, A. A. Pasa, M. E. Vela, *Langmuir* **2012**, *28*, 15278–15285.

[55] J. T. Koepsel, W. L. Murphy, *Chembiochem : a European journal of chemical biology* **2012**, *13*, 1717–24.

[56] K. Saha, S. S. Agasti, C. Kim, X. Li, V. M. Rotello, *Chemical reviews* **2012**, *112*, 2739–79.

[57] K. Öberg, J. Ropponen, J. Kelly, P. Löwenhielm, M. Berglin, M. Malkoch, *Langmuir* **2013**, *29*, 456–65.

[58] U. Brandt, A. Deters, A. Steinbüchel, *Applied Microbiology and Biotechnology* **2015**, *99*, 4545–4557.

[59] I. Berlanga, Á. Etcheverry-Berríos, A. Mella, D. Jullian, V. A. Gómez, N. Aliaga-Alcalde, V. Fuenzalida, M. Flores, M. Soler, *Applied Surface Science* **2017**, *392*, 834–840.

[60] A. Ulman, *Chemical Reviews* **1996**, *96*, 1533–1554.

[61] L. V. Romashov, V. P. Ananikov, *Chemistry (Weinheim an der Bergstrasse Germany)* **2013**, *19*, 17640–60.

[62] C. Combellas, M. Delamar, F. Kanoufi, J. Pinson, F. I. Podvorica, *Chemistry of Materials* **2005**, *17*, 3968–3975.

[63] T. Matrab, M. M. Chehimi, C. Perruchot, A. Adenier, A. Guillez, M. Save, B. Charleux, E. Cabet-Deliry, J. Pinson, *Langmuir* **2005**, *21*, 4686–4694.

[64] D.-e. Jiang, B. G. Sumpter, S. Dai, *Journal of the American Chemical Society* **2006**, *128*, 6030–1.

[65] V. Stockhausen, J. Ghilane, P. Martin, G. Trippé-Allard, H. Randriamahazaka, J.-C. Lacroix, *Journal of the American Chemical Society* **2009**, *131*, 14920–14927.

[66] H. Gehan, L. Fillaud, M. M. Chehimi, J. Aubard, A. Hohenau, N. Felidj, C. Mangeney, *ACS nano* **2010**, *4*, 6491–500.

[67] R. Ahmad, A. Mocaer, S. Gam-Derouich, A. Lamouri, H. Lecoq, P. Decorse, P. Brunet, C. Mangeney, *Polymer* **2015**, *57*, 12–20.

[68] D. Graham, R. Brown, W. Ewen Smith, *Chemical Communications* **2001**, 1002–1003.

[69] W. E. Doering, S. Nie, *Analytical chemistry* **2003**, *75*, 6171–6.

[70] M. L. Coluccio, G. Das, F. Mecarini, F. Gentile, A. Pujia, L. Bava, R. Tallerico, P. Candeloro, C. Liberale, F. De Angelis, E. Di Fabrizio, *Microelectronic Engineering* **2009**, *86*, 1085–1088.

[71] P. White, J. Hjortkjaer, *Journal of Raman Spectroscopy* **2014**, *45*, 32–40.

[72] T. Base, Z. Bastl, Z. Plzák, T. Grygar, J. Plesek, M. J. Carr, V. Malina, J. Subrt, J. Bohácek, E. Vecerníková, O. Kríz, *Langmuir : the ACS journal of surfaces and colloids* **2005**, *21*, 7776–85.

[73] R. A. Sperling, W. J. Parak, *Philosophical Transactions of the Royal Society A: Mathematical Physical and Engineering Sciences* **2010**, *368*, 1333 LP – 1383.

[74] E. Reimhult, F. Höök, *Sensors* **2015**, *15*, 1635–1675.

[75] J. H. Waite, *Nature materials* **2008**, *7*, 8–9.

[76] V. Leviel, *Journal of Neurochemistry* **2011**, *118*, 475–489.

[77] R. Rodríguez, M. Blesa, A. Regazzoni, *Journal of colloid and interface science* **1996**, *177*, 122–131.

[78] H. Lee, N. F. Scherer, P. B. Messersmith, *Proceedings of the National Academy of Sciences* **2006**, *103*, 12999–13003.

[79] P. B. Messersmith, *Science (New York N.Y.)* **2010**, *328*, 180–181.

[80] F. Yu, S. Chen, Y. Chen, H. Li, L. Yang, Y. Chen, Y. Yin, *Journal of Molecular Structure* **2010**, *982*, 152–161.

[81] H. Lee, S. M. Dellatore, W. M. Miller, P. B. Messersmith, *Science (New York N.Y.)* **2007**, *318*, 426–30.

[82] P. Glass, H. Chung, N. R. Washburn, M. Sitti, *Langmuir* **2009**, *25*, 6607–6612.

[83] J. Ryu, S. H. Ku, H. Lee, C. B. Park, *Advanced Functional Materials* **2010**, *20*, 2132–2139.

[84] S. M. Kang, I. You, W. K. Cho, H. K. Shon, T. G. Lee, I. S. Choi, J. M. Karp, H. Lee, *Angewandte Chemie - International Edition* **2010**, *49*, 9401–9404.

[85] F. Bernsmann, A. Ponche, C. Ringwald, J. Hemmerlé, J. Raya, B. Bechinger, J.-C. Voegel, P. Schaaf, V. Ball, *The Journal of Physical Chemistry C* **2009**, *113*, 8234–8242.

[86] J. Liebscher, R. Mrówczyński, H. A. Scheidt, C. Filip, N. D. Hădade, R. Turcu, A. Bende, S. Beck, *Langmuir* **2013**, *29*, 10539–10548.

[87] D. R. Dreyer, D. J. Miller, B. D. Freeman, D. R. Paul, C. W. Bielawski, *Langmuir* **2012**, *28*, 6428–6435.

[88] M. Sugumaran, *Federation of European Biochemical Societies* **1991**, *1*, 4–10.

[89] M. Yu, T. J. Deming, *Macromolecules* **1998**, *31*, 4739–4745.

[90] K. Huang, B. P. Lee, P. B. Messersmith, *Abstracts of Papers of the American Chemical Society* **2001**, *222*, U319–U319.

[91] H. Lee, B. P. Lee, P. B. Messersmith, *Nature* **2007**, *448*, 338–341.

[92] J. L. Dalsin, B.-H. Hu, B. P. Lee, P. B. Messersmith, *Journal of the American Chemical Society* **2003**, *125*, 4253–4258.

[93] A. R. Statz, R. J. Meagher, A. E. Barron, P. B. Messersmith, *Journal of the American Chemical Society* **2005**, *127*, 7972–7973.

[94] X. Fan, L. Lin, J. L. Dalsin, P. B. Messersmith, *Journal of the American Chemical Society* **2005**, *127*, 15843–15847.

[95] A. R. Statz, J. Kuang, C. Ren, A. E. Barron, I. Szleifer, P. B. Messersmith, *Biointerphases* **2009**, *4*, FA22–32.

[96] H. Lee, J. Rho, P. B. Messersmith, *Advanced Materials* **2009**, *21*, 431–434.

[97] S. H. Ku, C. B. Park, *Biomaterials* **2010**, *31*, 9431–9437.

[98] M. E. Wiseman, C. W. Frank, *Langmuir* **2012**, *28*, 1765–1774.

[99] R. G. Couston, M. W. Skoda, S. Uddin, C. F. van der Walle, *mAbs* **2013**, *5*, 126–39.

[100] E. Steen Redeker, D. T. Ta, D. Cortens, B. Billen, W. Guedens, P. Adriaensens, *Bioconjugate Chemistry* **2013**, *24*, 1761–1777.

[101] A. Kausaite-Minkstimiene, A. Ramanaviciene, J. Kirlyte, A. Ramanavicius, *Analytical Chemistry* **2010**, *82*, 6401–6408.

[102] C.-C. Yu, Y.-Y. Kuo, C.-F. Liang, W.-T. Chien, H.-T. Wu, T.-C. Chang, F.-D. Jan, C.-C. Lin, *Bioconjugate Chemistry* **2012**, *23*, 714–724.

[103] M. K. Araz, A. A. Apori, C. M. Salisbury, A. E. Herr, *Lab on a Chip* **2013**, *13*, 3910–3920.

[104] P. Viel, J. Walter, S. Bellon, T. Berthelot, *Langmuir* **2013**, *29*, 2075–2082.

[105] X. Sun, D. Montiel, H. Li, H. Yang, *Bioconjugate chemistry* **2014**, *25*, 1375–1380.

[106] J. Davila, D. Toulemon, T. Garnier, A. Garnier, B. Senger, J.-C. Voegel, P. J. Mésini, P. Schaaf, F. Boulmedais, L. Jierry, *Langmuir* **2013**, *29*, 7488–98.

[107] M. Fairhead, M. Howarth in *Site-Specific Protein Labeling: Methods and Protocols*, Humana Press, New York, NY, **2015**, pp. 171–184.

[108] W.-B. Tsai, C.-Y. Chien, H. Thissen, J.-Y. Lai, *Acta Biomaterialia* **2011**, *7*, 2518–2525.

[109] H. Jiang, X. Weng, D. Li, *Microfluidics and Nanofluidics* **2011**, *10*, 941–964.

[110] Y. Luo, X. Liu, T. Jiang, P. Liao, W. Fu, *Analytical Chemistry* **2013**, *85*, 8354–8360.

[111] H.-W. Chien, W.-H. Kuo, M.-J. Wang, S.-W. Tsai, W.-B. Tsai, *Langmuir* **2012**, *28*, 5775–5782.

[112] E. Faure, C. Falentin-Daudré, C. Jérôme, J. Lyskawa, D. Fournier, P. Woisel, C. Detrembleur, *Progress in Polymer Science* **2013**, *38*, 236–270.

[113] S. V. Rao, K. W. Anderson, L. G. Bachas, *Mikrochimica Acta* **1998**, *128*, 127–143.

[114] C. Mateo, O. Abian, M. Bernedo, E. Cuenca, M. Fuentes, G. Fernandez-Lorente, J. M. Palomo, V. Grazu, B. C. C. Pessela, C. Giacomini, G. Irazoqui, A. Villarino, K. Ovsejevi, F. Batista-Viera, R. Fernandez-Lafuente, J. M. Guisan, *Enzyme and Microbial Technology* **2005**, *37*, 456–462.

[115] J. McMurry, *Organic Chemistry 7th edition*, Cengage Learning, **2007**, p. 1424.

[116] D. Brady, J. Jordaan, *Biotechnology Letters* **2009**, *31*, 1639.

[117] L. Chen, Y. Zhang, L. Tan, S. Liu, Y. Wang, *Journal of Separation Science* **2015**, *38*, 2915–2923.

[118] Y. Zhang, M. E. Lynge, B. M. Teo, R. Ogaki, B. Städler, F. Caruso, J. Hernando, F. Busqué, D. Ruiz-Molina, *Biomater. Sci.* **2015**, *3*, 1188–1196.

[119] C. Pan, L. Chen, S. Liu, Y. Zhang, C. Zhang, H. Zhu, Y. Wang, *Journal of Materials Science* **2016**, *51*, 2427–2442.

[120] Y. Zhang, L. Chen, C. Zhang, S. Liu, H. Zhu, Y. Wang, *Talanta* **2016**, *150*, 375–387.

[121] H. Wei, J. Ren, B. Han, L. Xu, L. Han, L. Jia, *Colloids and surfaces. B Biointerfaces* **2013**, *110C*, 22–28.

[122] D. Cullen, C. Lowe, *Sensors and Actuators B: Chemical* **1990**, *1*, 576–579.

[123] C. E. Taylor, S. D. Garvey, J. E. Pemberton, *Analytical Chemistry* **1996**, *68*, 2401–2408.

[124] D. J. Miller, M. C. Biesinger, N. S. McIntyre, *Surface and Interface Analysis* **2002**, *33*, 299–305.

[125] H. Piao, N. S. McIntyre, *Surface and Interface Analysis* **2002**, *33*, 591–594.

[126] E. D. Giol, D. Schaubroeck, K. Kersemans, F. De Vos, S. Van Vlierberghe, P. Dubruel, *Colloids and Surfaces B: Biointerfaces* **2015**, *134*, 113–121.

[127] A. Vesel, K. Elersic, *Applied Surface Science* **2012**, *258*, 5558–5560.

[128] H. Vaisocherová-Lísalová, I. Víšová, M. Laura Ermini, T. Špriner, X. Chadtová Song, J. Mrázek, J. Lamačová, N. Scott Lynn Jr, P. Šedivák, J. Homola, *Biosensors and Bioelectronic* **2016**, *80*, 84–90.

[129] Trelleborg Sealing Solutions, *Surface Finish (Measurement Methods) Ra -Arithmetic Average Roughness*, **2008**, `http://www.alphaomegapt.com/pdffiles/ SurfaceFinishDefinitions.pdf(accessed2017-06-12)`.

[130] Y. M. Shin, Y. B. Lee, H. Shin, *Colloids and Surfaces B: Biointerfaces* **2011**, *87*, 79–87.

[131] E. Van De Walle, I. Van Nieuwenhove, E. Vanderleyden, H. Declercq, K. Gellynck, D. Schaubroeck, H. Ottevaere, H. Thienpont, W. H. De Vos, M. Cornelissen, S. Van Vlierberghe, P. Dubruel, *Biomacromolecules* **2016**, *17*, 56–68.

[132] E. D. Głowacki, R. R. Tangorra, H. Coskun, D. Farka, A. Operamolla, Y. Kanbur, F. Milano, L. Giotta, G. M. Farinola, N. S. Sariciftci, *J. Mater. Chem. C* **2015**, *3*, 6554–6564.

[133] F. E. Bartell, J. T. Smith, *Journal of Physical Chemistry* **1953**, *57*, 165–172.

[134] P. C. Weber, D. H. Ohlendorf, J. J. Wendoloski, F. R. Salemme, *Science (New York N.Y.)* **1989**, *243*, 85–88.

[135] P.-C. C. Lin, D. Weinrich, H. Waldmann, *Macromolecular Chemistry and Physics* **2010**, *211*, 136–144.

[136] S. L. Capehart, A. M. Elsohly, A. C. Obermeyer, M. B. Francis, *Bioconjugate Chemistry* **2014**, *25*, 1888–1892.

[137] Y. Ai, Y. Wei, J. Nie, D. Yang, *Journal of Photochemistry and Photobiology B: Biology* **2013**, *120*, 183–190.

[138] W.-B. Tsai, Y.-H. Chen, H.-W. Chien, *Journal of Biomaterials Science-Polymer Edition* **2009**, *20*, 1611–1628.

[139] L. Chaiet, F. J. Wolf, *Archives of Biochemistry and Biophysics* **1964**, *106*, 1–5.

[140] A. Uehara, Y. Isaka, K. Hashikawa, K. Kimura, T. Kozuka, T. Kamada, H. Etani, S. Yoneda, M. Imaizumi, *Journal of Nuclear Medicine* **1988**, *29*, 1264–1267.

[141] V. D. Bhat, G. A. Truskey, W. M. Reichert, *Journal of Biomedical Materials Research* **1998**, *41*, 377–385.

[142] D. MacDonald, B. Rapuano, N. Deo, M. Stranick, P. Somasundaran, A. Boskey, *Biomaterials* **2004**, *25*, 3135–3146.

[143] X. Yu, Z. Xiong, J. Li, Z. Wu, Y. Wang, F. Liu, F. Ran, C. Zhao, P. Couvreur, *RSC Adv.* **2015**, *5*, 107949–107956.

[144] R. N. Wenzel, *Industrial and Engineering Chemistry* **1936**, *28*, 988–994.

[145] A. Tuteja, W. Choi, M. Ma, J. M. Mabry, S. A. Mazzella, G. C. Rutledge, G. H. McKinley, R. E. Cohen, *Science (New York N.Y.)* **2007**, *318*, 1618–22.

[146] J. Rosales-Leal, M. Rodríguez-Valverde, G. Mazzaglia, P. Ramón-Torregrosa, L. Díaz-Rodríguez, O. García-Martínez,

M. Vallecillo-Capilla, C. Ruiz, M. Cabrerizo-Vílchez, *Colloids and Surfaces A: Physicochemical and Engineering Aspects* **2010**, *365*, 222–229.

Chapter 5

Processing methodology for the development of polymer microfluidics

"As a species, we tend to be doers, forever shaping and reshaping the world to better suit our purposes."

— Mariella Frostrup

5.1 Introduction

Besides being mass-manufacturable, the microfluidic components of the envisioned LoC sensor are required to fulfill certain additional criteria to meet the standards associated with optical applications. First, the surface roughness should ideally be well below 120 nm, *i.e.* one fifth of the wavelength used during the detection of the target analyte. This threshold can be derived from equation 5.1 that shows the amount of light scattering induced by surface roughness (equation 5.1).[1]

$$TIS(R_q) = R_0[1 - e^{-(\frac{4\pi R_q \cos \theta_i}{\lambda})^2}] \tag{5.1}$$

herein R_q is the RMS surface roughness (equation 4.4, section 4.4.2), θ_i the normal angle of incidence and λ the wavelength of the incident light.

Equation 5.1 is plotted in figure 5.1 for the wavelength that is applied in the laboratory demonstrator (λ = 661 nm) at different angles of incidence. It is clear that for a given angle of incidence, more incident laser light is lost by scattering as the surface roughness increases. This implies that the sensor's sensitivity will also decrease as the relative difference between the baseline and the SPR signal will be substantially lower. Figure 5.1 also shows the influence of the angle of incidence. SPR experiments performed on aqueous solutions result in an SPR dip at angles of incidence in the range of 75-85°as derived by modelling the SPR phenomenon based on equation 1.7 (chapter 1) for the 661 nm wavelength that will be applied in the proof-of-concept demonstrator.[2] Similar resonance angles were previously reported by Roh *et al.* for a gold-coated prisms applied in the Kretschmann configuration.[3] At these angles, the above-mentioned 60-130 nm threshold thus limits the losses due to scattering to below 10-30% of the incident light.

Secondly, SPR relies on TM-polarised light to induce surface plasmon polaritons (section 1.4), which is why birefringence should be minimised in the sensor chips. Birefringence is the phenomenon whereby the refractive index depends on the propagation direction as well as the polarisation of the incident light. This can be a result of stress introduced in the polymer material during processing, resulting in a potential alteration of the incident light's polarisation when passing through the material. This leads to lower sensitivities since TE-polarised light is not SPR active. The extent to which material stress results in birefringence is governed by the elasto-optic effect. This relationship expresses the change in refractive index that can be observed when stress is applied to a material and thus is extremely relevant in e.g. the drawing of optical fibers.[4]

Birefingence is common in polymers as the polymer chains are 'frozen' in a particular conformation as a result of too fast cooling of the polymer melt following processing. For transparent samples,
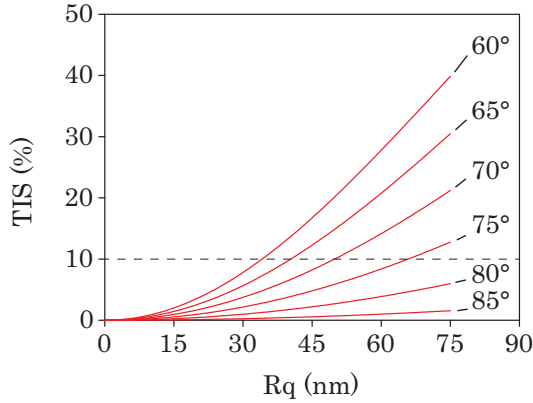
Figure 5.1: Graph showing the influence of a sample's surface roughness (R_q) on the observed total integrated scattering (TIS) at various angles of incidence for a wavelength of 661 nm.[1] For rougher samples, more incident light is lost due to scattering, which lowers the sensor's sensitivity.

these non-uniformities can easily be visualised by placing the sample between two crossed polarisers. The principle of this measurement is shown in figure 5.2. When two polarisers are fixed at an angle of 90°, no light will be able to pass the second polariser (figure 5.2a). When a birefringent sample is placed in between both polarisers, the polarisation of the propagating light will be altered resulting in a fraction of the original incident light to pass through the second polariser, or analyser (figure 5.2b). When this principle is applied in crossed polarisation microscopy, it becomes possible to visualise the non-uniformities in the sample, e.g. the material stress in an injection moulded part (figure 5.2c).[6] This effect is particularly significant when high aspect ratios are desired (e.g. the channels in microfluidic chips).[7] The presence of these features (i.e. the negative of a microfluidic channel) in the mould perturbs the flow of the melted material, thereby leading to additional stress in the material and the corresponding birefringence. Therefore, an optimisation process is needed to obtain the lowest level of birefringence in the obtained components.

Degradable polymers can be processed using similar techniques as applied for other thermoplasts keeping in mind their specific processing window. For example, the (co)polymers discussed in the pre-

(a)   **(b)**

(c)
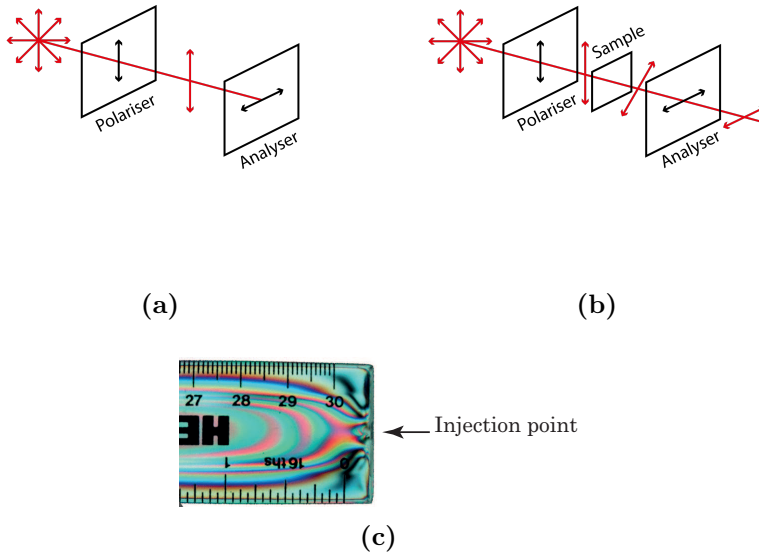
Figure 5.2: Schematic representation of the application of crossed-polarisers to demonstrate birefringence. No light will be able to pass through the crossed polarisers (a), unless a birefingent sample alters the light's polarisation before reaching the analyser (b). This is applied on a injection moulded ruler in (c), revealing the stress introduced by material flow.[5]

vious chapters show a thermal stability up to 280°C (chapters 2 and 3), thereby excluding higher processing temperatures. This stands in contrast with the high stability (> 400 °C) of e.g. cyclic olefin copolymers (COC) (see section 5.2). By selecting the appropriate processing parameters, polyesters can be processed into fibres, rods, films or moulded parts via extrusion, injection moulding, compression moulding or film casting.[8–10] 3D printing is currently also being explored as a tool for the production of complex parts composed of degradable materials, especially for prototyping of patient-specific implants in biomedical applications.[11–13]

As polyesters are prone to hydrolysis, the presence of moisture can lead to a decrease in molecular weight which may negatively affect the mechanical and thermal properties of the obtained parts. In

addition, water may act as a plasticiser, lowering the component's glass transition temperature. Therefore, contact with moisture during processing should be avoided and polymers should be properly dried prior to their processing.[8,9,14] The former can be ensured by performing the processing under inert atmosphere or *in vacuo*, while the latter can be achieved by drying the polymer material in a vacuum oven. Since amorphous polymer granules may fuse together when drying temperatures exceed the glass transition temperature, polymers are generally dried at room temperature.[8]

To minimise the above-mentioned stress-induced non-uniformities in the plastic parts, hot embossing will be applied to introduce microfluidic channels in plastics, since this technique is characterised by minimal material flow.[7] Next, laser welding will be applied to seal the thus obtained microstructured plastics. Before discussing the applied processing methodology in greater detail (section 5.3), the thermal properties of the materials that will be applied in this chapter will be discussed in the following section in order to select the appropriate processing parameters.

5.2   Characterisation of commercial polymers

As mentioned in chapters 2 and 3, the attainable quantities of the degradable polyesters developed within the framework of this PhD thesis were constrained to approximately 2 g as a result of the limited scale of the monomer syntheses and the large discrepancy between the obtained and the targeted molecular weight. For this reason, the processing methodology applied in the present chapter will be evaluated for a series of commercially available polymers. The applied materials are listed in table 5.1 and have been grouped based on their physicochemical similarities as will be discussed in section 5.4.2. The materials include a transparent grade of the biodegradable PLLA as well as other thermoplasts that are commonly applied for the fabrication of microfluidics.[15] Like the materials developed in the context of this PhD thesis (chapters 2 and 3), most materials are amorphous and transparent polymers. However, in order to be able to fully evaluate the potential of the laser welding process in microfluidic applications, also the opaque HDPE, PP and ABS were included. Full

details on the suppliers and applied grades is provided in the materials and methods (appendix A).

Since the processing of thermoplastic polymers is commonly performed in the melt phase, the materials' thermal stability was first determined via thermogravimetric analyses (TGA). As already discussed in chapters 2 and 3, these measurements allow the determination of the upper processing temperature, since processing a material near its degradation onset temperature may result in lower molecular weights compared to the applied granules.[16] This in turn affects the part's mechanical, optical as well as thermal properties (e.g. the T_g).[17]

The obtained degradation temperatures (1% mass loss) and the amounts of residue at 750 °C are listed in table 5.1. The results show that all materials under investigation are sufficiently stable to allow commonly applied processing methods, with degradation onsets starting at temperatures of 261 °C or higher. Two materials showed a much higher amount of residue as compared to the other materials under investigation. Poly(carbonate) (PC) was shown to give rise to more than 20% of residue. This observation can be easily rationalised by the polymer structure, which is characterised by aromatic rings present in the polymer main chain. These increase the chain's stiffness, thereby increasing stability and resulting in the formation of carbonaceous material known as char.[18] All other materials consist of aliphatic polymers, allowing complete degradation at elevated temperatures as indicated by the < 1% residue at 750 °C.[19]

Next, the materials were subjected to DSC analyses. The maximum temperature was set to the degradation onset (i.e. the temperature at which 1% mass loss was observed during the TGA experiments). For all materials, the glass transition temperature was derived and reported in table 5.1. Additionally, for some (semicrystalline) materials (HDPE, PA6, PP and PLLA), a melting transition could be observed. For the latter samples, the obtained melting temperatures and corresponding melting enthalpies have also been included in table 5.1. Since the softening temperature of a material is determined by either the T_g or, if present, the T_m, these experiments allow the determination of the lower processing temperature: the minimal temperature at which a polymer melt can be obtained.

Table 5.1: Overview of physicochemical material properties. The polymers are grouped based on physicochemical similarities (e.g. transparent/opaque, aromatic/aliphatic polymers) [a] Temperature corresponding to 1% mass loss; [b] Value obtained at 750 °C; [c] Derived from size exclusion chromatography; [d] Values obtained from the materials' melt-flow index; [e] Values obtained via viscosimetry in formic acid at 25 °C; [f] A value of -115 °C was reported by the supplier

Group	Material	$T_{\text{degr.}}$[a] [°C]	Residue[b] [%]	T_g [°C]	T_m [°C]	ΔH_m [J g^{-1}]	ΔH_c [J g^{-1}]	ΔH_{fus} [J g^{-1}]	DC [%]	M_n [kg/mole]	Đ[c] [-]
1	PC	421	23.09	143	-	-	-	-	-	19.9[c]	1.8
2	ABS	340	0.8	101	-	-	-	-	-	71.0[c]	2
	HDPE	416	0.15	< -90[f]	132	212.4	-	245	86.7	32-35[d]	-
	PA6	261	0.55	49	220	69.9	-	230	30.4	55.9[e]	-
	PP	380	0.68	-6	164	103	-	207	49.6	11.9-13.4[d]	-
3	COC	419	0.12	75	-	-	-	-	-	54.4[c]	1.8
	PLLA	296	0.67	54	164	41.1	32.4	93	9.4	65.1[c]	1.6
	PMMA$_{55}$	304	0.5	110	-	-	-	-	-	55.4[c]	1.7
	PMMA$_{58}$	288	0.25	104	-	-	-	-	-	58.0[c]	1.7
	PMMA$_{87}$	281	0.1	102	-	-	-	-	-	87.0[c]	1.6
	PS	285	0.17	83	-	-	-	-	-	98.0[c]	1.8

Besides the thermal properties, the molecular weight (M_n) of the studied materials was also determined, since chain length is one of the parameters determining the viscosity of macromolecules in the molten state.[20] The results which are listed in table 5.1, show that the molecular weights ranged from 11.9 kg mol^{-1} (PP) to 97.9 kg mol^{-1} (PS). Most samples were analysed via size exclusion chromatography (SEC), with the exception of PA6 and the polyolefins PE and PP due to their low solubility in common organic solvents. PA6 was therefore dissolved in formic acid and the resulting solution analyzed via capillary viscosimetry. The obtained relative and reduced viscosities were subsequently applied in the Billmeyer equation (equation 5.2) to estimate the intrinsic viscosity:[21]

$$[\eta] = 0.25 \, \eta_{red} + 0.75 \, ln(\frac{\eta_{rel}}{C}) \tag{5.2}$$

in which η_{rel} is the relative viscosity ($\eta_{rel} = \frac{\eta_{solution}}{\eta_{solvent}}$), η_{red} is the reduced viscosity ($\eta_{red} = \frac{\eta_{rel}-1}{C}$) and C the concentration of the polymer in g mL^{-1}.

The thus obtained value was in turn entered in the Mark-Houwink-Sakurada equation (equation 5.3).[22]

$$[\eta] = K \times M^a \tag{5.3}$$

in which $[\eta]$ is the intrinsic viscosity, M the average molecular weight, and K and a specific constants depending on the polymer, the applied solvent and the temperature.

The molecular weight of both polyolefins (HDPE and PP) was determined based on their reported melt flow indices.[23] This technique relies on the viscosity of the polymer melt and is thus commonly applied for polyolefins given their troublesome dissolution in organic solvents. For the materials analysed via SEC, the associated molecular weight distributions (Đ) were relatively high (> 1.6). Although the presence of chains with different lengths will result in more ill-defined properties (e.g. glass transition and melting temperatures),[18] these dispersity values are common for commercially available polymers applied for optical applications and were thus appropriate to be considered in the present work. Besides the different thermoplasts included in table 5.1, two additional grades of PMMA were included

to be able to assess the influence of molecular weight on the laser welding potential (section 5.4). As can be derived from table 5.1, the selected grades differ in molecular weight, while their thermal stability and glass transition temperature are very similar. PMMA was selected since this material is commonly applied in microfluidic prototypes.[24,25]

5.3 Processing of polymer granules

As already mentioned in this chapter's introduction (section 5.1), the fabrication of microfluidic sensors for optical biosensor applications should be performed in such a way that the surface roughness (R_q < 60-130 nm) as well as material stress resulting in birefringence are minimised. This can be achieved by combining hot embossing to introduce microfluidic channels with laser welding as a straightforward method to bond thermoplasts. Both techniques will be discussed in greater detail in section 5.4 and section 5.5. However, hot embossing requires flat polymer sheets into which the negative image of the mould is introduced, since the attainable surface roughness is limited by the size of the polymer granules when these are applied directly in the hot embossing process.[7] In order to be able to reach optical quality (R_q < 60-130 nm), the materials discussed in section 5.2, were therefore first processed into 1 mm thick polymer sheets at the Flemish Plastic Centre (Vlaams Kunststofcentrum, Kortrijk) via injection moulding.

Injection moulding is a common technique to process three-dimensional objects and thus can also be applied to produce smooth polymer disks or sheets. The process consists in a first part of melting the polymer material (as a granulate) in an extruder (figure 5.3). The rotating screw transports the material towards the nozzle. As the material moves forward, it is melted by both external heating elements as well as internal friction. In addition, the material gets compressed as the screw diameter gradually increases towards the nozzle.[10]

In modern injection moulding devices, a reciprocating screw is used. During the loading step, the screw moves back and the necessary amount of polymer melt is collected near the nozzle. During
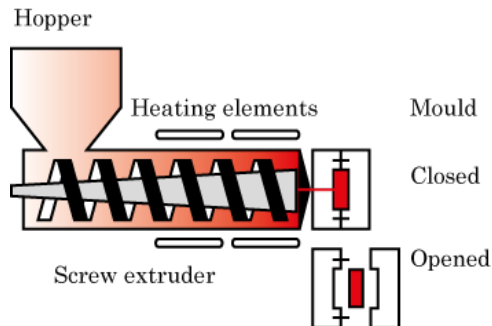
Figure 5.3: Schematic representation of the injection moulding process. Polymer granulate is added to a hopper and subsequently molten and transported by a reciprocating screw extruder. Once the nozzle is filled the molten thermoplast is injected in the closed mould. After an appropriate cooling time, the mould opens and the desired object is released.

the injection step, the molten material is then forced into the closed mould by moving the screw forward. Once the material has sufficiently cooled down, the object is released from the mould and the process is repeated. Given the very short cycle times (seconds to minutes depending on e.g. the mould design), injection moulding allows the fast replication of objects, thus increasing turnover while reducing costs.[7]

Taking into account the influence birefringence may have on the optical performance of moulded polymers (section 5.1), film injection was preferred over the more common point injection (figure 5.4). In the former case, the melted polymer is introduced via a wide opening (figure 5.4a) making the polymer flow in a straight line towards the opposing side of the mould. In contrast, point injection implies a radial expansion of the polymer into the mould (figure 5.4b). This introduces additional stress in the material, especially around the point of injection (as previously shown in figure 5.2c) and other features like corners and edges.

To justify the choice for film injection, PS samples previously prepared via conventional injection moulding (point injection) were evaluated using polarisation microscopy (figure 5.5). As can be seen in these figures, material stress is clearly present and appears as orange

(a) **(b)**
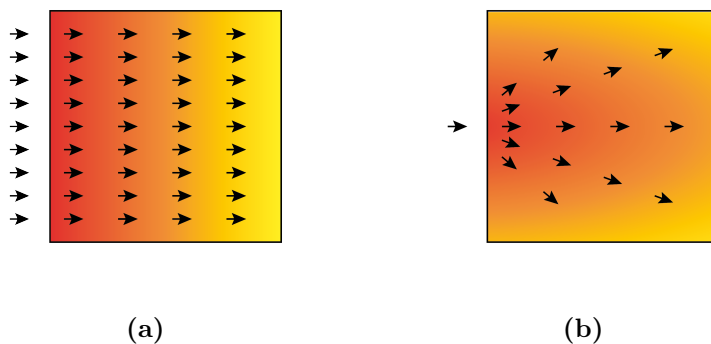
Figure 5.4: Illustration of the difference between film (a) and point injection (b). Film injection results in a more uniform flow pattern thereby reducing birefingence resulting from material stress.

and blue streaks when polarised light is applied to illuminate the sample.

5.4 Bonding of microfluidics via laser welding

Laser welding is a technique that is gaining interest in the field of LoC development since it enables the joining of polymer parts by locally melting the polymer material. The principle has been employed in industrial manufacturing for the welding of metals for some decades.[26,27] Since the advent of high power laser diodes in the 1990s, the field of laser welding has experienced new developments and improvements in recent years.[28–30] New applications have emerged which include the bonding of microfluidics to obtain leak-proof chips, where laser welding has become competitive with the already proven techniques such as thermal, adhesive and solvent bonding, argued in an extensive bonding review article by Tsao *et al.*[15] The latter methods are associated with considerable limitations, such as the requirement of pre- or post-processing. Particularly in optical biosensor applications, for which light needs to propagate through the welded layers, transparency and optical quality of the fluidic components are desired.

(a)   **(b)**
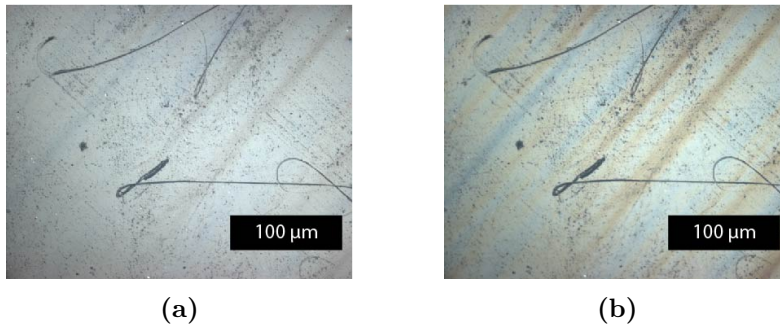
Figure 5.5: Visualisation of material stress via polarisation microscopy. (a) shows the PS sample obtained via injection moulding under illumination with unpolarised ligth. When polarised light is applied (b) stress lines appear as blue and orange streaks.

Glasses such as silica have played an important role in microfluidic device development. However, so far successful reports on the laser welding of glass are scarce and only weak bonding strengths up to several kPa have been achieved, which is insufficient for most microfluidic applications (> 1 MPa).[31] Many groups have also reported on the cracking of glass upon laser welding, but this can be avoided by selecting the appropriate sample preparation.[32] Weld strengths have also increased to 50-100 MPa by laser welding through ultrashort pulses focused at the interface of both layers which results in nonlinear absorption.[31,33,34]

Plastics have become attractive materials for microfluidic applications owing to their straightforward surface modification and shaping, low cost, disposability and optical properties.[25] Some thermoplasts were shown to lend themselves perfectly towards laser welding, since they can be heated until molten and re-solidify to their original state shortly after. Extensive modeling of this process has already been performed, such as by use of finite element methods,[35] or response surface methodology to predict weld strengths and seam widths.[36] A recent overview of these different simulation methods can be found in a review by Dal *et al.*[37]

Within laser welding, a distinction can be made between butt joint-welding, in which the edges of the materials are melted by a perpendicularly incident laser, and Through Transmission infrared
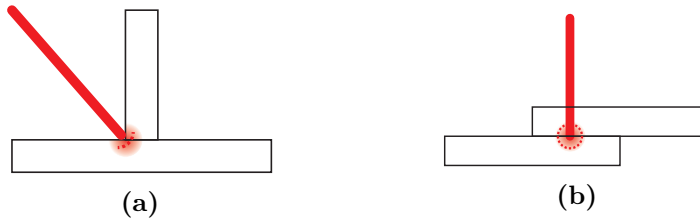
Figure 5.6: Visual representation of two welding methods, with (a) showing the butt joint welding of two parts that are positioned perpendicular to each other and (b) showing TTir welding of two overlapping sheets.

(TTir) laser bonding, in which the 'through transmission' refers to the fact that the laser passes through one sample plate to melt the interface between both plates. Both processes are schematically depicted in figure 5.6.

TTir is the most relevant technique for the sealing of LoCs and offers several advantages over other methods. The most important one is that TTir laser bonding is a pre-assembled method, which means that during bonding, only relative motion between the laser beam and the object is observed, while additional movement of the individual parts with respect to each other is prohibited.[38] Other important aspects are the instantaneous bonding and the highly localised heating, which limits possible damage to the vicinity of the weld seams.

On the other hand, some challenges associated with TTir remain. First, surfaces must be in intimate contact, as any gaps can result in voids, poorly welded regions or even failure of the component.[38,39] In addition, the laser scanning speed and laser power should be optimised to prevent deformation during welding. Since the laser needs to transmit through the top layer before reaching the interface and maintain enough energy to cause local melting, there are also some limitations in terms of part thickness and optical transmission.

Within TTir welding, two strategies can be distinguished. To date, the majority of applications focuses on clear-to-absorbing welding in the wavelength range of 800-1100 nm.[40] In this range, most of the common thermoplasts show high transmissions ($> 90\%$) and therefore an absorbing medium has to be added to efficiently absorb the incident laser energy. The absorbing medium comes in the form of an absorbing bottom layer under a transparent top layer (*e.g.* PMMA

on ABS) or two transparent layers with an intermediate absorbing layer.[39,41–47]

5.4.1 Clear-to-clear welding of thermoplasts

Besides adding an absorbing medium to the otherwise mostly transparent thermoplastics (800-1100 nm), other methods work in different wavelength ranges, at which the absorption characteristics are different and the use of an absorber is obsolete. These methods were uncommon until 7 years ago, but the recent rise of high power solid state and fiber lasers has led to an exponential growth of application fields, especially for wavelengths around 2 µm.[48–52]

True clear-to-clear welding may thus serve as a valuable tool in the bonding of microfluidics, thereby outperforming alternatives like thermal and solvent bonding with respect to achieving leak-proof channels. As already mentioned, these may result in deformation of the channels, which is undesirable since SPR is an optical detection method.[15] Indirect bonding by applying a layer of adhesive between both layers has also been explored, but the process becomes much more complex as clogging of the channels by the adhesive needs to be avoided.[53,54]

In order to determine the applicability of TTir laser welding for the development of microfluidics, the injection moulded plates (section 5.3) were first milled to square samples of 24 x 24 mm^2 that were welded together under a single lap shear joint. Two samples were placed over each other with an overlap region of 10 mm, as illustrated in figure 5.7. The weld structure was chosen based on the most common approach of using at least one transverse uniform weld line perpendicular to the direction of the shear tests to be performed. Several groups have opted for similar patterns using multiple (3) parallel transverse weld lines to distribute the applied force during shear tests more evenly.[55] To ensure even higher uniformity and to average out the performance difference between perpendicular and parallel weld lines, several parallel weld lines were added over the transverse lines, effectively obtaining an interconnected, uniformly welded rectangle optimizing tension distribution. The chosen grid of intersecting weld lines forms a rectangle of 20 x 8 mm^2, on the overlap area of both samples (24 x 10 mm^2), with 3 vertical lines and 6 horizontal
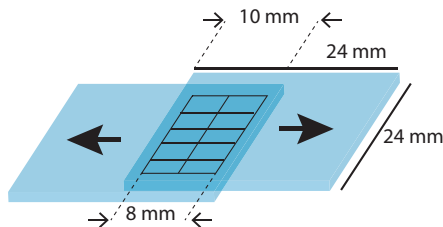
Figure 5.7: Illustration of the weld pattern on the overlap of two samples, along with the direction of the shear force on both samples in the performed shear tests.

lines with evenly distributed interdistance of 4 mm horizontally and vertically. This results in an effectively bonded surface area of 20.88 mm^2, taking into account weld seams with a 200 µm width (obtained as the width above the burn threshold from spray paint tests at 10 W laser power indicating the area where the polymer material will effectively melt).

Then, the shear strength of the welded bonds was evaluated in a typical adhesive lap joint shear strength test. This procedure is often used as a reference test to determine the bonding strength for a variety of bonding methods. [45,56,57] The welded samples were placed in a tensile tester with each polymer plate being fixed in one of the clamps. The deformation associated with the application of a certain force is recorded. Figure 5.8 shows a representative curve obtained for laser welded PMMA$_{55}$.

Table 5.2 shows the results of the shear tests performed on the different materials. The experimentally determined 'weldable range' is displayed, which gives an indication of the performance of the different materials across a range of different laser power densities (PDs), along with the optimal PD for each material. The latter was determined as the PD at which the highest shear strength was achieved in a reproducible manner. The mean value of the obtained shear strengths with corresponding standard deviations are included in table 5.2. Only materials that consistently resulted in reliable welding were considered. PA6 and PC did not and were therefore omitted.

The shear strength values in table 5.2 are given as strength per surface (MPa), which can be obtained from the force (N) at failure
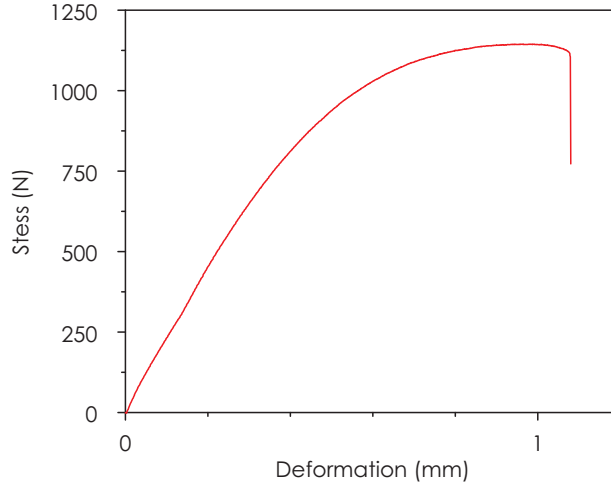
Figure 5.8: Stress-strain curve obtained for the shear strength experiment of laser welded PMMA.

tests by taking into account the total welded area (22.88 mm^2), according to the formula for shear stress (equation 5.4).
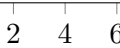
$$\tau = F_p/A \tag{5.4}$$

herein τ is the shear stress in MPa, F_p the weld strength in N and A the surface area in mm^2.

Successful examples of leak-proof channels after bonding have been shown to be possible from a minimum value of 1.43 MPa for PC and 1.92 MPa for PMMA,[58] while other researchers report microfluidic channel failure at pressures around 10 MPa for COC.[15] Other successful attempts do not mention any recommended shear strengths, as mechanical evaluation was not performed.[46,59] To account for the large range of recommended shear strengths found in literature and the variety of materials considered in the present chapter, in the current PhD thesis a benchmark value of 5 MPa was selected to evaluate laser welding's potential towards microfluidic chip bonding. Based on this value, the obtained shear strength values shown in table 5.2 indicate sufficient mechanical strengths for a number of materials at their optimal PD. The most promising candidates in this

Table 5.2: The range of power densities at which the materials were successfully welded are shown as a bar, together with the optimal laser power density (PD_{opt}) and average obtained shear strength at this power density with corresponding standard deviations (τ_{opt}).

Material	Power Density [kW mm^{-2}]	PD_{opt} [kW mm^{-2}]	τ_{opt} [MPa]
ABS		4.82	4.61 ± 2.69
COC		2.11	10.96 ± 1.03
HDPE		3.01	3.31 ± 1.42
PLLA		4.82	25.86 ± 0.69
PMMA$_{55}$		4.22	21.11 ± 2.21
PMMA$_{58}$		4.22	17.66 ± 6.10
PMMA$_{87}$		4.22	4.37 ± 1.17
PP		3.62	0.95 ± 0.75
PS		3.62	8.95 ± 4.00

2   4   6

respect are COC, PLLA, PMMA$_{55}$ and PMMA$_{58}$, which all consistently resulted in welds above 5 MPa. Also PS showed mean weld strengths above 5 MPa, but caution is advised for the latter given the relatively high associated standard deviation.

To benchmark the methodology applied in the present work, the above-mentioned shear strengths were compared to values reported in the state-of-the-art. However, it should be noted that a fair comparison is difficult as the applied laser welding set-ups were operating at different wavelengths or relied on non-linear absorption of pulsed lased light. Moreover, the applied polymer samples are generally not characterised in depth and the influence of e.g. the polymer molecular weight has not yet been reported in this context. Keeping these considerations in mind, the obtained results were thus compared from an application point of view with the optimal shear strength as main descriptor (table 5.3).

COC has already been reported to yield high shear strengths via solvent bonding (34.6 MPa),[60] but recently this material was also welded using a femtosecond fiber laser, achieving a shear strength in excess of 40 MPa.[61] Both values are significantly higher than our

average of 10.96 MPa. But this difference can be attributed to the non-linear absorption, which was previously introduced as a way to weld glass (section 5.4).

PMMA was successfully welded at 1030 nm by Volpe *et al.*, but no shear tests were performed.[59] However in a previous report, Yussuf *et al.* obtained weld strengths of 1-2 MPa for PMMA, using a high frequency microwave system at 2.45 GHz which corresponds to a wavelength of 122.4 mm.[58] Other researchers realised shear strengths of 13 MPa by applying a Thulium fiber laser at 2 µm.[50]

PS in turn was previously welded at 808 nm resulting in weld strengths of 14 MPa taking into account a weld seam width of 1.5 mm.[45] The latter result is higher than the value of 8.95 MPa obtained in this PhD at 1940 nm. However, the report of Juhl and co-authors can not be considered TTir laser welding as the authors added 0.4 wt% carbon black into the absorbing PS layer.

The laser welding of PLLA has only been reported once, with obtained strengths of around 15 MPa, well below the value obtained at 1940 nm.[62] In the same report, laser welding was shown to be superior to solvent bonding using chloroform.

Regarding the materials with a slightly lower performance in the shear tests, ABS was welded before at 808 nm with an average force at failure of around 300 N, for an irradiated surface of 40 x 0.75 mm^2, converting into 10.02 MPa.[63] This value exceeds the 4.61 MPa obtained at 1940 nm. Since this material is also styrene-based, this agrees with the hypothesis that laser welding at 808 nm is better suited for polystyrene.

Finally for HDPE, a maximum force at failure of 103 N was reported for welding at 532 nm.[47] Taking into account the covered surface area that corresponds to an unfocused laser spot of 100 mm^2, this would convert into 1.03 MPa, which is substantially lower than the value of 3.31 MPa at 1940 nm obtained in the present work.

5.4.2   Relating material properties to weldability

Given the relatively recent interest in laser welding for the development of LoCs, to date most efforts focused on the optimisation of the laser welding process towards a specific material. However, since the optical and thermal properties may differ fundamentally

Table 5.3: Comparison of the obtained shear strengths (τ) to values previously reported in literature. The main distinction between the applied set-up herein with the literature reports is indicated by specifying the experimental parameters applied in literature.

Material	$\tau_{Measured}$ [MPa]	$\tau_{Literature}$ [MPa]	Exp. parameters	Ref.
COC	10.96 ± 1.03	> 40	220 fs pulsed laser $\lambda = 1028$ nm	61
PMMA	21.11 ± 2.21	1-2	$\lambda = 122.4$ mm	58
		13	$\lambda = 2$ μm	50
PS	8.95 ± 4.00	14	$\lambda = 808$ nm	45
PLLA	25.86 ± 0.69	15	200 ns pulsed laser $\lambda = 1064$ nm	62
ABS	4.61 ± 2.69	10.02	$\lambda = 808$ nm	63
HDPE	3.31 ± 1.42	1.03	$\lambda = 532$ nm	47

when comparing different polymers, this section focuses on the correlation between welding performance and a number of selected polymer descriptors including among others optical transparency at 1940 nm, the glass transition temperature and the polymer molecular weight. In what follows, the influence of these properties on the weldability will be discussed.

Influence of transparency

First, the optical characterisation of the samples was performed by measuring the transmission in a wavelength range from 1900 nm to 1980 nm. The response of the materials in this range indicates how much energy absorption around 1940 nm is required for welding to occur.

In line with literature, absorption, being the main optical performance indicator, was used as the predictive parameter. This value was calculated from the transmission using the Lambert-Beer law:[47,52]

$$A = log\frac{I_0}{I_t} \tag{5.5}$$
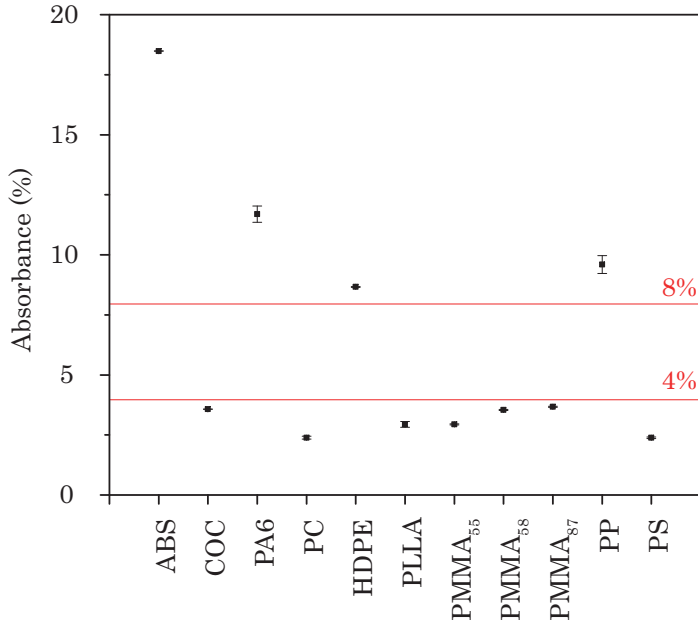
Figure 5.9: The absorbance of commercial thermoplasts at 1940 nm.

in which I_0 is the intensity of the incident light and I_t the intensity of the transmitted light.

Figure 5.9 shows that the absorption of materials resulting in welds strengths above 5 MPa, all lie below 4%. Other materials showed absorptions of more than 8% and performed poorly, which may indicate that a too large portion of the incident light energy had already been absorbed thereby hampering the efficient laser welding of these samples.

It should be noted that figure 5.9 excludes the influence of Fresnel reflection at normal incidence. For an interface between two media with a different refractive index, the Fresnel equations can be simplified to:[64]

$$R = (\frac{n_1 - n_2}{n_1 + n_2})^2 \tag{5.6}$$

With R the reflectance for a light beam passing from a medium with RI n_1 to a second medium with RI n_2.

From equation 5.6 it can be derived that approx. 4% of the incident light is lost due to reflection on an air ($n_1 \approx 1$) to glass ($n_2 \approx 1.5$) interface. Since the RI values for the studied polymers range from 1.4586 to 1.5915 for PLA and PS (both at 589.3 nm), respectively, the refractive index values are close to that of glass (e.g. 1.5159 for BK7 glass, at 589.3 nm). This implies that the reflectance of these materials will be very similar (approx. 4%).[65] The difference between the sample with the lowest RI (i.e. PLA, R = 3.4%) and the sample with the highest RI (i.e. PS, R = 5.2%) is < 2% based on equation 5.6. Therefore the influence of reflectance was not taken into account. Moreover, as was discussed in chapters 2 and 3, the refractive index decreases with increasing wavelength of the incident light, it is thus expected that at 1940 nm the effect will be lower than at 589.3 nm. However the true extent of the effect of reflectance could not be derived since no refractive indices have been reported at 1940 nm for the studied materials as conventional refractometers operate at much lower wavelengths.[66]

Although PC showed low absorption at 1940 nm, this material did not result in reliable welds for reasons that will be discussed in the upcoming section.

Influence of thermal properties

The welding process starts by locally heating the sample allowing the polymer chains to gain segmental motion. The formed entanglements will resolidify upon cooling and will act as physical cross-links between both polymer sheets. As a second pillar, the determination of the materials' thermal transitions was therefore performed in order to better understand the welding process and to determine the correlation of the thermal properties with the materials' weldability.

When the obtained weld strengths are plotted against the glass transition temperatures, the studied materials could be grouped as shown in figure 5.10. The sample present in group **I** (i.e. PC) contains aromatic moieties along the polymer main chain and does not result in welds at all. For this material, the local heating of the samples leads to degradation rather than welding, as the stiffness of the polymer chains opposes the formation of entanglements.[67–69] When the weldability of the samples is compared to the TGA results (section 5.2), it seems
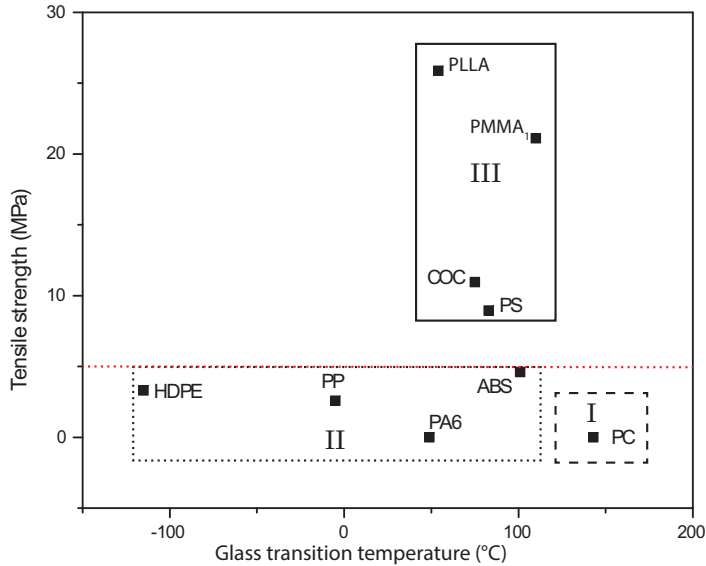
Figure 5.10: Plot showing the obtained weld strengths as a function of the glass transition temperature. Materials included in group **I** did not weld as a result of the presence of aromatic moieties along the polymer backbone; materials in **II** are characterised by higher degrees of crystallinity which led to inefficient welding; group **III** represents amorphous polymers characterised by strong welds.

apparent that polymers with aromatic backbones are inadequate for welding applications and are concomitant with char formation, as was indeed observed during the welding process.[70,71]

Next, the materials in group **II** consist of the semi-crystalline materials. As shown in table 5.1, PA6 had the highest melting point of the materials under investigation and exhibited a degree of crystallinity of 30.4% despite its clear appearance. It is therefore suggested that like chain rigidity, crystalline domains may oppose efficient welding of two polymer layers. This would also explain the unsatisfactory welding of polyethylene and polypropylene. By comparing the obtained melting enthalpies (ΔH_m) with the heat of fusion (ΔH_{fus}) for 100% crystalline materials (theoretical assumption), the degree of crystallinity (DC) could be derived and compared for the

semi-crystalline materials (table 5.1).* In case of PLLA, a signific-
ant amount of cold crystallisation was observed in the first heating
step, indicating that the material was unable to completely crystal-
lise in contrast to the readily crystallising HDPE, PP and PA6.[73]
Since laser welding occurred on the samples without any thermal
pretreatment, the obtained melting enthalpy was corrected by sub-
tracting the crystallisation enthalpy (ΔH_c). This resulted in a DC
of 9.4% for PLLA, which is considerably lower than for the other
semi-crystalline samples. It can be anticipated that scattering of the
incident laser light on the crystalline domains of HDPE, PP and PA6
was the reason for their reduced welding performance as previously
proposed by Rudolf Klein for clear-to-absorbing laser welding.[74]

Finally, the samples found in group **III** are characterised by strong
welds. These materials include the amorphous polymers with a re-
latively high glass transition temperature (> 50 °C). The polymer
chains thus gain sufficient mobility upon laser irradiation, while the
formed entanglements result in physical cross-links being established
at room temperature.

The opaque ABS forms a notable exception to the previous group
and was included in group **II** instead, even though ABS is an amorph-
ous material. Although ABS is commonly presented as a terco-
polymer, it consists of a continuous phase of styreneacrylonitrile co-
polymer (SAN) and a non-continuous rubber-like poly(butadiene)
phase.[75–77] Considering the reduced transmission at 1940 nm meas-
ured for ABS, scattering on the poly(butadiene) phase is anticipated
to reduce the effective laser power similarly to semi-crystalline ma-
terials, yielding poor weld strengths.

Influence of molecular weight

Finally, the influence of the molecular weight on the weldability was
studied for PMMA. Recalling table 5.1, three grades of PMMA were
included in the present study. When comparing the molecular weights
of these samples with the obtained shear strengths (table 5.4), weld-
ing performance decreased as the molecular weight increased. Since

---

*This methodology is commonly applied as a straightforward assessment of the
degree of crystallinity. However, more precise calculations are possible based on
the material's heat capacity in the liquid and solid state.[72]

the thermal and optical properties of the studied grades were found to be very similar (table 5.1 and figure 5.9), the effect is attributed to the influence of molecular weight on the melt viscosity of a material.[20] Indeed, as the viscosity increases, the formation of entanglements between both polymer plates would be impeded. A similar observation has been previously made for laser welding in the clear-to-absorbing regime.[78]

When plotting the shear strength of the other studied materials as a function of molecular weight, no clear trend was observed, indicating that the effect of molecular weight is material-dependent and should thus be derived for each material individually.

5.5   Fabrication of microfluidics via hot embossing

As mentioned earlier, the introduction of stress in the moulded parts occurs faster via injection moulding techniques, rendering hot embossing a more appropriate method to introduce microfluidic channels considering the application of polarised light in SPR-based sensors.

Hot embossing consists of a two-step process in which an appropriate mould is inserted into the hot embossing machine together with a thin thermoplastic polymer film. The process starts when the mould and polymer are heated in a vacuum chamber to a temperature slightly above the glass transition temperature.[79] This prevents air being trapped between the mould and the polymer, which would lead to incomplete filling of the cavities. Next, the heated mould is

Table 5.4: Obtained shear strengths (τ_{opt}) obtained for the three PMMA grades differing in molecular weight after laser welding at PMMA's optimal power density (4.22 kW mm^{-2}).

Material	M_n [kg mol^{-1}]	Đ [-]	τ_{opt} [MPa]
PMMA$_{55}$	55.4	1.7	21.11 ± 2.21
PMMA$_{58}$	58.0	1.7	17.66 ± 6.10
PMMA$_{87}$	87.0	1.6	4.37 ± 1.17
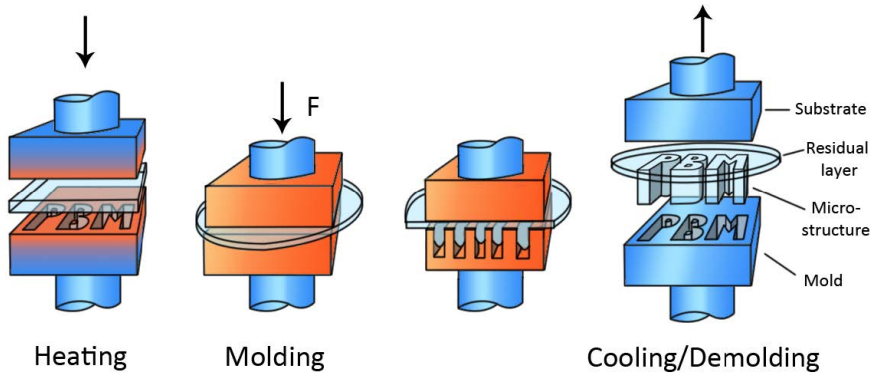
Figure 5.11: Schematic representation of the hot embossing process. The polymer sheet is heated and subsequently indented with a heated stamp. The polymer fills the cavities and after cooling the negative image of the mould is effectively transferred into the polymer. Image adapted from literature.[7]

pressed into the material using a high force (typically several tens of kN) to ensure the complete replication of the mould. The pressure is maintained during cooling, to compensate for part shrinkage. By cooling the set-up below the material's glass transition temperature, the negative image of the mould is fixated in the material and the part is demoulded.[80–82] A schematic representation of the process can be found in figure 5.11. Typical for the hot embossing process, is the occurrence of a residual layer (*i.e.* the flash) around the microstructure owing to the fact that the press and the mould are not closed completely.

It is important to note that the polymer only has to flow a very short distance (i.e. the size of the features of the mould) into the mould.[7] Moreover, the temperatures at which hot embossing is performed are generally lower than those required for e.g. injection moulding. It was proposed that the temperature difference between the embossing and de-embossing step should be as low as 25-40 °C to reduce thermal stress in the formed objects.[83] This implies that the polymer will not experience viscous flow inside the hot embosser. Instead, 'squeeze flow' is observed, which greatly reduces the amount of stress being introduced in the material, which is the reason why hot

embossing is preferred over injection moulding for the development of optical biosensors. The flow behaviour has been extensively studied both experimentally as well as via modelling approaches. [84–87]

In addition, the hot embossing process provides a lower cost per moulded part considering a low to intermediate number of replications compared to injection moulding. [7] Only for very large batches (approximately 5×10^3 pieces), the cost per part becomes lower for injection moulding.

As a proof of concept for the envisioned application, a microfluidic channel test design was hot embossed in three materials that performed well in the laser welding experiments i.e. PLLA, PS and COC. The first two were selected as a model for the materials developed in chapters 2 and 3 as PLLA is a polyester while poly(mandelic acid)'s thermal property closely match to those of poly(styrene). COC was included given its excellent properties with respect to microfluidic applications including high solvent resistance, excellent optical transmittance in the visible and UV part of the spectrum and good resistance to acids and bases. [15]

A metal mould that represents a negative of the microfluidic channel was first produced, taking into account existing design restrictions e.g. the absence of sharp corners and the use of smooth wall surfaces, preferably at a small inclination. These requirements are beneficial to allow the straightforward demoulding of the samples. [88,89] Various methods can be used to structure the mold such as mechanical micromachining, laser structuring, electric discharge machining, lithography with x-rays or electroplating. [80] For our purpose, the mold was formed via ultraprecision diamond tooling, which is a sophisticated micromachining technique that removes material in a controlled manner from e.g. metal substrates including brass. Leaded brass (also known as free machining brass) is particularly interesting for the intended use as mould material given its high durability. [90]

The designed channel pattern consisted of five straight channels of 22 mm and four 180° bends in between. The channels were 500 µm wide and 500 µm deep, with a channel interdistance of 500 µm. In order to asses the quality of the replicated structures, both the mould as well as a structured COC sample were characterised via optical profilometry. In figure 5.12, both the master (a) and the rep-

(a) Mould ($528.3 \pm 20.1\mu m$) **(b)** Channel ($516.5 \pm 20.9\mu m$)
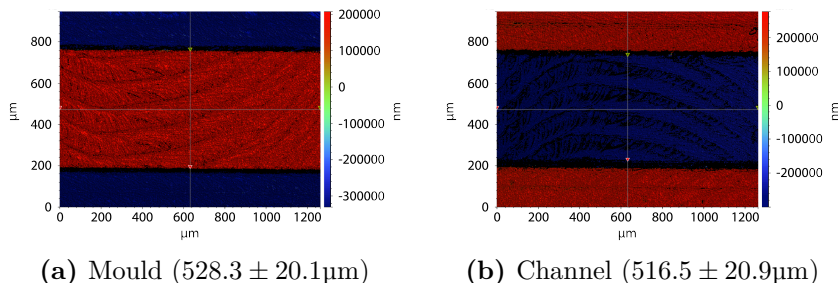
Figure 5.12: Topological evaluation of both the brass mould (a) and the replicated structure in COC (b) via optical profilometry.

licated structure (b) are shown. By measuring the width of both the mould as well as the replicated structure at 5 different positions, the average dimensions of both could be determined. The thus obtained values are also included in figure 5.12 and are not significantly different ($p > 0.05$). This was anticipated based on the minimal (0.1-0.7%) shrinkage observed for COC polymers.[91]

In the upcoming section, the obtained microstructured polymer samples will be evaluated for microfluidic applications.

5.5.1 Validating the processing methodology via static leak tests

To transform the hot embossed polymer plates into fully functional microfluidic chips, the sealing with a top plate with inlet and outlet was performed with the laser welding machine at the respective optimal welding power density, based on prior experience for PLLA, PS and COC (section 5.4).

Static leakage tests were performed to evaluate the water-tightness of the seal by injecting a blue ink into the inlet and allowing the ink to flow to the outlet. This method was selected based on previous reports from other groups that have performed similar experiments to prove the validity of their bonding technique.[46,59,92] The results for PS and COC are shown in figure 5.13. Unfortunately, no leak-proof samples were obtained for the PLLA samples. Figures 5.13a and 5.13b show the PS and COC sample respectively, after the injection of blue ink. For both materials, the channels of the chip were entirely filled with

(a) PS   **(b)** COC
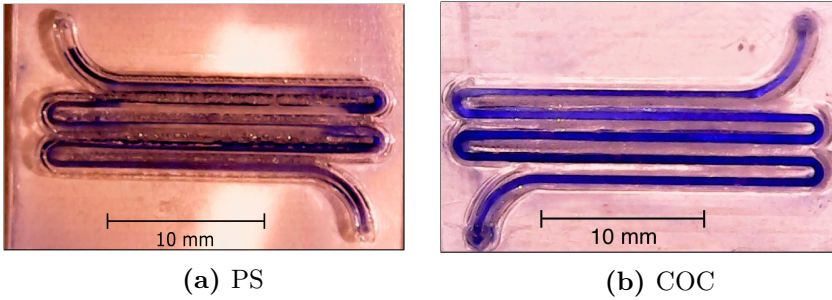
Figure 5.13: Pictures of a welded PS and COC microfluidic chip. After injection of a blue ink dye, no leaks were observed, thus showing the potential of TTir for the sealing of microfluidics

blue ink without observable leakage. However, as can be observed when comparing 5.13a and 5.13b, the channels in COC appear to be much smoother than the ones obtained in PS. Together with the leaky PLLA samples, this indicates that for microfluidic applications with closely spaced channels, the situation is not as straightforward as experienced during the initial shear tests. A possible explanation for these observations may lie in the materials' thermal expansion as expressed by the linear thermal expansion coefficient α. Both COC as well as PS have similar values of α with 6×10^{-5} °C^{-1} and $6 - 8 \times 10^{-5}$ °C^{-1} for COC and PS, respectively.[93] PLA on the other hand is characterised by a higher value of α (8.5×10^{-5} °C^{-1}).[93] Although this difference may seem small, the linear thermal expansion coefficient of PLLA was the highest of all materials studied in the current chapter, which may thus indicate that this parameter should be taken into account when designing the mould and selecting the appropriate welding parameters (e.g. the scan rate).

The microfluidic tests prove that the bonding by TTir laser welding does not only perform well in conceptual shear tests that give a reference benchmark for the bonding strength (shear tests), but are also suitable for tangible applications such as polymer-based microfluidic chips.

5.6 Conclusions

The present chapter focused on the processing of polymers into functional microfluidic chips. It was shown that the combination of injection moulding and hot embossing enables the fabrication of smooth ($R_q < 60\text{-}130$ nm) polymer sheets and the subsequent introduction of microfluidic channels.

Bonding of polymer sheets can be seen as a critical but necessary step in the development of microfluidic devices. Current techniques such as thermal, adhesive and solvent bonding, are either difficult to implement or require pre- or post-processing.[15,53,54] TTir laser welding at 1940 nm thus offers an interesting alternative that was proven to be successful for joining two polymer plates without prior processing nor including additives. The results presented here indicate that shear strengths exceeding 5 MPa were achieved for multiple materials (COC, PLLA, PMMA and PS), which translates into a bonding strength competitive with the state-of-the-art in polymer microfluidic bonding and even outperforming previous reports on the bonding of PMMA, PLLA and HDPE via laser welding. Static leak tests finally confirmed that the achieved weld strengths were sufficient to obtain leak-proof channels for COC and PS.

By optically and chemically characterizing the materials, a basis was established to explain the results obtained during the mechanical shear tests of the welded materials. It has been shown that the successfully welded materials are the ones with absorption values below 4% at 1940 nm. In addition, the materials to be welded should be amorphous or semi-crystalline with a degree of crystallinity $< 30.4\%$, aliphatic polymers with a glass transition temperature exceeding 50 °C. Although both PMMA grades with a molecular weight in the range of 55-60 $\mathrm{kg\,mol^{-1}}$ did not result in a significant difference in weldability ($p > 0.05$), a significant reduction in welding performance was observed for the PMMA grade with a molecular weight of 87.0 $\mathrm{kg\,mol^{-1}}$ ($p < 0.05$). The latter result confirms the hypothesis that weldability is also influenced by the molecular weight of the materials, since other studied parameters were very similar among the tested PMMA grades.

Future work should look into the effect that the observed heat of fusion of semi-crystalline materials has on their weldability. More-

over, supplementary material grades should be tested to evaluate the influence of molecular weight on the welding of other polymers (as this trend was only studied for PMMA). Additional tests with different laser powers and welding speed parameters might allow to further improve the obtained shear strengths. Finally, the study of additional polymers (*e.g.* PET, PTFE or PEEK) would allow the establishment of a full model to predict weldability based on optical and physico-chemical material properties.

Once the syntheses of the polyesters presented in chapters 2 and 3 have been sufficiently upscaled (> 100 g) and attainable molecular weights have been further increased to values around $30 \, \mathrm{kg \, mol^{-1}}$, the methodology presented herein can be applied to obtain truly disposable microfluidics, as the developed materials within the framework of this PhD are all aliphatic, amorphous thermoplasts with similar T_g values as observed for the successfully welded commercial polymers. Since the higher thermal expansion coefficient observed for PLLA has prevented the fabrication of leak-proof microfluidics, the influence of this parameter should be evaluated for the synthesised (co)polymers. In case deformation of the channel walls remains an issue, an optimised mould design may be applied to circumvent this issue. The latter may also be appropriate if the thermo-optic effect that can be expected during laser welding is found to locally alter the refractive index near the sensing zone.

References

[1] H. E. Bennett, J. O. Porteus, *Journal of the Optical Society of America* **1961**, *51*, 123.

[2] J. De Pelsmaeker, H. Thienpont, H. Ottevaere, *to be submitted in Optics Express*.

[3] S. Roh, H. Kim, B. Lee, *J. Opt. Soc. Am. B* **2011**, *28*, 1661–1667.

[4] P. L. Chu, T. Whitbread, *Applied Optics* **1982**, *21*, 4241–4245.

[5] J. A. Curran, *Injection-moulded polystyrene ruler - a photo on Flickriver*, **2002**, `http://www.flickriver.com/photos/core-materials/3840236363/(accessed2017-07-07)`.

[6] R. A. Carlton in *Pharmaceutical Microscopy*, Springer New York, New York, NY, **2011**, pp. 7–64.

[7] M. Worgull, *Hot Embossing - Theory and Technology of Microreplication*, Elsevier, **2009**, p. 345.

[8] J. C. Middleton, A. J. Tipton, *Biomaterials* **2000**, *21*, 2335–2346.

[9] L.-T. Lim, R. Auras, M. Rubino, *Progress in Polymer Science* **2008**, *33*, 820–852.

[10] G.-J. Graulus, T. Billiet, S. Van Vlierberghe, H. Thienpont, H. Ottevaere, P. Dubruel in *Handbook of Sustainable Polymers: Processing and Applications* (Eds.: V. K. Thakur, M. kumari Thakur), Pan Stanford Publishing, **2015**, Chapter 21, pp. 749–798.

[11] T. Desmet, E. Schacht, P. Dubruel in *Tissue Engineering: Roles, Materials and Applications* (Ed.: S. J. Barnes), Nova Science, **2008**, pp. 141–189.

[12] T. Billiet, M. Vandenhaute, J. Schelfhout, S. Van Vlierberghe, P. Dubruel, *Biomaterials* **2012**, *33*, 6020–41.

[13] A. Houben, J. Van Hoorick, J. Van Erps, H. Thienpont, S. Van Vlierberghe, P. Dubruel, *Annals of Biomedical Engineering* **2016**, 1–26.

[14] R. von Oepen, W. Michaeli, *Clinical materials* **1992**, *10*, 21–8.

[15] C.-W. Tsao, D. L. DeVoe, *Microfluidics and Nanofluidics* **2009**, *6*, 1–16.

[16] H. Hinsken, S. Moss, J.-R. Pauquet, H. Zweifel, *Polymer Degradation and Stability* **1991**, *34*, 279–293.

[17] X. Colin, J. Verdu, *Comptes Rendus Chimie* **2006**, *9*, 1380–1395.

[18] C. E. Carraher, R. B. R. B. Seymour, *Seymour/Carraher's polymer chemistry.*, CRC Press, **2007**, p. 738.

[19] G. Widmann, *Interpreting TGA curves*, Metler toledo technical report, **2001**.

[20] R. H. Colby, L. J. Fetters, W. W. Graessley, *Macromolecules* **1987**, *20*, 2226–2237.

[21] F. W. Billmeyer, *Journal of Polymer Science* **1949**, *4*, 83–86.

[22] *Polymer handbook*, (Eds.: J. Brandrup, E. Immergut, E. Grulke), Wiley, 4th ed., **1999**, p. 265.

[23] T. Bremner, A. Rudin, D. G. Cook, *Journal of Applied Polymer Science* **1990**, *41*, 1617–1627.

[24] A. Volpe, F. Di Niso, C. Gaudiuso, A. De Rosa, R. M. Vázquez, A. Ancona, P. M. Lugarà, R. Osellame, *Optics Express* **2015**, *23*, 4114–24.

[25] G. Luka, A. Ahmadi, H. Najjaran, E. Alocilja, M. DeRosa, K. Wolthers, A. Malki, H. Aziz, A. Althani, M. Hoorfar, *Sensors (Basel Switzerland)* **2015**, *15*, 30011–31.

[26] T. Tamaki, W. Watanabe, J. Nishii, K. Itoh, *Japanese Journal of Applied Physics* **2005**, *44*, L687–L689.

[27] X. Wang, H. Chen, H. Liu, *Materials and Design* **2014**, *55*, 343–352.

[28] S. H. Baghjari, S. Akbari Mousavi, S. A. A. A. Mousavi, S. Akbari Mousavi, *Materials and Design* **2013**, *43*, 1–9.

[29] A. Lisiecki, *Laser Technology 2012: Applications of Lasers*, **2013**, pp. 1–11.

[30] X.-L. Gao, L.-J. Zhang, J. Liu, J.-X. Zhang, *The International Journal of Advanced Manufacturing Technology* **2014**, *72*, 895–903.

[31] S. Richter, S. R. S. Döring, A. Tünnermann, S. Nolte, A. T. S. Nolte, *Applied Physics A: Materials Science and Processing* **2011**, *103*, 257–261.

[32] K. Cvecek, I. Miyamoto, J. Strauss, M. Wolf, T. Frick, M. Schmidt, *Applied Optics* **2011**, *50*, 1941.

[33] T. Tamaki, W. Watanabe, K. Itoh, *Optics Express* **2006**, *14*, 10460.

[34] A. Horn, I. Miyamoto, J. Gottmann, D. Wortmann, F. Yoshino, A. Horn, J. Gottmann, D. Wortmann, F. Yoshino, *Journal of laser micro/nanoengineering* **2007**, *2*, 57–63.

[35] X. He, *Materials and Manufacturing Processes* **2012**, *6914*, 120813105610000.

[36] B. Acherjee, D. Misra, D. Bose, K. Venkadeshwaran, *Optics and Laser Technology* **2009**, *41*, 956–967.

[37] M. Dal, R. Fabbro, *Optics and Laser Technology* **2016**, *78*, 2–14.

[38] D. Grewell, A. Benatar, *International Polymer Processing* **2007**, *22*, 43–60.

[39] N. Amanat, C. Chaminade, J. Grace, D. R. McKenzie, N. L. James, *Materials and Design* **2010**, *31*, 4823–4830.

[40] I. Jones in *Woodhead Publishing Series in Biomaterials* (Eds.: Y. Zhou, M. D. Breyen), Woodhead Publishing Limited, 1st ed., **2013**, Chapter 13, pp. 344–371e.

[41] V. Kagan, A. Chambers, R. Bray, *Journal of Reinforced Plastics and Composites* **2003**, *22*, 593–602.

[42] N. M. Woosman, R. a. Sallavanti, G. Corporation, *ANTEC* **2003**, 2522–2526.

[43] V. a. Kagan, N. M. Woosman, *Journal of Reinforced Plastics and Composites* **2004**, *23*, 351–359.

[44] M. Chen, G. Zak, P. J. Bates, *Journal of Materials Processing Technology* **2011**, *211*, 43–47.

[45] T. B. Juhl, J. D. C. Christiansen, E. A. Jensen, *Polymer Testing* **2013**, *32*, 475–481.

[46] A. Singh, W. Pfleging, M. Beiser, C. K. Malek, *Microsystem Technologies* **2013**, *19*, 445–453.

[47] G. Galtieri, A. Visco, D. Nocita, L. Torrisi, G. Cecciob, C. Scolaro, G. Ceccio, C. Scolaro, *Journal of Instrumentation* **2016**, *11*, C04013–C04013.

[48] T. S. Mccomb, R. A. Sims, C. C. C. Willis, P. Kadwani, V. Sudesh, L. Shah, M. Richardson, *Applied optics* **2010**, *49*, 6236.

[49] K. Scholle, S. Lamrini, P. Koopmann, P. Fuhrberg in *Frontiers in Guided Wave Optics and Optoelectronics* (Ed.: B. Pal), Intech, **2010**, Chapter 2.

[50] I. Mingareev, F. Weirauch, A. Olowinsky, L. Shah, P. Kadwani, M. Richardson, *Optics and Laser Technology* **2012**, *44*, 2095–2099.

[51] W. Shi, Q. Fang, X. Zhu, R. A. Norwood, N. Peyghambarian, *Applied Optics* **2014**, *53*, 6554–6568.

[52] S. Ruotsalainen, P. Laakso, V. Kujanpää, *Physics Procedia* **2015**, *78*, 272–284.

[53] F. Dang, S. Shinohara, O. Tabata, Y. Yamaoka, M. Kurokawa, Y. Shinohara, M. Ishikawa, Y. Baba, G. Sridharan, M. J. Schoning, *Lab on a Chip* **2005**, *5*, 472.

[54] C. Lu, L. J. Lee, Y.-J. Juang, *Electrophoresis* **2008**, *29*, 1407–1414.

[55] H. M. Shin, H. W. Choi, *The International Journal of Advanced Manufacturing Technology* **2014**, *75*, 1569–1576.

[56] J. Ma, M. Harooni, B. Carlson, R. Kovacevic, *Materials and Design* **2014**, *58*, 390–401.

[57] J. Maurice, J. Y. Cognard, R. Cre, *International Journal of Adhesion and Adhesives* **2011**, *31*, 715–724.

[58] A. A. Yussuf, I. Sbarski, M. Solomon, N. Tran, J. P. Hayes, *Journal of Materials Processing Technology* **2007**, *189*, 401–408.

[59] A. Volpe, F. Di Niso, C. Gaudiuso, A. De Rosa, R. Martìnez Vàzquez, A. Ancona, P. M. Lugarà, R. Osellame, *Laser-based Micro- and Nanoprocessing IX*, **2015**, p. 935106.

[60] D. A. Mair, M. Rolandi, M. Snauko, R. Noroski, F. Svec, J. M. J. Fréchet, *Analytical Chemistry* **2007**, *79*, 5097–5102.

[61] G.-L. Roth, S. Rung, R. Hellmann, G.-l. R. Stefan, R. Ralf, *Applied Physics A* **2016**, *122*, 1–4.

[62] M. Fiorini, G. Campana, N. Pagano, R. Morelli, *Procedia CIRP*, **2015**, pp. 412–417.

[63] E. Rodríguez-Vidal, I. Quintana, C. Gadea, *Optics and Laser Technology* **2014**, *57*, 194–201.

[64] E. Hecht, *Optics*, Pearson Addison Wesley 2002 (1), 4th ed., **2002**, pp. 95–100.

[65] N. Sultanova, S. Kasarova, I. Nikolov, *Acta Physica Polonica A* **2009**, *116*, 585–587.

[66] Anton   Paar,   *Refractometer*,   **2017**,   `http://www.`
     `anton-paar.com/uk-en/products/group/refractometer/`
     `(accessed2017-06-28)`.

[67] V. N. Tsvetkov, I. N. Shtennikova, *Macromolecules* **1978**, *11*,
     306–312.

[68] F. Kakali, J. K. Kallitsis, *Macromolecules* **1996**, *29*, 4759–4763.

[69] L. Delbreilh, A. Bernès, C. Lacabanne, J. Grenet, J.-M. Saiter,
     Materials Letters **2005**, *59*, 2881–2885.

[70] G. Montaudo, C. Puglisi, R. Rapisardi, F. Samperi, *Polymer
     Degradation and Stability* **1991**, *31*, 229–246.

[71] C. L. Beyler, M. M. Hirschler, *SPE Handbook of Fire Protection
     Engineering* **2001**, 110–131.

[72] V. B. F. Mathot, M. F. J. Pijpers, *Journal of Applied Polymer
     Science* **1990**, *39*, 979–994.

[73] X. Luo, *Effects of SureFlo ® on the Crystallization and Melting
     Behavior of Semi-Crystalline Polyethylene (PE) and Polypropyl-
     ene (PP) Systems*, Flow polymers llc technical report, **2017**.

[74] R. Klein, *Laser welding of plastics*, Wiley-VCH Verlag, **2011**,
     pp. 59–60.

[75] D. M. Kulich, S. K. Gaggar, V. Lowry, R. Stepien, *Acrylonitrile-
     Butadiene-Styrene Polymers*, **2001**, `http://doi.wiley.com/`
     `10.1002/0471440264.pst011`.

[76] R. Marissen, D. Schudy, A. V. J. M. Kemp, S. M. H. Coolen,
     W. G. Duijzings, A. Van Der Pol, A. J. Van Gulick, *Journal of
     Materials Science* **2001**, *36*, 4167–4180.

[77] D. P. Cole, J. C. Riddick, H. M. Iftekhar Jaim, K. E.
     Strawhecker, N. E. Zander, *Journal of Applied Polymer Science*
     2016, *133*, 12.

[78] T. B. Juhl, D. Bach, R. G. Larson, J. D. Christiansen, E. A.
     Jensen, *Polymer (United Kingdom)* **2013**, *54*, 3891–3897.

[79] D. Yao, V. L. Virupaksha, B. Kim, *Polymer Engineering and Science* **2005**, *45*, 652–660.

[80] B. D. Ratner, K. W. Gladhill, T. A. Horbett, *Journal of Biomedical Materials Research* **1988**, *22*, 509–527.

[81] H. Nishida, S. Suzuki, Y. Tokiwa, *Journal of Environmental Polymer Degradation* **1998**, *6*, 43–58.

[82] J. P. Eubeler, M. Bernhard, T. P. Knepper, *TrAC Trends in Analytical Chemistry* **2010**, *29*, 84–100.

[83] Y. J. Juang, L. Lee James, K. W. Koelling, *Polymer Engineering and Science* **2002**, *42*, 539–550.

[84] N. Bogdanski, M. Wissen, A. Ziegler, H. C. Scheer, *Microelectronic Engineering*, **2005**, pp. 598–604.

[85] H. D. Rowland, A. C. Sun, P. R. Schunk, W. P. King, *Journal of Micromechanics and Microengineering* **2005**, *15*, 2414–2425.

[86] H. D. Rowland, W. P. King, J. B. Pethica, G. L. W. Cross, *Science* **2008**, *322*, 720–724.

[87] J. M. Park, T. G. Kang, S. J. Park, *Korea-Australia Rheology Journal* **2011**, *23*, 139–146.

[88] M. Siotto, E. Sezenna, S. Saponaro, F. D. Innocenti, M. Tosin, L. Bonomo, V. Mezzanotte, *Journal of Environmental Management* **2012**, *93*, 31–37.

[89] J. P. Eubeler, S. Zok, M. Bernhard, T. P. Knepper, *TrAC Trends in Analytical Chemistry* **2009**, *28*, 1057–1072.

[90] S. Kuyucak, M. Sahoo, *Canadian Metallurgical Quarterly* **1996**, *35*, 1–15.

[91] TOPAS Advance Polymers GmbH, *Cyclic Olefin Copolymer (COC)*, Topas advance polymers gmbh technical report, **2017**.

[92] Y. Temiz, R. D. Lovchik, G. V. Kaigala, E. Delamarche, *Microelectronic Engineering* **2015**, *132*, 156–175.

[93] Omnexus by SpecialChem, *Coefficient of Linear Thermal Expansion*, **2017**, `https://omnexus.specialchem.com/polymer-properties/properties/coefficient-of-linear-thermal-expansion`.

Chapter 6

Conclusions and outlook

"An expert is a man who has made all the mistakes which can be made in a very narrow field."

— Niels Bohr

6.1 General conclusions

As indicated in this thesis' introduction, even today the microbiological contamination of water poses a serious health risk. Current detection techniques heavily rely on cell cultures in order to quantify the number of microorganisms present in a sample in order to meet the stringent water quality demands imposed by the World Health Organisation. However, these techniques are time-consuming (> 24 h), expensive (approx. € 150) and suffer from a lack of portability since they require specialised facilities. Lab-on-a-chip biosensors show great promise to overcome these drawbacks and more and more prototypes are being described in literature.

The present PhD research was situated within a project focused on the development of a portable surface plasmon resonance (SPR)-based sensor for the screening of water samples. SPR was selected as transduction method given its high sensitivity without the need for prior labeling of the target analyte and the possibility to perform analyses in real-time resulting in short measurements (approx. 30 minutes).

Since the consumption of contaminated water particularly affects those living in developing countries, the cost per analysis is another important parameter that was taken into consideration. The envisioned LoC sensor will therefore consist of a reusable external read-out system in combination with mass-manufacturable, single-use microfluidic cartridges, since microfluidic channels are generally difficult to rinse.[1,2] In this context, polymers were selected as sensor substrate as they are cost-effective and can be processed via common processing techniques such as injection moulding.

To minimise the environmental impact of the single-use microfluidics and introduce a straightforward route towards the recuperation of the noble metal layers applied in SPR-based sensing, degradable polymers were explored for application in disposable microfluidics. To achieve this goal, the current PhD explored the applicability of degradable polyesters as base material for the development of microfluidic sensors. In order to be applicable in developing countries in the tropics, the materials require dimensional stability at temperatures up to 60 °C and should be optically transparent at the wavelength applied to excite the SPPs i.e. 661 nm for the envisioned demonstrator. These constraints excluded the application of commonly applied degradable polyesters as poly(glycolide), poly(lactide) and poly(ε-caprolactone) as these materials are either semi-crystalline limiting their optical performance, or exhibit a relatively low glass-transition temperature (T_g up to 50 °C).

Chapter 2 therefore explored the copolymerisation of lactide and its mandelic acid analogue (i.e. mandelide) to obtain optically transparent polyesters with a T_g exceeding 60 °C. Mandelide was obtained via the acid-catalysed dimerisation, although the yield was limited to approx. 25% as only the (R,S)-mandelide diastereomer is suitable for the subsequent polymerisation in bulk or solution. This meso-mandelide was subsequently applied in bulk and solution polymerisations. Despite an earlier report, the bulk (co)polymerisation of mandelide did not result in satisfactory results. The solution polymerisations of lactide and mandelide on the other hand followed first-order kinetics. Although dispersities remained low during the polymerisations, a large discrepancy between the theoretical and obtained molecular weight was observed for mandelide-containing copolymers. A

detailed study of mandelide in a variety of solvents revealed the spontaneous racemisation of the meso-mandelide diastereoisomer in highly polar solvents (i.e. DMSO and DMF). An alcohol selective reaction with trichloroacetyl isocyanate, suggested that this racemisation occurred via an enol-intermediate. Although Liu *et al.* did not explain the racemisation of mandelide that was observed during the solution polymerisation of mandelide in acetonitrile, the formation of enolic-adduct may explain the lower than expected M_n values. Despite this issue, thermal analyses confirmed that the obtained copolymers were 100% amorphous with T_g values that could be effectively increased by incorporating mandelide in the polymer structure. The low molecular weights, however, did not allow the synthesis of copolymers with a T_g in excess of 60 °C as was the principle aim of the performed research efforts. Moreover, the molecular weights resulted in considerable stress-cracking in the solvent-cast samples, thereby reducing the optical clarity of the samples. The latter effect prevented the objective to synthesise highly transparent materials ($> 95\%$ transmission) to be fulfilled.

Given the low monomer yield and limited molecular weight associated with mandelide derived (co)polymers, O-carboxy anhydrides were presented in chapter 3 as a viable alternative to increase the monomer yield and increase the control over the obtained molecular weights. Both the lactic acid as well as the mandelic acid OCA derivative were synthesised via direct carbonylation of the α-hydroxy acids by diphosgene. As expected, the obtained yields were shown to be much higher for both monomers (58 % and 85% for lacOCA and manOCA, respectively), thus realising the objective to increase the monomer yield. Given the toxicity of the diphosgene required for the monomer synthesis, the scale at which the OCA-monomers could be synthesised in a safe way was limited. Therefore, the potential of flow chemistry for the continuous synthesis of OCA-monomers was explored. These preliminary experiments revealed that a conversion of 17% could be obtained within 4 minutes, which is promising with respect to the upscaling of the monomer synthesis. The obtained monomers are subsequently applied in solution (co)polymeriations that yield structurally identical polymers to the ones obtained by polymerising cyclic diesters. Polymerisations of manOCA yielded polyesters

with a molecular weight around $10 \, \text{kg} \, \text{mol}^{-1}$ with excellent dispersities (approximately 1.05). Moreover, the discrepancy between the expected and obtained M_n observed for mandelide polymers could be removed by applying the appropriate polymerisation conditions for manOCA. However, the addition of lacOCA to the monomer feed negatively affected the obtainable molecular weights. This observation was attributed to the poor stability of the lacOCA monomer, which led to the formation of additional initiating species. Despite the low molecular weight found for copolymers of lacOCA and manOCA, the obtained glass transition temperature showed a clear correlation with the composition of the monomer feed. The manOCA homopolymer was able to exceed the predefined target of 60 °C for the T_g. However, the limited molecular weight of the copolymers again resulted in stress-cracking, diminishing the optical transparency.

Chapter 4 focused on the surface modification of the metal layer that is required for the excitation of surface plasmon polaritons. In order to correlate changes in the observed SPR response to the sample's composition, the sensor should be made selective towards the analyte of interest. Given the fact that silver has superior optical properties compared to gold and that silver-based SPR sensors have been reported to have a higher sensitivity, silver was selected in the framework of this PhD. Given the weak nature of the silver-sulphur bond, the formation of a self-assembled monolayer of thiol-containing compounds is not straightforward. Therefore, the surface functionalisation of silver was explored by applying a bioinspired modification methodology relying on poly(dopamine). The amount of surface anchors (i.e. biotin moieties) was regulated by codepositing biotinylated poly(ethylene imine) with poly(dopamine). X-ray photoelectron spectroscopy, atomic force microscopy and static contact angle measurements confirmed the binding potential of the deposited layers towards streptavidin. However, no significant difference could be observed for the applied modification protocols. Therefore, a second series of experiments was performed in which PEGylated PEI was codeposited to reduce aspecific binding on the surface. Moreover, the samples were finally incubated in a solution of biotinylated antibodies to immobilise these biorecognition molecules on the surfaces for subsequent *E. coli* detection. Although a clear trend in terms of nitrogen content

could be observed, the anticipated effect of PEG on the occurrence of aspecific binding could not be demonstrated.

Finally chapter 5, introduced the processing methodology applied to convert polymer materials into leak-proof microfluidic chips. Considering their application in an SPR-based sensor, the formed parts have to meet the requirements associated with optical quality. This implies that the obtained surfaces need to be smooth as indicated by a rooth-mean-square surface roughness (R_q < 130 nm) to minimise scatter losses. Since SPR is only observed for TM-polarised light, internal material stress resulting in birefringence should also be avoided. Both prerequisites can be obtained by applying hot embossing to introduce channels in the polymer materials as this techniques is associated with limited material flow. Since hot embossing results in open channels, the thus obtained chips have to be sealed in such a way that the optical quality of the parts is conserved, which is difficult with conventional techniques as solvent or thermal bonding. To this end, through transmission laser welding was evaluated as a tool to seal the microfluidics in a straightforward way. The potential of laser welding was first evaluated for a series of commercial polymers. The obtained shear strengths were subsequently correlated to the optical and physicochemical properties of these materials in order to predict the applicability for the degradable polyesters discussed in chapters 2 and 3. Transparent, aliphatic polymers were shown to yield the best results. Moreover, the degree of crystallinity should be lower than 30%. These characteristics correspond to the desired properties for the copolymers of lactic and mandelic acid and thus laser welding is expected to be a suitable method for the sealing of polyester microfluidics. By evaluating different grades of PMMA, the weldability was also shown to decrease with increasing molecular weight. Three polymers that performed well in the laser welding experiments, were subsequently hot embossed and sealed via laser welding to obtain microfluidic chips. The leak-proof nature of these chips was finally evaluated by means of static leak tests which revealed that both COC and PS resulted in leak-proof channels, while chips made in PLLA did not. The latter may be a result of the larger coefficient of thermal expansion reported for PLLA. The latter effect should thus be taken

into account when selecting the appropriate mould designs and processing parameters (e.g. scan rate).

With the obtained results directed at increasing the T_g of lactic acid based copolymers, the continuous synthesis of OCA monomers and the processing of amorphous thermoplasts to leak-proof microfluidics, the first hurdles towards truly disposable LoCs were cleared. Moreover, the proposed surface modification methodology was shown to be appropriate to immobilise *E. coli*-specific antibodies on silver and has thus contributed to the development of selective and sensitive silver-based SPR sensors for the detection of *E. coli* in water samples.

6.2   Future perspectives

As detection limits of biosensors are continuously being improved, LoCs are expected to become economically viable for an increasing number of applications. As can be derived from figure 6.1, the research efforts in the field of biosensors and microfluidics have been booming since the early 2000s and at present, biosensor technology is gradually being introduced to the market as point-of-care diagnostics in clinical settings.[3–5] It is expected that this trend will continue in the years to come.[6]

With respect to the materials presented in this PhD, biodegradable polymers are catching up with their non-degradable counterparts despite their inherent higher production cost.[7] At present, biodegradable polyesters are emerging in applications that directly benefit from their degradability including biomedical implants and devices.[8–10] In addition, legislative pressure and growing ecological awareness act as driving forces to advance the field of degradable materials. We expect this research field to further mature as more specialty monomers/polymers become available and current processing issues are resolved.

To date, the polyesters described in this thesis exhibit relatively low molecular weights which negatively affects their thermal, mechanical and optical properties. In order for these materials to be effectively applied in LoC sensor chips, further increasing the molecular weights forms a first objective for future research. Given the spontaneous ring-opening of OCA monomers and the observed racemisation
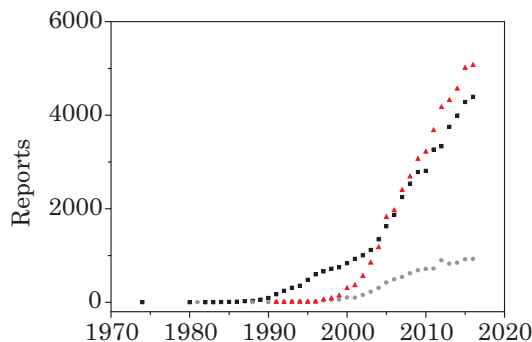
Figure 6.1: Graph showing the increasing research efforts in the field of biosensor development as derived from the number of papers being published annually using the keywords: "biosensor" (black ■) "lab-on-a-chip" (grey ●) and "microfluidics" (red ▲). The data was exported from the Web of Science™ database.

of mandelide in solution polymerisations, bulk (co)polymerisations of mandelide and lactide may be revisited as the highest reported molecular weights for poly(mandelide) were obtained in bulk polymerisations. In this respect, performing the polymerisation in the absence of additional initiator and at lower catalyst amounts may further improve the attainable molecular weight. By increasing the molecular weight to values exceeding 30 kg mol^{-1}, the materials' mechanical, thermal and optical properties (transmission $> 95\%$) can be greatly improved, allowing the synthesis of degradable polyesters with a T_g in excess of 60 °C and good optical clarity. Based on the Fox equation, this implies that the developed materials should contain $> 55\%$ manOCA in order to reach the targeted glass transition temperature.

Once control over the molecular weight has been achieved, another objective will be found in the upscaling of the synthesis (> 100 g). These amounts will enable the fabrication of proof-of-concept laboratory demonstrators via injection moulding and hot embossing. As was discussed in chapter 3, the application of flow chemistry shows potential for the safe synthesis of sufficient amounts of OCA monomers while the amount of diphosgene present in the reactor can be kept low. The highest yield (17%) in flow was obtained after 4

minutes of reaction at 40 °C, while longer reactions or higher reaction temperatures decreased the yield. Therefore, it is proposed that shorter reactions ($<$ 4 min) at lower temperatures (room temperature $\rightarrow$ 0 °C) should be explored, since it is expected that high temperatures result in considerably more ring-opening of the formed OCA monomer. Once the conditions for manOCA have been sufficiently optimised, the same procedure can be translated to other α-hydroxy acids e.g. lactic acid in the context of the present PhD. Once optimised, the reaction can then be transferred to larger scale flow reactors, thereby further increasing the production capacity ($> \times 2$ considering the available laboratory systems).

Next, when larger amounts of monomers are available, the polymerisations can subsequently be performed at a larger scale (e.g. $>$ 100 g) thereby removing batch-to-batch differences. The synthesis of larger amounts of copolymers will also allow thorough degradation studies to be conducted. Based on the reported degradation kinetics of both poly(lactide) and poly(mandelide) it is expected that the samples of the proposed copolymers will exhibit a 50% mass loss in a time frame of 10 - 225 days (50 °C, PBS buffer pH 7.4). Since the influence of the degradation conditions has not been studied for poly(mandelide), the influence of enzymes and/or microorganisms should be evaluated.

After appropriate upscaling of the monomer and polymer syntheses, the produced materials can be applied in processing trials. Considering the applied injection moulding process (chapter 5), this implies multiple kilos of the copolymers will have to be available. Since this is a large step from the 2 g scale mentioned in chapter 3, micro-injection moulding setups like the Xplore introduced by DSM (Geleen, The Netherlands) may offer an alternative for the optimisation of the moulding temperature and pressure on a gram-scale. As mentioned in chapter 1 (section 1.5), discolouration of the polymer during the subsequent processing steps should be avoided. The ideal parameters can then be translated to larger injection moulding set-ups to produce flat polymer sheets with minimal internal stress. Next, the hot embossing set-up available at BPHOT can be applied to process these polymer sheets (Ø up to 30 cm), allowing the simultaneous microstructuring of a large number of microfluidic chips for

application in proof-of-concept demonstrations. The validated channel design should ultimately be translated to an injection moulding insert that can be applied for the mass-manufacturing of the sensor chips. Special care should be taken to select the appropriate cooling times to achieve similar levels of stress as can be reached via hot embossing. The effect of the local heating during laser welding on the material's refractive index should also be evaluated. Should this thermo-optic effect be sufficiently large to negatively affect sensor performance, an optimised mould design may be designed in which the channel diameter in the sensing zone is increased. This would reduce the influence of the laser welding process on the active site, considering the highly localised nature of this bonding technique.

At present, a laboratory demonstrator has been constructed relying on both gold- as well as silver-coated glass prisms. Preliminary measurements using standard solutions with a known refractive index are in accordance with previously performed simulations.[11] Moreover, the results confirm silver's superiority over gold, when considering the attainable sensitivities and indicate that the limit of detection for silver-based measurements can be improved by a factor 10-100 compared to commercial SPR set-ups. The accurate determination of the limit of detection (RIU^{-1}) is planned for the near future. In a second phase, the surface chemistry discussed in chapter 4 will be applied on these silver-coated prisms to perform presence/absence tests for solutions containing a known number of *E. coli bacteria*. From these measurements the limit of detection in $CFU \, mL^{-1}$ can be obtained, allowing the set-up to be compared to commercial SPR set-ups as well as other sensor prototypes presented in literature.[12–15] In this respect, the thickness of the layers deposited on the metal layer should be evaluated (e.g. via ellipsometry), as thinner sensing layers enable the analyte to interact with a larger portion of the evanescently decaying surface plasmon wave. Subsequently, the complexity of the samples will be gradually increased to better represent the conditions experienced during the analysis of actual water samples including turbidity, the presence of other solutes and/or other bacteria. The latter will allow the assessment of the selectivity of the sensor by determining the number of false positive and false negative results.

Finally, the portability of the set-up can be improved by further miniaturising the sensor as well as incorporating external components (e.g. light sources and detectors) on the chip. Moreover, the sensing methodology will require an additional preconcentration step such as immunomagnetic separation and/or a culture time in order to reach the low detection limits imposed by the WHO, which may also be performed on chip.[16,17] Once a satisfactory prototype is available, the potential of multiplexed systems can also be explored, as e.g. SPRi measurements are able to detect multiple analytes during one experiment, thereby further reducing the total analysis time or improving the specificity by including multiple markers.[18,19]

References

[1] F. S. Rodrigues Ribeiro Teles, L. A. Pires de Távora Tavira, L. J. Pina da Fonseca, *Critical Reviews in Clinical Laboratory Sciences* **2010**, *47*, 139–169.

[2] T. Nguyen, S. Kwak, S. J. Karpowicz, *BioTechniques* **2014**, *57*, 267–271.

[3] T. M. Squires, S. R. Quake, *Reviews of Modern Physics* **2005**, *77*, 977–1026.

[4] K. Sato, K. Mawatari, T. Kitamori, *Lab Chip* **2008**, *8*, 1992–1998.

[5] S. Choi, J. Chae, *Microfluidics and Nanofluidics* **2009**, *7*, 819–827.

[6] G. Luka, A. Ahmadi, H. Najjaran, E. Alocilja, M. DeRosa, K. Wolthers, A. Malki, H. Aziz, A. Althani, M. Hoorfar, *Sensors (Basel Switzerland)* **2015**, *15*, 30011–31.

[7] K. Madhavan Nampoothiri, N. R. Nair, R. P. John, *Bioresource technology* **2010**, *101*, 8493–501.

[8] S. S. Lee, P. Hughes, A. D. Ross, M. R. Robinson, *Pharmaceutical research* **2010**, *27*, 2043–53.

[9] B. D. Ulery, L. S. Nair, C. T. Laurencin, *Journal of polymer science. Part B Polymer physics* **2011**, *49*, 832–864.

[10] S. Doppalapudi, A. Jain, W. Khan, A. J. Domb, *Polymers for Advanced Technologies* **2014**, *25*, 427–435.

[11] J. De Pelsmaeker, H. Thienpont, H. Ottevaere, *to be submitted in Optics Express*.

[12] A. D. Taylor, Q. Yu, S. Chen, J. Homola, S. Jiang, *Sensors and Actuators B: Chemical* **2005**, *107*, 202–208.

[13] A. D. Taylor, J. Ladd, Q. Yu, S. Chen, J. Homola, S. Jiang, *Biosensors and Bioelectronics* **2006**, *22*, 752–758.

[14] J. W. Waswa, C. Debroy, J. Irudayaraj, *Journal of Food Process Engineering* **2006**, *29*, 373–385.

[15] Y. Wang, Z. Ye, C. Si, Y. Ying, *Sensors (Basel Switzerland)* **2011**, *11*, 2728–2739.

[16] S. M. Yoo, S. Y. Lee, *Trends in Biotechnology* **2015**, *34*, 7–25.

[17] O. Torun, I. s. Hakkı Boyacı, E. Temür, U. Tamer, Ö. Torun, I. s. Hakkı Boyacı, E. Temür, U. Tamer, *Biosensors and Bioelectronics* **2012**, *37*, 53–60.

[18] I. Stojanović, R. B. M. Schasfoort, L. W. M. M. Terstappen, *Biosensors and Bioelectronics* **2014**, *52*, 36–43.

[19] M. Puiu, C. Bala, *Sensors (Basel Switzerland)* **2016**, *16*, 870.

Appendix A

Materials and methods

A.1 Materials

All commercial chemicals used in the present work are listed in table
table A.1 on the following pages and were used as received unless
stated otherwise.

A.1.1 Monomer purification

Lactide was recrystallised from hot ethyl acetate prior to use and the
obtained crystals were dried *in vacuo* for 48 hours.

A.1.2 Procedures applied to obtain dry solvents

Dry THF, methylene chloride, triethylamine and acetonitrile were ob-
tained from a solvent purification system (SPS, Prof. Richard Hoo-
genboom) and stored over molecular sieves (4 Å) until used.

Other solvents were refluxed over sodium/benzophenone (toluene,
diethyl ether, hexane) or calcium hydride (ethyl acetate, neohexanol,
neopentanol) and collected over molecular sieves (4 Å). In case of
toluene and hexane, 20 mL of tetraglyme was added to solubilise the
benzophenone.

Table A.1: Overview of commercial chemicals used in the present work

Compound	Supplier	Grade
(+)-Biotin	Acros Organics (Geel, Belgium)	98%
Acetone	Univar (Brussels, Belgium)	Technical grade
Acetone-d6	Sigma-Aldrich (Bornem, Belgium)	99.9%D
Acetonitrile	Sigma-Aldrich (Bornem, Belgium)	Anhydrous (99.8%)
Acetonitrile	Sigma-Aldrich (Bornem, Belgium)	HPLC grade($\geq$ 99.9%)
Acetonitrile-d3	Sigma-Aldrich (Bornem, Belgium)	99.8%D
Activated Carbon	Sigma-Aldrich (Bornem, Belgium)	Granular (mesh 4-8)
Ammonium chloride	Sigma-Aldrich (Bornem, Belgium)	$\geq$ 99.5%
Calcium hydride	Acros Organics (Geel, Belgium)	$\pm$93%
Chloroform	Chem-Lab Analytical (Diegem, Belgium)	$\geq$ 99%
Chloroform	Sigma-Aldrich (Bornem, Belgium)	HPLC grade ($\geq$ 99.5%)
Cyanuric chloride	Sigma-Aldrich (Bornem, Belgium)	99%
Deuterium oxide	Euriso-Top (Saint-Aubin Cedex, France)	99.90%D
Deuteroform, CDCl3	Euriso-Top (Saint-Aubin Cedex, France)	99.80%D
Dichloromethane	TCI Europe (Zwijndrecht, Belgium)	HPLC grade ($\geq$ 99.5%)
Diethyl ether	Chem-Lab Analytical (Diegem, Belgium)	$\geq$ 99%
Dimethyl formamide	Sigma-Aldrich (Bornem, Belgium)	Anhydrous (99.8%)
Dimethyl sulfoxide	Acros Organics (Geel, Belgium)	99.7%
Dimethylaminopyridine	Sigma-Aldrich (Bornem, Belgium)	$\geq$ 99%

Continued on next page

Table A.1 – *Overview of commercial chemicals used in the present work - Continued from previous page*

Compound	Supplier	Grade
Dimethylsulfoxide-d6	Euriso-Top (Saint-Aubin Cedex, France)	99.80%D
Diphosgene	Sigma-Aldrich (Bornem, Belgium)	≥ 97%
Dopamine hydrochloride	Sigma-Aldrich (Bornem, Belgium)	98%
Ethyl acetate	Univar (Brussels, Belgium)	Technical grade
1-Ethyl-3-(3-dimethylaminopropyl) carbodiimide hydrochloride	Sigma-Aldrich (Bornem, Belgium)	≥ 98%
Hexane	Chem-Lab Analytical (Diegem, Belgium)	≥ 99%
Isopropanol	Chem-Lab Analytical (Diegem, Belgium)	≥ 99%
Lactic Acid	Acros Organics (Geel, Belgium)	98%
Lactide	Sigma-Aldrich (Bornem, Belgium)	≥ 98%
Mandelic acid	Acros Organics (Geel, Belgium)	≥ 99%
Methanol	Chem-Lab (Diegem, Belgium)	≥ 99%
Methanol	Sigma-Aldrich (Bornem, Belgium)	HPLC grade (≥ 99.9%)
Methanol-d4	Sigma-Aldrich (Bornem, Belgium)	99.80%D
Methylene chloride-d2	Euriso-Top (Saint-Aubin Cedex, France)	99.90%D
Molecular sieves 3 Å	Sigma-Aldrich (Bornem, Belgium)	Mesh 10
Molecular sieves 4 Å	Sigma-Aldrich (Bornem, Belgium)	Mesh 10
Molecular sieves 4 Å, deuterated	Euriso-Top (Saint-Aubin Cedex, France)	Mesh 8-12, 99.8%D
Neohexanol	Sigma-Aldrich (Bornem, Belgium)	98%
Neopentanol	Sigma-Aldrich (Bornem, Belgium)	99%

Continued on next page

Table A.1 – *Overview of commercial chemicals used in the present work - Continued from previous page*

Compound	Supplier	Grade
N-Hydroxysuccinimide	Sigma-Aldrich (Bornem, Belgium)	98%
Poly(ethylene glycol) methylether	Sigma-Aldrich (Bornem, Belgium)	$2 \mathrm{~kg\,mol^{-1}}$
Poly(ethylene imine)	Sigma-Aldrich (Bornem, Belgium)	$60 \mathrm{~kg\,mol^{-1}}$, branched
Potassium carbonate	Sigma-Aldrich (Bornem, Belgium)	Anhydrous ($\geq$ 99%)
p-Toluenesulfonic acid monohydrate	Janssen Chimica (Geel, Belgium)	$\geq$ 98%
Pyridine	Sigma-Aldrich (Bornem, Belgium)	Anhydrous (99.8%)
Sodium	Sigma-Aldrich (Bornem, Belgium)	99.9%
Sodium bicarbonate	Acros Organics (Geel, Belgium)	$\geq$ 99.7%
Sodium chloride	Sigma-Aldrich (Bornem, Belgium)	$\geq$ 99%
Stannous (II) octoate	Sigma-Aldrich (Bornem, Belgium)	$\geq$ 92%
Tetrahydrofuran	Sigma-Aldrich (Bornem, Belgium)	Anhydrous $\geq$ 99.9%
THF-d8	Sigma-Aldrich (Bornem, Belgium)	$\geq$ 99.5%D
Toluene	Chem-Lab (Diegem, Belgium)	$\geq$ 99.7%
Toluene-d8	Sigma-Aldrich (Bornem, Belgium)	99.6%D
Trizma base	Sigma-Aldrich (Bornem, Belgium)	$\geq$ 99.9%
Trizma hydrochloride	Sigma-Aldrich (Bornem, Belgium)	$\geq$ 99.9%
Water	Millipore (Overijse, Belgium)	Milli Q ($54.9.~\mathrm{nSv\,cm^{-1}}$)
Water	Millipore (Overijse, Belgium)	Milli RO ($27.2~\mathrm{\mu Sv\,cm^{-1}}$)
Xylenes	Sigma-Aldrich (Bornem, Belgium)	Reagent grade

Table A.2: Overview of the commercial polymers applied in chapter 5

Abbreviation	Material	Supplier	Grade
ABS	acrylonitrile butadiene styrene copolymer	Trinseo	Magnum 3453
COC	cyclic olefin copolymer	Topas	Grade 6013
HDPE	high density polyethylene	Equistar	Alathon H5618
PA6	polyamide 6	Lanxess	Durethan B29
PC	polycarbonate	Covestro	Makrolon 2205
PLLA	poly(L-lactic acid)	Natureworks	Ingeo 3251D
$PMMA_1$	poly(methylmethacrylate)	Evonik	Plexiglas 99542
$PMMA_2$	poly(methylmethacrylate)	Evonik	Plexiglas 7N
$PMMA_3$	poly(methylmethacrylate)	Arkema	Altuglas V046102
PP	polypropylene	Ineos	402-CB12
PS	polystyrene	Trinseo	Styron C-Tech

A.2   Synthesis procedures

A.2.1   Chapter 2: polyesters from cyclic diesters

Synthesis of mandelide

Mandelide was prepared following a slightly adapted procedure found in literature.[1] In brief, 20 g (132 mmol) DL-mandelic acid and 0.68 g (3.96 mmol) p-toluenesulfonic acid were dissolved in 2000 mL of mixed xylenes. The solution was degassed by passing a nitrogen stream through the solution for half an hour while stirring at room temperature. A Dean-Stark trap and condenser were mounted on the flask and the set-up was subsequently purged with nitrogen. The solution was refluxed for 3 days under nitrogen atmosphere. Next, the reaction was allowed to cool to room temperature during which precipitation occurred. The precipitated racemic mandelide (5.286 g, η=30%) was removed by filtration and dried *in vacuo*.

- ^{1}H-NMR(CDCl$_3$, ppm): 7.3-7.7 (5H, m), 6.61 (1H, s)

- ^{13}C-NMR (CDCl$_3$, ppm): 166.8, 132.5, 129.5, 128.8, 126.3, 77.8

- FT-IR (ATR, cm^{-1}): 3065 (ν(aromatic C-H)), 1754 (ν(C=O)), 1499 (ν(C=C)), 1071 (ν_{as}(C-O)), 743 (δ aromatic C-H)

- GC-MS(EI, m/z): 268

The filtrate was washed with a saturated sodium bicarbonate solution (3 x 100 mL) and brine (3 x 100 mL) and dried over anhydrous magnesium sulphate. After filtration, the solvent was removed by rotary evaporation and the formed precipitate recrystallized from hot ethyl acetate (80 °C) to yield 4.405 g meso-mandelide (η=25%).

- ^{1}H-NMR(CDCl$_3$, ppm): 7.3-7.7 (5H, m), 6.41 (1H, s)

- ^{13}C-NMR (CDCl$_3$, ppm): 164.8, 131.2, 130.0,129.3,126.6,77.9

- FT-IR (ATR, cm^{-1}): 3066 (ν(aromatic C-H)), 1731 (ν(C=O)), 1498 (ν(C=C)), 1039 (ν_{as}(C-O)), 739 (δ aromatic C-H)

- GC-MS(EI, m/z): 268

Bulk (co)polymerisation of cyclic diesters

0.58 g of meso-lactide (4 mmol) and a magnetic stirring bar were added to a priorly flame-dried schlenk vial. Next, 40 µL neohexanol solution (1 mol L^{-1} in toluene) and 20 µL stannous octoate solution (1 mol L^{-1} in toluene) were added to the vial via syringe. The solvent was removed *in vacuo* and the vial was deoxygenated by performing three freeze-pump-thaw cycles. The vial was then placed in an oil bath at 140 °C and stirred for 24 hours. The reaction was then cooled to 4 °C. The content of the schlenk vial was dissolved in dichloromethane and subsequently precipitated in cold methanol. Finally, the precipitate was filtered of and dried *in vacuo*.

The above-mentioned protocol was repeated for different monomer ratios and degrees of polymerisation. The conditions are shown in table A.3

Table A.3: Conditions applied in the melt polymerisation of cyclic diesters.

| Entry | Lactide | Mandelide | | Init. | Cat. |
| | | rac | meso | | |
	[mmol]	[mmol]	[mmol]	[mmol]	[mmol]
a	20.83	-	-	0.42	0.21
b	13.89	-	-	0.27	0.14
c	13.89	-	-	0.14	0.07
d	13.89	-	-	0.07	0.03
e	4	-	-	0.02	0.01
f	69	-	-	0.69	0.35
g	-	6.92	13.88	0.42	0.21
h	-	3.73	7.46	0.02	0.01
i	-	-	11.18	0.22	0.01
j	6.94	-	1.87	0.21	0.11

Solution (co)polymerisation of cyclic diesters

0.58 g of meso-lactide (4 mmol) was added to a priorly flame-dried schlenk vial and dissolved in 4 mL anhydrous toluene. Next, 40 µL neohexanol solution (1 mol L^{-1} in toluene) and 20 µL stannous octoate solution (1 mol L^{-1} in toluene) were added to the vial via syringe. The solution was deoxygenated by performing three freeze-pump-thaw cycles. The vial was then placed in an oil bath at 100 °C and stirred for 24 hours. The reaction was then cooled down to 4 °C. The contents of the schlenk vial was dissolved in dichloromethane and subsequently precipitated in cold methanol. Finally, the precipitate was filtered of and dried *in vacuo*.

The above-mentioned protocol was repeated for different monomer ratios, temperatures and degrees of polymerisation. The conditions are shown in table A.4

Table A.4: Conditions applied in the Sn(II) catalysed solution polymerisation of cyclic diesters performed at 1 mol L^{-1} in acetonitrile (ACN) or toluene (tol.).

Entry	Lactide	Mandelide		Init.	Cat.	Solv.	T
		rac	meso				
	[mmol]	[mmol]	[mmol]	[mmol]	[mmol]		[°C]
a	-	3.73	7.46	0.22	0.11	ACN	70
b	-	3.73	7.46	0.11	0.055	ACN	70
c	4	-	0	0.02	0.01	ACN	70
d	3	-	1	0.02	0.01	ACN	70
e	2	-	2	0.02	0.01	ACN	70
f	1	-	3	0.02	0.01	ACN	70
g	0	-	4	0.02	0.01	ACN	70
h	-	-	1	0.02	0.01	Tol.	100
i	-	-	2.5	0.025	0.0125	Tol.	100
j	0.625	-	1.875	0.025	0.0125	Tol.	100
k	1.25	-	1.25	0.025	0.0125	Tol.	100
l	1.875	-	0.625	0.025	0.0125	Tol.	100
m	2.5	-	-	0.025	0.0125	Tol.	100

A.2.2   Chapter 3: OCA-based materials

Synthesis of lacOCA

1.2 g activated charcoal was added to a flame-dried Schlenk vial and dried *in vacuo* for 2 h. Next, the vial was brought under Ar atmosphere and 7.45 mL D,L-lactic acid (100 mmol) was added to the vial under a blanket of Ar gas. The vial was fitted with a rubber septum and purged with Ar gas followed by the addition of 180 mL anhydrous THF and 2.09 mL triethylamine (15 mmol). The vial was cooled by means of an ice bath (0 °C). 14.48 mL diphosgene (120 mmol) was added dropwise to the stirred reaction medium. The reaction was stirred overnight under Ar atmosphere, while the reaction temperature was allowed to increase to room temperature. The suspension was finally filtered over a celite cake followed by concentrating the filtrate *in vacuo* until ± 10 mL solution remained. This solution was finally layered with 160 mL dry hexane and placed in the fridge (5 °C) to induce crystallisation. After 16 h, white needle-like crystals were obtained (η= 57%) which were washed with dry hexane and dried *in vacuo* and stored under Ar atmosphere at -20 °C.

- ^{1}H-NMR(CDCl$_3$, ppm): 5.09 (1H, q), 1.65 (3H, s)
- FT-IR (ATR, cm^{-1}): 1879 (ν(C=O)), 1788 (ν(C=O)), 1256 (CO-O), 1126 (CO-O), 1101 (C-O), 1075 (C-O), 1035 (CO-O-CO)

Synthesis of manOCA

1.2 g activated charcoal and 15.22 g D,L-mandelic acid (100 mmol) were added to a flame-dried Schlenk vial and dried *in vacuo* for 2 h. Next, the vial was brought under Ar atmosphere and 180 mL anhydrous THF was added. The vial was cooled by means of an ice bath (0 °C). 14.48 mL diphosgene (120 mmol) was added dropwise to the stirred reaction medium. The reaction was stirred overnight under Ar atmosphere, while the reaction temperature was allowed to increase to room temperature. The suspension was finally filtered over a celite cake followed by concentrating the filtrate *in vacuo* until ± 10 mL solution remained. This solution was finally layered with 160 mL dry hexane and placed in the fridge (5 °C) to induce crystallisation.

After 16 h, white cubic crystals were obtained (η= 85%) which were washed with dry hexane and subsequently dried *in vacuo* and stored under Ar atmosphere at -20 °C.

- ^{1}H-NMR(CDCl$_3$, ppm): 7.6-7.3 (5H, m), 5.93 (1H, s)
- FT-IR (ATR, cm^{-1}): 1879 (ν(C=O)), 1788 (ν(C=O)), 1600 (ν(C=C)), 1501 (ν(C=C)), 1256 (CO-O), 1126 (CO-O), 1101 (C-O), 1075 (C-O), 1035 (CO-O-CO), 733 (δaromatic C-H), 698 (δaromatic C-H)

Synthesis of mandelic acid-pyridine adduct

0.84 g mandelic acid (5.5 mmol) was placed in a predried two-neck flask equipped with a rubber septum and a vacuum connector. The system was extensively purged with Ar gas, followed by the addition of 10 mL anhydrous THF. Next, 0.435 mL anhydrous pyridine (5.4 mmol) was added to the flask via syringe. The reaction was stirred overnight after which the flask was placed in the freezer (-20 °C) to induce crystallisation. After 24h, the formed crystals were removed via filtration and dried *in vacuo*.

- ^{1}H-NMR(DMSO-d6, ppm): 7.8.58 (2H, m), 7.82 (1H, m), 7.5-7.2 (7H, m), 5.85 (1H, s), 5 (1H, s)

Synthesis of manOCA via flow chemistry

Solutions of D,L-mandelic acid and diphosgene in anhydrous THF or DCM were continuously pumped through various microreactors by means of two Chemyx (Stafford, USA) Fusion 200 syringe pumps. The first experiments were performed on a Labtrix set-up from Chemtrix (Geleen, The Netherlands), while subsequent reactions were performed in a custom-build reactor consisting of PTFE tubing or an Asia Solid Phase Reactors from Syrris Ltd (Royston, United kingdom). The specific amounts and reaction conditions for each reactor type are included in table A.5. The reactor temperature was controlled by means of the accompanying temperature controller in case of the Labtrix set-up, while for the other reactors the reactor volume was submerged in a thermostated oil bath. In all cases, the resulting

solution leaving the reactor outlet was collected in a glass vial under a continuous nitrogen stream. When changing the experimental parameters, a delay of three times the retention time was considered before collecting samples for subsequent ^{1}H-NMR or mass spectroscopy.

Solution (co)polymerisation of OCA monomers

0.5 g of manOCA (5 mmol) and a magnetic stirring bar were added to a priorly flame-dried schlenk vial and dissolved in 5 mL anhydrous toluene. Next, 50 μL dry neohexanol (1 mol L^{-1} in anhydrous toluene) and 50 μL anhydrous pyridine (1 mol L^{-1} in anhydrous toluene) were added to the vial via syringe. The solvent was deoxygenated by performing three freeze-pump-thaw cycles. The vial was fitted with an Ar-filled balloon and placed in an oil bath at 100 °C and stirred for 24 hours. The reaction was then cooled to 4 °C. The content of the schlenk vial was dissolved in dichloromethane and subsequently precipitated in cold methanol. Finally, the precipitate was filtered of and dried *in vacuo*.

Based on the above-mentioned protocol was repeated for different monomer ratios, temperatures and degrees of polymerisation. The amounts are shown in table A.6.

Table A.5: Overview of the observed yield for the synthesis of manOCA under flow conditions for three reactor designs. †: relative to mandelic acid; *:7 equivalents of DIPEA were included.

	Reactor type	Solvent	$M_{mandelic\ acid}$ [mol L^{-1}]	Eq. diphosgene† [-]	Flow [µL min^{-1}]	t [min]	T [°C]	Yield [%]
a	Labtrix microreactor	THF	0.56	1.2	Batch	960	RT	88
b	Labtrix microreactor	THF	0.2	0.5	22	0.5	40	-
c	Labtrix microreactor	THF	0.2	0.5	11	1	40	-
d	Labtrix microreactor	THF	0.2	0.5	2.2	5	40	-
e	Labtrix microreactor	THF	0.2	0.5	22	0.5	60	-
f	Labtrix microreactor	THF	0.2	0.5	11	1	60	-
g	Labtrix microreactor	THF	0.2	0.5	2.2	5	60	-
h	Teflon tubing	THF	0.09	0.55	800	2	RT	-
i	Teflon tubing	THF	0.09	0.55	400	4	RT	-
j	Teflon tubing	THF	0.09	0.55	200	8	RT	-
k	Teflon tubing	DCM	0.09*	0.55	800	2	RT	-
l	Teflon tubing	DCM	0.09*	0.55	400	4	RT	-
m	Teflon tubing	DCM	0.09*	0.55	200	8	RT	-
n	Packed bed reactor	THF	0.2	1	320	4	RT	17
o	Packed bed reactor	THF	0.2	1	640	8	RT	14
p	Packed bed reactor	THF	0.2	1	320	4	60	-
q	Packed bed reactor	THF	0.2	1	640	8	60	-

Table A.6: (co)polymerisation conditions for OCA monomers.

Entry	manOCA [mmol]	lacOCA [mmol]	[M]/[I]/[C] [-]	cat. [-]	init. [-]	solv. [-]	T [°C]	[M] [mol L^{-1}]
a	5	-	100/1/1	pyridine	neohexanol	Tol.	100	2
b	3.75	1.25	100/1/1	pyridine	neohexanol	Tol.	100	2
c	2.5	2.5	100/1/1	pyridine	neohexanol	Tol.	100	2
d	1.25	3.75	100/1/1	pyridine	neohexanol	Tol.	100	2
e	-	5	100/1/1	pyridine	neohexanol	Tol.	100	2
f	-	25	100/1/1	pyridine	neohexanol	Tol.	100	2
g	25	-	100/1/1	pyridine	neohexanol	Tol.	100	2
h	-	8.62	100/1/1	pyridine	neohexanol	Tol.	100	2
i	-	8.62	500/1/1	pyridine	neohexanol	Tol.	100	2
j	-	8.62	100/1/1	DMAP	neohexanol	Tol.	100	2
k	5.61	-	100/1/1	pyridine	neohexanol	Tol.	100	2
l	5.61	-	100/1/1	DMAP	neohexanol	Tol.	100	2
m	5.61	-	500/1/1	pyridine	neohexanol	Tol.	100	2
n	1.25	3.75	500/1/1	pyridine	neohexanol	Tol.	100	2
o	2.5	2.5	500/1/1	pyridine	neohexanol	Tol.	100	2
p	3.75	1.25	500/1/1	pyridine	neohexanol	Tol.	100	2
q	2.5	-	100/1/1	pyridine	neohexanol	Tol.	100	1
r	-	2.5	100/1/1	pyridine	neohexanol	Tol.	100	1

Continued on next page

Table A.6 – *(co)polymerisation conditions for OCA monomers - Continued from previous page*

Entry	manOCA [mmol]	lacOCA [mmol]	[M]/[I]/[C] [-]	cat. [-]	init. [-]	solv. [-]	T [°C]	[M] [mol L^{-1}]
s	2.5	-	100/1/1	pyridine	neohexanol	DCM	25	1
t	-	2.5	100/1/1	pyridine	neohexanol	DCM	25	1
u	2.5	-	500/1/1	pyridine	neohexanol	Tol.	100	1
v	1.25	1.25	500/1/1	pyridine	neohexanol	Tol.	100	1
w	-	2.5	500/1/1	pyridine	neohexanol	Tol.	100	1
x	10	-	100/1/1	pyridine	n-octanol	Tol.	100	1
y	7.5	2.5	100/1/1	pyridine	n-octanol	Tol.	100	1
z	5	5	100/1/1	pyridine	n-octanol	Tol.	100	1
aa	2.5	7.5	100/1/1	pyridine	n-octanol	Tol.	100	1
ab	-	10	100/1/1	pyridine	n-octanol	Tol.	100	1
ac	5	-	100/1/1	DMAP	neopentanol	Tol.	100	1
ad	25	-	500/1/1	DMAP	neopentanol	Tol.	100	1
ae	5	-	100/1/1	DMAP	neopentanol	DCM	25	1
af	25	-	500/1/1	DMAP	neopentanol	DCM	25	1
ag	-	2.5	100/1/1	pyridine	neohexanol	DCM	25	1
ah	-	2.5	100/1/1	DMAP	neopentanol	DCM	25	1
ai	12.5	-	100/1	mandelic acid pyridine adduct		Tol.	100	2
aj	12.5	-	100/1	mandelic acid pyridine adduct		DCM	25	2
ak	3	-	100/1	mandelic acid pyridine adduct		DCM	25	2

Continued on next page

Table A.6 – *(co)polymerisation conditions for OCA monomers - Continued from previous page*

Entry	manOCA [mmol]	lacOCA [mmol]	[M]/[I]/[C] [-]	cat. [-]	init. [-]	solv. [-]	T [°C]	[M] [mol L^{-1}]
al	-	12	100/1	mandelic acid	pyridine adduct	DCM	25	2
am	3	-	100/1/1	pyridine	neopentanol	DCM	25	2
an	-	12	100/1/1	DMAP	neopentanol	DCM	25	2
ao	10	-	100/1	mandelic acid	pyridine adduct	DCM	25	2
ap	10	-	500/1	mandelic acid	pyridine adduct	DCM	25	2
aq	10	-	100/1/1	pyridine	neohexanol	DCM	25	2
ar	10	-	100/1/1	pyridine	neopentanol	DCM	25	1
as	10	-	100/1/1	pyridine	neopentanol	DCM	25	2
at	10	-	100/1/1	pyridine	neopentanol	DCM	25	4
au	5	-	100/1/1	pyridine	neohexanol	DCM	25	2
av	5	-	100/1/1	pyridine	neopentanol	DCM	25	2
aw	5	-	100/1/1	pyridine	neohexanol	Tol.	100	2
ax	5	-	500/1/1	pyridine	neohexanol	DCM	25	2

A.2.3   Chapter 4: surface modification strategies

Synthesis of PEI-g-PEG

Poly(ethylene glycol) methylether (mPEG, M_n 2000 kg mol^{-1}) was covalently coupled to poly(ethylene imine) (PEI, M_n 25 kg mol^{-1}) according to a procedure found in literature.[2] Therefore, 4.44 g of mPEG (2.2 mmol) was dissolved in 800 mL of anhydrous toluene. To this solution, 1.23 g of cyanuric chloride (6.7 mmol) was added. The reaction mixture was stirred overnight at room temperature, after which the solution was concentrated via rotary evaporation prior to precipitating the modified mPEG using hexane. The precipitate was subsequently redissolved in a minimal amount of toluene and reprecipitated in hexane. This precipitation/dissolution process was repeated 3 times to remove the excess of cyanuric chloride. Next, 100 mg poly(ethylene imine) (PEI, M_n 60 kg mol^{-1}) was dissolved in 10 mL deionised water. The pH was adjusted to 13 by the dropwise addition of a NaOH solution (3 mol L^{-1}). Next, the modified mPEG was dissolved in 10 mL deionised water (Milli Q) and added to the PEI solution. The resulting solution was stirred overnight at 45 °C followed by the removal of the unreacted mPEG via dialysis against deionised water (molecular weight cut-off 12,4 kg mol^{-1}) for 24 h with 6 water changes during this period. The resulting solution was concentrated to approx. 25 mL and subsequently diluted to 2 mg mL^{-1} and applied as such in the subsequent surface modification experiments.

- ^{1}H-NMR(D$_2$O, ppm): 3.70 (34 H, s), 2.68 (1 H, m)
- ^{13}C-NMR(D$_2$O, ppm): 71.81, 71.07, 69.65, 60.43, 58.13

Synthesis of PEI-g-biotin

D-biotin was covalently coupled to PEI (M_n 60 kg mol^{-1}) according to a procedure proposed by Tsai *et al.*[3] Therefore, 100 mg of PEI (0.55 mmol of primary amines) was dissolved in 10 mL of deionised water (Milli Q). To this solution, 203 mg of D-Biotin (0.8 mmol), 129 mg of (EDC, 0.8 mmol and 96 mg of N-hydroxy succinimide (NHS, 0.8 mmol were added. The reaction mixture was stirred overnight at room temperature, after which the solution was dialysed (molecular

weight cut-off 12,4 kg mol^{-1}) against distilled water (Milli Q) for 24 hours with 6 water changes during this period. The resulting solution was diluted to 0.08 mg mL^{-1} and applied as such in the subsequent surface modification experiments.

- ^{1}H-NMR(D$_2$O, ppm): 4.57 (1 H, m), 4.40 (1 H, m), 3.41 (1 H, m), 3.31 (2 H, m), 3.2-2.2 (20 H ,m) 2.15 (2 H, t), 1.70 (2 H, m), 1.58 (2 H, m), 1.38 (2 H, m)
- ^{13}C-NMR(D$_2$O, ppm): 183.37, 165.24, 61.99, 60.25, 55.44, 39.83, 37.43, 28.42, 27.81, 25.78

Surface modification of silver samples

Silver-coated glass substrates, obtained via magnetron sputtering, were first rinsed with isopropanol and left to dry in air prior to their surface modification.

A series of samples (AgD) were incubated in a dopamine solution (0.04 mg mL^{-1}) which serves as a control. Next, two series of samples placed in a mixture of an aqueous PEI solution (0.04 mg mL^{-1}) and dopamine (1 mg mL^{-1}) dissolved in tris buffer (10 mmol L^{-1}, pH 8.5). The difference between both series lies in the relative amount of biotinylated PEI to dopamine which was higher in the case of AgP2 (1 to 50) as compared to AgP1 (1 to 100). Deionised water (Milli Q) was added to ensure all modifications were performed at the same final dopamine concentration of 0.25 mg mL^{-1}. The relative amounts are listed in table A.7 It should be noted that the dopamine solution already started to darken, thus indicating the autopolymerisation had already been initiated prior to the addition of the PEI solution.

The samples were incubated in these solutions for a period of 2 hours during which the solutions further darkened indicating the continuing formation of polydopamine. During the incubation time, the solutions were continuously shaken to prevent the deposition of polydopamine clusters. The modified samples were finally removed form their respective solutions and air dried.

Finally, both the modified (AgD, AgP1 and AgP2) and unmodified silver samples were incubated in a streptavidin solution (0.1 mg mL^{-1}). After 2 h, the samples were removed from the solutions and rinsed with PBS buffer (pH 7.8).

Table A.7: Overview of the conditions applied in the surface modification of silver. The relative amounts of the various solutions are listed below: Ag (unmodified silver), AgD (polydopamine coated silver), AgP1 (codeposition of biotinylated PEI and polydopamine (m/m 1/100) on silver), AgP2 (codeposition of biotinylated PEI and polydopamine (m/m 1/50) on silver)

	Dopamine [1 mg mL^{-1}] Eq.	PEI-biotin [0.04 mg mL^{-1}] Eq.	Milli Q Eq.
Ag	N.A.	N.A.	N.A.
AgD	1	0	3
AgP1	1	0.5	2.75
AgP2	1	1	2.5

	Dopamine [2 mg mL^{-1}] Eq.	PEI-PEG [2 mg mL^{-1}] Eq.	PEI-biotin [0.08 mg mL^{-1}] Eq.	Milli Q Eq.
AgD	0.5	0	0	3.5
AgD$_{PEG}$	0.5	2	0	1.5
AgP1$_{PEG}$	0.5	2	0.25	1
AgP2$_{PEG}$	0.5	2	0.5	0.5

Since no significant difference was observed for the previous surface modifications, the experiments were repeated in the presence of the PEGylated PEI following a similar procedure. The relative amounts of the various stock solutions are also given in table A.7. The modified samples were subsequently incubated in a streptavidin solution (0.1 mg mL^{-1})for 2 h, rinsed 7 times with PBS buffer (pH 7.8) and ultimately incubated in a 0.1 mg L^{-1} solution of biotinylated *E. coli* specific antibodies for 2 hours. The samples were air dried prior to their analysis via XPS, AFM and SCA experiments.

A.3 Methods

A.3.1 Nuclear magnetic resonance spectroscopy

^{1}H-NMR spectroscopy was performed on a Bruker (Brussels, Belgium) Avance 300 MHz Ultrashield spectrometer at room temperature. In addition, ^{13}C-NMR spectra were recorded on a Bruker Avance II 400 MHz spectrometer at room temperature. Analyses of the obtained spectra were performed using the ACD/Spectrus Processor (ACD labs).

A.3.2 Fourier Transform Infrared spectroscopy

Fourier transform Infrared (FT-IR) spectroscopy was performed on PerkinElmer Frontier FT-IR/FIR Spectrometer operating in Attenuated Total Reflection mode. The recorded spectra were analysed using the PerkinElmer Spectrum software.

A.3.3 UV-VIS spectroscopy

UV-VIS spectra mentioned in chapter 2 (2.2.1) were recorded on a UVIKON XL spectrometer (Bio-Tek Instruments) equipped with thermostated cuvette holders. Mandelide was dissolved in various solvents at a concentration of $1 \, \text{mg} \, \text{mL}^{-1}$ in quartz cuvettes and the absorbance of the resulting solutions was determined in a wavelength range of 180-900 nm.

A.3.4 Gas Chromatography - Mass Spectrometry

Mass spectroscopy was performed on a Hewlett Packard 5890 gas chromatograph, coupled to a Hewlett Packard G1800B GCD MS-single quadrupole detector (electron impact ionisation) with a mass range of $10\text{-}450 \, \text{g} \, \text{mol}^{-1}$.

A.3.5 X-ray Diffraction analysis

To confirm the chemical structures, X-ray intensity data were collected on a Agilent Supernova Dual Source (Cu at zero) diffractometer equipped with an Atlas CCD detector using CuKα radiation

(λ= 1.54178 Å) and ω scans, at room temperature. The images
were interpreted and integrated with the program CrysAlisPro (Agi-
lent Technologies).[4] Using Olex2,[5] the structure was solved by direct
methods using the ShelXS structure solution program,[6] and refined by
full-matrix least-squares on F^2 using the ShelXL program package.[7]
Non-hydrogen atoms were anisotropically refined and the hydrogen
atoms in the riding mode and isotropic temperature factors fixed at
1.2 times U(eq) of the parent atoms.

Crystal data for meso-mandelide. $C_{16}H_{12}O_4$, M = 268.26, mono-
clinic, space group $P2_1/c$ (No. 14), α= 6.2098(17) Å, b = 7.3905(18)
Å, c = 27.250(9) Å, β= 92.74(3)°, V = 1249.2(6) $Å^3$, Z = 4, T =
293.15 K, ρ_{calc} = 1.426 g cm^{-3}, μ(Cu-Kα) = 0.852 mm^{-1}, F(000) =
560, 20569 reflections measured, 2341 unique (Rint = 0.0906) which
were used in all calculations. The final R1 was 0.0735 (I >2σ(I)) and
wR2 was 0.2166 (all data).

These data can be obtained free of charge from the Cambridge
Crystallographic Data Centre (12 Union Road, Cambridge CB2 1EZ,
UK; fax: (+44-1223-336033; or deposit@ccdc.cam.uk) or online at
www.cam.ac.uk/conts/retrieving.html.

A.3.6 Size Exclusion Chromatography

To study the molecular weight and corresponding dispersities, 10 mg
of polymer was dissolved in 2 mL of HPLC grade chloroform. The
resulting solutions were passed through a 0.45 µm syringe filter and
transferred to a mass vial. The samples were then analysed via size ex-
clusion chromatography (SEC) on a Waters (Zellik, Belgium) Alliance
2596 set-up coupled to an Agilent (Machelen, Belgium) guard column
(PLGel 5 µm) and a mixed D 5 µm column from Agilent (Machelen,
Belgium). The column was eluted with HPLC grade chloroform at a
flow rate of 1 mL min^{-1}. Detection was based on a Waters refractive
index detector 2414. The molecular weights were determined from
the obtained retention times via an external calibration curve using
polystyrene standards (1.2 - 177 kg mol^{-1}).

A.3.7 Capillary viscosimetry

The PA6 (chapter 5, section 5.2) molecular weight was obtained via capillary viscosimetry on a Lauda Proline PV15 (Lauda-Königshofen, Germany) equipped with a Lauda DLK10 thermostat set at 25 °C. PA6 was dissolved in formic acid (5 mg mL^{-1}) at 25 °C and transferred to a Type 1 micro-ubellohde ($\oslash$ 0.4 mm, according to DIN 51562-2). Both the solvent as well as the polymer solution were analyzed in triplicate.

A.3.8 Thermogravimetric Analysis

Thermogravimetric analyses (TGA) were performed on a TA Instruments (Zellik, Belgium) Q50 TGA device. Samples (5-20 mg) were placed in a Pt sample pan and automatically loaded into the furnace. All experiments were performed under inert atmosphere (N_2) unless specified otherwise. When the sample had been placed in the furnace, the temperature was set to equilibrate at 45°C after which the temperature was ramped to 800 celsius at a heating rate of 10 °C min^{-1}. Data analysis was performed using TA Instruments' Universal Analysis software and provided the temperature at which respectively 1% and 5% mass loss was observed, the degradation onset temperature and the amount if residue at 750 °C.

A.3.9 Differential Scanning Calorimetry

Differential scanning calorimetry (DSC) was performed on a TA Instruments (Zellik, Belgium) Q2000 DSC device. Samples (5-10 mg) were placed in hermetic T_0™ aluminium sample pans and subsequently sealed using an aluminium hermetic lid. Samples were then introduced to the device furnace and equilibrated at 45 °C and subsequently ramped at 10°C min^{-1} to the temperature at which 1% mass loss was observed in the preceding TGA analysis. The sample was kept isothermal for 5 minutes and cooled at 10°C min^{-1} to -90 °C followed by another isothermal period of 5 minutes. Finally, the sample was reheated to the previous maximum temperature at 10°C min^{-1}. Data analysis was performed using TA Instruments' Universal Analysis software and provided the glass transition and, if present, the crystallisation and the melting temperature for the studied materials.

A.3.10   Optical transmission measurements

Transmission measurements were performed in a wavelength range of 250-1800 nm using a high-performance optical spectrum analyser with one channel AvaSpec 3648 for UV/VIS and NIR regions (200-1100 nm) and a second channel AvaSpec 256 NIR 1,7 for the NIR region (1000-1800 nm). The spectrum analyser operated at a spectral resolution of 1.4 nm for the first channel and 4 nm for the second channel. Two light sources were applied to span the above-mentioned wavelength regions: a 30 W deuterium lamp for the UV region (emitting between 190 nm and 400 nm) and a 20 W halogen lamp for the VIS–NIR (emitting between 350 and 1800 nm) region. The light was guided from these sources towards the sample via an optical fibre and subsequently focused onto the sample. Polymer samples solvent-cast on glass slides were placed on the opening in a 30 mm diameter integrating sphere (Avantes) and subsequently coupled into another optical fiber which guides the light to the entrance slit of the optical spectrum analyser.

The optical transmission and reflection measurements mentioned in chapter 5 were performed at a wavelength range of 1900-1980 nm using a Jasco V-670 UV-VIS/NIR Spectrophotometer with a total wavelength range of 400 to 2000 nm. Measurements were performed on a minimum of 4 samples per material and a maximum of 7 samples per material. Prior cleaning with isopropanol was done to remove dust and stains before the measurements.

A.3.11   Refractometry

Refractive indices were determined on an Anton Paar (Gentbrugge, Belgium) Abbemat MW refractometer equipped with 8 wavelength filters (435.8 nm, 468.1 nm, 514.5 nm, 532.0 nm, 546.1 nm, 589.1 nm, 645.2 nm and 655.7 nm) and operating in ATR-mode. Samples (1 cm) were clamped against the measuring crystal to ensure a close contact during the analyses. Experiments were performed in fivefold and the results are presented as mean values with the corresponding standard deviation.

A.3.12 Magnetron sputtering of metal layers

Silver layers were deposited by magnetron sputtering using a Balzers deposition tool (Sint-Truiden, Belgium). A base pressure of 5×10^7 mbar was reached and the Ar pressure during sputtering was 5×10^3 mbar. The Ag was sputtered from an elemental sputter target for 11 minutes at 150 W, allowing the deposition of 100 nm thick layers onto glass slides (approximately 1 cm^2). Glass samples were rinsed with isopropanol prior to metal deposition.

A.3.13 Atomic Force Microscopy

The surface roughness of the samples mentioned in chapter 4, was characterised using an atomic force microscope. The images were obtained under ambient conditions on a Digital Instruments (Bresso, Italy) multimode scanning probe microscope equipped with a Nanoscope IIIa controller. After recording 25 µm scans in tapping mode using a Veeco (New York, USA) silicon cantilever, surface roughness analysis was performed using the Nanoscope software (version4.43r8).

A.3.14 Static Contact Angle Measurements

To assess the hydrophilic or hydrophobic nature of materials the static contact angle (SCA) was determined on a Dataphysics (Filderstadt, Germany) SCA20 instrument equiped with a light source and high-speed CCD camera. The sessile drop method was applied to determine the static contact angles for (un)modified silver surfaces. In this method, a drop of water is placed on the surface of interest. Based on the surface's hydrophilicity, the water drop will spread out. The static contact angle was determined 5 s after the first contact with the surface using the circle fitting tool of the SCA20 imaging software (version 2.1.5). For each condition, three samples were analysed with each sample being measured on at least three positions. The results are given as mean values with corresponding standard deviations.

A.3.15 X-ray Photoelectron Spectroscopy

To determine the elemental composition of the subsequently deposited layers during silver modification, X-ray photo-electron spectroscopy

was applied on an ESCA S-probe VG monochromatised spectrometer equipped with an Al K_α X-ray source (1486 eV). Survey scans were recorded on three positions of each sample and the elemental composition of the top surface could be determined by calculating the peak areas in the obtained spectra. A minimum of 2 samples per condition were analysed. The results are given as mean values with corresponding standard deviations.

A.3.16   Micro injection moulding

Micro injection moulding was performed on a DSM (Geleen, The Netherlands) Xplore twin screw compounder combined with the micro injection moulding accessory. PCL and PS granules were melted at respectively 120 and 140 °C and recycled through the compounder until a homogeneous melt was obtained. The material was subsequently extruded in the sample reservoir of the injection moulding accessory (T > 100 °C) and injected in a custom-made mould (Ø 40 mm, thickness 1 mm) which was thermostated at 70 °C. The mould was allowed to cool down to room temperature while maintaining a holding pressure of 2 bar before ejecting the sample.

A.3.17   Injection moulding

The predried materials studied in the framework of the laser welding process were processed into 1 mm thick sheets by means of injection moulding on a Arburg Allrounder 320 S 500-150 for all materials, except the COC by Topas which was ordered in 1 mm sheets from the Kunststoff-Zentrum in Leipzig. From these sheets, samples of dimension 24 mm x 24 mm were milled and used in the subsequent tests.

A.3.18   Hot embossing

Hot embossing was applied to introduce microfluidic channels in the injection moulded sheets. A Jenoptik (Jena, Germany) Hex04 Hot embossing device was applied for all hot embossing experiments. A custom-made mould characterised by five straight channels of 22 mm and four 180° bends in between, was used as an insert. Channels are

500 µm wide and 500 µm deep, with a channel interdistance of 500 µm.

A.3.19   Optical Microscopy

Optical microscopy was performed on a Zeiss (Zaventem, Belgium) Axioplan2. Images included in the present work were captured at a 20x magnification which was achieved by applying a 10x objective in combination with an internal magnification of 2x. The recorded images at this level of magnification correspond to an area of 230x310 µm^2. The associated resolutions in the x- and y-direction is respectively 0.85 µm and 0.99 µm.

By applying polarised light for sample illumination, internal stress in transparent polymers was visualised as coloured streaks spanning the recorded images.

A.3.20   Optical profilometry

The surface roughness of the different materials discussed in chapter 5 were obtained on a BRUKER (Evere, Belgium) Contour GT-I white light interferometric 3D surface metrology optical microscope.

The area of the samples that was investigated had dimensions of 0.85 mm x 1.1 mm, resulting in a total area of 0.935 mm^2. After measuring the average surface roughness which is the average height difference in nm between the measured points in the investigated area, the Root Means Square (RMS) difference over this area was calculated.

A.3.21   Laser Welding

The laser welding is performed on a LPKF Precisionweld 3000 machine. This machine employs a fiber laser at 1940 nm. Its linewidth FWHM is 0.7 nm. It has a modulated Continuous Wave operation mode with a modulation frequency up to 1 kHz. The maximum emission power is 120 W and a power stability of 1% over 4 hours of operation. It optical noise is 1% RMS and beam quality (M^2) of the TEM_{00} mode is < 1.1. The laser has a minimum achievable weld seam width of 100 µm, but spray paint weld tests showed that the

actual Heat Affected Zone (HAZ) is as large as 200 µm, meaning that
any feature within this region around the laser center will inevitably
be affected by the laser in operation. Therefore, a minimum inter-
feature distance between laser welding lines of around 500 µm was
maintained[8–10].

Internally a mirror system is responsible for the controlled move-
ment of the laser over the designed welding circuit with a precision
of approximately 10 µm. This mirror system can also adjust the ver-
tical focus of the laser beam to ensure that it lies in the interface
between the two samples to be welded. The device has a vacuum
pump to provide suction to the aluminum plate upon which samples
are placed as well as an internal clamping system that can build up
pressures up to 6 bar inside the sample holder chamber closed off by
an anti-reflection coated glass window.

Relevant parameters of laser welding include the laser power,
movement speed of the laser, the laser beam size and uniformity.
The welding speed v is fixed to 10 mm s^{-1} in all experiments. In the
present work, the employed laser powers will be expressed as a power
density PD, which represents the laser power P (in W) per irradiated
surface S (in mm^2) in kW mm^{-2}. The irradiated surface in our case
is calculated to be 3.3*10^{-3} mm^2.

The power density is then defined as:

$$PD = \frac{P}{S} = \frac{P}{3.3 * 10^{-3}} \tag{A.1}$$

Other groups have commonly used either the laser power itself
(which is not a proper indicator for the laser power irradiating the
actual welding area, because it does not take into account the irra-
diation zone over which it is distributed) or just the energy per unit
length E (in J mm^{-1}), which can be calculated using the laser power
P (in W) and the laser scanning speed v (in mm s^{-1}).[11]

A.3.22   Mechanical evaluation of weld strengths

All shear tests for the mechanical characterization were performed
using a Universal Testing Machine (UTM) from Instron of the model
5885H. All experiments were first performed using a load cell of 500 N,

the samples that resulted in higher than 500 N strength were further examined with a 10 kN load cell.

At least 10 trials were attempted with each of the materials exposed to various power densities to obtain an average and standard deviation and a range of PDs at which the materials will successfully weld, which gives a clear indication of the PDs at which the material can be welded. After determination of this PD range, an optimal PD was decided at which shear strengths proved to be highest and then a minimum of 4 tests were performed for each material at this laser power.

A.3.23 Statistical analysis

When comparing samples and conditions, significant difference were identified via the student t-test on a 95% confidence interval. Originlab (Northampton, USA) Origin 8.5 was used as statistical software and two values were considered significantly different if $p < 0.05$.

References

[1] T. Liu, T. L. Simmons, D. A. Bohnsack, M. E. Mackay, M. R. Smith, G. L. Baker, E. Lansing, *Macromolecules* **2007**, *40*, 6040–6047.

[2] W.-B. Tsai, Y.-H. Chen, H.-W. Chien, *Journal of Biomaterials Science-Polymer Edition* **2009**, *20*, 1611–1628.

[3] W.-B. Tsai, C.-Y. Chien, H. Thissen, J.-Y. Lai, *Acta Biomaterialia* **2011**, *7*, 2518–2525.

[4] Agilent, *CrysAlis Pro*, **2014**.

[5] O. V. Dolomanov, L. J. Bourhis, R. J. Gildea, J. A. K. Howard, H. Puschmann, *Journal of Applied Crystallography* **2009**, *42*, 339–341.

[6] G. Sheldrick, *Acta Crystallography* **2008**, *A64*, 112–122.

[7] G. Sheldrick, *Acta Crystallography* **2015**, *C71*, 3–8.

[8] G. Zak, L. Mayboudi, M. Chen, P. J. Bates, M. Birk, *Journal of Materials Processing Technology* **2010**, *210*, 24–31.

[9] B. Acherjee, A. S. Kuar, S. Mitra, D. Misra, *CAD/CAM, Robotics and Factories of the Future*, **2016**, pp. 13–21.

[10] H. Liu, W. Liu, D. Meng, X. Wang, *Materials and Design* **2016**, *92*, 246–260.

[11] H. M. Shin, H. W. Choi, *The International Journal of Advanced Manufacturing Technology* **2014**, *75*, 1569–1576.

Appendix B

Supplementary information

> *"You can have data without information, but you cannot have information without data"*
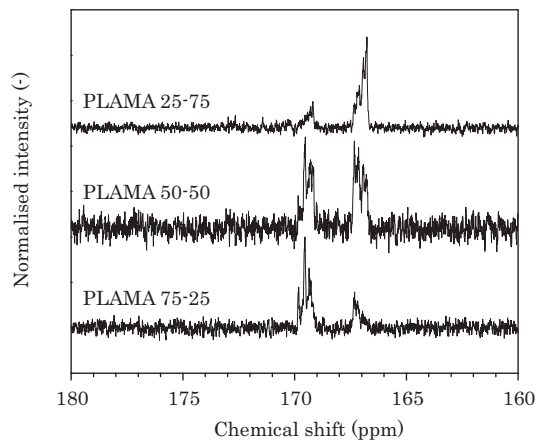>
> — Daniel Keys Moran

Figure B.1: Zoom of the carbonyl region of the ^{13}C-NMR spectra of lactide-mandelide copolymers. The broad carbonyl peaks may be consistent with statistical copolymers, which would imply that the Fox equation is appropriate.

Bijlage C

Nederlandstalige samenvatting

"Mensen van weinig woorden zijn de beste."
— William Shakespeare, Henry V

C.1 Inleiding

Tot op de dag van vandaag zorgt verontreinigd water voor ernstige gezondheidsproblemen. Dit is in het bijzonder het geval in ontwikkelingslanden.[1,2] Vooral de microbiologische besmetting is moeilijk op te sporen omwille van de complexiteit van de micro-organismen en omwille van het feit dat zelfs één pathogeen zich kan vermenigvuldigen tot schadelijke concentraties. Dit bleek ook uit de recente uitbraak van Enterohemorragische *Escherichia coli* (EHEC) in 2011 die in West-Europa aan 53 mensen het leven kostte. Dit zorgt ervoor dat de Wereldgezondheidsorganisatie zeer strenge kwaliteitsregels oplegt voor drinkwater (0 *E.coli* bacteriën per 100 mL).[3,4]

E.coli wordt als indicatororganisme aangewend, omdat deze bacterie in groten getale aanwezig is in de stoelgang van warmbloedige dieren en dus makkelijker te detecteren is dan schadelijke organismen die minder voorkomend zijn.[5] *E.coli* wordt vandaag de dag voornamelijk opgespoord aan de hand van celculturen. Het waterstaal wordt

aan de ideale groeiomstandigheden blootgesteld, waardoor de aanwezige micro-organismen zich kunnen vermenigvuldigen tot detecteerbare aantallen. Deze strategie is echter zeer tijdrovend (> 24 uur), duur ($> € 160$ per analyse) en beperkt tot laboratoria die beschikken over de nodige infrastructuur en geschoolde analisten.[6] Deze nadelen vormen een drempel naar de wijdverbreide toepassing van microbiologische analyses, in het bijzonder in ontwikkelingslanden.

Om deze reden stijgt de interesse voor zogenoemde "labo-op-een-chip"-technologie (LoC). Zoals de naam doet vermoeden, is het doel alle laboratoriumhandelingen te miniaturiseren om het gewicht van de sensor te reduceren ($m < 20$ kg) en zo tot een draagbaar systeem te komen. Dergelijke LoCs vereisen veel minder reagentia en solventen. Specifiek voor sensortoepassingen zorgt de kleinere schaal bovendien voor een reductie van de analysetijden en een verhoging van de gevoeligheid (tot 1-100 amol L^{-1}, afhankelijk van het analiet en de gebruikte transductie methode).[6,7]

Binnen het LoC onderzoek gaat veel interesse uit naar biosensoren. Dit zijn toestellen waarin de binding van de te detecteren verbinding met een gevoelig biologisch herkenningselement (bv. antilichamen, nucleotiden, enzymen, ...) wordt omgezet in een meetbaar signaal.[8] Er bestaan verschillende soorten biosensoren, maar diegene die de binding met het herkenningselement detecteren aan de hand van optische methoden behoren tot de gevoeligste types.[9–11] Oppervlakte plasmon resonantie (SPR) detectie is een voorbeeld hiervan en wordt gebruikt om brekingsindexveranderingen te meten. Wanneer TM-gepolariseerd (transvers magnetisch) licht invalt op een metaalgecoat prisma, zal vanaf een bepaalde invalshoek totale interne reflectie optreden. Voor een welbepaalde golflengte zal bij een bepaalde hoek (ϑ_{SPR}) het licht echter niet gereflecteerd maar geabsorbeerd worden. De hoek waarbij dit wordt waargenomen is afhankelijk van de brekingsindex van het staal dat in contact staat met het metaalgecoat prisma, wat bijzonder interessant is voor biosensor toepassingen.[12]

Omwille van deze gevoeligheid kadert dit doctoraatswerk in de ontwikkeling van een SPR-gebaseerde biosensor. In een eerste deel van het onderzoek werd onderzocht of copolymeren van melk- en amandelzuur voldoen aan de materiaalvereisten voor optische biosensoren. Vervolgens werd de oppervlakmodificatie van zilver bestudeerd

om selectiviteit te kunnen introduceren op het metaaloppervlak. Vervolgens werd de polymeerverwerking via hot embossing en laserlassen geëvalueerd aan de hand van een reeks commerciële polymeren.

C.2 Degradeerbare polyesters

Microfluïdische sensor chips worden doorgaans voor eenmalig gebruik ontworpen, gezien de smalle kanalen moeilijk schoon te spoelen zijn.[13] Hierdoor zouden metingen beïnvloed worden door voorafgaande experimenten, wat de betrouwbaarheid van het verkregen resultaat vermindert. Gezien steeds meer prototypes worden voorgesteld en de eerste biosensoren op de markt komen, zal ook de daarbijhorende afvalstroom toenemen. Dit doctoraatsonderzoek tracht daaarom in te spelen op de vraag naar 'wegwerp'-sensoren door degradeerbare materialen aan te wenden voor de fabricage van de microfluïdische sensorchips. Deze strategie laat toe om de gecontamineerde chips af te breken tot monomeren, die op hun beurt gebruikt kunnen worden in de synthese van nieuwe materialen. Bovendien kunnen de voor SPR vereiste edele metalen op een eenvoudige manier gerecupereerd worden.

Gezien SPR zal worden aangewend als detectiemethode dient het gebruikte materiaal te voldoen aan een aantal vereisten: het materiaal dient optisch transparant (T $>95\%$) te zijn bij de gebruikte golflengte (661 nm) en mechanisch stabiel bij de gebruiksomstandigheden (0-50 °C). Binnen de degradeerbare materialen bestaat de kopgroep uit polyesters als poly(melkzuur), poly(glycolzuur) en poly(ε-caprolacton).[14,15] Deze materialen zijn echter semikristallijn (en dus niet transparant) of vertonen een lage glastransitietemperatuur (T_g <50 °C) wat kan leiden tot vervorming van de chip tijdens het gebruik.

Om polyesters te kunnen toepassen dient de T_g verhoogd (T_g >60 °C) te worden om de vormvastheid van amorfe polyesters te verhogen. Gezien de glastransitietemperatuur bepaald wordt door de flexibiliteit van de polymeerketen, kunnen comonomeren met een grotere zijgroep deze ketenmobiliteit reduceren waardoor de T_g verhoogt.[16] Dit zorgt ervoor dat het materiaal pas bij hogere temperaturen zal vervormen.

Amandelzuur is een melkzuuranaloog waarbij de kleine methylgroep vervangen is door een grote fenylgroep.

Met het oog op de verhoging van de glastransitietemperatuur, werden in dit doctoraatsonderzoek copolymeren van melk- en amandelzuur onderzocht. Twee verschillende monomeerklasses werden vergeleken: enerzijds de gekende cyclische diesters en anderzijds O-carboxyanhydrides.

In het geval van de cyclische diesters werd eerst het cyclisch amandelzuurdimeer, mandelide,[17] gesynthetiseerd en vervolgens gecopolymeriseerd met het commerciële lactide. De bekomen polymeren vertoonden een stijgende glastransitietemperatuur naarmate meer mandelide werd toegevoegd aan het monomeermengsel (figuur C.1a). Karakterisering van de materialen via kernspinresonantie spectroscopie bewees dat beide monomeren succesvol werden ingebouwd in de polymeren. De bekomen moleculaire gewichten vertoonden echter een grote discrepantie met het beoogde moleculair gewicht wanneer mandelide werd gebruikt als (co)monomeer. Een gedetailleerde studie van het mandelide monomeer bracht de spontane racemisering via een enol-derivaat aan het licht. De vorming van enolaten tijdens de polymerisatie is een mogelijke verklaring voor de lager dan verwachte moleculaire gewichten. Optische transmissiemetingen toonden een hoge transparantie aan voor poly(melkzuur) ($> 95\%$). Wanneer meer mandelide werd ingemengd, werden lagere transmissiewaarden opgemeten (figuur C.1b). Visuele inspectie van de stalen toonde aan dat kleine barstjes in het materiaal het invallend licht verstrooiden. Dit fenomeen hangt samen met het lage moleculaire gewicht van de stalen.

Omwille van de onbevredigende moleculaire gewichten voor mandelide copolymeren, werden O-carboxyanhydrides (OCAs) geselecteerd als alternatieve monomeren. Hoewel hogere rendementen ($\eta > 85\%$ voor het amandelzuur-OCA, manOCA) werden bekomen vergeleken met de lactide-analogen ($\eta = 25\%$ voor het overeenkomstige amandelzuur dimeer), was het toxische difosgeen vereist voor de synthese van deze verbindingen. Daarom werd eveneens een aanzet gegeven voor de toepassing van continue *flow* chemie voor de synthese van manOCA. Tot op heden bleek het rendement onder deze condities echter veel lager (ca. 20%) dan bovenvermelde conversie in batch, hoewel de reactietijd sterk gereduceerd kon worden ($t < 10$ min). Zo-

(a)   (b)
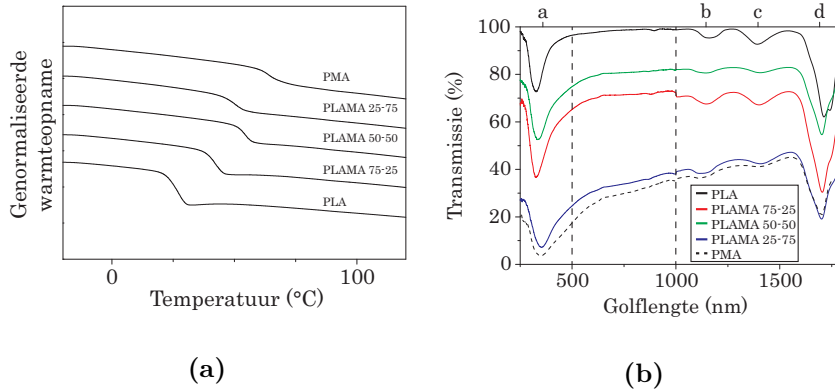
Figuur C.1: Evaluatie van de beoogde eigenschappen. Grafiek (a) toont de toenemende glastransitietemperatuur naarmate meer mandelide wordt ingemengd. Grafiek (b) toont de optische transmissie waarden bekomen voor het golflengtedomein 250-1800 nm. Omwille van de lagere moleculaire gewichten barsten de materialen die mandelide bevatten makkelijk, wat leidt tot meer verstrooiing van het invallend licht.

wel manOCA als het melkzuuranaloog (lacOCA) werden toegepast in polymerisatiereacties.[18] Dankzij de inherent hogere reactiviteit van OCA-monomeren kan de reactie uitgevoerd worden onder mildere reactieomstandigheden (kamertemperatuur). In tegenstelling tot de situatie voor lactide monomeren, werd een goede overeenkomst met het beoogde moleculair gewicht gerealiseerd voor manOCA homopolymeren. Wanneer echter lacOCA werd toegevoegd, werden lager dan verwachte moleculaire gewichten bekomen (ca. 40% van het beoogde moleculaire gewicht). Desondanks toonden thermische analyses van de materialen aan dat de T_g lineair verhoogd kon worden met toenemend manOCA gehalte (figuur C.2), hetgeen een belangrijk doel vormde met oog op de toepassing in microfluïdische biosensoren.
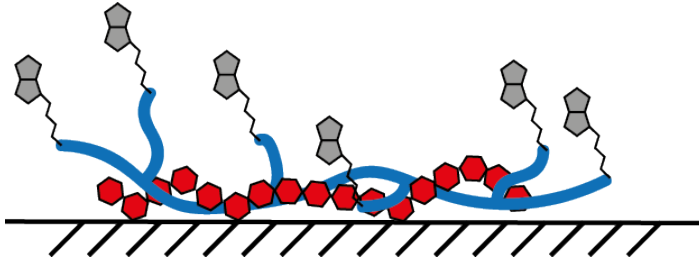
C.3 Oppervlakmodificatie van zilverlagen

De functionalisering van de metaallaag vormt een tweede belangrijke pijler voor succesvolle SPR-biosensoren. In SPR-opstellingen wordt voornamelijk gebruik gemaakt van goud, en in mindere mate zilver.[10] In het geval van goud is de functionalisering met onder andere thi-

(a)

(b)
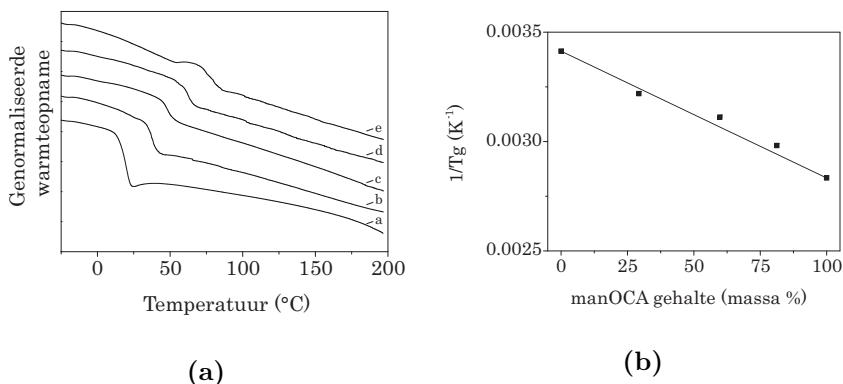
Figuur C.2: Overzicht van de DSC-resultaten voor OCA-copolymeren. Grafiek (a) toont de genormaliseerde warmteopname in functie van de temperatuur voor 5 copolymeren. De gemeten glastransitietemperaturen vertonen een lineaire correlatie met het manOCA gehalte (b). De zwarte lijn geeft de verwachte T_g's weer gebaseerd op de T_g's van beide homopolymeren en de samenstelling van het monomeermengsel in massa%, terwijl ■ de expermenteel bepaalde waarden weergeven.

olen uitgebreid bestudeerd.[19] Zilver wordt gekenmerkt door superieure optische eigenschappen, maar is tot op heden minder bestudeerd omdat zilver sneller dof wordt door interactie met onder meer zwavelbevattende verbindingen.[20] Bovendien vormen thiolen met zilver minder stabiele verbindingen dan met goud. Zilverlagen werden daarom gefunctionaliseerd aan de hand van een biogeïnspireerde poly(dopamine) laag. Om controle te krijgen over het aantal chemische ankers dat wordt geïntroduceerd, werd codepositie van een gebiotinyleerd poly(ethyleen imine) toegepast. Analyses van de afgezette lagen, via x-straal foto-elektron spectroscopie (XPS), atomaire krachtmicroscopie (AFM) en contacthoekmetingen (SCA-metingen), toonden aan dat deze strategie resulteerde in homogene lagen. De biotinemoleculen werden gebruikt om vervolgens streptavidine moleculen te binden. De gebruikte modificatiestrategieën resulteerden in een significante vermindering van de aspecifieke binding vergeleken met zilverlagen. Gebiotinyleerde oppervlakken vertoonden echter geen significante verschillen met een controle bestaande uit puur poly(dopamine). Gezien deze waarneming kan wijzen op aspecifieke

Figuur C.3: Illustratie van de toegepaste oppervlakmodificatie. Gebiotinyleerd PEI (blauwe keten met grijze biotine groepen) werd samen met polydopamine (rode ⬡) afgezet op het zilveroppervlak.

binding van streptavidine op poly(dopamine), werd een tweede derivaat van poly(ethyleen imine) gesynthetiseerd waarbij de primaire amines vervangen werden door PEG-ketens (poly(ethylene glycol)). PEG is in dit opzicht erg interessant gezien het aspecifieke binding aan allerhande oppervlakken reduceert.[21] De nieuwe reeks stalen werd geanalyseerd aan de hand van XPS, AFM en SCA-metingen. Hoewel het stikstofgehalte stelselmatig toenam wanneer de stalen achtereenvolgens werden geïncubeerd in oplossingen van streptavidine en gebiotinyleerde antilichamen, kon het verwachte effect van de PEG ketens echter niet worden aangetoond.

C.4 Polymeerverwerking tot microfluïdica

Om te komen tot microfluïdische biosensorchips dienen de ontwikkelde polymeren verwerkt te worden. Gezien de lage moleculaire gewichten en beperkte hoeveelheden van de gesynthetiseerde polyesters, werd dit deel van het onderzoek uitgevoerd aan de hand van commerciële polymeren. De kanaalstructuur werd aangebracht aan de hand van *hot embossing.*[22] In deze methode wordt het materiaal verwarmd tot boven zijn verwekingstemperatuur, waarna een gestructureerde mal met het negatief van de aan te brengen kanaalstructuur in het materiaal wordt gedrukt. Na afkoelen wordt een negatief van de mal bekomen. Vervolgens dient het gestructureerde substraat afgesloten te worden met een dekplaat. Conventionele bindingsmethoden die gebruik maken van lijmen, temperatuursverhogingen of solventen zijn
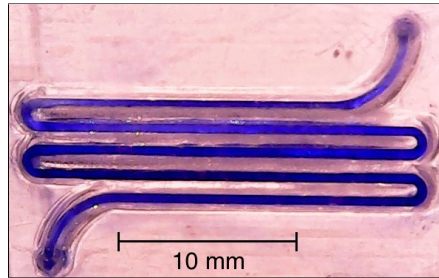
Figuur C.4: Foto van een microfluïdische chip die werd afgesloten door middel van laserlassen. Injectie van een blauwe inktoplossing toont aan dat laserlassen een geschikte methode is om lekvrije kanalen te bekomen.

vaak ongeschikt voor optische toepassingen.[23] Daarom werd in het kader van dit project gebruik gemaakt van een laserlastoestel. Door de interface tussen beide polymeer plaatjes lokaal te versmelten kunnen lekvrije kanalen worden bekomen. Dit werd bevestigd aan de hand van statische lektesten aan de hand van een inktoplossing (figuur C.4). Gezien de beperkte literatuur over het laserlasproces werden 10 verschillende materialen onderworpen aan deze verwerkingstechniek om zo materiaaleigenschappen te correleren aan de toepasbaarheid van deze methoden. Er kan worden geconcludeerd dat goede lasresultaten worden bekomen wanneer de polymeren amorf (of een graad van kristalliniteit <30%) en alifatisch zijn en een hoge transparantie vertonen bij de gebruikte golflengte (1940 nm).

C.5   Conclusies

Het doctoraatswerk droeg bij aan de ontwikkeling van een SPR-gebaseerde biosensor en had als eerste doel om degradeerbare, amorfe materialen te synthetiseren met een glastransitietemperatuur van meer dan 60 °C. Gezien de glastransitietemperatuur kan verhoogd worden door volumineuze zijgroepen in polymeren in te bouwen, werd amandelzuur voorgesteld als interessant comonomeer. Twee verschillende syntheseroutes werden met elkaar vergeleken waarbij melk- en amandelzuur enerzijds werden omgezet in cyclische diesters en anderzijds in O-carboxyanhydrides. Voor beide routes, is dit de eerste melding van de ring opening copolymerisatie van melk- en amandelzuur. Bo-

vendien werd aangetoond dat deze strategie geschikt is om te komen tot amorfe, degradeerbare polyesters met een verhoogde glastransitie-temperatuur. Voor beide monomeerklasses, bleek een grote afwijking te bestaan tussen het bekomen en het verwachte moleculaire gewicht, hetgeen de transparantie beperkte omwille van verstrooiing op barst-jes in de polymeerstalen.

Om detectie via SPR mogelijk te maken, is een dunne metaallaag vereist. De beschikbare literatuur en uitgevoerde simulaties tonen aan dat zilver toelaat de gevoeligheid te verhogen vergeleken met de meer gangbare goud-gebaseerde systemen.[24] Zilver is echter min-der geschikt voor de vorming van *self-assembled monolayers.* In dit doctoraatswerk werden de zilveroppervlakken daarom gefunctionali-seerd met biotine moleculen via codepositie van een gebiotinyleerd poly(ethyleen imine) en poly(dopamine). De oppervlakken waren in staat streptavidine te binden, hetgeen de deur opent naar de koppe-ling van gebiotinyleerde antilichamen.

Ten slotte, dienden de materialen verwerkt te worden tot micro-fluïdische chips. Hiertoe werd een combinatie van hot-embossing en laserlassen toegepast. Het laserlassen van twee transparante lagen is een relatief jonge techniek, maar bleek uitermate geschikt te zijn om gestructureerde polymeer plaatjes af te sluiten om lekvrije sensorchips te bekomen. Bovendien werd aangetoond dat de te lassen materia-len aan een aantal vereisten dienen te voldoen om tot bevredigende resultaten te komen.

Om degradeerbare biosensoren te bekomen, blijft bijkomend on-derzoek evenwel nodig. De bekomen moleculaire gewichten dienen verhoogd te worden ($M_n > 30$ kg mol^{-1}) om zo de mechanische en optische eigenschappen verder te verbeteren. Daarnaast dient de hoe-veelheid aspecifieke binding op de metaallagen verder gereduceerd te worden om de specificiteit van de sensor te verbeteren. Ten slotte, dient het gebonden streptavidine aangewend te worden voor de kop-peling van antilichamen.

Referenties

[1] A. Prüss-Üstün, R. Bos, F. Gore, J. Bartram, *World Health Organization* **2008**, 53.

[2] L. Liu, H. L. Johnson, S. Cousens, J. Perin, S. Scott, J. E. Lawn, I. Rudan, H. Campbell, R. Cibulskis, M. Li, C. Mathers, R. E. Black, *The Lancet* **2012**, *379*, 2151–2161.

[3] The Council of the European Union, *Official Journal of the European Communities* **1998**, *L330*, 32–54.

[4] US Environmental Protection Agency, *National Primary Drinking Water Regulations*, **2007**.

[5] H. Leclerc, D. a. Mossel, S. C. Edberg, C. B. Struijk, *Annual review of microbiology* **2001**, *55*, 201–34.

[6] S. J. Trietsch, T. Hankemeier, H. J. van der Linden, *Chemometrics and Intelligent Laboratory Systems* **2011**, *108*, 64–75.

[7] S. Prakash, M. Pinti, B. Bhushan, *Philosophical Transactions of the Royal Society A: Mathematical Physical and Engineering Sciences* **2012**, *370*, 2269–2303.

[8] J. Kirsch, C. Siltanen, Q. Zhou, A. Revzin, A. Simonian, *Chemical Society Reviews* **2013**, *42*, 8733.

[9] S. Lofas, M. Malmqvist, I. Ronnberg, E. Stenberg, B. Liedberg, I. Lundstrom, *Sensors and Actuators B-Chemical* **1991**, *5*, 79–84.

[10] J. Homola, S. S. Yee, G. Gauglitz, *Sensors and Actuators B-Chemical* **1999**, *54*, 3–15.

[11] C. Situ, M. H. Mooney, C. T. Elliott, J. Buijs, *TrAC - Trends in Analytical Chemistry* **2010**, *29*, 1305–1315.

[12] J. J. Homola, *Analytical and Bioanalytical Chemistry* **2003**, *377*, 528–539.

[13] T. Nguyen, S. Kwak, S. J. Karpowicz, *BioTechniques* **2014**, *57*, 267–271.

[14] K. Madhavan Nampoothiri, N. R. Nair, R. P. John, *Bioresource technology* **2010**, *101*, 8493–501.

[15] M. A. Woodruff, D. W. Hutmacher, *Progress in Polymer Science* **2010**, *35*, 1217–1256.

[16] C. E. Carraher, R. B. R. B. Seymour, *Seymour/Carraher's polymer chemistry.*, CRC Press, **2007**, p. 738.

[17] T. Liu, T. L. Simmons, D. A. Bohnsack, M. E. Mackay, M. R. Smith, G. L. Baker, E. Lansing, *Macromolecules* **2007**, *40*, 6040–6047.

[18] O. Thillaye Du Boullay, E. Marchal, B. Martin-Vaca, F. P. Cossío, D. Bourissou, *Journal of the American Chemical Society* **2006**, *128*, 16442–16443.

[19] H. Hakkinen, *Nat Chem* **2012**, *4*, 443–455.

[20] C. Wang, S. Wang, W. Cai, X. Shao, *Talanta* **2017**, *162*, 123–129.

[21] R. Konradi, C. Acikgoz, M. Textor, *Macromolecular rapid communications* **2012**, *33*, 1663–76.

[22] M. Worgull, *Hot Embossing - Theory and Technology of Microreplication*, Elsevier, **2009**, p. 345.

[23] C.-W. Tsao, D. L. DeVoe, *Microfluidics and Nanofluidics* **2009**, *6*, 1–16.

[24] J. De Pelsmaeker, H. Thienpont, H. Ottevaere, *to be submitted in Optics Express*.

Appendix D

Summary in layman's terms

The consumption of contaminated water constitutes a major health issue in the developing world. When considering microbiological contamination, the presence of *Escherichia coli* can act as a powerful indicator for the water's safety. At present the detection of *E. coli* relies primarily on cell culture based techniques, which are time consuming and require skilled technicians and the proper laboratory infrastructure. In the present work, a contribution is made to the development of photonic biosensors that will allow the fast and straightforward microbiological screening of water samples. These lab-on-chips (LoCs) will consist of single-use cartridges that are placed in an external read-out system. A first part of the present work discusses the synthesis of degradable polymers that allow the fabrication of disposable LoCs. Two classes of monomers were compared to obtain optically transparent polymers exhibiting a sufficiently high glass transition temperature and the capability to mass manufacture. Given the interesting properties of silver with respect to biosensor sensitivity, a bio-inspired immobilisation methodology for *E. coli*-specific antibodies on silver was explored. Next, the fabrication of microfluidic LoCs by means of novel polymer processing techniques was explored for a number of commercial polymers. The obtained results contributed to the better understanding of the relevant polymer properties and offer an improvement to the state-of-the-art. Finally, as a proof-of-concept

a laboratory prototype was developed. The implementation of lab-on-chip technologies will enable a paradigm shift in water contaminant detection by enabling a low-cost, straightforward, real-time and reliable analysis of water samples. To achieve this goal future work should focus on the upscaling of the polymer synthesis and miniaturisation of the final set-up.

Appendix E

List of Publications

"Either write something worth reading or do something worth writing"

— Benjamin Franklin

E.1 Publications in peer reviewed journals

1. J. De Pelsmaeker, **G.-J. Graulus**, S. Van Vlierberghe, H. Thienpont, D. Van Hemelrijk, P. Dubruel, H. Ottevaere, *J. Mater. Process. Technol.* **2018**, (accepted).

2. A. Mignon, J. Vermeulen, **G.-J. Graulus**, J. C. Martins, P. Dubruel, N. De Belie, S. Van Vlierberghe, *Carbohydr. Polym.* **2017**, 168, 44–51.

3. A. Mignon, D. Devisscher, **G.-J. Graulus**, B. Stubbe, J. C. Martins, P. Dubruel, N. De Belie, S. Van Vlierberghe, *Carbohydr. Polym.* **2017**, 155, 448–455.

4. M. A. Pereira Gomes De Araujo, S. Van Vlierberghe, J. L. Garcia Feiteira, **G.-J. Graulus**, K. Van Tittelboom, J. C. Martins, P. Dubruel, N. De Belie, *Mater. Des.* **2016**, 98, 215–222.

5. I. Van Nieuwenhove, A. Salamon, K. Peters, **G.-J. Graulus**, J. C. Martins, D. Frankel, K. E. N. Kersemans, F. De Vos, S.

Van Vlierberghe, P. Dubruel, *Carbohydr. Polym.* **2016**, 152, 129–139.

6. A. Mignon, **G.-J. Graulus**, D. Snoeck, J. C. Martins, N. De Belie, P. Dubruel, S. Van Vlierberghe, *J. Mater. Sci.* **2015**, 50, 970–979.

7. **G.-J. Graulus**, A. Mignon, S. Van Vlierberghe, H. Declercq, K. Fehér, M. Cornelissen, J. C. Martins, et al., *Eur. Polym. J.* **2015**, 72, 494–506.

8. A. Salamon, S. Van Vlierberghe, I. Van Nieuwenhove, F. Baudisch, **G.-J. Graulus**, V. Benecke, K. Alberti, H.-G. Neumann, J. Rychly, J. C. Martins, et al., *Materials (Basel).* **2014**, 7, 1–17.

9. I. Van Nieuwenhove, B. Stubbe, **G.-J. Graulus**, S. Van Vlierberghe, P. Dubruel, *Macromol. Rapid Commun.* 2014, 35, 1351–1355.

E.2   Publications submitted to peer reviewed journals

1. **G.-J. Graulus**, N. Van Herck, K. Van Hecke, H. Thienpont, H. Ottevaere, S. Van Vlierberghe, P. Dubruel, *React Funct Polym.* **2018**.

E.3   Published book chapters

1. **G.-J. Graulus**, T. Billiet, S. Van Vlierberghe, H. Thienpont, H. Ottevaere, P. Dubruel, in *Handbook of Sustainable Polymers: Processing and Applications* (Eds.: V.K. Thakur, M. kumari Thakur), Pan Stanford Publishing, **2015**, pp. 749–798.

2. S. Van Vlierberghe, **G.-J. Graulus**, S. K. Samal, I. Van Nieuwenhove, P. Dubruel, in *Biomedical Foams for Tissue Engineering Applications* (Ed.: P.A. Netti), Woodhead, Cambridge, UK, **2014**, pp. 335–390.